The ionising radiation and gas-phase metallicity in the narrow-line regions of Seyfert galaxies

Adam Douglas Thomas

A thesis submitted for the degree of Doctor of Philosophy of The Australian National University

Research School of Astronomy and Astrophysics
College of Science

December 2018

I hereby declare that the work in this thesis is that of the doctoral candidate, except where indicated in the text. The work was undertaken between February 2015 and June 2018 while I was a PhD student at the Australian National University, Canberra. This thesis has not been submitted in whole or in part for any other degree at this or any other university.

Adam Douglas Thomas

Typeset in $\LaTeX\,2_\varepsilon$

To James Watson

Acknowledgements

A PhD student cannot complete their degree without the support of a great many people, and I'm grateful to all those who've aided me along the way. I'm extremely grateful for the time and expertise offered by the members of my supervisory panel: Lisa Kewley, Mike Dopita, Brent Groves, Andrew Hopkins, and Anne Medling. I would also, in particular, like to thank my officemates, Rajika Kuruwita, Adam Rains, and Eloise Burchill, for their excellent company and the bucket loads of fun we've had together.

On a more formal note, the research presented in this thesis was possible because of the financial support provided by an Australian Government Research Training Program (RTP) Scholarship, an Australian Astronomical Observatory (AAO) PhD Scholarship, an ANU Supplementary Scholarship, a Joan Duffield Scholarship (2017), and other funding from the ANU Research School of Astronomy and Astrophysics (RSAA). I acknowledge the travel funding I've been awarded through the ANU Space Plasma, Astronomy & Astrophysics Scholarship (2016) and the RSAA Alex Rodgers Travelling Scholarship (2018). This research was partially supported by the Australian Research Council Discovery Projects funding scheme (project DP160103631). Parts of this research were supported by the Australian Research Council Centre of Excellence for All Sky Astrophysics in 3 Dimensions (ASTRO 3D), through project number CE170100013.

Abstract

The physical conditions in the narrow-line regions (NLRs) of active galactic nuclei (AGN) may be constrained by comparing spectroscopic observations with photoionisation models. The key parameters are the gas-phase abundances, the ionisation parameter, the gas pressure, and the shape of the ionising spectrum. The first part of this thesis presents a model of the ionising continuum radiation in Seyfert AGN. This model, OXAF, preserves the physically-motivated shapes of existing theoretical models while simplifying them to a three-parameter form designed for photoionisation modelling. The second part of the thesis presents the full data release of the Siding Spring Southern Seyfert Spectroscopic Snapshot Survey (S7). Three-dimensional data cubes, two-dimensional emission-line fits, and other products are provided to the astronomical community, along with a large number of maps of gas kinematics across the S7 sample. In the third part of the thesis, a Bayesian parameter estimation code is presented and used to compare photoionisation model grids with observed emission line fluxes. This code, NebulaBayes, is agnostic to model parameters, dimensionality, and the chosen emission lines. Grids of MAPPINGS photoionisation models are calculated and used with NebulaBayes to study extended NLRs in two dimensions across four 'pure Seyfert' S7 galaxies. The results provide the first robust two-dimensional measurements of gas-phase metallicity in Seyfert NLRs, and show steep metallicity gradients into extraplanar ionisation cones in the case of edge-on galaxy NGC 2992, and an inverse metallicity gradient in the galaxy ESO 138-G01. The near-constant ionisation parameter measurements suggest that radiation pressure regulates the density structure of NLRs on multi-kiloparsec scales. The ionising radiation is measured to be harder in ionisation cones than elsewhere, but the results are sensitive to spectral contamination. The fourth part of this thesis addresses mixing of NLR emission and H II-region emission in star-forming galaxies. The NebulaBayes code is coupled with a 'mixing' grid (combining H II and NLR model grids) and applied to a statistically powerful sample from the Sloan Digital Sky Survey (SDSS), thereby measuring the H II-AGN 'mixing fractions' in SDSS for the first time. For the majority of Seyfert-classified SDSS spectra, the majority of the Balmer emission is found to arise in H II regions as opposed to NLRs. The final results presented in the thesis are the first systematic and robust measurements of the gas-phase metallicities of active galaxies in the SDSS. The SDSS AGN follow a locus in mass-metallicity space that parallels the high-mass end of the star-forming galaxy sequence. We measure a $\sim$0.1 dex increase in oxygen abundance over the observed range of AGN host galaxy masses.

Contents

List of Figures

List of Tables

List of Publications

The articles listed below present research undertaken during the PhD candidature.

First author

Thomas, A. D., Groves, B. A., Sutherland, R. S., et al. 2016, *A Physically based Model of the Ionizing Radiation from Active Galaxies for Photoionization Modeling*, ApJ, 833, 266 (Chapter 2)

Thomas, A. D., Dopita, M. A., Shastri, P., et al. 2017, *Probing the Physics of Narrow-line Regions in Active Galaxies. IV. Full Data Release of the Siding Spring Southern Seyfert Spectroscopic Snapshot Survey (S7)*, ApJS, 232, 11 (Chapter 3)

Thomas, A. D., Dopita, M. A., Kewley, L. J., et al. 2018, *Interrogating Seyferts with NebulaBayes: Spatially Probing the Narrow-line Region Radiation Fields and Chemical Abundances*, ApJ, 856, 89 (Chapter 4)

Thomas, A. D., Kewley, L. J., Dopita, M. A., et al. 2018, *Mixing between Seyfert and HII-region excitation in local active galaxies*, ApJL, 861, L2 (Chapter 5)

Thomas, A. D., Kewley, L. J., Dopita, M. A., et al. 2018, *The mass-metallicity relation of local active galaxies* (submitted to ApJ) (Chapter 6)

Other

Merluzzi, P., Busarello, G., Dopita, M. A., et al. 2018, *An Interacting Galaxy Pair at the Origin of a Light Echo*, ApJ, 852, 113

Green, A. W., Croom, S. M., Scott, N., et al. 2018, *The SAMI Galaxy Survey: Data Release One with emission-line physics value-added products*, MNRAS, 475, 716

Hampton, E. J., Medling, A. M., Groves, B., et al. 2017, *Using an artificial neural network to classify multicomponent emission lines with integral field spectroscopy from SAMI and S7*, MNRAS, 470, 3395

Childress, M. J., Tucker, B. E., Yuan, F., et al. 2016, *The ANU WiFeS SuperNovA Programme (AWSNAP)*, PASA, 33, e055

Alone in grand surrounds she hides without a sound:
Her appetite – which roars inside – will not subside.
With home so bare and not a morsel to be found,
There's naught to do but dream of plenty – hope, and hide.
But lo! In time, the palace does with fare abound!
Her emptiness that reached beyond the point of hurt
Will now be fought: for wreathing tendrils, briefly wound
And spun, she offers, twirling out her dusty skirt,
The riches to her maw. Oh joy: her playing-ground,
it welcomes in a friend! With glee they dance, draw near,
Cavorting hand in hand and chasing round and round
Until their play's complete. Then all's again austere –
  But sated, calm, she lies beneath enchanting skies
  And blowing bubbles upward, marvels at their rise.

A.D.T.
June 2018

1

Introduction

1.1 Active galactic nuclei

A diverse assortment of extragalactic sources radiating across the electromagnetic spectrum are now recognised as belonging to the class of objects known as Active Galactic Nuclei (AGN). Each of these sources is powered in the extremely compact central region of a galaxy, but nevertheless an AGN may have an energy output comparable to the starlight of its entire host galaxy. Examples of AGN include radio galaxies with associated jets and lobes, Seyfert galaxies (Seyfert 1943) with optically bright nuclei and line emission, the Low Ionisation Nuclear Emission-line Regions (LINERs; Heckman 1980) found mostly in elliptical galaxies, and distant radio quasars. In the case of quasars and QSOs (quasi-stellar objects; optically-detected quasars), the presence of the host galaxy of a very luminous, unresolved AGN may not be apparent. In the local universe a minimum of 10% of galaxies are known to contain active nuclei (Ho 2008). A concise historical review of the study of AGN is provided by Osterbrock (1991).

Accretion onto a black hole is the only plausible mechanism by which a luminous

AGN may persistently release large quantities of energy from a small volume. It is now believed that every large galaxy has a supermassive black hole (SMBH) lying at its centre, with typical masses of $10^6 - 10^9$ $M_\odot$ (where $M_\odot$ is the mass of the Sun). The Milky Way hosts a relatively passive SMBH with a measured mass of $\sim 4 \times 10^6$ $M_\odot$ (Gillessen et al. 2009) at the location of the radio source Sgr A^* in the Galactic centre. This object is unequivocally known to be a SMBH because it is confined to a compact region with a minimum measured mass density of 6.5×10^{21} $M_\odot$ pc^{-3} (Shen et al. 2005).

1.1.1 The unified model of active galactic nuclei

The many types of AGN are now classified under the umbrella of the so-called 'unified model' of AGN (e.g. Antonucci 1993; Urry & Padovani 1995). This model attempts to ascribe variations in observed properties of AGN as being primarily due to differences in the viewing angle, although the black hole accretion rate must also play a role.

The fundamental idea of the unified model is illustrated in Figure 1.1, which shows how the varying properties of different AGN types may be largely due to orientation effects.

The geometrical model is axisymmetric and consists of the following major physical components:

- A central SMBH, surrounded by an accretion disc. The accretion disc emits continuum radiation at a range of temperatures, and high-energy X-rays are produced by inverse-Compton scattering of photons from the disc in a corona of hot electrons (e.g. Jin et al. 2012).

- The broad-line region (BLR). This region consists of high-density gas clouds moving relatively closely around the SMBH, at radii of $0.01 - 1$ pc. The BLR clouds have high Keplerian velocities and therefore produce emission lines with extreme Doppler broadening ($1000 - 20000$ km s^{-1}; e.g. Netzer 2015). High BLR densities suppress forbidden line emission through collisional de-excitation (Osterbrock & Ferland 2006).

- The narrow-line region (NLR). This region consists of photoionised lower-velocity gas clouds more distant from the SMBH, in the galaxy at large. The

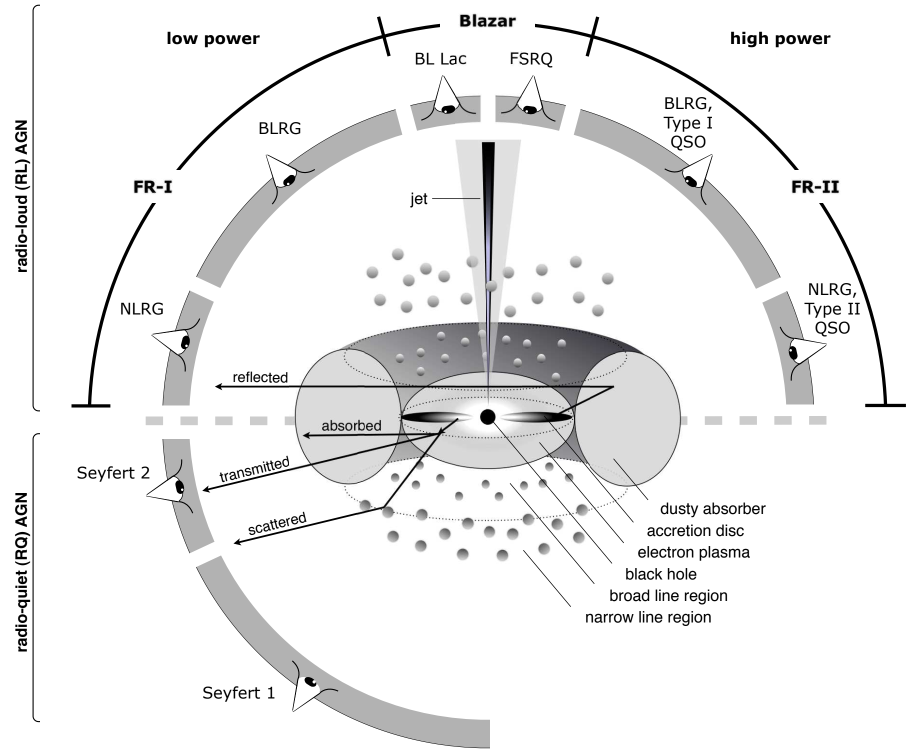

Figure 1.1 Schematic from Beckmann & Shrader (2012) showing how the unified model of AGN massively reduces the number of intrinsic types of AGN by ascribing many observed properties to viewing angle.

NLR produces relatively narrow forbidden and permitted emission lines and may extend over many kiloparsecs in the form of bipolar 'ionisation cones'.

- A dusty absorbing torus (Toroidal Obscuration Required by Unification Schemes, Elitzur 2008), which obscures the accretion disc and BLR from certain viewing angles. The inner edge of the dusty torus is likely determined by the dust sublimation radius, which may lie at distances of up to 0.1 pc from the central engine (Rose et al. 2015). The geometry of the torus is poorly constrained, with contributions to the obscuration potentially arising over a huge range of scales – from outer warps of the SMBH accretion disc up to the large-scale galactic disc (Netzer 2015).

The accretion rate onto the nuclear SMBH determines the power released by the AGN and is the most fundamental difference between the major sub-classes of AGN. These sub-classes and their place within the unified model are as follows:

- Radio-loud AGN (top half of Figure 1.1; relatively low luminosity). These AGN have radio-point source cores and powerful polar jets which are visible in radio wavelengths due to synchrotron radiation. They occur primarily in early-type galaxies and are divided into classes (Fanaroff & Riley 1974):

  – The relatively low-powered FR-I class is associated with jets that have radio emission generally decreasing with distance from the AGN.

  – The relatively high-powered FR-II class is associated with jets that have radio emission generally increasing with distance from the AGN.

  – Blazars. These are high-energy, relativistically beamed jets viewed end-on.

- Radio-quiet AGN (lower half of Figure 1.1; relatively high luminosity). These AGN occur primarily in late-type galaxies and are characterised by optical emission lines and weak or undetected radio emission.

  – Seyfert 1 (Sy 1) galaxies, or 'Type I AGN'. In these galaxies, permitted emission lines have a very broad component (from the BLR), and may also have a narrow component (from the NLR). In addition, UV and X-ray emission from the accretion disc and corona are detectable.

  – Seyfert 2 (Sy 2) galaxies, or 'Type II AGN'. In these galaxies, permitted emission lines have a narrow component only. However, the detection of polarised (i.e. scattered) broad Balmer emission in Seyfert 2 galaxies suggests that BLRs may be present in many or all Seyfert 2 galaxies, but are simply hidden by the dusty torus. The torus obscures much or all of the UV continuum and X-ray emission from the central engine.

Seyfert galaxies, and particularly Seyfert 2 galaxies, are the focus of this thesis. Seyferts may be categorised as intermediate between types 1 and 2 (e.g. type 1.5) depending on the relative strength of the broad and narrow emission line components.

In addition to the types listed above, some galaxies with a LINER nucleus are powered by a low-luminosity AGN. Note that LINERs do not have a definite place in the classical unified model, and LINER spectra in many galaxies are believed to result from shocks (e.g. Dopita et al. 2015) or diffuse ionised gas that are not associated with SMBH activity (e.g. Belfiore et al. 2016).

The unified model is a simple conceptual framework that in an abstract sense bridges two disparate regimes. Galaxies have physical extents on the scale of kiloparsecs, and each galaxy has a unique morphology, star formation history, accretion and merger history, etc. Conversely, SMBHs have sub-parsec extents, and are nearly identical in that a black hole is completely described by only two numbers, the mass and spin. The unified model of AGN is a partial description of the physical connection between these very different length scales and levels of heterogeneity. The success of the unified model to date likely rests on the extreme similarities between SMBHs, but nevertheless we expect that the large-scale heterogeneity of galaxies limits the applicability of the general scheme.

In a recent review, Netzer (2015) discusses the current evidence regarding various aspects of the AGN model and its general applicability. It has emerged that dusty AGN torii must be clumpy, but there remain many uncertainties about the nature of the torus. There is ongoing confusion about the large fraction of Type II AGN that do not seem to fit into the simple unification scheme due to a lack of polarised broad lines in deep spectropolarimetry.

One key uncertainty is how the torus 'covering factor' varies with luminosity. At higher luminosities, the dust sublimation radius and hence the inner edge of the torus are further from the SMBH. Depending on the variation in torus scale height with AGN luminosity, we may therefore expect a higher ratio of Seyfert 1 galaxies to Seyfert 2 galaxies for more luminous AGN (due to reduced obscuration of the BLR, see Figure 1.1). Although the Sy 1/Sy 2 ratio and AGN luminosity are measured to be positively correlated, the actual relationship between these two quantities does not appear to match existing models (e.g. Oh et al. 2015). Netzer (2015) is of the view that there are a range of covering factors for a particular luminosity.

Another poorly understood aspect of the unified model is how the vertical thickness of the torus can be maintained. The 'stickiness' of clouds in the ISM should lead a dusty torus to collapse into a thin disc within a small number of dynamical timescales. One explanation for how a torus can maintain a non-trivial covering fraction is that it may not be a static structure, but instead could be produced by radiation pressure-driven vertical circulation of dusty gas. Hydrodynamical simulations show that these 'radiation-driven fountains' inside the central $\sim$10 pc of an AGN may be able to naturally produce line-of-sight column densities and resulting covering fractions that are consistent with observations (e.g. Wada 2015, and references therein).

1.1.2 The radiative mode

The 'radiative mode' of nuclear activity (the lower half of Figure 1.1) is associated with radiatively efficient accretion, relatively high SMBH accretion rates, radiation pressure-driven winds, radio-quiet AGN and late-type (discy) host galaxies (Heckman & Best 2014). The other major mode, the kinetic mode or radio mode (upper half of Figure 1.1), is generally associated with lower accretion rates, radiatively inefficient accretion, radio jets, and early-type (elliptical) host galaxies (Fabian 2012). The fundamental physics regarding how differing accretion rates produce such different phenomena is poorly understood.

This thesis focuses on the 'radiative mode' and on the Seyfert galaxies that are associated with this mode. However, it should be noted that the S7 survey, which is described in Chapter 3 and which furnishes data for Chapter 4, consists of Seyferts that were selected for having been detected in the radio.

Radiative mode AGN have relatively high mass accretion rates, and the accretion occurs from an accretion disc that is relatively cool, optically thick and geometrically thin (Heckman & Best 2014; Yuan & Narayan 2014). As the accretion rate increases, more energy is released in the accretion disc and both the luminosity and the hardness (weighting of emission to higher photon energies) of the radiation increase.

Figure 1.2 illustrates how different types of AGN reside in different host galaxies, showing the distribution of local galaxies in the stellar mass versus specific star formation rate (sSFR) plane. The sSFR is the star formation rate per unit stellar mass, and decreases over time as a galaxy evolves. The overplotted contours show that AGN with relatively high bolometric luminosities $L_{\rm bol}$ (mostly radiative-mode AGN) reside in high-mass, normal star-forming galaxies, and in the 'green valley' between the 'blue cloud' and the 'red sequence'.

Figure 1.3 shows a schematic of the spectral energy distribution (SED) of a Seyfert AGN. Both 'intrinsic' and 'reprocessed' emission are important features of the typical SED of a Seyfert galaxy. The hatched area is an inaccessible range (energies between 13.6 eV and $\sim$200 eV) in which direct observations are precluded due to absorption by hydrogen, helium, and (for soft X-rays) inner-shell ionisation of heavy elements.

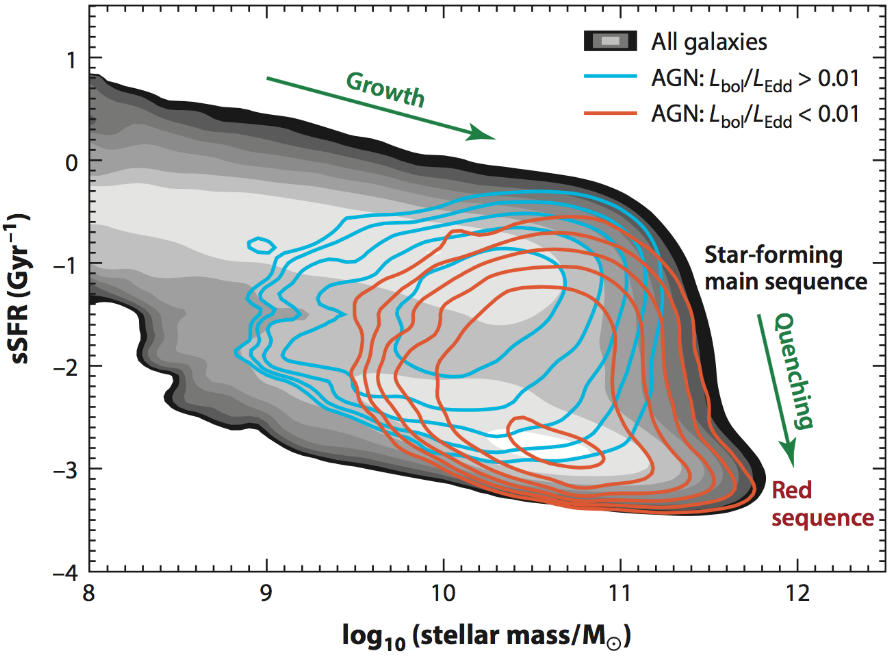

Figure 1.2 Figure 2 from Heckman & Best (2014) showing that low- and high-Eddington ratio AGN have different host galaxies. The data are from the Sloan Digital Sky Survey (SDSS; York et al. 2000) and the contours are separated by a factor of two. The 'All galaxies' shaded region shows the bimodal distribution of the galaxy population in the local universe: galaxies mostly fall on either the 'star-forming main sequence'/'blue cloud' (marked 'growth') or on the 'red sequence'. This thesis is concerned with Seyfert AGN, for which $L_{\rm bol}/L_{\rm Edd} > 0.01$ ($L_{\rm Edd}$ is the 'Eddington luminosity', a crude theoretical estimate of the maximum possible luminosity for a given black hole mass).

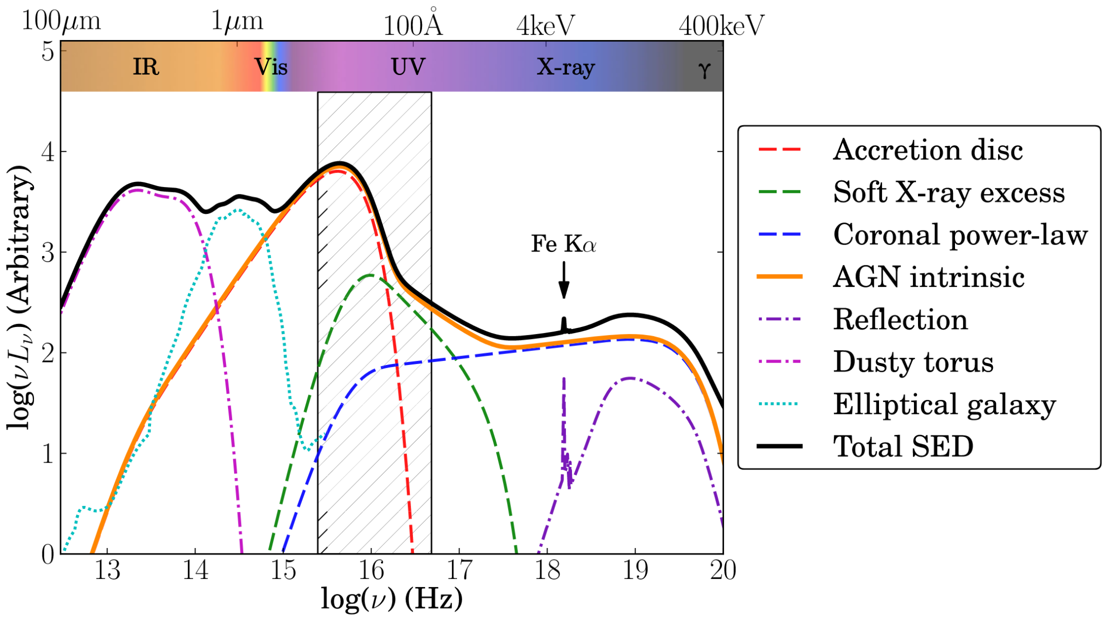

Figure 1.3 Figure 1 of Collinson et al. (2017) showing a schematic of the SED of a radiative-mode AGN. Intrinsic AGN emission is shown by dashed lines, reprocessed emission by dot-dash lines, and starlight (for simplicity that of an elliptical galaxy) by the dotted line. Emission lines other than the Fe Kα fluorescent line are not included.

1.2 Optical spectroscopy of active and star-forming galaxies

Optical spectroscopy is the primary observational tool used in this thesis to constrain the physics of Seyfert galaxies. This section will briefly describe how physical inferences may be made from measurements of the emission lines in optical spectra.

1.2.1 Emission-line spectra

Figure 1.4 shows example optical spectra for three types of emission-line galaxy. Approximately the same suite of lines is detected in each galaxy, but the relative flux (area under the curve) and velocity width of a line varies between the different classes of objects. These differences correspond to differences in the excitation and dynamics of the ionised plasmas.

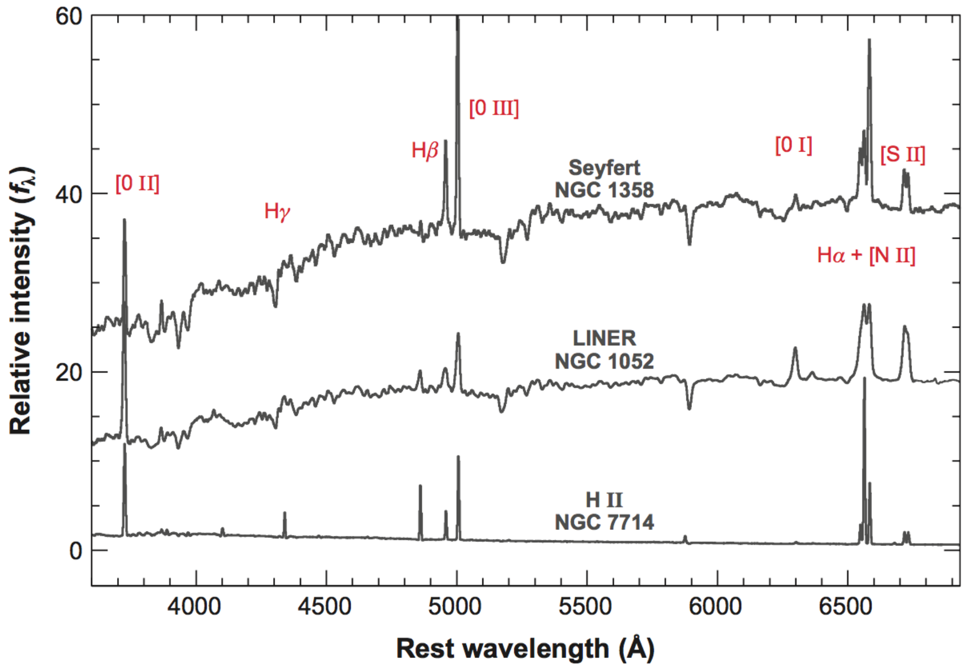

Figure 1.4 Figure 1 of Ho (2008) showing typical spectra of three different types of optical emission-line galaxies: a Seyfert 2 galaxy, a LINER galaxy, and a normal star-forming galaxy showing emission from H II regions ionised by hot young stars. The wavelength units of Angstroms (Å; 10^{-10} m) are used throughout this thesis.

The emission lines come in two principal varieties. The first are the 'permitted' recombination lines (e.g. the H α, Hβ and Hγ hydrogen Balmer-series lines labelled in the figure), which are emitted when an electron cascades down energy levels after recombining with an ion. The second variety are 'forbidden' lines, denoted by square brackets around the ion (e.g. [O II] or [O III] denoting forbidden lines of O^+ and O^{++} oxygen ions respectively). The forbidden lines are produced when ions are collisionally excited to a 'meta-stable state' and emit a photon through a magnetic dipole (M1) transition, which is termed a 'forbidden' transition because it is not allowed by the classical selection rules. In the UV, emission lines may also include the 'semi-forbidden' electric quadrupole (E2) transitions, termed 'intercombination' lines (denoted by a single square bracket on the right of the ion).

In Figure 1.4 it is evident that the emission line widths are greater in the Seyfert 2 and LINER galaxies than in the purely star-forming galaxy. In addition, the ratios of fluxes of the emission lines also differ markedly. In particular, the line [O III] λ5007 (often abbreviated to [O III]) is much stronger relative to Hβ in the Seyfert galaxy than in the other objects. This is a defining feature of Seyfert NLRs and arises because the ionising radiation in NLRs is relatively hard and intense compared to the ionising radiation in LINERs and star-forming galaxies.

1.2.2 Emission-line diagnostics

The ratios of fluxes of emission lines give important insights into the physics of ionised nebulae. Interesting ratios are theoretically and empirically calibrated to yield 'diagnostics' that are then applied to observed spectra of galaxies to classify the source of the excitation or measure physical parameters.

Diagnostics that classify the source of the ionzing photons rely on the fact that the state of ionisation of the plasma differs between different types of nebula. A chosen flux ratio may compare a strong line from a species associated with a relatively high ionisation potential (e.g. [O III]) to a line from a lower ionisation species (e.g. H I). The two lines are typically chosen to have a small wavelength separation, to minimise variation in the observed ratios due to flux calibration problems and interstellar reddening. Nebulae such as those in AGN and LINERs feature relatively high values of the diagnostic ratios compared to spectra dominated by excitation from young stars.

The diagnostic ratios are often visualised using optical diagnostic diagrams (e.g. Baldwin et al. 1981; Veilleux & Osterbrock 1987), which plot pairs of emission-line ratios. Figure 1.5 shows the classic optical diagnostic diagrams for galaxies in the Sloan Digital Sky Survey (SDSS). The degree of excitation of the emission-line gas increases from bottom-left to top-right in each panel, and the regions of the diagram have been labelled with the corresponding classifications. In the most commonly used [N II]/Hα panel, there is a narrow sequence of star-forming galaxies occupying the curved 'H II sequence', and a branch of the data that extends up to high values of [O III]/Hβ, characteristic of AGN. Intermediate between star-forming galaxies and AGN are 'composite' galaxies.

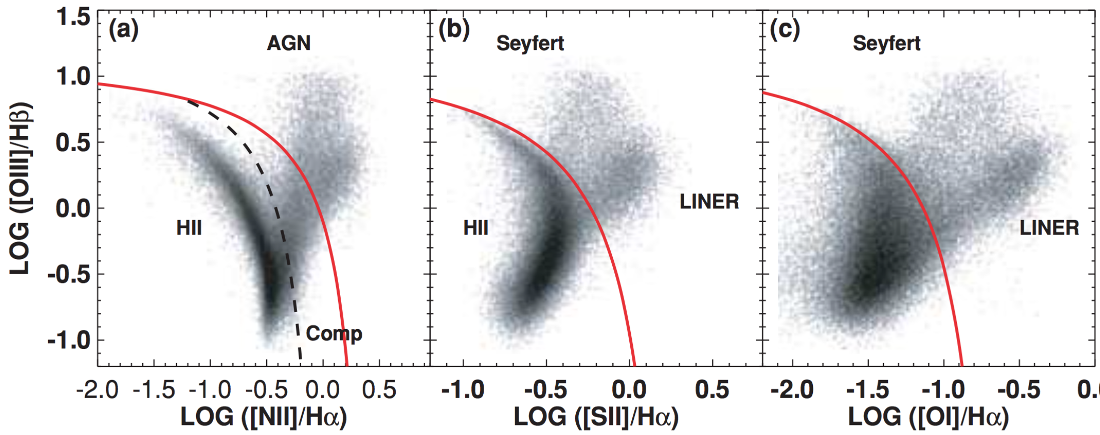

Figure 1.5 Figure 1 from Kewley et al. (2006), showing the (a) [NII]/Hα, (b) [SII]/Hα, and (c) [OI]/Hα optical diagnostic diagrams (Baldwin et al. 1981; Veilleux & Osterbrock 1987) for the SDSS galaxy sample.

Emission-line diagnostics may also be used to measure interesting physical parameters. In the H II regions produced by hot young stars, the parameters that have the most effect on the emission line spectrum are the metallicity, Z, and the ionisation parameter, U. The dimensionless ionisation parameter U is defined as the ratio of the number densities of ionising photons and atoms. Alternatively, some authors use the (dimensional) ionisation parameter Q (where $Q = U/c$ and c is the speed of light), which may be interpreted as the speed of an ionisation front (Dopita & Sutherland 2003a). Both Z and U may be estimated using line flux ratios. It is also possible to measure the temperature or electron density of the plasma using the ratio of two lines in a doublet, for example the [O II] λ3726,29 and [S II] λ6716,31 doublets.

The predicted behaviour of various optical emission line flux ratios as a function of metallicity (parametrised by the oxygen abundance) is illustrated in Figures 1.6 and 1.7 for H II regions and NLRs respectively. Here the solar oxygen abundance is $12 + \log \mathrm{O/H} = 8.76$ (Nicholls et al. 2017), where 12 is added to the logarithm for purely historical reasons.

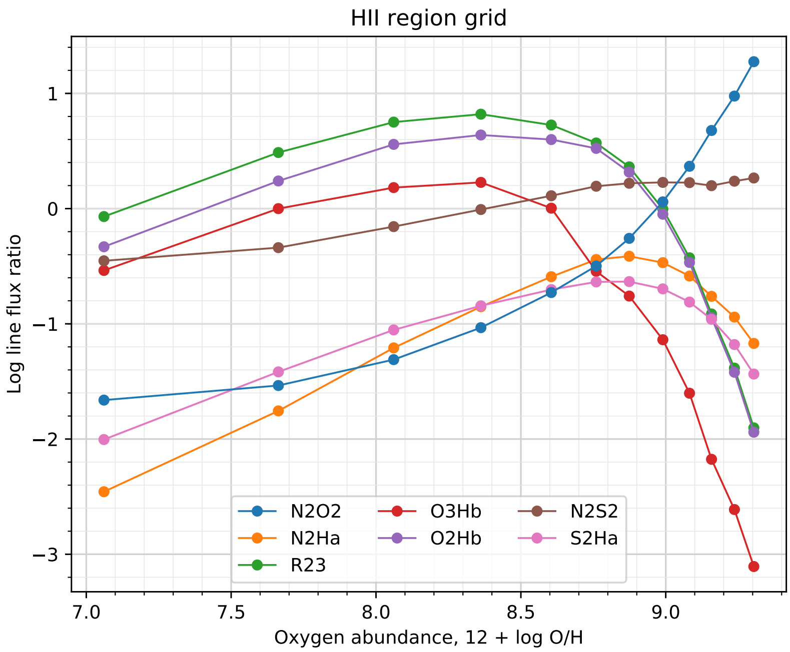

Figure 1.6 Ratios of emission line fluxes for model H II region nebulae. The models use the MAPPINGS V photoionisation model (Sutherland & Dopita 2017), with a gas pressure of $\log P/k\,(\mathrm{cm^{-3}\,K}) = 5.4$ and an ionisation parameter of $\log U = -3.0$. The model grid is described in more detail in Chapter 4.

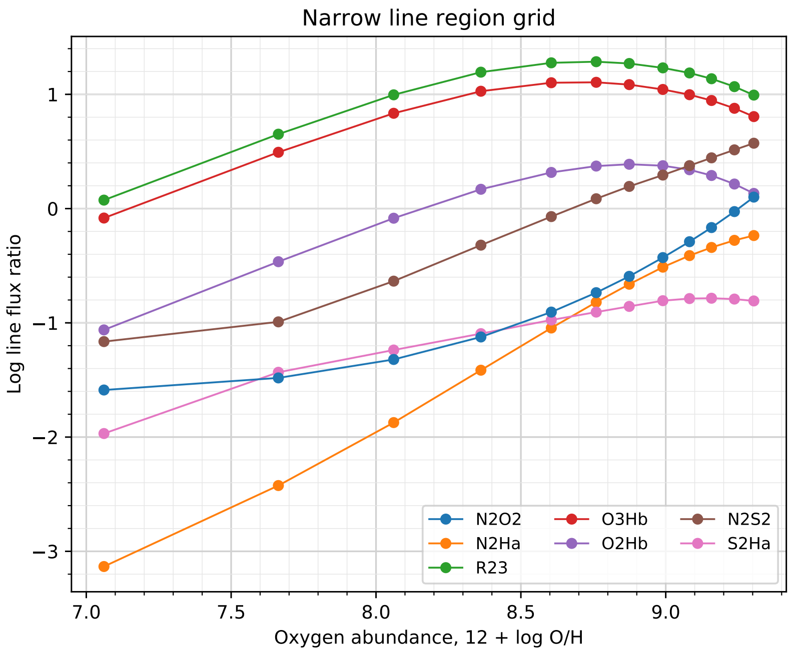

Figure 1.7 Ratios of emission line fluxes for model AGN narrow line regions. The models use the MAPPINGS V photoionisation model (Sutherland & Dopita 2017), with a gas pressure of $\log P/k\,(\mathrm{cm^{-3}\,K}) = 7.0$ and an ionisation parameter of $\log U = -2.2$. The ionising spectrum has a peak at $\log E_{\mathrm{peak}}\,(\mathrm{keV}) = -1.5$ and has 15% of the energy allocated to an X-ray power-law tail with photon index $\Gamma = 2.0$. The model grid is described in more detail in Chapter 4.

The line ratios shown in the diagrams are the ratios commonly used in the literature. These are N2O2 ([N II] λ6584 / [O II] λ3726+29), N2Ha (or simply 'N2'; [N II] λ6584 / H α λ6563), R23 (([O II] λ3726+29 + [O III] λ4959+5007) / Hβ λ4861), O3Hb ([O III] λ5007 / Hβ λ4861), O2Hb ([O II] λ3726+29 / Hβ λ4861), N2S2 ([N II] λ6584 / [S II] λ6716+31), and S2Ha ([S II] λ6716+31 / H α λ6563).

Some important aspects of the behaviour of these line ratios are the following:

1. At sufficiently low metallicities, forbidden line fluxes increase with metallicity, simply because a greater abundance of the relevant species produces more emission. However, at sufficiently high metallicities, line fluxes decrease with metallicity. This is because the addition of metals enhances line cooling in the nebula, resulting in lower nebular temperatures, reduced collisional excitation and correspondingly less forbidden line emission. Hence ratios of a forbidden to a recombination line are intrinsically double-valued with metallicity.

2. The gradient of a line in Figures 1.6 and 1.7 reflects how sensitive the line ratio is to changes in metallicity, with a steeper line suggesting that a ratio may be a more useful metallicity diagnostic within a given metallicity range.

3. Unfortunately, emission line ratios are usually affected by parameters other than metallicity. In particular, diagnostic line ratios such as R23 suffer severe degeneracies with respect to changes in the ionisation parameter (Kewley & Dopita 2002).

4. At low metallicity, useful diagnostics include R23 and N2. At high metallicity, useful diagnostics include N2O2 and R23. Note that R23 has two 'branches': this ratio increases at low metallicities and decreases at high metallicities while being sufficiently sensitive in both regimes to be useful for metallicity measurements. Above approximately $0.5\,Z_\odot$ ($12 + \log O/H = 8.46$), N2O2 is a very attractive diagnostic for H II regions, because it is not affected by the ionisation parameter and is highly sensitive to the metallicity (Kewley & Dopita 2002). In addition, N2O2 is monotonic over the entire metallicity range.

5. There is an awkward intermediate range of metallicities for both H II regions and NLRs in which the stengths of the forbidden oxygen lines are at their peak, and therefore these lines have very little sensitivity to metallicity. Measurements of metallicity using the oxygen lines in this regime are sensitive to systematic over- or under-prediction of line fluxes, such that both relative and absolute metallicity measurements will likely be unreliable. These 'turn overs'

are shifted to higher metallicities in NLRs compared to H II regions.

6. The effect of X-rays in AGN NLRs is evident in Figure 1.7. At high metallicity, emission-line ratios do not vary as sharply with metallicity in AGN than in H II regions. This is because NLR nebulae are kept warm by X-rays despite relatively strong line cooling. The important diagnostic ratios are less sensitive to metallicity, and as a result it is more difficult to accurately measure metallicities from optical spectra of NLRs compared to H II regions.

It is also possible to measure the ionisation parameter U using emission-line flux ratios. The ratio O3O2 ([O III] $\lambda5007$ / [O II] $\lambda3726 + 29$) is used to probe U (e.g. Baldwin et al. 1981), although this ratio also depends on metallicity (e.g. Kewley & Dopita 2002; Dopita et al. 2013). The photon energy required to ionise O I to O II (ionisation potential of O I) is 13.62 eV, very similar to the 13.60 eV ionisation potential of a hydrogen atom, and the energy required to ionise O II to O III is 35.12 eV, higher than for the other ions emitting strong optical lines. Hence this ratio effectively probes the degree of ionisation of a nebula, which is strongly dependent on the ionisation parameter.

1.2.3 Emission-line fitting

Deriving physical parameters from the emission-line fluxes in an observed galaxy spectrum depends upon accurate measurements of the fluxes. After a spectrum is trivially corrected for redshift, the extraction of the line fluxes is unfortunately complicated by several important issues. Firstly, the emission lines in a galaxy spectrum are superimposed on the continuum spectra produced by the stars in the galaxy. Secondly, the emission-line profiles themselves may be complex due to differing motions of gaseous components (with possibly different physical conditions) along the line of sight. Thirdly, over any non-trivial wavelength range there will be important effects due to interstellar reddening, which preferentially blocks light to bluer wavelengths and must be accounted for in order to measure accurate relative line fluxes. In high-opacity objects the blue emission lines will preferentially sample the foreground nebulae, with light from more deeply obscured sources being lost.

The problem of the stellar continuum is typically handled by fitting and then subtracting models of synthetic simple stellar population (SSP) spectra (e.g. García-Lorenzo et al. 2015; Sánchez et al. 2016; Ho et al. 2016, among many others). The model fitting excludes the regions of a spectrum affected by the emission lines. After subtracting the fitted stellar contribution, a 'pure emission' spectrum remains.

An important aspect of the subtraction of the stellar continuum is that it corrects for line absorption in stellar atmospheres. For example, in optical spectra, the Balmer emission lines from the interstellar medium are superimposed on Balmer *absorption* lines in the stellar spectra. Correcting for any absorption is particularly important for emission with low equivalent width (i.e. when the continuum emission is strong relative to the emission lines), and for low-resolution spectra, for which the instrumental spectral resolution is comparable to the width of the stellar absorption profile.

The flux, velocity offset, and width ('velocity dispersion') of an emission line are measured by fitting a model profile to the observed spectrum. The most common functional form used in the literature is a Gaussian, although there are several alternative profiles: Lorentz, Voigt, and the first few terms of a Gauss-Hermite series (e.g. Riffel 2010). Only the last possibility may account for asymmetry in the emission-line profile; in general multiple components must be used to properly fit an asymmetric profile.

It is often unclear how many components are appropriate to fit to an emission line with a skewed or complex profile (e.g. Ho et al. 2016). Figure 1.8 shows example spectra that clearly require up to three Gaussian components to properly fit the data. A model with more components has more free parameters and therefore will generally improve the fit to the data. Unfortunately, statistical model selection approaches do not satisfactorily reproduce the choice of spectral decomposition that would be made by a trained astronomer (e.g. Hampton et al. 2017).

Recently completed and ongoing large integral field spectroscopy (IFS) surveys are rapidly increasing the volume of available data (Sánchez et al. 2012; Bundy et al. 2015; Dopita et al. 2015; Green et al. 2018). The large data volumes require solutions to the above line-fitting problems that operate without significant human intervention. Unfortunately the available solutions (e.g. Hampton et al. 2017) are not yet mature, and the problem is worsened by a lack of standardisation in the field – a very large number of different line-fitting codes and approaches are used by the astronomical community, even among astronomers working in the same wavelength regime.

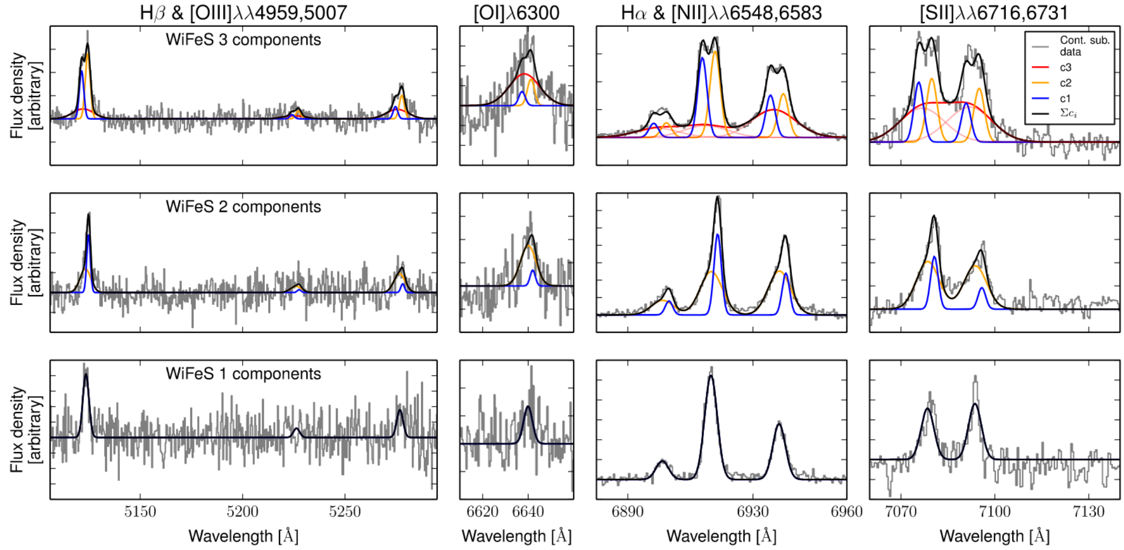

Figure 1.8 Figure 4 of Ho et al. (2014) showing optical emission-line spectra that clearly show 1, 2 or 3 independent kinematic components.

1.3 Photoionisation modelling

1.3.1 Fundamental principles

Photoionisation modelling is the computation of the emergent spectrum from an astrophysical gas cloud that has been illuminated by an external ionising radiation field. The calculations must in general account for many microphysical processes that impact the energy balance and ionic abundances in each part of the nebula. These processes include the following (Dopita & Sutherland 2003b):

- Radiative transitions (bound-bound emission): An electron in an atom or ion transitions to a lower-energy state and a photon is emitted with energy equal to that lost by the electron. The emitted light has a characteristic wavelength - an 'emission line'.

- Photoionisation: An atom or ion absorbs a photon with enough energy to liberate an electron (a 'photoelectron')

- Collisional excitation: An atom or ion collides with a charged species (electron or proton), and an electron is excited to a higher-energy state

- Radiative recombination (free-bound emission): an electron is captured by an ion, with the lost energy emitted as a photon

- Two-photon emission: An electron transitions to a lower-energy state and two photons are emitted with a total energy equal to that lost by the electron

- Charge exchange: An atom of neutral H or He collides with an ion and an electron is acquired by the ion

Many important quantum-physical details and additional processes have been omitted from the above list.

A photoionisation model proceeds in a series of steps such that the physical properties of the nebula are calculated at a series of distances from the starting point. At each step it is necessary to determine the ionisation state (relative abundances of ionisation stages of each element), the populations of excited states in the atoms and ions, the rates of emission, excitation and de-excitation from processes including those listed above, the temperature of the gas, and the shape of the ionising spectrum (which changes through the model). The calculations are significantly complicated by the fact that these important quantities are all interrelated – the ionisation balance and cooling balance equations are coupled. The total energy that is radiated away depends upon the ionisation state and electronic excitation, but these in turn depend on the temperature which depends on the total energy being lost. In an equilibrium state, the energy absorbed from the ionising spectrum must balance the energy lost through radiated photons (in a single constant-temperature model step).

Photoionisation simulations are typically one-dimensional. However, even in a one-dimensional model the treatment of the input radiation field may account for geometric effects. For example, the radiation may be diluted due to distance from a source as the model progresses (a 'spherical' geometry), or alternatively the radiation may be undiluted (a 'slab' geometry). Models can also include the effects of a diffuse ionising field under these two geometries, and account for resonance-line trapping of photons.

The following are the most important parameters that affect the structure of the model and therefore the emergent spectrum:

- The abundances of the elements. Higher abundances result in more cooling by line emission through radiative transitions, thereby strongly affecting the temperature and energy balance. Larger atoms may also be ionised to higher stages and thereby provide more free electrons to the plamsa.

- The ionisation parameter U, the ratio of the number densities of ionising photons to atoms, which is typically specified at the inner edge of the model. A greater relative density of ionising photons increases the overall ionisation of the nebula.
- The gas pressure P. The rates of collisional excitation (and collisional de-excitation, which is relevant at higher densities) vary with the square of the density, which is determined by the pressure and temperature T (because $P = nkT$, where n is the number density of free particles (electrons, ions and atoms) and k is Boltzmann's constant).
- The shape of the input ionising spectrum. The modelling code must track the number and local absorption of ionising photons in each spectral bin for each step of the model. The ionising spectrum is ultimately the energy source for emission from the model nebula.

The most widely used photoionisation model in the literature is CLOUDY (Ferland et al. 1998; Shaw et al. 2005; Ferland et al. 2013). In this thesis I use the MAPPINGS (Modelling And Prediction in PhotoIonised Nebulae and Gasdynamical Shocks) shock and photoionisation model developed at ANU (Sutherland & Dopita 1993; Allen et al. 2008; Dopita et al. 2013; Sutherland & Dopita 2017). Another code, which operates on a three-dimensional grid, is MOCASSIN (MOnte CArlo SimulationS of Ionised Nebulae Ercolano et al. 2003, 2005, 2008; Hubber et al. 2016).

1.3.2 Narrow-line region models

Narrow-line region emission has for decades been widely assumed to be mostly powered by photoionisation (e.g. Osterbrock & Ferland 2006), although shocks may also make a significant contribution (e.g. Dopita & Sutherland 1995, 1996; Allen et al. 1998). Outflows from the nucleus are ubiquitous in active galaxies (King & Pounds 2015, and references therein), and are commonly evidenced in optical spectra by a broad ($200 - 500\,\mathrm{km\,s^{-1}}$) wing extending blueward from the core of the [O III] line. The observed gas dynamics strongly suggest that shocks should contribute to the line emission in optical AGN, but a full understanding of the power source is hindered by the fact that fast shocks (with speed $v_s \gtrsim 300\,\mathrm{km\,s^{-1}}$) may produce similar diagnostic line ratios to Seyfert photoionisation (e.g. Allen et al. 2008).

Remarkably constant ionisation parameters (typically $\log U \sim -2$) are inferred both within and between Seyfert galaxies, which has previously challenged simple models of photoionised NLR emission. This consistency was explained by Dopita et al. (2002) as being due to the effects of radiation pressure on the NLR cloud structure.

Dust plays an important role in NLR physics through its effect on radiation pressure, photoelectric heating, and competing with free atoms and ions to absorb ionising photons. A toy model of Dopita et al. (2002) is illustrated in Figure 1.9. The authors picture dynamic clouds being both compressed and accelerated by the radiation pressure. Photoionisation modelling simulates the 'stagnation line', which is the highest-emissivity region and also where the local radiation pressure gradient is matched by the gas pressure gradient such that the models may be static.

Radiation pressure is most significant for the dust component of a gas cloud. The UV opacity of dust is much larger than the opacity of ions, which in turn is much larger than the scattering opacity of electrons. The absorption cross-section σ_d for a dust grain is three orders of magnitude larger than the Thomson cross section σ_T for an electron ($\sigma_d/\sigma_T \sim 1000$; e.g. Ishibashi & Fabian 2015). Although radiation pressure is strongest on the dust component of a NLR cloud, the charged dust grains are very strongly coupled to the gas through Coulomb interactions, and as a consequence the radiation pressure influences the ionised cloud as a whole.

Figure 1.10 shows the structure of a dusty photoionisation model by Groves et al. (2004) that includes the effects of radiation pressure. The degree of ionisation decreases through the model such that emission from different species generally arises in different parts of the cloud. In AGN NLRs the X-radiation produces a long partially-ionised zone behind the nebula. This is in contrast to H II-region nebulae, which are characterised by a sharp edge to the ionised nebula (at the Strömgren radius), where the plasma recombines over a relatively short distance.

1.4 Thesis overview

This thesis addresses firstly theory, secondly observations, and finally sophisticated analyses that combine both the theory and the observations. There are five chapters that each present a significant portion of the work completed during the candidature in the form of a journal article:

- Chapter 2 presents theoretical work that takes advantage of recent advances

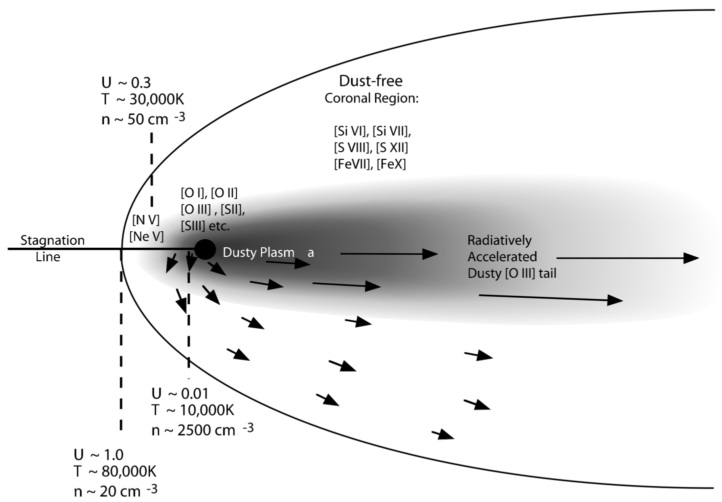

Figure 1.9 Figure 1 from Dopita et al. (2002) showing a photoevaporating, dusty molecular cloud (filled circle) in a NLR. The parameters shown (ionisation parameter U, temperature T and number density n) are typical values for each region inside and surrounding a NLR cloud in the famous active galaxy NGC 1068.

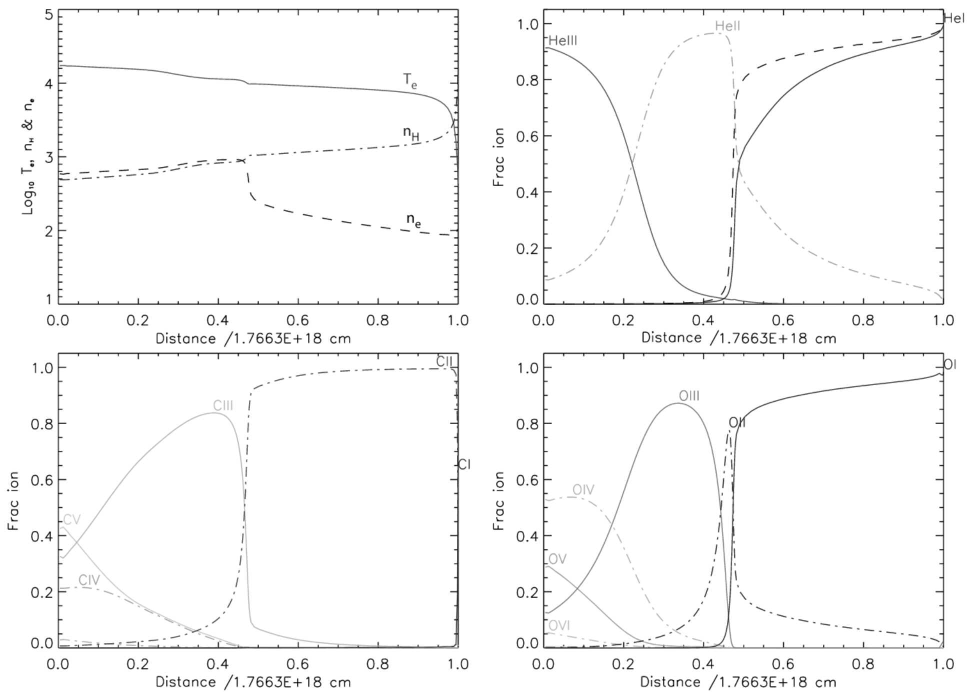

Figure 1.10 Diagrams showing the ionisation structure of a MAPPINGS III NLR photoionisation model from Figure 3 of Groves et al. (2004). This model includes dust, has a solar metallicity, and has $\log U = -2.0$. The top left panel shows the variation of the electron temperature T_e, the number density of hydrogen n_H, and the number density of electrons n_e, as a function of distance through the 1D model. The remaining three panels show the variation in the abundances of different ionisation stages of helium, carbon and oxygen as a function of distance through the model. The highest ionisation states exist at the start of the model, and the level of ionisation decreases with distance. There is a recombination boundary at approximately 0.45 on the x-axis, but a partially ionised zone extends past this boundary for the remainder of the model.

in the understanding of the accretion structure in radiative mode AGN. A state-of-the-art model of the ionising radiation in Seyfert galaxies is adapted for convenient use in photoionisation modelling.

- Chapter 3 presents observations that are part of a new wave of large-scale surveys using integral field spectroscopy. When published, the data set presented in Chapter 3 was the largest available sample of active galaxies observed in an IFS survey.

- Chapter 4 combines some of the theory in Chapter 2 and observations in Chapter 3 with grids of photoionisation models and a new analysis code. The results for four nearby active galaxies are the first comprehensive two-dimensional constraints on NLR parameters.

- Chapters 5 and 6 represent the first steps toward being able to measure important parameters such as the gas-phase metallicity while accounting for arbitrary mixing between different sources of excitation in an emission-line spectrum. Chapter 5 is concerned with directly measuring the degree of mixing between H II-region and AGN excitation. Chapter 6 presents the first comprehensive measurements of the gas-phase metallicity and its relation to galaxy stellar mass in a large sample of local active galaxies.

Further background on each of these topics is included in the relevant chapters.

1.5 References

Allen, M. G., Dopita, M. A., & Tsvetanov, Z. I. 1998, ApJ, 493, 571 (ADS entry)

Allen, M. G., Groves, B. A., Dopita, M. A., Sutherland, R. S., & Kewley, L. J. 2008, ApJS, 178, 20 (ADS entry)

Antonucci, R. 1993, ARA&A, 31, 473 (Link)

Baldwin, J. A., Phillips, M. M., & Terlevich, R. 1981, PASP, 93, 5 (ADS entry)

Beckmann, V., & Shrader, C. 2012, in Proceedings of 'An INTEGRAL view of the high-energy sky (the first 10 years)', 69 (ADS entry)

Belfiore, F., et al. 2016, MNRAS, 461, 3111 (ADS entry)

Bundy, K., et al. 2015, ApJ, 798, 7 (ADS entry)

Collinson, J. S., Ward, M. J., Landt, H., Done, C., Elvis, M., & McDowell, J. C. 2017, MNRAS, 465, 358 (ADS entry)

Dopita, M. A., Groves, B. A., Sutherland, R. S., Binette, L., & Cecil, G. 2002, The Astrophysical Journal, 572, 753 (Link)

Dopita, M. A., & Sutherland, R. S. 1995, ApJ, 455, 468 (ADS entry)

—. 1996, ApJS, 102, 161 (ADS entry)

Dopita, M. A., & Sutherland, R. S. 2003a, Astrophysics of the diffuse universe (Springer Science & Business Media)
—. 2003b, Astrophysics of the diffuse universe (Berlin, New York: Springer) (Link)
Dopita, M. A., Sutherland, R. S., Nicholls, D. C., Kewley, L. J., & Vogt, F. P. A. 2013, ApJS, 208, 10 (ADS entry)
Dopita, M. A., et al. 2015, ApJS, 217, 12 (Link)
Dopita, M. A., et al. 2015, ApJ, 801, 42 (ADS entry)
Elitzur, M. 2008, New Astronomy Reviews, 52, 274 (Link)
Ercolano, B., Barlow, M. J., & Storey, P. J. 2005, MNRAS, 362, 1038 (ADS entry)
Ercolano, B., Barlow, M. J., Storey, P. J., & Liu, X.-W. 2003, MNRAS, 340, 1136 (ADS entry)
Ercolano, B., Young, P. R., Drake, J. J., & Raymond, J. C. 2008, ApJS, 175, 534 (ADS entry)
Fabian, A. 2012, ARA&A, 50, 455 (Link)
Fanaroff, B. L., & Riley, J. M. 1974, MNRAS, 167, 31P
Ferland, G. J., Korista, K. T., Verner, D. A., Ferguson, J. W., Kingdon, J. B., & Verner, E. M. 1998, PASP, 110, 761 (ADS entry)
Ferland, G. J., et al. 2013, RMXAA, 49, 137 (ADS entry)
García-Lorenzo, B., et al. 2015, A&A, 573, A59 (ADS entry)
Gillessen, S., Eisenhauer, F., Trippe, S., Alexander, T., Genzel, R., Martins, F., & Ott, T. 2009, The Astrophysical Journal, 692, 1075 (Link)
Green, A. W., et al. 2018, MNRAS, 475, 716 (ADS entry)
Groves, B. A., Dopita, M. A., & Sutherland, R. S. 2004, ApJS, 153, 9 (ADS entry)
Hampton, E. J., et al. 2017, MNRAS, 470, 3395 (ADS entry)
Heckman, T. M. 1980, A&A, 87, 152 (ADS entry)
Heckman, T. M., & Best, P. N. 2014, ARA&A, 52, 589 (Link)
Ho, I.-T., et al. 2014, MNRAS, 444, 3894 (ADS entry)
—. 2016, Ap&SS, 361, 280 (ADS entry)
Ho, L. C. 2008, ARA&A, 46, 475 (Link)
Hubber, D. A., Ercolano, B., & Dale, J. 2016, MNRAS, 456, 756 (ADS entry)
Ishibashi, W., & Fabian, A. C. 2015, MNRAS, 451, 93 (ADS entry)
Jin, C., Ward, M., & Done, C. 2012, MNRAS, 422, 3268 (Link)
Kewley, L. J., & Dopita, M. A. 2002, ApJS, 142, 35 (ADS entry)
Kewley, L. J., Groves, B., Kauffmann, G., & Heckman, T. 2006, MNRAS, 372, 961 (ADS entry)
King, A., & Pounds, K. 2015, ARA&A, 53, 115 (ADS entry)
Netzer, H. 2015, ARA&A, 53, 365 (ADS entry)
Nicholls, D. C., Sutherland, R. S., Dopita, M. A., Kewley, L. J., & Groves, B. A. 2017, MNRAS, 466, 4403 (ADS entry)
Oh, K., Yi, S. K., Schawinski, K., Koss, M., Trakhtenbrot, B., & Soto, K. 2015, ApJS, 219, 1 (ADS entry)
Osterbrock, D., & Ferland, G. 2006, Astrophysics of Gaseous Nebulae and Active Galactic Nuclei, 2nd edn. (University Science Books) (Link)
Osterbrock, D. E. 1991, Reports on Progress in Physics, 54, 579 (ADS entry)
Riffel, R. A. 2010, Ap&SS, 327, 239 (ADS entry)
Rose, M., Elvis, M., & Tadhunter, C. N. 2015, MNRAS, 448, 2900 (Link)
Sánchez, S. F., et al. 2012, A&A, 538, A8 (ADS entry)
—. 2016, RMXAA, 52, 21 (ADS entry)

Seyfert, C. K. 1943, ApJ, 97, 28 (ADS entry)
Shaw, G., Ferland, G. J., Abel, N. P., Stancil, P. C., & van Hoof, P. A. M. 2005, ApJ, 624, 794 (ADS entry)
Shen, Z.-Q., Lo, K. Y., Liang, M.-C., Ho, P. T. P., & Zhao, J.-H. 2005, Nature, 438, 62 (Link)
Sutherland, R. S., & Dopita, M. A. 1993, ApJS, 88, 253 (ADS entry)
—. 2017, ApJS, 229, 34 (ADS entry)
Urry, C. M., & Padovani, P. 1995, PASP, 107, 803 (Link)
Veilleux, S., & Osterbrock, D. E. 1987, ApJS, 63, 295 (ADS entry)
Wada, K. 2015, ApJ, 812, 82 (ADS entry)
York, D. G., et al. 2000, AJ, 120, 1579 (ADS entry)
Yuan, F., & Narayan, R. 2014, ARA&A, 52, 529 (Link)

2

Modelling the ionizing spectra of Active Galactic Nuclei

This chapter presents the content of the article *A physically-based model of the ionizing radiation from active galaxies for photoionization modeling* (Thomas et al. 2016). The abstract is as follows:

> We present a simplified model of Active Galactic Nucleus (AGN) continuum emission designed for photoionization modeling. The new model OXAF reproduces the diversity of spectral shapes that arise in physically-based models. We identify and explain degeneracies in the effects of AGN parameters on model spectral shapes, with a focus on the complete degeneracy between the black hole mass and AGN luminosity. Our re-parametrized model OXAF removes these degeneracies and accepts three parameters which directly describe the output spectral shape: the energy of the peak of the accretion disk emission $E_{\rm peak}$, the photon power-law index of the non-thermal emission Γ, and the proportion of the total flux which is emitted in the non-thermal component $p_{\rm NT}$. The parameter $E_{\rm peak}$ is presented as a function of the black hole mass, AGN luminosity,

and 'coronal radius' of the OPTXAGNF model upon which OXAF is based. We show that the soft X-ray excess does not significantly affect photoionization modeling predictions of strong emission lines in Seyfert narrow-line regions. Despite its simplicity, OXAF accounts for opacity effects where the accretion disk is ionized because it inherits the 'color correction' of OPTXAGNF. We use a grid of MAPPINGS photoionization models with OXAF ionizing spectra to demonstrate how predicted emission-line ratios on standard optical diagnostic diagrams are sensitive to each of the three OXAF parameters. The OXAF code is publicly available in the Astrophysics Source Code Library.

2.1 Introduction

Active galactic nuclei (AGN) feature narrow-line regions (NLRs) in which continuum radiation from the central engine photoionizes the surrounding interstellar medium (ISM). The relatively hard AGN continuum emission injects more energy and photoionizes the ISM to higher ionization states than the ionizing spectra of OB stars at the centers of HII regions.

Many insights into the physics of the the ISM in active galaxies have been gained through the use of photoionization models. The results of photoionization modeling facilitate the routine diagnosis of the density, temperature, and cause of ionization of NLR gas from observed emission-line spectra. Photoionization models have been used to explain the very similar NLR ionization parameters observed across the population of active galaxies - this effect is caused by the gas pressure gradient balancing the radiation pressure gradient in dusty NLR clouds such that the 'local' ionization parameter is self-regulated (Dopita et al. 2002; Groves et al. 2004). Models are an important tool in investigating the effects of various ISM parameters on emission-line spectra; e.g. determining the effects of changing abundances (Groves et al. 2006). Recently, Davies et al. (2016) showed how comparisons between models and spatially-resolved spectroscopy may reveal where extended NLRs are radiation pressure-dominated or gas pressure-dominated on scales of tens to hundreds of parsecs.

The emission line spectra of NLRs in active galaxies strongly depend upon the shape of the spectrum of the central source at energies immediately above the Lyman limit at 13.6 eV. These ionizing photons are not directly observable because they are very strongly absorbed in the NLR and broader ISM of the host galaxy, as well as in the ISM of the Milky Way.

Up to the present, ionizing AGN spectra for photoionization modeling have almost exclusively been constructed using piecewise functions of one to three simple power-laws (e.g. Viegas-Aldrovandi & Contini 1989; Murayama & Taniguchi 1998; Allen et al. 1998; Evans et al. 1999; Contini & Viegas 2001; Collins et al. 2009). Groves et al. (2004) use a conventional range of power-law indices of $\alpha = -2.0$ to $\alpha = -1.2$, for a single power-law covering 0.005 to 1 keV. The authors find that a steeper power-law leads to weaker high-ionization lines and relatively stronger H lines, due to the relative excess of H- but not He-ionizing photons. A more physically-motivated empirical two-component model for the ionizing spectrum is used, for example, in Bland-Hawthorn et al. (2013)).

In this work we seek to develop a modern AGN continuum emission model for use as the input spectrum in photoionization models, based on physically-derived models, and including for example ionization effects in the shape of the accretion disk spectrum. We aim to identify the important AGN parameters which influence the shape of the ionizing spectrum and hence the predicted emission-line ratios. This allows us to minimize the parameter space used to cover a large range of model spectra. A small parameter space is easier to handle conceptually and computationally, and the process of combining fully and partially degenerate parameters into a smaller set of parameters results in insights into how the shape of the ionizing spectrum may arise from various combinations of fundamental AGN parameters.

In photoionization modeling we assume that the model ionizing spectrum will be intrinsic when it reaches the modeled clouds, i.e. that there is no significant absorption between the central engine and the modeled clouds. Hence the spectra will primarily feature a peak formed by a superposition of pseudo-blackbodies due to the accretion disk, and a power-law non-thermal component resulting from Compton upscattering of disk photons. A physical model of these spectra may be expected to be well-described by few parameters.

A detailed model of continuum emission from AGN must rely on theoretical emissivities from accretion disk models. The standard Novikov-Thorne 'thin disk' accretion model (Novikov & Thorne (1973), building on the work of Shakura & Sunyaev (1973)) is applicable over much of the accretion rate regime of Seyfert galaxies ($\sim$0.05 to $\sim$0.3 $L/L_{\rm Edd}$). This model has parameters such as the SMBH mass, spin, and accretion rate, which influence the theoretical ionizing AGN spectrum.

Understanding how the key parameters control the shape of the ionizing EUV-soft X-ray spectrum of AGN allows us to produce a model which keeps the number of free parameters to a minimum. Our simplified spectral modeling is, however, based firmly on the OPTXAGNF model (Done et al. 2012; Jin et al. 2012a,b,c). We chose this model because it is a recent, widely-used model, it calculates theoretical spectra using physics such as the Novikov-Thorne thin accretion disk model, and because it uses a 'color temperature correction' which accounts for electron-scattering opacity in parts of the disk where hydrogen is ionized. The OPTXAGNF model provides the basis for a new physically-based model of the ionizing AGN spectrum for photoionization modeling.

In photoionization modeling, the ionization parameter and density are important input parameters, so the flux incident on the model cloud is easily calculated. However the actual luminosity of the ionizing source is important only if the modeler is interested in determining the distance of the modeled cloud from the source. We are primarily concerned with the shape of the ionizing spectrum, because this determines the relative emission-line fluxes. Any parameter redundancies may render more difficult the interpretation of the NLR spectrum caused by a given AGN ionizing spectrum. In this work we identify and explain various spectral-shape degeneracies, such as the complete degeneracy between the black hole mass and luminosity in the Novikov-Thorne emissivity, and successfully remove the degeneracies by constructing a new model.

We simplify the OPTXAGNF model by carefully removing and merging degenerate parameters. The resulting model, OXAF, satisfies our requirements by generating realistic model spectral shapes using the fewest possible parameters, and with all of the parameters having a direct impact on the shape of the model spectrum. We then investigate the effect of the OXAF parameters on photoionization models of NLR clouds.

In Section 2.2 we describe the spectral-shape degeneracies that arise in the thin-disc accretion model and in the the OPTXAGNF model, and in Section 2.3 we describe the parameters used to re-parametrize OPTXAGNF. In Section 2.4 we explain how these parameters are used to construct our simplified model OXAF and describe the implementation and validation of the new model. In Section 2.5 we explore how the OXAF parameters affect photoionization model predictions for diagnostic emission lines. Our conclusions are presented in Section 2.6.

2.2 Relationships between parameters in AGN spectral models

The unified model of AGN describes a central, accreting supermassive black hole (SMBH) surrounded by a broad line region, a dusty obscuring torus, and a narrow-line region (Antonucci 1993). The powerful continuum radiation from the central accretion structure illuminates the broad and narrow-line regions.

Important parameters which determine the spectrum of the central accretion structure are the Eddington ratio $L/L_{\rm Edd}$, the SMBH mass $M_{\rm BH}$, the dimensionless SMBH spin a^*, and the innermost radius at which the disk is directly visible. In this section we describe the effects of these parameters on the shape of the ionizing spectrum and the relationships between the parameters.

2.2.1 The relationship between the SMBH mass and Eddington rate

The Novikov-Thorne thin disk model produces a clean relationship between $M_{\rm BH}$ and $L/L_{\rm Edd}$, with these parameters having the same effect on the model spectral shape.

The temperature T at a given radius of the accretion disk r_1 may be calculated using the following equation for the 'outer' region of the disk (Equation 5.10.1 in Novikov & Thorne 1973):

$$T(M_{\rm BH}, \dot{M}_{\rm BH}, a^*, r_1) = \left[\frac{3GM_{\rm BH}\dot{M}_{\rm BH}}{8\pi\sigma_{\rm SB}r_1^3} \mathcal{B}^{-1}\mathcal{C}^{-1/2}\mathcal{Q} \right]^{\frac{1}{4}} \tag{2.1}$$

where $M_{\rm BH}$ is the black hole mass, $\dot{M}_{\rm BH}$ is the accretion rate, a^* is the dimensionless spin parameter, $\sigma_{\rm SB}$ is the Stefan-Boltzmann constant, and G is the gravitational constant. With r defined as the radius normalized by the gravitational radius r_g ($r_g = GM_{\rm BH}/c^2$; $r = r_1/r_g$), the quantities $\mathcal{B}(r, a^*)$, $\mathcal{C}(r, a^*)$ and $\mathcal{Q}(r, a^*)$ are complicated dimensionless radial functions associated with relativistic corrections in the analytic accretion disk solution of Novikov & Thorne (1973) (the $\mathcal{Q}$ function was presented in the follow-up work of Page & Thorne (1974); $\mathcal{B}$, $\mathcal{C}$ and $\mathcal{Q}$ tend to 1 at large r).

Using $L = \epsilon(a^*)\,\dot{M}_{\rm BH}\,c^2$ where $\epsilon(a^*)$ is the total accretion efficiency, and with the definition of r given above, Equation 2.1 may be rewritten as

$$T(M_{\rm BH}, L, a^*, r) = \left[\frac{C}{\epsilon(a^*)r^3}\frac{L}{M_{\rm BH}^2}\mathcal{S}(r, a^*)\right]^{\frac{1}{4}} \tag{2.2}$$

where C is a collection of physical and numerical constants and $\mathcal{S}(r, a^*) = \mathcal{B}(r, a^*)^{-1} \times \mathcal{C}(r, a^*)^{-1/2}\mathcal{Q}(r, a^*)$. Inverting Equation 2.2, we find that

$$\frac{L/L_{\rm Edd}}{M_{\rm BH}} = F((r, T), a^*) \tag{2.3}$$

for a function F, since $L_{\rm Edd} \propto M_{\rm BH}$. Specifying the temperature at a particular normalized radius as well as the spin uniquely determines the ratio $(L/L_{\rm Edd})/M_{\rm BH}$ such that the parameters $L/L_{\rm Edd}$ and $M_{\rm BH}$ are degenerate in their effects on the spectral shape.

2.2.2 The OPTXAGNF model

The OPTXAGNF model (Done et al. 2012; Jin et al. 2012a,b,c) is a significant effort in the development of theoretical models of continuum radiation from accretion onto black holes that match observed optical, UV and X-ray continuum spectra. The model is available for use with the XSPEC spectral fitting package, under the name OPTXAGNF.

The model aims to capture the essential features of the continuum emission from a relativistic thin accretion disk with a Comptonizing corona in the equatorial plane of a rotating black hole. It is assumed that material is accreted only through the outer disk, and the released gravitational energy is divided between three spectral components:

- A pseudo-thermal accretion disk component
- A high-energy, power-law non-thermal component, formed by Compton up-scattering from an optically thin, high-temperature medium
- An intermediate ('soft X-ray excess') component formed by Compton up-scattering from a Compton-thick, low-temperature medium

The model implements the following:

- The standard Novikov & Thorne (1973) thin-disk relativistic accretion disk emissivity
- A disk spectrum produced by summing blackbodies in successive annuli, with the temperature of the blackbody spectrum corrected if necessary using an empirical color temperature correction $f_{\rm col}$. The correction is required due to the absorption opacity varying with temperature, density and wavelength; in particular it is used where hydrogen is ionized in the inner parts of the disk in an attempt to account for modifications to the spectrum due to the disk not being locally thermalized and due to electron-scattering opacity (Davis et al. 2006). The correction becomes increasingly important as the temperature of the disk increases (as the luminosity increases or black hole mass decreases).
- The disk luminosity between the innermost stable circular orbit $r_{\rm ISCO}$ and $r_{\rm cor}$, the 'coronal radius', is all emitted as Comptonized radiation.
- The Comptonized radiation is split between the soft, intermediate component (assumed to arise in the accretion structure itself) and the hard X-ray power-law tail. The seed photons for Comptonization in both cases come from a blackbody with the same (corrected) temperature as the disk at $r_{\rm cor}$.
- The total luminosity from all three components of the emission (disk, Comptonized soft X-ray excess, Comptonized hard X-ray tail) is fixed by the accretion rate and SMBH spin.

The following are the parameters required by OPTXAGNF to characterize the various physical components of the model:

- $M_{\rm BH}$, the black hole mass
- $L/L_{\rm Edd}$, the AGN luminosity in units of the Eddington luminosity, which is proportional to $M_{\rm BH}$.
- a^*, the dimensionless black hole rotation parameter, between 0 and 1 (assuming prograde accretion)
- $r_{\rm cor}$, the coronal radius (inner edge of the visible portion of the disk), in units of the gravitational radius ($r_g = GM_{\rm BH}/c^2$, proportional to $M_{\rm BH}$)
- $r_{\rm out}$, the outer radius of the modeled disk, in units of the gravitational radius, proportional to $M_{\rm BH}$

- T, the temperature of the Compton optically thick material which produces the soft X-ray excess
- τ, the optical thickness of the Compton optically thick material
- $f_{\rm PL}$, the proportion of the corona power emitted in the hard power-law component; $1 - f_{\rm PL}$ is the proportion in the Compton optically thick component
- Γ, the negative of the photon power-law index of the hard X-ray tail component

2.2.3 Relationships between OPTXAGNF model parameters

We explored the behavior of the disk and non-thermal power-law components of the OPTXAGNF model across a wide parameter space (the parameter ranges given in Section 2.3.2) and showed that there are strong spectral-shape degeneracies between key parameters. The following sections discuss these degeneracies, which are in addition to the total degeneracy between $M_{\rm BH}$ and $L/L_{\rm Edd}$ which originates in the Novikov-Thorne model.

Relationship between disk coronal radius, SMBH mass and Eddington rate

Higher disk temperatures lead to higher-energy disk emission, and in particular the high-energy cutoff of the disk emission is set by the maximum temperature of the directly visible part of the accretion disk. Increasing the temperature of the highest-temperature visible parts of the disk and thereby producing higher-energy disk emission is achievable by increasing $(L/L_{\rm Edd})/M_{\rm BH}$ (increasing the luminosity and/or decreasing the mass), or alternatively by reducing $r_{\rm cor}$. Consequently $r_{\rm cor}$ is partially degenerate in its effects on the disk spectrum with $L/L_{\rm Edd}$ and $M_{\rm BH}$. The degeneracy is not total, because changing the innermost visible normalized radius modifies the shape of the disk spectrum in ways that changing $(L/L_{\rm Edd})/M_{\rm BH}$ cannot.

Relationship between SMBH spin and disk coronal radius

Changing the spin a^* with the other parameters fixed has the effect of changing the relative flux contribution of the disk and non-thermal components. This effect is illustrated in Figure 2.1, which shows models with no intermediate component. As the spin of a SMBH increases, more energy is released by infalling matter; the additional energy is released close to the SMBH event horizon. When we fix the mass, coronal radius and luminosity, increasing the spin serves primarily to apportion more of the fixed luminosity to the part of the disk within the coronal radius, and hence to the non-thermal component. Hence a^* has a similar effect to $r_{\rm cor}$ in that it changes the relative contributions of the disk and non-thermal components.

Figure 2.1 shows that the shape of the two spectral components is not strongly affected by a^* (with $r_{\rm cor} = 10\,r_g$). However the parameters $r_{\rm cor}$ and a^* are not entirely degenerate in their effects on the spectral shape, since a^* affects the spectral shape through modifying the radial functions $\mathcal{B}(r, a^*)$, $\mathcal{C}(r, a^*)$ and $\mathcal{Q}(r, a^*)$ in Equation 2.1, whereas $r_{\rm cor}$ determines which values of r contribute to the disk emission.

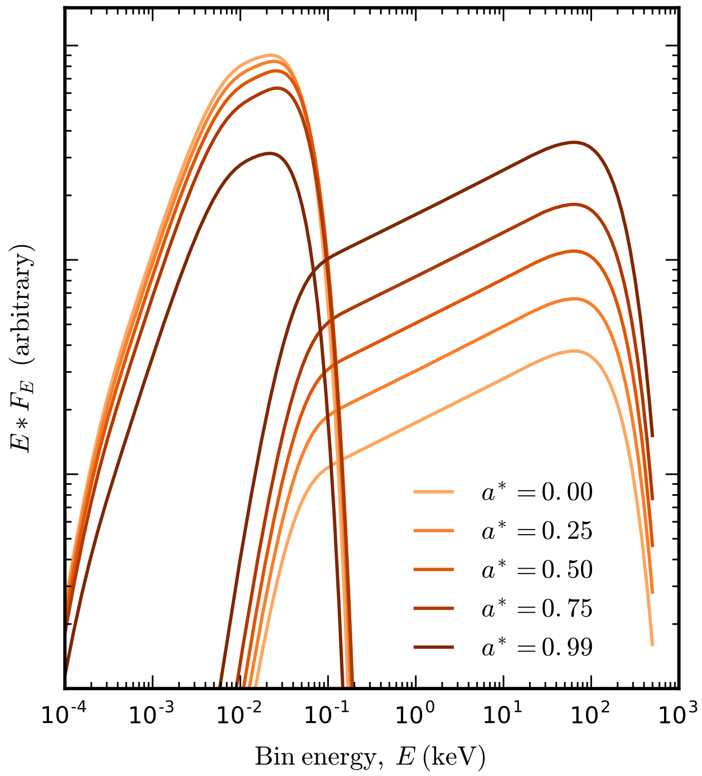

Figure 2.1 The disk and high-energy non-thermal emission components for varying spin parameter a^*, with the other key OPTXAGNF parameters fixed at $M_{\rm BH} = 10^8\ M_\odot$, $L/L_{\rm Edd} = 0.1$, $r_{\rm cor} = 10\ r_g$, and $\Gamma = 1.8$. The intermediate component is not considered ($f_{\rm PL} = 1$). Varying a^* changes the relative contributions of the disk and non-thermal components to the total spectrum. Note that the shape of these components remains relatively independent of a^*.

The full and partial degeneracies discussed in the previous sections suggest that $M_{\rm BH}$, $L/L_{\rm Edd}$, $r_{\rm cor}$ and a^* could be combined into two parameters in a simplified model of the spectral shape - one parameter which shifts the disk emission in energy space, and one parameter which controls the relative flux between the disk and non-thermal components.

2.3 Shrinking the spectral model parameter space

We reduce the free parameter space of the OPTXAGNF model by fixing or neglecting some parameters, and by reparametrizing the remaining parameter space.

2.3.1 Neglected or fixed parameters

Intermediate soft X-ray component

The origin of the widely-observed soft X-ray excess in AGN remains uncertain, despite recent progress. In particular, two general explanations are currently favored, which attempt to explain the relatively constant energy of the soft excess ($kT_e \sim$0.1–0.2 keV). These explanations are Comptonized disk emission (e.g. the treatment in OPTXAGNF), and blurred reflection from the ionized accretion disk (e.g. Walton et al. 2013). Additionally, absorption has been seriously considered (e.g. Gierliński & Done 2004), and there is evidence that a contribution to the soft X-ray excess comes from the wider NLR (e.g. Bianchi et al. 2006).

The possible physical processes that give rise to the centrally-originating soft excess may be constrained using hard and soft time lags (hard X-rays lagging soft X-rays and soft X-rays lagging hard X-rays) and correlations between spectral components. The time-delay of soft X-ray time lags is strongly correlated with black hole mass (De Marco et al. 2013).

Each soft X-ray excess photon with energy in the range $\sim 0.2 - 2$ keV will have less effect on the ionization state of the nebula than a photon with energy in the range $0.01 - \sim 0.2$ keV. In the pilot study of Dopita et al. (2014) we found that the intermediate soft X-ray component was not required to achieve satisfactory fits to the optical emission-line spectrum of the Seyfert galaxy NGC 5427 with photoionization models, although the observed spectrum did not include high-ionization lines. We do however expect that the abundances of high ionization potential species such as ArX (423 eV), FeXIV (361 eV) and FeX (234 eV) would be affected by dominant soft X-ray excesses. Additionally, a strong soft X-ray excess extends the partially-ionized zone, where Auger electrons produced by X-ray bombardment partially ionize the gas, and therefore must to some extent enhance emission of lines such as [O I] and [S II].

We performed an investigation on the effect of the soft excess on photoionization modeling of NLR clouds, using ionizing spectra from the OPTXAGNF model. The parameters of the MAPPINGS 5.1[1] (Sutherland et al. 2016, in prep.) models and OPTXANGF spectra were fixed, apart from two quantities: the relative strength of the soft excess which ranged from 0% to 100% of the non-thermal flux, and the coronal radius which ranged from $r_{\rm cor} = 20$ to $r_{\rm cor} = 60$. The models were ionization-bounded and ended when the nebula was 99% neutral. The results are presented in standard optical diagnostic diagrams (Baldwin, Phillips and Terlevich 1981; Veilleux & Osterbrock 1987) in Figure 2.2, with the fiducial model parameter values listed in the caption. The standard optical diagnostic diagrams use ratios of lines associated with different ionization levels in the gas to distinguish nebulae based on the cause of ionization. Ionization increases from bottom-left to top-right on the diagrams. The lower-left of each of the diagnostic diagrams is associated with H II regions of varying metallicity and ionization parameter, whereas the top-right is associated with ionization by harder AGN spectra or shocks. The standard dividing lines on the diagrams are described in the caption.

The results shown in Figure 2.2 confirm that the soft X-ray excess is not of primary importance when predicting diagnostic optical emission-line ratios. The line ratios are evidently most sensitive to variation in the coronal radius or weighting of spectral components when most of the energy released inside the coronal radius is emitted in the power-law component as opposed to the soft excess. For the tested $r_{\rm cor}$ values larger than 20 r_g, the [S II]/Hα and [O I]/Hα ratios are significantly increased by increasing the proportion of the flux emitted in the power-law tail, resulting in some outlying points to the right of the second and third panel in the figure. The positions of these points are due to the partially-ionized zone being extended by hard X-rays in improbably hard ionizing spectra. If we do not consider these power-law dominated models (shown for completeness), the range of points representing the different soft excess strengths is small compared to the variation that may be produced by varying the ionization parameter or metallicity, for example. If the proportion of the energy emitted in the soft excess as opposed to the power-law component does not vary as strongly between real objects as it does in our experiment, and additionally if

[1] Available at `http://miocene.anu.edu.au/Mappings`

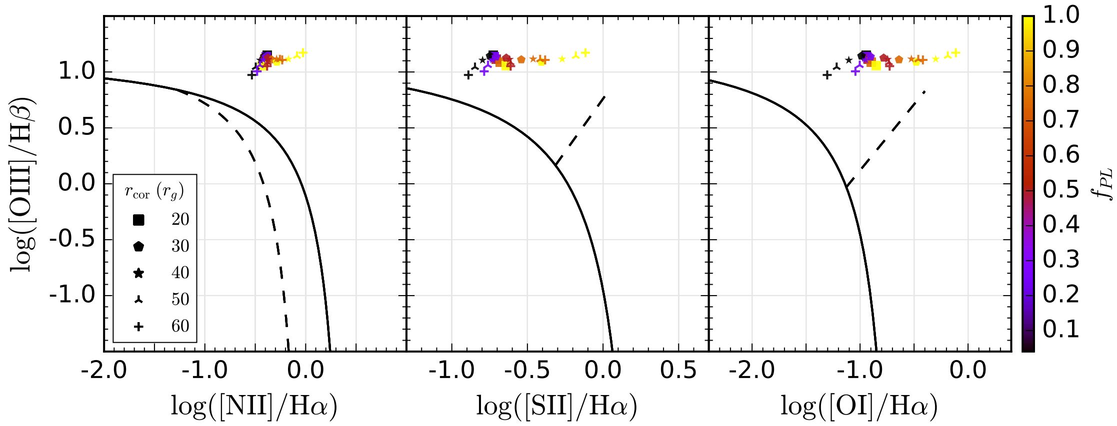

Figure 2.2 Predicted emission-line ratios produced by MAPPINGS photoionization models using OPTXAGNF input ionizing spectra, shown on optical diagnostic diagrams (Baldwin, Phillips and Terlevich 1981; Veilleux & Osterbrock 1987). The solid lines (Kewley et al. 2001) and the dashed line in the left panel (Kauffmann et al. 2003) divide HII regions (below) and nebulae with higher ionization states (above). The dashed lines in the rightmost panels (Kewley et al. 2006) divide LINERs (below) and Seyferts (above). The fraction of the energy inside the coronal radius that goes to the power-law component as opposed to the intermediate Comptonized component was set to each of $f_{PL} = 0.04, 0.25, 0.5, 0.75, 1.00$ and for each of these values we considered coronal radii of $r_{\rm cor} = 20, 30, 40, 50, 60\ r_g$. Points are colored by f_{PL} and the marker shape indicates $r_{\rm cor}$. We argue in Section 2.3.1 that the results in this figure demonstrate that photoionization modeling of the strong optical lines is insensitive to the soft X-ray excess. For this experiment the MAPPINGS models were configured with metallicity $Z = 2\ Z_\odot$, ionization parameter $U(H) = 10^{-2}$, and a constant pressure of $P/k = 10^6$ K cm^{-3}. The other parameters of OPTXAGNF were set to $M_{\rm BH} = 5 \times 10^7\ M_\odot$, $L/L_{\rm Edd} = 10^{-0.5}$, $a^* = 0$, $\Gamma = 2.0$, and (for the Comptonized soft excess) $kT = 0.2$ keV with $\tau = 15$.

real objects are mass-bounded as opposed to ionization-bounded (i.e. hard X-rays escape the NLR), then the ranges shown in Figure 2.2 would represent approximate upper bounds on the sensitivity to the soft excess.

In the remainder of this work we do not include the intermediate Comptonized component, such that the fraction of the corona power in the power-law tail is set to $f_{PL} = 1$, and the parameters for the temperature and optical thickness of the Comptonizing optically-thick medium have no effect.

Neglecting the intermediate component enables a vast simplification of the model. Including the soft excess would complicate the comparison of photoionization models to observed NLR emission-line spectra due to uncertainty regarding the origin, time-averaged behavior, and importance relative to other spectral components of the soft X-ray excess. We note that recently Pal et al. (2016) attributed ∼60 − 80% of the ∼0.3 − 2 keV emission observed in the AGN II Zw 177 to the soft excess, with significant variation observed between observations separated by 11 years. Another recent work is a study of the AGN RE J1034+396 (Czerny et al. 2016), in which the best-fitting models suggested that ~90% of the power produced inside the coronal radius is emitted in the intermediate component. Although the strength of the soft excess has been measured in sources such as II Zw 177 and RE J1034+396, the properties of the soft X-ray excess across the population of Seyfert galaxies, not just those that have been studied in X-rays, are unknown.

The black hole spin

The spins of astrophysical black holes have long been expected to be non-zero. It is now routine to 'map' the central ~20 r_g of AGN accretion structures by studying X-ray reverberation lags and blurred accretion disk reflection (Fabian 2016). Identifying the innermost radius required by spectral blurring analysis with the Innermost Stable Circular Orbit (ISCO) allows the black hole spin to be measured. Spin measurements performed to date generally demonstrate high spins (Reynolds 2014). However because radiative efficiency increases by up to a factor of 5 with increasing spin, the very high calculated spins for many AGN with spin measurements are associated with a strong selection bias (Fabian 2016).

As demonstrated above in Section 2.2.3, the black hole spin is partially degenerate with $r_{\rm cor}$ in that it changes the relative contributions of the disk and non-thermal components to the total spectrum. The coronal radius will be set larger than radii for which we expect the disk spectrum shape to be strongly affected by the SMBH spin. Figure 2.1 shows that changing the spin changes the relative energy in the disk and non-thermal components by an order of magnitude (between spins of 0 and 1); in our simplified model this effect will be accounted for by an explicit parameter for this scaling. The SMBH spin was set to $a^* = 0$.

Outer edge of accretion disk

The outer disk produces non-ionizing optical and IR emission, and therefore does not contribute to the NLR heating. The parameter defining the outer edge of the accretion disk was set to 10^4 r_g, a default value.

2.3.2 Reparametrizing the AGN continuum model

As a result of the simplifications discussed in the Section 2.3.1, the OPTXAGNF parameters have been reduced to the four most important parameters $M_{\rm BH}$, L, $r_{\rm cor}$ and Γ. Exploration of the properties of the theoretical AGN spectra and development of a simplified model (Section 2.4) were performed over the following ranges of these four parameters:

- $-5.0 \leq \log_{10}(L/L_{\rm Edd}) \leq 0.0$
- $6.0 \leq \log_{10}(M_{\rm BH}/M_{\odot}) \leq 9.0$
- $1.4 \leq \Gamma \leq 2.6$
- $10\ r_g \leq r_{\rm cor} \leq 100\ r_g$

The maximum luminosity of Eddington was chosen because the Novikov-Thorne thin disk model cannot plausibly be used beyond this limit; indeed a *slim* disk prescription is necessary for a luminosity above $\sim$0.3 $L/L_{\rm Edd}$. The range of SMBH masses covers the observed range in AGN except for extreme objects (c.f. Figure 4 in Vika et al. (2009)). The broad range in Γ covers the approximate range of observed values (c.f. Figure 4 in Molina et al. (2013)), corresponding to very soft ($\Gamma = 2.6$) through to very hard ($\Gamma = 1.4$) power-law tails.

The physical extent of the corona has been constrained using analysis of blurred X-ray reflection, modeling of X-ray reverberation, and microlensing observations; these methods suggest that the Comptonizing corona lies within approximately 10 r_g of the black hole (Fabian 2016). However because of the selection bias discussed in Section 2.3.1, coronal geometries inferred in X-ray studies are not necessarily representative of the population of Seyfert galaxies. We chose a lower bound for the coronal radius of 10 r_g here; our experimentation showed that below this value the high-energy part of the accretion disk emission becomes too strongly affected by relativistic corrections for easy simplification of the model. Setting a minimum coronal radius of 10 r_g will primarily affect the high-energy part of the accretion disk emission by removing it from the disk spectrum. The top end of the $r_{\rm cor}$ range was selected to include the range suggested by Done et al. (2012).

Reparametrizing the disk component

A highly desirable simplification is combining the three fully or partially degenerate parameters L, M_{BH} and r_{cor} into a single parameter that is able to parametrize (at least approximately) the position in energy space and shape of the Big Blue Bump (BBB) disk emission. The parameter which was chosen to replace the degenerate trio (L, M_{BH}, r_{cor}) was E_{peak}, the peak of the BBB when the disk spectrum is given in a log-log plot of energy flux versus energy (e.g. Figure 2.1). The location of the single peak is a reliable and easily-calculated feature of a model BBB.

The value of E_{peak} was determined for a grid of OPTXAGNF spectra over the relevant ranges of the three parameters affecting E_{peak}, which are L, M_{BH} and r_{cor}. The results were systematically analyzed for each value of r_{cor}, before all the analyses for various r_{cor} values were combined into an empirical formula for calculating E_{peak} as a function of (L, M_{BH}, r_{cor}). An example of the analysis that was applied for a single value of r_{cor} is presented in Figure 2.3.

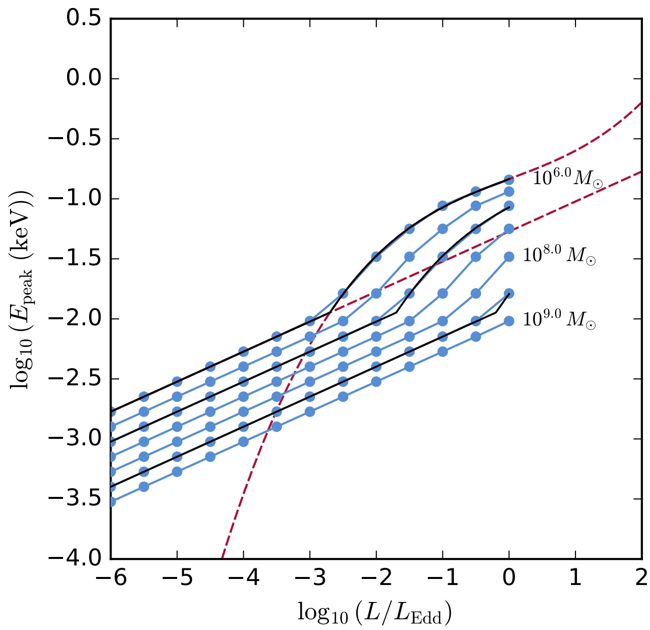

Figure 2.3 We can characterize the dominant AGN emission in the EUV, the Big Blue Bump (BBB), in terms of the peak of its energy distribution, E_{peak}. Here we show the E_{peak} predicted by OPTXAGNF as a function of L/L_{Edd} (blue points) and M_{BH} (blue curves as labeled, spaced at 0.5 dex), for $r_{\mathrm{cor}} = 24.5\ r_g$. To predict E_{peak} for a given r_{cor} and M_{BH} we use a model with the functional form $\max(f_1(L/L_{\mathrm{Edd}}), f_2(L/L_{\mathrm{Edd}}))$ (Equation 2.4) where f_1 is a power-law (at low L/L_{Edd}) and f_2 is a log-space cubic (at high L/L_{Edd}). Both f_1 and f_2 are illustrated for $M_{\mathrm{BH}} = 10^6$ by the red dashed curves. Model fits for $M_{\mathrm{BH}} = 10^{6.0}, 10^{7.0}$ and $10^{8.5}\ M_\odot$ are overlaid in black.

Figure 2.3 demonstrates how fits for E_{peak} at a given r_{cor} must account for the 'piecewise' behavior of $E_{\rm peak}$ as a function of $M_{\rm BH}$ and L. Our solution to this problem was to use a combination of linear and cubic functions as described in the figure and caption. The coefficients of these linear and cubic functions varied as a function of $r_{\rm cor}$. To construct a general function applicable over the entire three-dimensional (L, $M_{\rm BH}$, $r_{\rm cor}$) parameter space, we required a means to determine the coefficients of the linear and cubic functions from $r_{\rm cor}$. Linear and quadratic functions of $\log r_{\rm cor}$ produced satisfactory fits to the values of these coefficients.

The analysis in Figure 2.3 was applied for $r_{\rm cor}$ = 6, 10, 15, 24, 39, 63, 100 r_g. The analysis for $r_{\rm cor} = 6\ r_g$ (i.e. at the innermost stable circular orbit, such that the corona is effectively absent) was found to be generally inconsistent with the analyses for the larger $r_{\rm cor}$ values, presumably due to the effect of strong general relativistic corrections. We thus did not use the analysis for $r_{\rm cor} = 6\ r_g$.

The combined analysis for the various $r_{\rm cor}$ values culminated in the following equation for a hypersurface to predict $E_{\rm peak}$ as a function of L, $M_{\rm BH}$ and $r_{\rm cor}$:

$$\log_{10}\ E_{\rm peak}(L, M_{\rm BH}, r_{\rm cor}) = \max(f_1, f_2) \tag{2.4}$$

where

$$f_1(L, M_{\rm BH}, r_{\rm cor}) = (A_{x^2}\ R(r_{\rm cor})^2 + A_{x^1}\ R(r_{\rm cor}) + A_{x^0}) + B\ S(L, M_{\rm BH}) \tag{2.5}$$

and

$$\begin{aligned} f_2(L, M_{\rm BH}, r_{\rm cor}) = {} & (b_{3,x^1}\ R(r_{\rm cor}) + b_{3,x^0})(S(L, M_{\rm BH}) + 6)^3 + \\ & (b_{1,x^2}\ R(r_{\rm cor})^2 + b_{1,x^1}\ R(r_{\rm cor}) + b_{1,x^0})(S(L, M_{\rm BH}) + 6) \\ & +\ (a_{x^2}\ R(r_{\rm cor})^2 + a_{x^1}\ R(r_{\rm cor}) + a_{x^0}) \end{aligned} \tag{2.6}$$

Here the energy of the BBB peak $E_{\rm peak}$ is in keV, $S(L, M_{\rm BH}) = \log_{10}((L/L_{\rm Edd})/M_{\rm BH})$ where $M_{\rm BH}$ is in $M_\odot$, and $R(r_{\rm cor}) = \log_{10}(r_{\rm cor}/r_g)$. The fit parameters are given in Table 2.1. Note that L and $M_{\rm BH}$ appear explicitly in Equations 2.5 and 2.6 only through the quantity $S(L, M_{\rm BH})$, due to the complete degeneracy in their effects on the spectral shape (Section 2.2.1; note that there is an implicit dependence on $M_{\rm BH}$ in the normalization of L and $r_{\rm cor}$). The arbitrary constant 6 occurs with $S(L, M_{\rm BH})$ in Equation 2.6 only because it was propagated through the analysis from the cubic functions such as those in Figure 2.3, where the cubic was fitted to the $\log M_{\rm BH}/M_\odot = 6$ data (the lowest $M_{\rm BH}$ value we considered), and was shifted appropriately to apply to other $M_{\rm BH}$ values. Equations 2.4 to 2.6 in conjunction with Table 2.1 predict $E_{\rm peak}$ with a standard deviation of ∼2% in linear energy space.

Table 2.1 Fit parameters for Equations 2.5 and 2.6

Parameter	Value	Parameter	Value
A_{x^2}	-0.18 ± 0.04	b_{1,x^2}	0.391 ± 0.008
A_{x^1}	0.0 ± 0.1	b_{1,x^1}	-0.83 ± 0.02
A_{x^0}	0.59 ± 0.08	b_{1,x^0}	0.61 ± 0.02
B	0.250 ± 0.004	a_{x^2}	-0.30 ± 0.03
b_{3,x^1}	0.034 ± 0.002	a_{x^1}	0.4 ± 0.1
b_{3,x^0}	-0.019 ± 0.003	a_{x^0}	-0.82 ± 0.07

The shape of the BBB spectrum depends (to first order) only on the energies it covers, so we use $E_{\rm peak}$ to parametrize both the location in energy space and shape of the BBB emission. The construction of a simplified BBB model using this approach is discussed in Section 2.4.1.

Reparametrizing the non-thermal component

The shape of the non-thermal component is determined by the shape of the seed photon spectrum and by the parameter Γ. The seed photon spectrum is a blackbody with a temperature which will be determined by the single parameter $E_{\rm peak}$, so we have already reparametrized the shape of the non-thermal component such that it depends on only two parameters. The construction of the non-thermal emission component is discussed in Section 2.4.2.

2.4 The OXAF model

This section describes the construction of the OXAF model. In particular OXAF is a 3-parameter model, and the name OXAF, a contraction of OPTXAGNF, was chosen to reflect that OXAF is in some sense a 'reduced' OPTXAGNF.

The three parameters of the OXAF model are the energy of the peak of the Big Blue Bump (BBB) $E_{\rm peak}$, the photon power-law index Γ, and the proportion of the total energy flux emitted in the non-thermal component $p_{\rm NT}$, with the remainder being in the BBB.

In optxagnf the shape of the BBB and the proportion of energy which goes to the power-law component are not independent, because both are affected by $r_{\rm cor}$. However in oxaf, the parameters $E_{\rm peak}$ (which determines the BBB shape) and $p_{\rm NT}$ are independent by construction. For a given $E_{\rm peak}$, oxaf does not have any parameters available to reproduce the variation in optxagnf BBB shapes which occurs as $r_{\rm cor}$ changes. However the variation of the BBB shape with $r_{\rm cor}$ is a small effect, so a single oxaf BBB is able to satisfactorily reproduce optxagnf BBBs which have the same peak energy but a range of $r_{\rm cor}$ (Section 2.4.4).

The following sections show how we construct a BBB using only one parameter, the energy of the BBB peak $E_{\rm peak}$, and a non-thermal component using only two parameters ($E_{\rm peak}$ and Γ).

2.4.1 Modeling the accretion disk emission

The BBB is parametrized using only one parameter, the energy of the BBB peak $E_{\rm peak}$. The oxaf model must use this input to determine the shape of the BBB, in particular for relatively high BBB peak energies, when the color correction becomes important.

The modeled BBBs are considered in terms of log-log plots of energy flux (i.e. keV/cm^2/s) versus energy. The effects of the color correction in this space are illustrated in Figure 2.4.

The oxaf model constructs the BBB as follows: sixth-order polynomials were fit to a series of optxangf BBBs at different energies ($\log_{10}(E_{\rm peak}/{\rm keV}) = -3.0$, -2.4, -1.9, -1.4, -1.2, -0.7) roughly representative of the range of shapes shown in Figure 2.4. The BBBs were normalized to have the same peak flux and position of the peak flux in energy space before fitting. The coefficients of the fits are stored in the oxaf code. To determine the shape of an oxaf BBB for a given input $E_{\rm peak}$, the code (log-)linearly interpolates between the polynomial fits for the nearest $E_{\rm peak}$ values above and below the input $E_{\rm peak}$. The resulting polynomial BBB shape is a weighted sum of the two 'nearest' polynomials. The interpolated polynomial is shifted in energy space so the peak aligns with the input $E_{\rm peak}$ value.

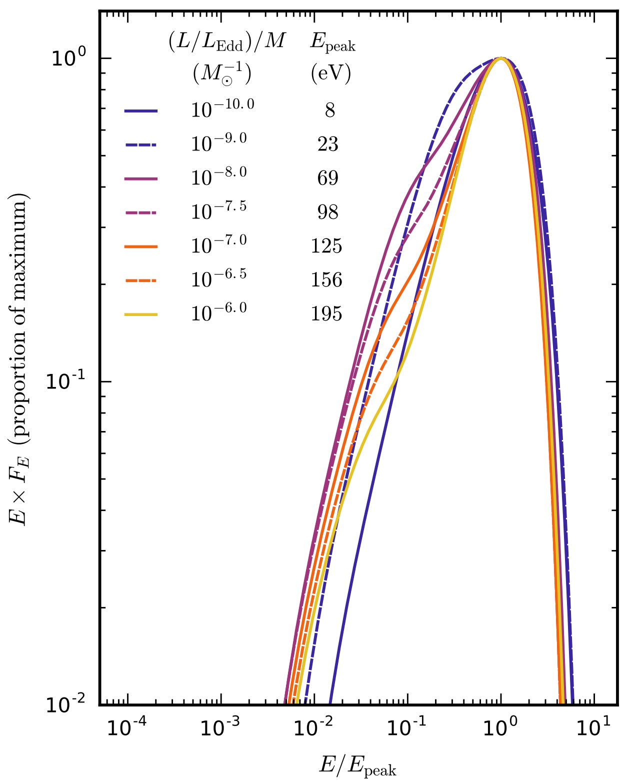

Figure 2.4 Normalized Big Blue Bump (BBB) accretion disk component OPTXAGNF spectra, shown for varying $(L/L_{\rm Edd})/M_{\rm BH}$ and for $r_{\rm cor} = 10\ r_g$. The models were generated using a standalone version of OPTXAGNF produced using a simple fortran wrapper. The shape of the BBB changes due to the increasingly important color correction for higher-energy BBBs. The curves are normalized to have the same flux in the bin with maximum flux, and shifted in logarithmic energy space to have coinciding peaks.

2.4.2 Modeling the non-thermal emission

The non-thermal component is parametrized using two quantities: $E_{\rm peak}$ and Γ.

The OXAF model uses the *Nthcomp* routine to generate an inverse-Compton scattered non-thermal component. The fortran subroutines *donthcomp* (Zdziarski et al. 1996; Życki et al. 1999), and *thcompton* with *thermlc* (Lightman & Zdziarski 1987) from XSPEC were incorporated into OXAF.

There is one difference in the modeling of the non-thermal component between OXAF and OPTXAGNF. In OPTXAGNF the seed blackbody spectrum temperature is set to $T_{\rm cor}$, the color-corrected temperature of the disc at $r_{\rm cor}$. To approximate this method in OXAF it was necessary to convert the $E_{\rm peak}$ parameter to an estimate of $T_{\rm cor}$, despite the OXAF model lacking an explicitly calculated $r_{\rm cor}$. The conversion was achieved by extracting $T_{\rm cor}$ values for 72 representative OPTXAGNF models across the parameter space and relating them to the $E_{\rm peak}$ values calculated for these models using Equation 2.4. The following linear fit from this comparison is used by OXAF to relate the two parameters:

$$\log_{10}(kT_{\rm cor}) = 0.96\ \log_{10}(E_{\rm peak}) - 0.39 \tag{2.7}$$

where both $kT_{\rm cor}$ and $E_{\rm peak}$ are measured in keV. Here the gradient and intercept have errors of 0.02 and 0.03 dex respectively, and the resulting error on $\log_{10}(kT_{\rm cor})$ is 0.07 dex. The non-thermal spectrum is constructed by converting $E_{\rm peak}$ to $T_{\rm cor}$ using Equation 2.7 before inputting Γ, $T_{\rm cor}$ and an assumed Comptonizing plasma temperature of 100 keV into the OXAF *donthcomp* function, which in turn calls *thcompton*, which calls *thermlc*.

2.4.3 Implementation

The OXAF model was implemented as a module *oxaf.py* written in the programming language python, with a design focus on convenience of use. The module depends only on the standard third-party numerical Python library *numpy*, is a single file which may be used with both python 2 and python 3, and requires no compilation step to run (the included fortran codes were converted to python). The module may simply be run as a command line script to output a model spectrum to stdout, or alternatively may be imported to be used in python code. The module is thoroughly self-documented and is available on the Astrophysics Source Code Library (ASCL) [2].

The *oxaf.py* module includes functions to find $E_{\rm peak}$, the peak of the Big Blue Bump (BBB) disk emission (i.e. implement Equation 2.4), calculate an accretion disk spectrum (as described in Section 2.4.1), calculate a non-thermal component spectrum (as described in Section 2.4.2), and sum these two components using a given weighting.

The output spectrum is a function of only three parameters, being $\log_{10}(E_{\rm peak}/{\rm keV})$, Γ, and $p_{\rm NT}$, which is the proportion of the total flux over the range $0.01 < E$ (keV) $<$ 20 which is assigned to the non-thermal component, with $1 - p_{\rm NT}$ being the proportion assigned to the BBB disk component.

The functions which return the individual components and the full spectrum (sum of the two components) normalize the spectra so that the sum of the bin fluxes over

[2] Available at `https://github.com/ADThomas-astro/oxaf`

the range $0.01 < E(\mathrm{keV}) < 20$ is equal to one.

2.4.4 Validation

The OXAF model was validated against the OPTXAGNF model by comparing OXAF output with OPTXAGNF output for many models across the parameter space. The BBB and non-thermal components were considered separately. The OPTXAGNF parameters used were chosen so that their various combinations did not give multiple identical BBB peak energies and hence multiple identical OXAF spectra. The chosen values were $\log_{10}(L/L_{\mathrm{Edd}}) = -5.00$, -3.75, -2.85, -2.15, -1.60, -1.20, -0.80, -0.40, 0.00; $\log_{10}(M_{\mathrm{BH}}/M_{\odot}) = 6.0$, 6.5, 7.0, 7.5, 8.0, 8.5, 9.0; $r_{\mathrm{cor}} = 10$, 25, 40, 50, 63, 100 r_g and $\Gamma = 1.4$, 1.7, 2.0, 2.3, 2.6, for a total of 1890 OPTXAGNF spectra. The range of parameters was chosen for completeness; not all of the tested parameter space necessarily corresponds to observed AGN.

Figures 2.8 and 2.9 in the appendix demonstrate the performance of the OXAF model in reproducing the output spectra of OPTXAGNF. The figures show that over the relevant energy range, from the Lyman limit to above the energy at which iron may be fully ionized (0.01 to ~20 keV), OXAF predictions are sufficiently close to OPTXAGNF predictions for our purposes (differences are far less than modeling uncertainties). The interquartile range displayed in each figure indicates that over the relevant energy range, OXAF predictions tend to be within ~10-20% of the OPTXAGNF value for the BBB component, and within ~5% for the non-thermal component. The largest deviations tend to occur for energies which are probably too high to have a strong impact on photoionization model results (1-10 keV) or are in an unlikely part of the parameter space (e.g. $r_{\mathrm{cor}}{\sim}60\ r_g$). The most extreme discrepancies (i.e. 95th percentile and upwards) for the BBB comparisons tend to be due to irrelevant cases where only a small fraction of the total flux is in the relevant ionizing energy range, and hence the normalization over this range inflates a small section of the spectrum and magnifies proportional differences between the two models. For the non-thermal component the differences are due only to the small scatter in the fit given in Equation 2.7, i.e. the seed blackbody spectra for OXAF and OPTXAGNF have slightly different temperatures.

The OXAF spectra reproduce the OPTXAGNF models with sufficient accuracy for photoionization modeling of optical diagnostic emission lines. The differences between OXAF and OPTXAGNF are smaller than the uncertainties due to, for example, any of the following:

- The angular dependence of the accretion disk spectrum, including the effects of special relativistic beaming, gravitational beaming/light bending, and limb darkening (Laor & Netzer 1989). Gravitational redshifts are an additional consideration.

- Uncertainties in fundamental aspects of the thin disk model, such as the α-prescription, and aspects of the geometry of the accretion disk and corona including the variation with black hole spin (e.g. You et al. 2012). The luminosity range over which the model is applicable is another consideration, e.g. for luminosities over $\sim$0.3 $L_{\rm Edd}$ a 'slim' disk is a more appropriate model.

- Radiative transfer effects; for example, the use of a color correction in the OPTXAGNF model neglects H and He edges (see Figure 1 in Done et al. 2012)

Two simple tests were performed to compare MAPPINGS 5.1 photoionization models based on OPTXAGNF and OXAF spectra. For the first test the input OPTXAGNF spectrum was configured with ($L/L_{\rm Edd}$, $M_{\rm BH}$, $r_{\rm cor}$, Γ) = (0.2, 10^7 $M_\odot$, 15 r_g, 2.2), while the OXAF spectrum was configured with ($E_{\rm peak}$, Γ, $p_{\rm NT}$) = (68.3 eV, 2.2, 0.223), where $E_{\rm peak}$ was calculated from Equation 2.4 and $p_{\rm NT}$ was calculated to match the proportion in the OPTXAGNF spectrum. The plane-parallel MAPPINGS models for this test were configured with a metallicity of $2Z_\odot$, an ionization parameter of $U(H) = 10^{-2}$, and a constant pressure of $P/k = 10^6$ K cm^{-3}. The resulting line fluxes were broadly consistent between the two models. Of 43 optical lines with predicted fluxes of more than 1% of Hβ, all had a flux discrepancy of less than 10% of the flux predicted using the OPTXAGNF model. All but 4 line fluxes showed a difference of less than 5%; these 4 lines from N I or O I had differences of $\sim$7 − 8%. The reason for this discrepancy is that these lines from low-ionization species are very sensitive to small differences in the shape of the hard photon spectrum since the emission is produced mostly in a partially ionized zone heated by Auger electrons.

For the second test the input OPTXAGNF spectrum was configured with ($L/L_{\rm Edd}$, $M_{\rm BH}$, $r_{\rm cor}$, Γ) = (0.3, 10^8 $M_\odot$, 20 r_g, 1.8), while the OXAF spectrum was configured with ($E_{\rm peak}$, Γ, $p_{\rm NT}$) = (19.9 eV, 1.8, 0.342). The MAPPINGS models used a metallicity of $3Z_\odot$, an ionization parameter of $U(H) = 10^{-2.5}$, and a constant pressure of $P/k = 10^6$ K cm^{-3}. With the somewhat softer ionizing spectrum and different nebular parameters, there were only 31 optical lines with predicted fluxes of more than 1% of Hβ, and all of those lines had a flux discrepancy below 2%, with 24 having a discrepancy under 1%. The accuracy of oxaf is more than sufficient for our purposes of photoionization modeling.

2.5 The effect of oxaf parameters on predicted emission-line ratios

A grid of mappings photoionization models was used to explore the effect of the oxaf parameters on emission-line ratios on the standard optical diagnostic diagrams. The grid was run over a range of photoionization model parameters and a range of all three oxaf parameters. The results are shown in Figure 2.5 for the dusty, plane-parallel mappings models configured with metallicity $Z = 1.5\ Z_{\odot}$, ionization parameter $U(H) = 10^{-3}$, and a constant pressure of $P/k = 10^{7}$ K cm^{-3}. Each model was iteratively re-run three times to ensure that the total pressure (including radiation pressure) was close to the input pressure, with this constraint applied where the model nebula was 50% ionized. The iterations for each gridpoint culminated in a model which ended when the nebula was 99% neutral.

Also plotted in Figure 2.5 are gray points showing the measured spatially-resolved line flux ratios for the galaxy NGC 1365 from the S7 galaxy survey (Dopita et al. 2015). Each point represents the line ratios for the narrowest Gaussian kinematic component in the spectrum of a 1”×1” spatial pixel (the seeing FWHM was ∼1.1”). A S/N cut of 10 was applied to the linear flux ratios. In the leftmost two columns of diagrams these points form a ‘mixing sequence’ from line-ratios associated with excitation purely due to star formation (at the bottom) to excitation purely by AGN radiation (at the top).

The predicted line ratios for our fiducial mappings models approximately coincide with some of the measured ‘pure-AGN’ line ratios, especially in the leftmost column. Predictions of the weaker [O I]λ6300 line however are inconsistent with the observations. This line is produced predominantly in the partially ionized zone that arises due to the hard EUV and X-ray photons. The temperature and size of this region and thus the strength of the [O I] line are sensitive to the hard ionizing spectrum. In addition the fractional ionization state of oxygen is strongly dependent upon charge exchange reactions and as a result this line is very difficult to predict accurately. The [S II]λλ 6716, 6731 doublet can also arise from this partially ionized region and is also somewhat inconsistent with the observations, albeit to a lesser

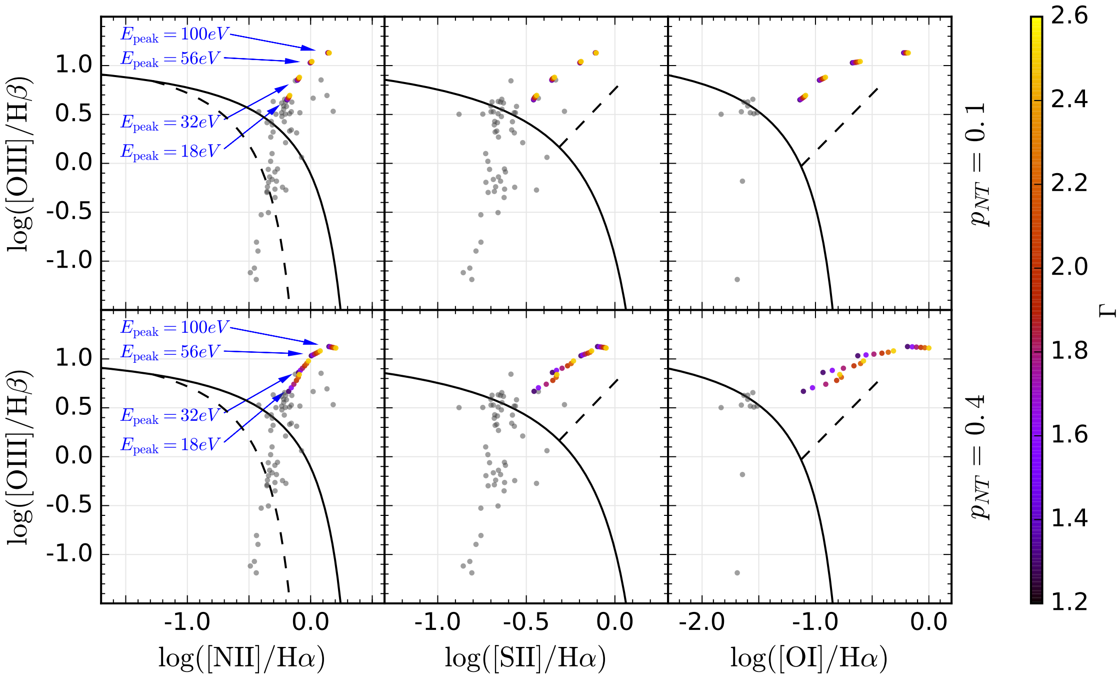

Figure 2.5 Optical diagnostic diagrams showing the effect of the OXAF parameters E_{peak}, Γ and p_{NT} on MAPPINGS photoionization model predictions. Dividing lines are the same as in Figure 2.2. The top row of diagrams is for $p_{\text{NT}} = 0.1$ and the bottom row is for $p_{\text{NT}} = 0.4$. The gray points are observed line ratios for the galaxy NGC 1365 from the S7 galaxy survey (Dopita et al. 2015), with each point representing the line ratios for the narrowest Gaussian kinematic component in a single spatial pixel. See Section 2.5 in the text for more information and interpretation of the diagrams.

degree. The overpredicted fluxes from these species could to some extent be due to the NLR clouds being mass-bounded as opposed to ionization-bounded (as in the models), i.e. more of the high-energy photons escape and the partially-ionized zones are shorter for the observed ensemble of NLR clouds in NGC 1365 compared to the models.

2.5.1 Effect of the individual OXAF parameters

In this section we discuss Figure 2.5 and interpret the effect of each OXAF parameter on the model predictions.

Energy of the peak of the disk emission E_{peak}

The logarithmically-spaced values of E_{peak} in Figure 2.5 show that increasing the energy of the peak of the disk emission, and thereby increasing the energy of the ionizing photons, increases both the relative ionization state and the temperature of the nebula. The sensitivity of optical diagnostic line ratios to $E_{\rm peak}$ is comparable to the sensitivity to the ionization parameter.

Proportion of flux in non-thermal component, p_{NT}

We first consider the expected range of values of $p_{\rm NT}$. Jin et al. (2012a) study a sample of 51 unobscured Seyfert 1 galaxies and fit the full three-component OPTXAGNF model to the observed SEDs. The proportion of the bolometric luminosity emitted in the power-law component in the best-fit model is less than 0.05 for ∼20% of the sample, less than 0.2 for ∼50% of the sample, and less than 0.4 for ∼80% of the sample. Although the soft excess is a significant component (allocated more flux than the power-law component for ∼70% of the sample), it is effectively an extension of accretion disk emission to higher energies, so the proportion of flux in the power-law tail is comparable to the $p_{\rm NT}$ OXAF parameter. Hence we take $p_{\rm NT} \sim 0.1 - 0.4$ as an appropriate range for typical ionizing AGN spectra.

The values $p_{\rm NT} = 0.2, 0.7$ were included in the model grid but are not shown in Figure 2.5. The diagnostic line-ratio predictions for $p_{\rm NT} = 0.2$ were intermediate between those of $p_{\rm NT} = 0.1$ and $p_{\rm NT} = 0.4$ and were similar to those of $p_{\rm NT} = 0.1$. The value $p_{\rm NT} = 0.7$ was very high, with only a few extreme objects in the Jin et al. (2012a) sample having such power-law-dominated SEDs. Hence the figure requires only the values $p_{\rm NT} = 0.1$, 0.4 to indicate the effect of $p_{\rm NT}$ and show the approximate magnitude of strong line-ratio variations due to $p_{\rm NT}$ variations that may occur between Seyfert galaxies.

Increasing the value of $p_{\rm NT}$ increases the length of the trailing partially ionized zone in the photoionization models. For $E_{\rm peak}$ = 32 eV, Γ = 1.8, log U = -2.0 and Z = 1.5 $Z_\odot$, variation of $p_{\rm NT}$ from 0.1 to 0.7 increased the length of the modeled cloud by a factor of ∼4 to 1.5 pc. Extending the partially-ionized zone increases the [SII]/Hα and [OI]/Hα line ratios, as the figure shows for $p_{\rm NT} = 0.1 \rightarrow 0.4$.

Photon index of the power-law tail Γ

For values of $p_{\rm NT} \lesssim 0.2$, the predicted emission-line ratios do not show strong sensitivity to Γ. Figure 2.5 shows how as Γ increases, [SII] and [OI] line emission is enhanced relative to Hα. Increasing Γ allocates more of the non-thermal energy to relatively soft X-ray photons which are more easily absorbed by the nebula, causing more emission in the partially ionized zone. Hence Γ has a similar effect to p_{NT}. As p_{NT} increases, the sensitivity to Γ increases due to the greater relative effect of X-ray power-law photons on the nebula ionization structure.

2.5.2 Comparison with default CLOUDY AGN spectrum

In this section we compare OXAF spectra with the default spectrum produced by the AGN spectral model supplied with the CLOUDY (Ferland et al. 2013) photoionization code. We also compare the predicted optical diagnostic emission-line ratios produced by using these ionizing spectra in MAPPINGS photoionization models.

The CLOUDY AGN spectral model uses an analytic formula consisting of exponential and power-law factors and terms. The default CLOUDY AGN model was configured with the following default values: a BBB temperature of $T = 1.5 \times 10^5$ K, an X-ray to UV ratio of $\alpha_{ox} = -1.4$, a low-energy BBB slope of $\alpha_{uv} = -0.5$, and an X-ray power-law index of $\alpha_x = -1$ (corresponding to $\Gamma = 2$).

Figure 2.6 shows the CLOUDY default SED, along with two 'equivalent' OXAF spectra. The first OXAF spectrum has (E_{peak}, Γ, p_{NT}) = (6.9 eV, 2.0, 0.46), chosen to match the BBB peak energy and the 'height' of the power-law tail, and has the same normalization as the normalized CLOUDY default SED. The second 'equivalent' OXAF spectrum has (E_{peak}, Γ, p_{NT}) = (9.9 eV, 2.0, 0.414) to match the shape and position of the high-energy slope of the BBB and match the 'height' of the power-law tail. This second OXAF spectrum is shown with a different normalization, with only 73% of the energy flux of the CLOUDY spectrum, to show how it follows the shape of the CLOUDY spectrum in the important region associated with H-ionizing FUV photons.

Clear differences between the spectral models are apparent in Figure 2.6. The CLOUDY model uses a single blackbody curve combined with a power-law to produce the BBB, resulting in a BBB much wider than the OXAF BBB. The physical model used to calculate the power-law tail in OXAF produces a power-law cutoff that is much steeper than the simple piecewise ν^{-2} cutoff in the CLOUDY model.

Results of MAPPINGS photoionization model runs using the three spectra in Figure 2.6 are presented in Figure 2.7. The plane-parallel dusty MAPPINGS models were all configured with a metallicity of $3\,Z_{\odot}$, an ionization parameter of $\log U = -2.0$, and a constant pressure of $P/k = 10^6$. All three models produced similar

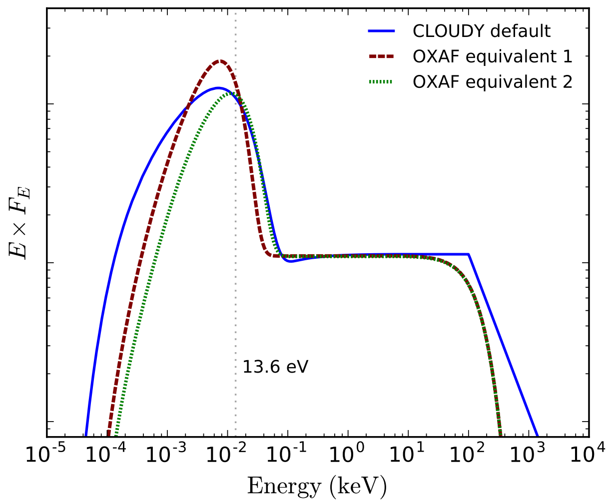

Figure 2.6 Comparison between a default CLOUDY ionizing AGN spectrum and two OXAF spectra chosen to be 'equivalent' in differing ways. The parameters used for the spectra are listed in Section 2.5.2.

optical diagnostic line ratios. The second OXAF model resulted in line ratios closer to those due to the CLOUDY default spectrum, which confirms that the most important part of the spectrum for ionization modeling is the region immediately on the high-energy side of the H ionization threshold, where these spectra were very similar by design. The first OXAF model results in relatively lower [OIII]/Hβ, which is presumably a consequence of the lower proportion of hydrogen-ionizing EUV photons.

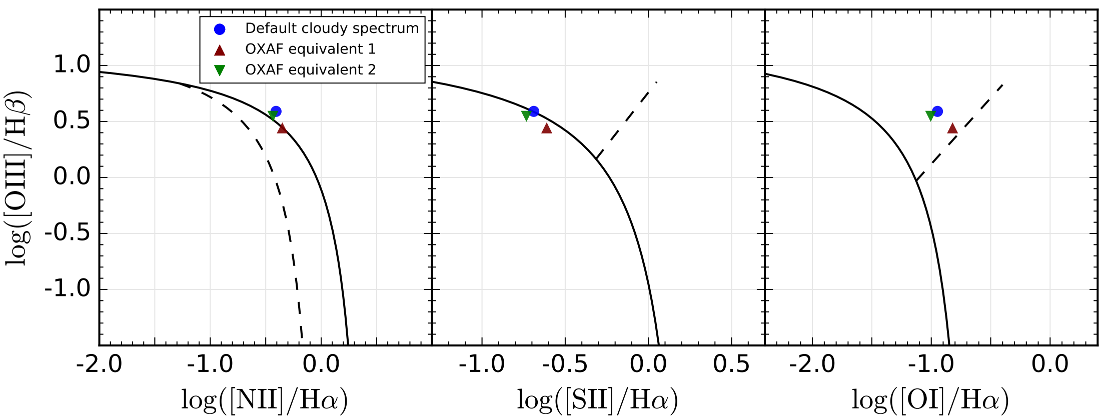

Figure 2.7 Optical diagnostic diagram showing predicted emission-line flux ratios from MAPPINGS photoionization models using the three different ionizing spectra shown in Figure 2.6. The dividing lines are the same as in Figure 2.2. The three ionizing spectra are the default CLOUDY AGN spectrum and two OXAF spectra that are 'equivalent' in differing ways to the CLOUDY spectrum; colors in this figure correspond to the colors of these three spectra in Figure 2.6. The plane-parallel dusty MAPPINGS models were all configured with a metallicity of $3\,Z_\odot$, an ionization parameter of $\log U = -2.0$, and a constant pressure of $P/k = 10^6$.

The results show that oxaf spectra may produce predicted diagnostic line ratios that are very similar to those resulting from analytic ionizing spectra not based on physical models, provided the spectral shapes are sufficiently well-matched in the most important part of the spectrum, the hydrogen-ionizing EUV.

2.6 Conclusions

We present a model of AGN continuum emission, oxaf, designed for use in photoionization modeling and featuring spectral shapes based on physical models. The oxaf model removes degeneracies between AGN parameters in terms of their effect on the ionizing spectral shape; in particular, in the thin disk accretion model the black hole mass and AGN luminosity are entirely degenerate with respect to their impact on the spectral shape. We base oxaf on the optxagnf model (Done et al. 2012), and explain and remove some additional spectral-shape degeneracies between AGN parameters when we reparametrize optxagnf.

We show that the soft X-ray excess is not important to photoionization modeling of the standard optical strong diagnostic lines, so we do not include it in the oxaf model. However the soft excess must be important in modeling forbidden high-ionization lines.

The model oxaf contains only three parameters - the energy of the peak of the accretion disk emission E_{peak}, the photon power-law index for the non-thermal Comptonized component Γ, and the proportion of the total flux which goes to the non-thermal component p_{NT}. These parameters intuitively describe the physical shape of the produced spectrum.

We show that predicted ratios of strong lines on standard optical diagnostic diagrams are sensitive to all three oxaf parameters. The parameter E_{peak} directly affects the degree of ionization of the mappings model nebulae. The parameters Γ and p_{NT} are similar in their effects in that they change the length of the partially-ionized zone. Predicted line-ratios are more sensitive to Γ as p_{NT} is increased. Measured strong emission-line ratios for the Seyfert galaxy NGC 1365 are approximately consistent with the predictions of some fiducial photoionization models using input oxaf ionizing spectra.

Users of oxaf may further explore the effects of changing the shape of the ionizing spectrum on predicted emission-line spectra.

Acknowledgements

B.G. gratefully acknowledges the support of the Australian Research Council as the recipient of a Future Fellowship (FT140101202). L.K. and M.D. acknowledge support from ARC discovery project #DP160103631. C.J. acknowledges the support by the Bundesministerium für Wirtschaft und Technologie/Deutsches Zentrum für Luft- und Raumfahrt (BMWI/DLR, FKZ 50 OR 1604) and the Max Planck Society. We are grateful to both Chris Done, who received an early draft of this paper, and the anonymous referee for helpful comments.

2.7 References

Allen, M. G., Dopita, M. A., & Tsvetanov, Z. I. 1998, ApJ, 493, 571
Antonucci, R. 1993, ARA&A, 31, 473
Baldwin, J. A., Phillips, M. M., & Terlevich, R. 1981, PASP, 93, 5
Bianchi, S., Guainazzi, M., & Chiaberge, M. 2006, A&A, 448, 499
Bland-Hawthorn, J., Maloney, P. R., Sutherland, R. S., & Madsen, G. J. 2013, ApJ, 778, 58
Collins, N. R., Kraemer, S. B., Crenshaw, D. M., Bruhweiler, F. C., & Meléndez, M. 2009, ApJ, 694, 765
Contini, M., & Viegas, S. M. 2001, ApJS, 132, 211
Czerny, B., You, B., Kurcz, A., et al. 2016, A&A, 594, A102
Davies, R. L., Dopita, M. A., Kewley, L., et al. 2016, ApJ, 824, 50
Davis, S. W., Done, C., & Blaes, O. M. 2006, ApJ, 647, 525
Done, C., Davis, S. W., Jin, C., Blaes, O., & Ward, M. 2012, MNRAS, 420, 1848
De Marco, B., Ponti, G., Cappi, M., et al. 2013, MNRAS, 431, 2441
Dopita, M. A., Groves, B. A., Sutherland, R. S., Binette, L., & Cecil, G. 2002, ApJ, 572, 753
Dopita, M. A., Scharwächter, J., Shastri, P., et al. 2014, A&A, 566, A41
Dopita, M. A., Shastri, P., Davies, R. L., et al. 2015, ApJS, 217, 12
Evans, I., Koratkar, A., Allen, M., Dopita, M., & Tsvetanov, Z. 1999, ApJ, 521, 531
Fabian, A. C. 2016, Astronomische Nachrichten, 337, 375
Ferland, G. J., Porter, R. L., van Hoof, P. A. M., et al. 2013, RMxAA, 49, 137
Gierliński, M., & Done, C. 2004, MNRAS, 349, L7
Groves, B. A., Dopita, M. A., & Sutherland, R. S. 2004, ApJS, 153, 9
Groves, B. A., Heckman, T. M., & Kauffmann, G. 2006, MNRAS, 371, 1559
Jin, C., Ward, M., Done, C., & Gelbord, J. 2012, MNRAS, 420, 1825
Jin, C., Ward, M., & Done, C. 2012, MNRAS, 422, 3268
Jin, C., Ward, M., & Done, C. 2012, MNRAS, 425, 907
Kauffmann, G., Heckman, T. M., Tremonti, C., et al. 2003, MNRAS, 346, 1055
Kewley, L. J., Dopita, M. A., Sutherland, R. S., Heisler, C. A., & Trevena, J. 2001, ApJ, 556, 121
Kewley, L. J., Groves, B., Kauffmann, G., & Heckman, T. 2006, MNRAS, 372, 961
Laor, A., & Netzer, H. 1989, MNRAS, 238, 897

Lightman, A. P., & Zdziarski, A. A. 1987, ApJ, 319, 643
Molina, M., Bassani, L., Malizia, A., et al. 2013, MNRAS, 433, 1687
Murayama, T., & Taniguchi, Y. 1998, ApJL, 503, L115
Novikov, I. D., & Thorne, K. S. 1973, Black Holes (Les Astres Occlus), 343
Page, D. N., & Thorne, K. S. 1974, ApJ, 191, 499
Pal, M., Dewangan, G. C., Misra, R., & Pawar, P. K. 2016, MNRAS, 457, 875
Reynolds, C. S. 2014, Space Sci. Rev., 183, 277
Shakura, N. I., & Sunyaev, R. A. 1973, A&A, 24, 337
Thomas, A. D., Groves, B. A., Sutherland, R. S., et al. 2016, ApJ, 833, 266
Veilleux, S., & Osterbrock, D. E. 1987, ApJS, 63, 295
Viegas-Aldrovandi, S. M., & Contini, M. 1989, A&A, 215, 253
Vika, M., Driver, S. P., Graham, A. W., & Liske, J. 2009, MNRAS, 400, 1451
Walton, D. J., Nardini, E., Fabian, A. C., Gallo, L. C., & Reis, R. C. 2013, MNRAS, 428, 2901
You, B., Cao, X., & Yuan, Y.-F. 2012, ApJ, 761, 109
Zdziarski, A. A., Johnson, W. N., & Magdziarz, P. 1996, MNRAS, 283, 193
Życki, P. T., Done, C., & Smith, D. A. 1999, MNRAS, 309, 561

2.8 Appendix: Plots comparing OXAF and OPTXAGNF

Plots comparing OXAF with OPTXAGNF are presented in Figures 2.8 and 2.9.

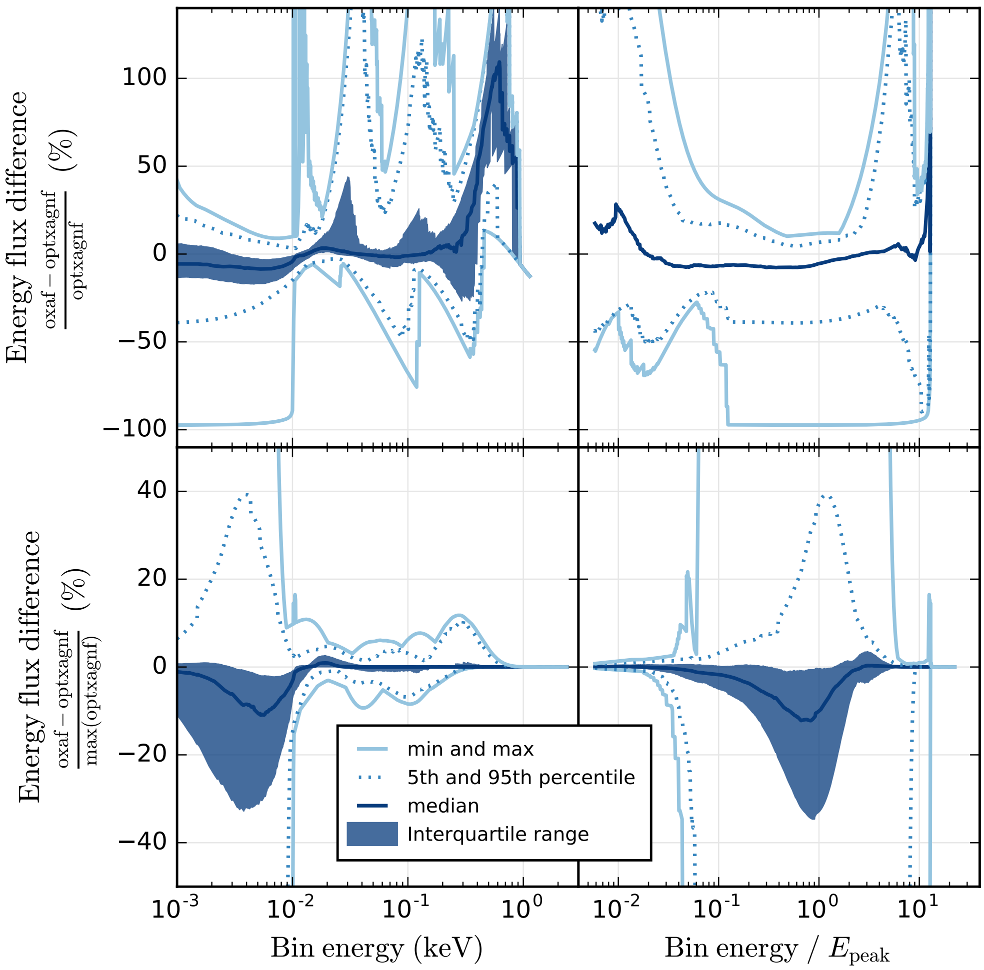

Figure 2.8 Comparison of the predicted Big Blue Bump (BBB) disk emission between the OXAF and OPTXAGNF models. For each spectrum the predicted total OXAF flux in each bin minus the predicted total OPTXAGNF flux in each bin is calculated. In the subplots in the top row, this difference is reported as a percentage of the OPTXAGNF flux in each bin; in the subplots in the bottom row, the difference is reported as a percentage of the maximum predicted OPTXAGNF bin flux in the energy range 0.01 – 20 keV. The statistics in each spectral bin were taken over OXAF-OPTXAGNF comparisons at ∼1900 points in the parameter space, and are plotted as a function of bin energy (left column), and bin energy normalized by the energy of the peak of the disk emission E_{peak} (right column). For subplots in the top row, a bin in a spectrum was only included in the statistics if the OPTXAGNF bin flux was more than 0.1% of the maximum OPTXAGNF flux for a bin in the range 0.01 – 20 keV. The accuracy of OXAF in reproducing the OPTXAGNF spectra is more than adequate over the relevant energy range of 0.01 – ∼20 keV.

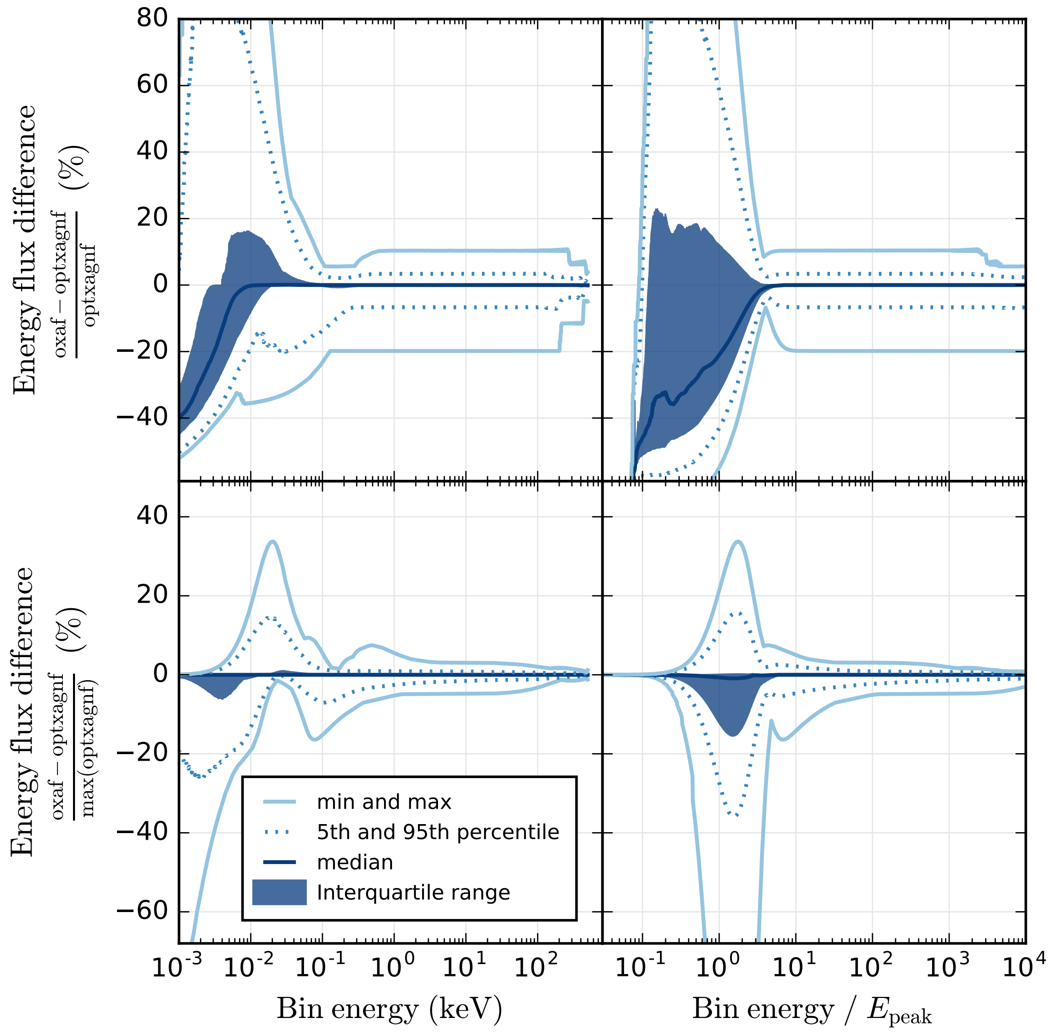

Figure 2.9 Comparison of the predicted hard non-thermal emission between the OXAF and OPTXAGNF models. For each spectrum we calculate the predicted total OXAF flux in each bin minus the predicted total OPTXAGNF flux in each bin. In the subplots in the top row, this difference is reported as a percentage of the OPTXAGNF flux in each bin; in the subplots in the bottom row, the difference is reported as a percentage of the maximum predicted OPTXAGNF bin flux in the energy range 0.01 – 20 keV. The statistics in each spectral bin were taken over OXAF-OPTXAGNF comparisons at ∼1900 points in the parameter space, and are plotted as a function of bin energy (left column), and bin energy normalized by the energy of the peak of the disk emission E_{peak} (right column). For subplots in the top row, a bin in a spectrum was only included in the statistics if the OPTXAGNF bin flux was more than 0.1% of the maximum OPTXAGNF flux for a bin in the range 0.01 – 20 keV. The accuracy of OXAF in reproducing the OPTXAGNF spectra is more than adequate over the relevant energy range of 0.01 – ∼20 keV.

3

The S7 galaxy survey

This chapter presents the content of the article *Probing the Physics of Narrow Line Regions in Active Galaxies IV: Full data release of The Siding Spring Southern Seyfert Spectroscopic Snapshot Survey (S7)* (Thomas et al. 2017). The abstract of this chapter is as follows:

> We present the second and final data release of the *Siding Spring Southern Seyfert Spectroscopic Snapshot Survey* (S7). Data are presented for 63 new galaxies not included in the first data release, and we provide 2D emission-line fitting products for the full S7 sample of 131 galaxies. The S7 uses the WiFeS instrument on the ANU 2.3m telescope to obtain spectra with a spectral resolution of $R = 7000$ in the red (540 - 700 nm) and $R = 3000$ in the blue (350 - 570 nm), over an integral field of 25×38 arcsec^2 with 1×1 arcsec^2 spatial pixels. The S7 contains both the largest sample of active galaxies and the highest spectral resolution of any comparable integral field survey to date. The emission-line fitting products include line fluxes, velocities and velocity dispersions across the WiFeS field of view, and an artificial neural network has been used to determine the optimal number of Gaussian kinematic components for

emission lines in each spaxel. Broad Balmer lines are subtracted from the spectra of nuclear spatial pixels in Seyfert 1 galaxies before fitting the narrow lines. We bin nuclear spectra and measure reddening-corrected nuclear fluxes of strong narrow lines for each galaxy. The nuclear spectra are classified on optical diagnostic diagrams, where the strength of the coronal line [FeVII] λ6087 is shown to be correlated with [OIII]/ Hβ. Maps revealing gas excitation and kinematics are included for the entire sample, and we provide notes on the newly observed objects.

Section 3.7 was written by Mike Dopita, who also generated the three-colour excitation maps in the second panel for each galaxy in Figure 3.8 to Figure 3.18. Rebecca Davies produced Figure 3.3 and wrote the three paragraphs in Section 3.1.3 describing her recent articles (Davies et al. 2016a,b, 2017). I wrote the remainder of this chapter and did the majority of the work preparing the data release. I also personally observed approximately 40% of the galaxies included in the data release in February and May 2016.

3.1 Introduction

Supermassive black holes (SMBHs) with masses of $\sim 10^6 - 10^9$ $M_\odot$ lie at the hearts of all massive galaxies. The close relationship between host galaxy properties and the black hole mass (e.g. Magorrian et al. 1998; Ferrarese & Merritt 2000; McConnell & Ma 2013) has been interpreted as implying that black holes and their host galaxies 'co-evolve' (Kormendy & Ho 2013); the black holes affect their host galaxies when they are 'active' as Active Galactic Nuclei (AGN), and the host galaxies control the supply of gas needed to grow the black hole during an active phase. Activity in galactic nuclei is split into two regimes - bolometric luminosities below approximately 0.01 Eddington, associated with radio galaxies and low-luminosity AGN (LLAGN), and luminosities above 0.01 Eddington and approaching or even exceeding Eddington, associated with 'radiative mode' Seyfert galaxies (Heckman & Best 2014). In Seyfert galaxies an accretion disk around the central SMBH produces ionizing radiation that photoionizes the ISM in the immediate surrounds and potentially the galaxy at large. The 'duty cycle' of a Seyfert nucleus, or the fraction of the time it is active, is estimated to be $\sim 5 - 10\%$ (e.g. Diamond-Stanic & Rieke 2012).

Seyfert galaxies are observed to have a wide variety of emission features such as narrow and/or broad emission lines with varying polarization properties. The apparent diversity of AGN is explained to some extent by the 'unified model' of AGN (Antonucci 1993). This simple axially-symmetric geometrical model postulates that if the orientation of the axis of the system is close to being along the line of sight, then we are able to view the extremely Doppler-broadened emission lines from the broad-line region (BLR) and possibly the accretion disk emission - we observe a Seyfert 1 (Sy 1). On the other hand, if our line of sight is closer to equatorial, a 'torus' of dusty material obscures these features, and instead we only observe the excited gas in clouds in the wider narrow-line region (NLR) - we observe a Seyfert 2 (Sy 2).

The EUV radiation from the SMBH accretion structure that photoionizes the NLR during a Seyfert episode may ionize kiloparsec-scale regions of the host galaxy in an 'extended NLR' (ENLR). An ENLR often has the shape of a double 'ionization cone'. Additionally a Seyfert nucleus affects the ISM of the host galaxy by driving outflows into the surrounding material. Measured emission-line flux ratios of Seyfert (E)NLRs occupy a limited region in the standard optical diagnostic diagrams (Baldwin, Phillips and Terlevich 1981; Veilleux & Osterbrock 1987), which show the [O III] $\lambda5007/\mathrm{H}\beta$ ratio against [N II] $\lambda6584/\mathrm{H}\,\alpha$, [S II] $\lambda\lambda6717{,}31/\mathrm{H}\,\alpha$ and [O I] $\lambda6300/\mathrm{H}\,\alpha$. The very similar line ratios between Seyfert galaxies occur because the ENLR is generally radiation-pressure dominated (Dopita et al. 2002; Groves et al. 2004a,b); an equilibration occurs due to radiation pressure compressing gas at the ionization front such that the local ionization parameter is held effectively constant and the optical emission-line spectrum is not strongly affected by the ionization parameter.

Approximately 10% of galaxies in the local universe host a Seyfert nucleus (Ho 2008). The most prevalent class of non-star forming nuclear activity in the local universe are the low-ionization nuclear emission-line regions (LINERs) (Heckman 1980), which are detected in $\sim$20$-$30% of galaxies (Ho 2008). LINER emission is often thought to be associated with low luminosity AGN activity (e.g. Storchi-Bergmann et al. 1997; Eracleous & Halpern 2001; Ulvestad & Ho 2001; Ho et al. 2001), but may also be associated with other physical processes including shock excitation (e.g. Heckman 1980; Dopita & Sutherland 1995; Lípari et al. 2004; Monreal-Ibero et al. 2006; Rich et al. 2011; Ho et al. 2014) and photoionization from post-asymptotic giant branch stars (e.g. Binette et al. 1994; Kehrig et al. 2012; Belfiore et al. 2016).

3.1.1 Integral field spectroscopy of Seyferts and LINERs

Spatially resolved spectroscopy of Seyfert and LINER hosts provides an important tool for understanding the effects of a Seyfert/LINER period of SMBH growth on the host galaxy. Integral field data reveals information about the impact of an active nucleus on the host galaxy through the spatial distribution of emission-line flux ratios (indicative of shocks or photoionization), kinematic signatures evident in emission-line profiles, and stellar populations.

Recently Karouzos et al. (2016a,b) investigated AGN-driven outflows in a sample of 6 luminous Seyfert 2 galaxies observed with the Gemini Multi-Object Spectrograph (GMOS) on the Gemini South Telescope. The authors identify outflowing emission-line gas and kinematically measure the size of the outflows.

Ricci et al. (2014a,b, 2015a,b) study a sample of 10 AGN in early-type galaxies using GMOS. The authors use PCA Tomography and emission-line fitting to investigate LINER emission and the circum-nuclear gas excitation and morphology in their sample.

A recent example of a large sample of galaxies studied with optical IFU data is the work presented in Rich et al. (2014, 2015). In this work the authors study a sample of 27 nearby luminous and ultra-luminous infrared galaxies ((U)LIRGs) using the WiFeS instrument on the ANU 2.3 m telescope. The authors find that the proportion of the observed Hα emission-line flux attributable to shock excitation may increase to as much as one half in late-stage mergers. Three-quarters of the objects in their sample would appear to have an AGN contribution to gas excitation in nuclear spectra using a naïve classification, due the strong effect of shock excitation on emission-line ratios.

A sample of 17 luminous local Seyfert 2 galaxies was studied with IFU data by McElroy et al. (2015) using the SPIRAL fiber array instrument on the Anglo-Australian Telescope. The authors find that observed emission line profiles and flux ratios are suggestive of outflows and shocks being driven by the Seyfert nuclei.

An ongoing project to observe a large sample of Seyfert galaxies with IFUs is the Close AGN Reference Survey (CARS) (Rothberg et al. 2015; McElroy et al. 2016; Husemann et al. 2016), which will consist of 39 local Sy 1 galaxies at $0.01 < z < 0.06$. This project uses the Multi Unit Spectroscopic Explorer (MUSE) instrument on the Very Large Telescope (VLT) to obtain optical integral field data over a $1' \times 1'$ field of view, and aims at a multi-wavelength study of unobscured AGN in the nearby Universe.

The VIRUS-P Exploration of Nearby Galaxies (VENGA) survey is an ongoing integral field survey of 30 nearby spiral galaxies, using the VIRUS-P IFU (an array of $4\farcs24$ optical fibres with a $1\farcm7 \times 1\farcm7$ field of view) on the Harlan J. Smith telescope at McDonald Observatory (Blanc et al. 2013). The VENGA data has a spectral resolution of $\sim$5 Å over a $3600 - 6800$ Å range and the sample includes the famous AGN NGC 1068.

Observations of AGN using NIR IFUs on 8 m-class telescopes are able to probe Seyfert galaxies at $z \sim 2$. Förster Schreiber et al. (2014) attribute strong nuclear outflows in eight massive $z \sim 2$ star-forming galaxies to AGN. The authors use data from the SINS/zC-SINF survey (Förster Schreiber et al. 2009; Mancini et al. 2011), which uses the Spectrograph for INtegral Field Observations in the Near Infrared (SINFONI) instrument on Unit Telescope 4 at the VLT.

Another IFU providing very high spatial resolution in the IR is the OH-Suppressing Infra-Red Imaging Spectrograph (OSIRIS) mounted on Keck 1. The ongoing Keck OSIRIS Nearby AGN (KONA) survey (Müller-Sánchez et al. 2018) aims to observe the nuclei of 40 Seyfert galaxies to probe molecular and ionized gas flows and stellar dynamics in the immediate environs of the SMBHs.

The Near-Infrared Integral Field Spectrometer (NIFS) on the Gemini North telescope has been used to similarly investigate gas feeding and feedback in local Seyfert galaxies. Flux distributions and kinematics for both H_2 and ionized gas, including both forbidden and recombination lines, give information about the complex environment of AGN. Data for various Seyfert galaxies provide evidence of molecular inflows traced by H_2, ionized outflows traced by [Fe II] and lines from other ionized species, as well as the morphological relationship between radio outflows and optical/IR line emission (e.g. Riffel et al. 2008, 2009; Storchi-Bergmann et al. 2009, 2010; Riffel & Storchi-Bergmann 2011a,b; Riffel et al. 2013).

3.1.2 Large integral field galaxy surveys

The astronomical community is currently entering a golden age of integral field unit (IFU) galaxy surveys. It is now routine to study IFU data for samples of dozens of galaxies, and samples of hundreds of galaxies are becoming commonplace. In this section we survey the largest samples of galaxies that are now being studied with IFU data. The studies described above occur in the context of these ongoing next-generation massive IFU surveys, which do not target AGN specifically, but will nevertheless contain large numbers of AGN.

The Calar Alto Legacy Integral Field Area (CALIFA) survey (Sánchez et al. 2012, 2016) is a recently completed integral field survey of ~600 local galaxies with $0.005 < z < 0.03$. The observations with the 3.5 m telescope at the Calar Alto observatory used a hexagonal optical fiber bundle consisting of 331 fibers each with a 2.7 arcsec diameter. The subsample presented in the second data release (García-Benito et al. 2015) of 257 galaxies contained at least 12 Seyfert galaxies and 48 LINER galaxies based on optical diagnostic diagram classifications of 3 arcsec-aperture nuclear spectra (Singh et al. 2013). The CALIFA data has a spectral resolution of $R = 850$ and $R = 1650$ in two different optical configurations, with the majority of galaxies being observed with both configurations.

Singh et al. (2013) use CALIFA data to study a sample of 48 galaxies with LINER-like emission. The authors show that radial emission-line surface brightness profiles are not consistent with photoionization by AGN illumination and argue that extended LINER-like emission is widely attributable to ionizing radiation from post-AGB stars.

The SAMI Galaxy Survey (Bryant et al. 2015; Sharp et al. 2015; Allen et al. 2015) is an ongoing survey of $\sim 2000 - 3000$ galaxies at $z < 0.12$. The survey uses the Sydney-AAO Multi-object Integral field spectrograph (SAMI) (Croom et al. 2012) on the Anglo-Australian Telescope (AAT) to observe 12 galaxies simultaneously using fiber bundles ('hexabundles'). Assuming that ~10% of galaxies in the local universe are Seyferts (Ho 2008), we expect that the SAMI sample will ultimately contain approximately 200-300 Seyfert galaxies. The SAMI data has a spectral resolution of $R = 1700$ in the blue (3700 – 5700 Å) and $R = 4500$ in the red (6300 – 7400 Å).

Recently Ho et al. (2016) used a sample of 40 edge-on disk galaxies from the SAMI Galaxy Survey to explore the nature of excited extraplanar gas. The authors used both gas kinematics and emission-line flux ratios to classify spectra as being from galaxies dominated by diffuse ionized gas through to those dominated by galactic winds. The wind galaxies were found to have enhanced star formation rate (SFR) surface densities and to have had bursts of star formation in the recent past.

Data from the SAMI Galaxy Survey was also recently used to study two AGN in which the narrow emission lines were at a different line-of-sight velocity to the systemic velocity (Allen et al. 2015). The authors concluded that understanding the cause of kinematically offset emission lines requires integral field spectroscopy, and that the observed kinematics were not due to binary SMBHs.

The Mapping Nearby Galaxies at Apache Point Observatory (MaNGA) survey (Bundy et al. 2015) is one component of the ongoing fourth iteration of the Sloan Digital Sky Survey (SDSS-IV), and aims to study 10^4 nearby galaxies using a multi-IFU instrument also making use of fibre bundles. Again assuming that ~10% of galaxies in the local universe are Seyferts, the MaNGA data will ultimately contain on the order of 1000 Seyferts. The spectral resolution of the MaNGA data ranges from a minimum of $R \sim 1400$ in the blue to a maximum of $R \sim 2600$ in the red.

Recently Belfiore et al. (2016) used MaNGA data for 646 galaxies to study low-ionization emission-line regions (LIERs), finding that this emission occurs not just in the centers of galaxies where it is associated with LINERs, but that it also occurs extended throughout galaxies. The authors conclude that LIER emission is powered by post-AGB stars since the line emission follows the continuum surface brightness and the EW(Hα) is nearly constant for LIER emission.

Large IFU galaxy surveys are also now being performed in the IR. An ongoing high-redshift IFU galaxy survey is KMOS^{3D}, which has a target sample of over 600 galaxies at $0.7 < z < 2.7$ and uses the K-band Multi-Object Spectrograph (KMOS) on the VLT (Wisnioski et al. 2015). Another high-redshift survey using KMOS is the KMOS Redshift One Spectroscopic Survey (KROSS), which aims to observe 795 typical star-forming galaxies at $z = 0.8 - 1.0$ (Stott et al. 2016). The KMOS^{3D} survey includes AGN in its target catalogue, but AGN were explicitly excluded from the KROSS survey.

We refer the interested reader to Section 6 in Bundy et al. (2015) for a detailed comparison of the largest optical integral field galaxy surveys.

Clearly, studying large samples of galaxies with IFUs is now the norm as opposed to the exception in optical astronomy.

3.1.3 The S7

The *Siding Spring Southern Seyfert Spectroscopic Snapshot Survey* (S7) (Dopita et al. 2015, hereafter Paper II) was performed over 2013 - 2016 using the Wide Field Spectrograph (WiFeS) on the ANU 2.3 m telescope at Siding Spring Observatory. The WiFeS instrument is mounted on a Nasmyth platform and has a field of view of 38 × 25 arcsec^2 composed of a grid of 1 × 1 arcsec^2 spatial pixels ('spaxels'). The instrument design and performance are described in Dopita et al. (2007) and Dopita et al. (2010) respectively.

The S7 is an important addition to the IFU surveys discussed above because of its high spectral resolution, large number of active galaxies (∼130), and high physical spatial resolution due to the very low redshift of the sample. The spectral resolution is $R = 7000$ in the red (FWHM $\sim 40\,\mathrm{km\,s^{-1}}$ over $540 - 700\,\mathrm{nm}$) and $R = 3000$ in the blue (FWHM $\sim 100\,\mathrm{km\,s^{-1}}$ over $350 - 570\,\mathrm{nm}$). The high spectral resolution allows studies of independent velocity components in emission lines, and the high spatial resolution allow separation of regions ionized by the AGN, star formation and shocks, as well as analysis of the morphology of ENLRs.

The S7 sample was selected from the Véron-Cetty & Véron (2006, 2010) catalogs of AGN. The galaxies were mostly selected to be radio-detected, nearby, southern, and away from the plane of the Galaxy. More information on the sample is provided in Section 3.2.

A number of studies utilizing S7 data have already been published or are nearly complete. In Dopita et al. (2014) (hereafter Paper I), the authors used the optical AGN ENLR and H II region spectra of the nearby spiral galaxy NGC 5427 (z = 0.009) to constrain the shape of the AGN EUV spectrum, the mass of the black hole and the bolometric luminosity of the AGN. The EUV spectra of AGN encode important information about AGN accretion physics, the mechanical energy input of the central AGN, and the formation of broad- and narrow-line regions, but the EUV spectrum may not be observed directly. The relative intensities of the emission lines in optical ENLR spectra are sensitive to the shape of the EUV spectrum but are also strongly dependent on the chemical abundances. The authors of Paper I measured the abundances of individual H II regions in the disk of NGC 5427 using the ratios of strong emission lines, calculated the gas phase metallicity gradient and subsequently determined the nuclear metallicity to be approximately three times the solar value (3 $Z_\odot$). The MAPPINGS IV photoionization code was then used to generate a grid of emission line ratios for a 3 $Z_\odot$ nebula illuminated by model Seyfert radiation fields for a range of black hole masses and Eddington ratios. The ENLR spectrum of NGC 5427 is best fit by a model with a black hole mass of 5×10^7 $M_\odot$ and a bolometric luminosity of $\log(L_{bol}) = 44.3 \pm 0.1$ erg s^{-1} (approximately 10% of the Eddington luminosity).

Thomas et al. (2016) develop a new model of the ionizing EUV spectrum from Seyfert galaxies, OXAF, designed for photoionization modeling of NLR clouds. The authors explore how the spectral-shape parameters of the ionizing spectrum affect predicted emission-line ratios. Predicted line ratios are shown to be consistent with 'pure-AGN' Seyfert line ratios, with an example being the 'pure-AGN' line-ratios at the top of the 'mixing sequence' between 'pure-H II' and 'pure-AGN' line-ratios on a standard optical diagnostic diagram of S7 data for the Seyfert galaxy NGC 1365.

Although the majority of the S7 galaxies are Seyferts, there are also a number of interesting LINER galaxies in the sample. The authors of Dopita et al. (2015) (Paper III) combined S7 integral field data with *Hubble Space Telescope* Faint Object Spectrograph (HST FOS) spectroscopy to conduct a detailed study of the dynamical structure and the origin of the LINER emission in the nearby galaxy NGC 1052 (z = 0.005). Along the major axis of the galaxy they find evidence for a dusty, turbulent accretion flow forming a small-scale accretion disk. Along the minor axis of the galaxy buoyant bubbles of plasma are rising into the extended interstellar medium, forming a large scale outflow and ionization cone. Part of the outflow region is ionized by the AGN, but there are clear signatures of shock excitation in the inner accretion disk and the region surrounding the radio jet. The emission-line properties of NGC 1052 can be modeled with a 'double shock' in which the accretion flow first passes through an accretion shock (with a velocity of 150 km s^{-1}) in the presence of hard X-ray radiation, and the accretion disk is then processed by a pair of cocoon shocks (with velocities of 200-300 km s^{-1}) driven by the ram pressure of the radio jet. The emission-line model is sensitive to the ratio of the cocoon shock emission to the accretion shock emission but is virtually insensitive to the shock velocities. This type of model may therefore offer a generic explanation for the excitation of LINER galaxies.

Davies et al. (2016a) used S7 data to investigate the relative significance of gas pressure and radiation pressure across AGN ENLRs. The accretion energy of a Seyfert nucleus couples to the gas in the host galaxy primarily through radiation pressure that can drive galaxy-scale outflows, potentially removing large quantities of molecular gas from the galaxy disk. Davies et al. (2016a) showed that there exist two distinct types of AGN fraction sequences ('starburst-AGN mixing sequences') on standard emission line ratio diagnostic diagrams. In some galaxies, radiation pressure is dominant across the ENLR and the ionization parameter remains constant. In other galaxies, radiation pressure is important in the nuclear regions but gas pressure becomes dominant at larger radii as the ionization parameter in the ENLR decreases. Where radiation pressure is dominant, the AGN regulates the density of the interstellar medium on kiloparsec scales and may therefore have a direct impact on outflows and/or star formation far beyond the zone of gravitational influence of the black hole. Both radiation pressure and gas pressure dominated ENLRs are dynamically active with evidence for outflows, indicating that radiation pressure may be an important source of feedback even when it is not dominant over the entire ENLR.

The spectra of Seyfert galaxies are often dominated by strong emission lines that contain information about the rates of star formation and AGN accretion and the physical properties of the ionized gas. However, these properties are degenerate with the relative contributions of different ionization mechanisms to the line emission. Davies et al. (2016b) demonstrated how integral field data of Seyfert galaxies can be used to spatially and spectrally separate emission associated with star formation and AGN activity. The spatially resolved spectra of the S7 galaxies NGC 5728 and NGC 7679 form clear starburst-AGN mixing sequences on standard emission line ratio diagnostic diagrams. The emission line luminosities of the majority of the spectra along each mixing sequence can be reproduced by linear combinations of the star formation and AGN dominated 'basis spectra' that form the endpoints of the mixing sequence. Davies et al. (2016b) separate the H α, Hβ, [N II], [S II] and [O III] luminosities of all spectra along each mixing sequence into contributions from star formation and AGN activity. The SFRs and AGN bolometric luminosities calculated from the decomposed flux measurements are mostly consistent with independent estimates from data at other wavelengths. The recovered star forming and AGN components also have distinct spatial distributions that trace structures seen in high resolution imaging of the galaxies.

A very similar technique (varying only in the method for selecting the basis spectra) can be used to separate emission associated with star formation, shock excitation and AGN activity in galaxies where all three ionization mechanisms are prominent.

Davies et al. (2017) isolate the contributions of star formation, shock excitation and AGN activity to the strong emission lines across the central 3×3 kpc^2 region of the nearby spiral galaxy NGC 613 (z = 0.005). The star formation component traces the B-band stellar continuum emission, and the AGN component forms an ionization cone. The SFR and AGN bolometric luminosity calculated from the decomposed emission line maps are consistent with independent estimates from data at other wavelengths. The shock component traces the outer boundary of the AGN ionization cone and may be produced by outflowing material interacting with the surrounding interstellar medium. Our new decomposition technique makes it possible to determine the properties of star formation, shock excitation and AGN activity from optical spectra, without contamination from other ionization mechanisms.

We have carried out radio observations with the aim of searching for kiloparsec-scale radio outflows in Seyfert galaxies and probing their interactions with ENLR clouds. A sub-sample of 38 S7 Seyfert and LINER galaxies was observed at 610 and 1390 MHz with the Giant Metrewave Radio Telescope (GMRT), and a subsample of 6 galaxies was observed at 5 and 9 Ghz with the Australia Telescope Compact Array (ATCA). The GMRT targets lie within the declination range of ±10 degrees, not readily accessible to ATCA, and have integrated flux densities greater than 20 mJy at 1.4 GHz. The sources span the redshift range of 0.004 − 0.02, which translates to spatial scales of ∼200 to ∼750 parsec at the GMRT resolution of ∼2 arcsec at 1.4 GHz. We have detected kiloparsec-scale radio structures (KSRs) in a majority of the GMRT sub-sample; this is a much higher fraction than previously observed in the literature. The lower frequency observations at 610 MHz are also resulting in detections of host galaxy disk emission in a much larger fraction of targets compared to observations at 1.4 and 5 GHz in the literature. The 610 − 1390 MHz spectral index images are providing useful and unique information about contributions from the AGN and star formation to the radio emission. Results from this study will be presented in a forthcoming paper by Kharb et al. (2017).

Recently Scharwächter et al. (2016) gave an update on the S7 and presented a mosiac of 6 WiFeS pointings on the Seyfert galaxy NGC 6300. Emission lines in the ENLR showed a correlation between [N II]/Hα and line width.

Future work on S7 data will include a study of the forbidden high-ionization emission lines observed in the nuclei of some galaxies in the sample, among other projects.

In this work we present data for the full S7 sample including value-added products, to assist the astronomical community in taking advantage of the enormous potential of the data set.

In Section 3.2 we describe the properties of the full S7 sample, including the global properties of the galaxies. In Section 3.3 we describe the observations and data reduction. In Section 3.4 we present the S7 data products that we are making available to the community. In Section 3.5 we discuss S7 nuclear spectra and the related emission-line analyses and AGN classifications. Section 3.6 presents maps of the spatial properties of the S7 galaxies over the observed field of view, showing the gas ionization and kinematics. In Section 3.7 we describe basic properties evident in the S7 data for individual galaxies not already discussed in Paper II. Our conclusions are presented in Section 3.8.

3.2 The S7 sample

The S7 sample consists of 131 nearby active galaxies, mostly with detected 20 cm radio emission. The sample was selected from the AGN catalog of Véron-Cetty & Véron (2006, 2010), to fulfill the following criteria:

- Declination below +10°, to ensure acceptable zenith distances. Atmospheric dispersion differs by nearly 6 arcsec between 3500 and 7000 Å at a zenith distance of 60°, which is a substantial fraction of the WiFeS field of view. The highest declination in the sample is $\delta = +8.9°$ for NGC 7469.
- Galactic latitude more than 20° away from zero, to avoid severe extinction and a high density of foreground stars along the plane of the Galaxy. This restriction was relaxed for 18 galaxies in the sample that were known to have an interesting ENLR. Of these, only the four galaxies NGC 6300 ($b = -14.05°$), NGC 6221 ($b = -9.57°$), ESO 138-G01 ($b = -9.44°$) and ESO 138-G34 ($b = -7.10°$) have $|b| < 15°$.
- A measured radio flux density at 20 cm of larger than approximately 20 mJy from Véron-Cetty & Véron (2006, 2010) for most galaxies with declinations above $\delta = -40$. The Véron-Cetty & Véron data is from the NRAO VLA Sky Survey (NVSS; Condon et al. 1998) or from the Faint Images of the Radio Sky at Twenty centimeters (FIRST) survey (Becker et al. 1995), and is available only for objects with $\delta \gtrsim -40$. Of the 131 S7 galaxies, 104 have a declinaton above -40, and of these, 88 have a measured radio flux density of larger than

20 mJy. Of the 27 galaxies with declination below -40, only two had 20 cm radio fluxes available in the Véron-Cetty & Véron catalog.

- Redshift $z \lesssim 0.02$, to achieve a physical spatial resolution of ~400 pc arcsec^{-1} or better. This spatial resolution allows detailed spatial analysis of the ENLR. An additional consequence of the close redshift cutoff is that the diagnostic [SII] doublet is below the limit of the $R = 7000$ red WiFeS grating. The distribution of redshifts in the sample is shown in Figure 3.1. Apart from the $z = 0.679$ QSO PKS 0056-572 (included in the sample due to an incorrect redshift in the Véron-Cetty & Véron catalog), there are 7 galaxies in the sample with $z > 0.02$, with NGC 5252 having the largest redshift of $z = 0.023$. The galaxies with $z > 0.02$ were included either due to imprecise redshifts in the Véron-Cetty & Véron catalog or as filler targets.

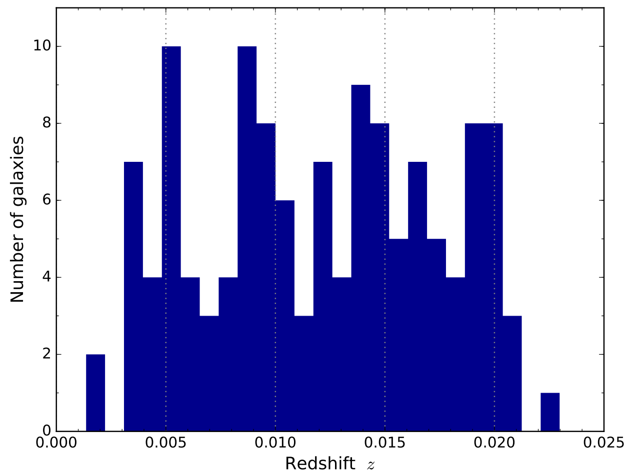

Figure 3.1 The distribution of redshifts of the galaxies in the S7 sample. The QSO PKS 0056-572 at $z = 0.679$ is excluded.

In this work we present data cubes for 63 new galaxies. Data cubes for 68 of the 131 S7 galaxies were already presented in Paper II. Additionally in this work we provide emission-line fitting products and nuclear spectra for all 131 galaxies.

3.2.1 Global galaxy properties of the S7 sample

The full S7 sample of 131 galaxies consists of approximately 18 Seyfert 1 galaxies, 77 Seyfert 2 galaxies, 27 LINER galaxies, 11 galaxies showing signs of gas excitation by star formation only, at least 4 galaxies showing strong post-starburst signatures, 1 radio elliptical galaxy showing little line emission (3C 278), and one Seyfert 1 QSO (PKS 0056-572). At least 34 of the Seyfert 2 galaxies also show signs of star formation in either nuclear spectra or in other parts of the galaxy. The classifications of the galaxies based upon S7 nuclear spectra are presented in Section 3.5.

Morphological classifications from HyperLeda suggest that the S7 sample consists of approximately 71 spiral galaxies, 35 lenticular galaxies, 19 ellipticals and an irregular galaxy (ESO 350-IG38). A small number of S7 galaxies are undergoing interactions, for example both galaxies in the interacting pair NGC 833 and NGC 835 are included in the sample.

Stellar masses and SFRs were estimated for the S7 galaxies using IR photometry. Stellar masses were calculated from WISE W1 (3.4 μm) luminosities using a constant mass-to-light ratio of 0.7, as described in Cluver et al. (2014). The SFRs were calculated using the 60 and 100 μm flux densities, using the formula from Helou et al. (1988) to convert the flux densities into the FIR flux, the conversion of FIR luminosity to total IR luminosity from Calzetti et al. (2000) ($L_{\rm IR} = 1.75 \times L_{\rm FIR}$), and the IR SFR calibration from Kennicutt (1998).

Figure 3.2 shows where the S7 galaxies lie relative to the star-forming main sequence of local galaxies. The S7 galaxies lie scattered along the top end of the main sequence and extend through the 'green valley' – the location of a large proportion of Seyfert 2 galaxies in the local universe – and into the 'red cloud', where a large proportion of local LINERs are found. The S7 'star-forming only'-classified galaxies lie approximately along the main sequence, as expected. The LINER and Seyfert S7 galaxies that lie above the SDSS main sequence in Figure 3.2 are likely galaxies in which the IR luminosity is significantly enhanced by AGN contamination.

3.3 Observations and data reduction

In this section we describe the observations and reduction of the S7 data.

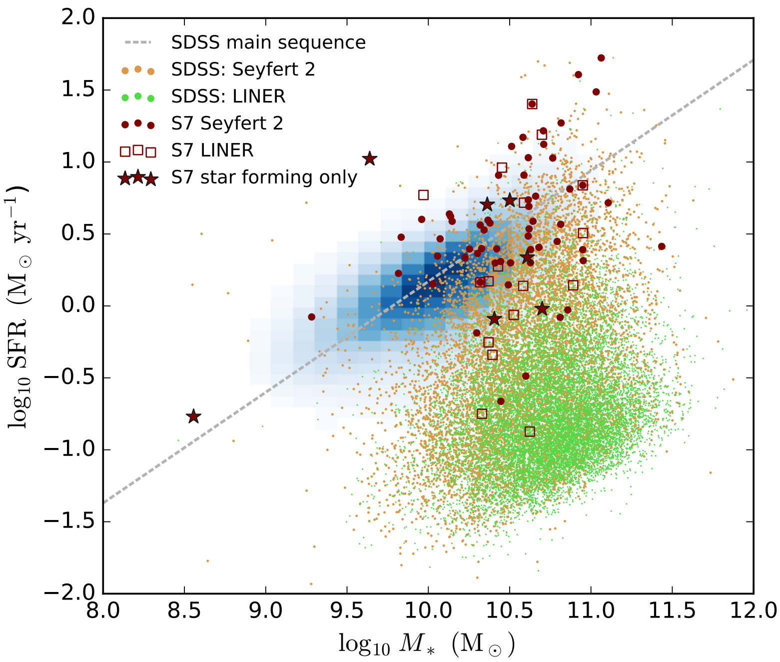

Figure 3.2 The position of the S7 galaxies relative to the star-forming main sequence. The SDSS classifications are from Leslie et al. (2016). The blue grid shows the SDSS star-forming galaxies, and the dotted line shows the best-fit SDSS main sequence for $z \sim 0$ star-forming galaxies from Equation 5 in Elbaz et al. (2007).

3.3.1 Observations

Galaxies were observed with a single pointing centered on the nucleus, with the exception of NGC 5252 and NGC 5643, for which the observations consisted of two mosaiced pointings with the mosaic centered on the nucleus. The observing strategy generally involved alternating between sky and object targets, with three exposures being taken on the object then only one exposure for the corresponding sky. The observing plans were designed so that the sky frames from both before and after the three exposures on a galaxy target could usually be used for sky subtraction when reducing the galaxy data. Spectrophotometric calibration was performed using spectrophotometric standard stars[1] observed at the beginning and the end of each night (conditions permitting); additionally telluric standard stars with smooth spectra observed once or twice a night were used to better correct for telluric absorption features.

The observing log for the 63 new galaxies not presented in Paper II is presented in Table 3.1. This table supplements Table 1 in Paper II; the full table is available as part of the catalogue provided in this data release. Table 3.1 shows the galaxies

[1] http://www.mso.anu.edu.au/~bessell/FTP/Bohlin2013/GO12813.html

arranged in order of RA, showing the galaxy coordinates, redshift, classifications, observing date, WiFeS rotator PA, total exposure time, seeing FWHM, and a note if a galaxy was observed in non-photometric conditions. Sixteen galaxies in the full sample were observed more than once, but only the data for the 'best' observation is presented here. The 'best' observation was chosen based on a combination of the seeing, the total exposure time, and whether or not the conditions were photometric.

Table 3.1 also includes NGC 1346, NGC 3281 and NGC 4636, which were not included in the corresponding table (Table 1) in Paper II.

We note that NGC 7552 has been removed from the S7 sample since the first data release. It was included in Table 1 of Paper II but is a star-forming galaxy that had very poor quality observations.

The seeing FWHM measurements presented in Table 3.1 were recorded in the observer's log during the relevant observations. The observer judged appropriate values for the seeing FWHM using time series of periodic measurements of the guide star PSF during the relevant exposures.

3.3.2 Reduction of raw observations

In this section we describe the reduction of the raw data, the registration to determine sky coordinates, and the expected accuracy of the WCS, flux calibration and wavelength calibration.

The raw frames from the WiFeS CCDs were combined and reduced with the pyWiFeS data reduction pipeline, which is described in detail in Childress et al. (2014). The data reduction procedure corrects for the detector bias levels and for cosmic ray strikes. It uses arc lamp frames taken on each night of observing to perform wavelength calibration, uses observations of spectrophotometric stars to perform flux calibration, and uses observations of telluric standard stars to correct for telluric absorption. Corrections for Differential Atmospheric Refraction (DAR; Filippenko 1982) are applied when forming the spectral cubes.

The pyWiFeS code initializes variances with photon counting noise and detector read noise after subtracting the overscan, repairing bad pixels, and subtracting a global 'superbias' (combined bias frame). Full statistical propagation of uncertainties is then applied over subsequent pipeline steps, in particular the subtraction

Table 3.1 Log of the new S7 observations

Object name	RA (J2000)	Dec (J2000)	z	Type[a]	Type (Veron)	PA (°)	Date of Observation	Exposure Time (s)	Seeing[d] (arcsec)
MARK938	00 11 06.60	-12 06 27.00	0.0196	SB+Sy 2	S2	0	2013-08-03	3000	2.0
ESO350-IG38	00 36 52.90	-33 33 29.16	0.0206	SB	H2	90	2014-08-22	2400	1.6
NGC1068	02 42 40.70	+00 00 47.16	0.0038	Sy 2	S1h	45	2014-08-23	2400	1.2
IC1858	02 49 08.50	-31 17 21.84	0.0202	SB	S3	0	2014-08-23	2400	1.2
NGC1194	03 03 49.10	-01 06 13.00	0.0136	SB+Sy 2	S1.9	135	2014-08-22	2400	1.5
NGC1217	03 06 05.90	-39 02 09.96	0.0210	LINER	S3	45	2016-02-09	2700	1.5
NGC1266	03 16 00.70	-02 25 37.92	0.0072	LINER	S?	90	2014-08-24	2700	1.0
NGC1320	03 24 48.70	-03 02 32.00	0.0089	Sy 2	S2	315	2014-08-24	2700	1.0
NGC1346	03 30 13.20	-05 32 35.00	0.0135	SB	S1	90	2013-11-02	3000	1.4
NGC1365	03 33 36.41	-36 08 24.00	0.0055	Sy 1	S1.8	60	2016-02-10	2700	1.1
ESO420-G13	04 13 49.70	-32 00 24.12	0.0121	SB+Sy 2	S2	90	2016-02-09	2700	1.7
NGC1672	04 45 42.19	-59 14 51.00	0.0044	SB+Sy 2	S	90	2016-02-07	2700	1.9
NGC1667	04 48 37.20	-06 19 12.00	0.0152	Sy 2	S2	0	2016-02-08[b]	2700	1.6
UGC3255	05 09 50.21	+07 28 59.16	0.0189	LINER	S2	20	2016-02-07[b]	2700	2.4
ESO362-G08	05 11 09.00	-34 23 35.00	0.0157	PSB+Sy 2	S2	0	2016-02-06[b]	2700	1.8
ESO362-G18	05 19 35.80	-32 39 27.00	0.0124	Sy 1	S1.5	135	2016-02-10	2700	1.1
NGC2110	05 52 11.40	-07 27 23.04	0.0078	Sy 2	S1h	0	2016-02-08	2700	1.4
NGC2217	06 21 39.70	-27 14 00.96	0.0054	LINER	S3	90	2016-02-10	2700	1.3
ESO565-G19	09 34 43.80	-21 55 41.88	0.0163	LINER or Sy 2	S2	0	2016-02-09	2700	2.2
NGC2945	09 37 41.09	-22 02 06.00	0.0154	LINER	S	90	2016-02-08	2700	1.8
NGC2974	09 42 33.30	-03 41 57.00	0.0063	SB+Sy 2	S2	45	2016-02-05[b]	1800	2.0
ESO500-G34	10 24 31.49	-23 33 10.08	0.0122	SB+PSB+Sy 2	S2	0	2016-02-07	2700	1.8
NGC3281	10 31 52.10	-34 51 12.96	0.0116	Sy 2	S2	135	2016-02-09	2700	1.7
MCG-02-27-009	10 35 27.30	-14 07 47.00	0.0151	LINER or Sy 2	S2	90	2016-02-05	2700	1.8
NGC3312	10 37 02.50	-27 33 56.16	0.0096	LINER	S3	0	2016-02-08	2700	1.4
NGC3390	10 48 04.39	-31 31 59.88	0.0102	SB	S3	0	2016-02-07	2700	1.5
NGC3393	10 48 23.40	-25 09 43.92	0.0125	Sy 2	S2	45	2016-02-08	2700	1.5
NGC3831	11 43 18.60	-12 52 42.00	0.0176	LINER	S2	30	2016-02-09	2700	2.4
NGC3858	11 45 11.70	-09 18 50.00	0.0191	SB	S2	45	2016-02-08	2700	1.6
NGC4418	12 26 54.70	-00 52 41.88	0.0073	SB	S2	60	2016-05-04	2700	1.5
NGC4472	12 29 46.80	+08 00 02.16	0.0033	SB	S2	0	2016-05-05	2700	1.2
NGC4507	12 35 36.50	-39 54 33.12	0.0118	Sy 2	S1h	60	2016-02-10	2400	1.2
NGC4593	12 39 39.40	-05 20 39.00	0.0083	Sy 1	S1.0	45	2016-02-05[b]	2700	2.0
NGC4594	12 39 59.30	-11 37 23.16	0.0037	SB+Sy 2	S3	90	2016-02-07	2700	2.0
IC3639	12 40 52.90	-36 45 20.88	0.0109	Sy 2	S1h	135	2016-02-10	2700	1.3
NGC4636	12 42 49.99	+02 41 16.08	0.0031	LINER	S3b	45	2014-04-08	1800	1.3
NGC4691	12 48 13.01	-03 19 59.16	0.0037	SB	S1	90	2016-05-04	2700	1.4
NGC4696	12 48 49.30	-41 18 39.96	0.0099	LINER	S3	90	2016-05-03[b]	900	2.0
ESO443-G17	12 57 44.90	-29 45 59.04	0.0102	SB+Sy 2	H2	0	2016-02-10	2700	1.4
NGC4845	12 58 01.20	+01 34 32.88	0.0041	SB+Sy 2	S2	90	2016-05-04	2700	1.3
NGC4939	13 04 14.30	-10 20 23.00	0.0104	Sy 2	S2	0	2016-05-06	2100	1.4
ESO323-G77	13 06 26.21	-40 24 51.84	0.0156	Sy 1	S1.2	45	2016-02-10	2700	1.2
NGC4968	13 07 05.40	-23 40 36.84	0.0099	Sy 2	S2	45	2016-05-06	2700	1.3
PKS1306-241	13 08 41.81	-24 22 57.00	0.0139	SB+Sy 2	S2	90	2016-05-05	2700	1.3
ARK402	13 08 50.11	-00 49 01.92	0.0178	SB+Sy 2	S2	90	2016-05-04	2700	1.5
NGC4990	13 09 17.30	-05 16 22.08	0.0106	SB+Sy 2	H2	90	2016-05-05	2700	1.0
MCG-03-34-064	13 22 24.50	-16 43 41.88	0.0165	Sy 1	S1h	90	2016-05-04	2700	1.3
NGC5128	13 25 28.01	-43 01 00.12	0.0018	Sy 2	B?	90	2016-05-06	1200	1.4
NGC5135	13 25 43.99	-29 50 02.04	0.0137	PSB+Sy 2	S2	135	2016-05-06[b]	2400	1.6
ESO383-G35	13 35 53.70	-34 17 44.00	0.0077	Sy 1	S1.2	90	2016-05-06	2100	1.7
NGC5252	13 38 15.89	+04 32 33.00	0.0230	Sy 2	S2	0	2016-05-06	2400[c]	1.4
IC4329A	13 49 19.30	-30 18 33.84	0.0161	Sy 1	S1.2	45	2016-05-04	2700	1.4
NGC5427	14 03 25.90	-06 01 50.16	0.0092	Sy 2	S2	90	2016-05-06[b]	2400	1.8
NGC5643	14 32 40.70	-44 10 27.84	0.0040	Sy 2	S2	0	2016-05-04	1980[c]	1.4
PKS1521-300	15 24 33.41	-30 12 20.88	0.0195	SB+Sy 2	S1	90	2016-05-03	2700	1.9
NGC5990	15 46 16.49	+02 24 56.16	0.0128	SB+PSB+Sy 2	S2	90	2016-05-03[b]	2700	1.9
NGC6328	17 23 40.90	-65 00 36.00	0.0144	SB+Sy 2	S3	0	2014-08-22	2400	1.3
IC4777	18 48 11.30	-53 08 51.00	0.0187	Sy 2	S2	135	2016-05-06	2700	1.7
ESO460-G09	19 30 26.60	-31 52 38.00	0.0196	SB+Sy 2	S	90	2016-05-03	2700	1.8
MCG-02-51-008	20 17 06.31	-12 05 51.00	0.0186	SB+Sy 2	S3	90	2014-08-24	2700	1.3
IC4995	20 19 58.99	-52 37 18.84	0.0161	Sy 2	S2	0	2014-08-22	2400	1.3
NGC6936	20 35 56.30	-25 16 48.00	0.0195	SB+Sy 2	S3	0	2014-08-22	2400	1.9
MCG-04-49-001	20 46 37.20	-23 37 49.08	0.0201	LINER	S3	0	2014-08-23	2400	1.9
ESO287-G42	21 38 07.90	-42 36 18.00	0.0187	Sy 1	S1.8	120	2016-05-06[b]	2700	1.7
NGC7172	22 02 01.90	-31 52 08.04	0.0087	SB+Sy 2	S2	90	2014-08-23	2400	1.3
IC5169	22 10 10.00	-36 05 19.00	0.0104	SB+Sy 2	S2	30	2016-05-04	2700	1.2
IC1481	23 19 25.30	+05 54 20.88	0.0204	SB+Sy 2	S3	90	2014-08-24	2700	1.3
NGC7682	23 29 03.91	+03 31 59.88	0.0171	Sy 2	S1h	0	2014-08-24	2700	1.0

[a] SB = Starburst, PSB = Post-starburst
[b] Conditions were not photometric
[c] Effective exposure time doubled in mosaic overlap region
[d] The seeing FWHM in arcseconds

of sky frames, co-adding of multiple frames and flat-fielding. PYWIFES does not account for any covariance between adjacent spectra in a slitlet.

The output of the data reduction pipeline is two independently processed 'data cube' files, one for each of the red and blue arms of the WiFeS instrument. The files are provided for every S7 galaxy as part of this data release. Each file contains both a flux cube and a variance cube; the data format is described in more detail in Section 3.4.1.

Registration of the data cubes was performed by summing the red cubes in the wavelength direction and cross-correlating the resulting synthetic pseudo-continuum images with DSS2 r-band images. The recorded telescope position angle was assumed to be correct, and the cross-correlation took advantage of the fact that both the S7 and DSS2 data consisted of 1 arcsec square pixels. The results were manually inspected for each galaxy, and typically the registration (which was not attempted to sub-pixel accuracy) was clearly valid to within 1-2 arcsec. Very nearby galaxies often had overexposed centres in the DSS2 images (indicated in the 'S7_WCS_flags' field in the catalogue table and in the 'WCS_QLTY' FITS header keyword in the data products), and for the few worst objects the resulting WCS simply used the telescope pointing model, and may be incorrect by tens of seconds of arc.

We investigated the consistency of the flux calibration by comparing duplicate observations of four galaxies - NGC 7496, NGC 6915, NGC 835, and ESO330-G11. These objects were each observed twice in photometric conditions, once without dedicated sky exposures for sky subtraction and once with the dedicated exposures. Binned nuclear spectra were compared between observations to give an indication of the quality of the flux calibration. We found that the spectra were always systematically higher or lower in flux between the two observations, with the differences being consistent between the red and blue arms. For NGC 6915 and ESO330-G11 the duplicate observations were a year apart over $2013 - 2014$. The flux differences between the two observations were $15 - 20\%$, with the 2013 observations higher than the 2014 observations for both galaxies. The repeat observations of NGC 7496 and NGC 835 were separated by three months in 2013. The flux differences between the two observations were $4 - 9$ per cent for these galaxies. Overall these differences could plausibly be accounted for by the different sky-subtraction methods and slightly different apertures between the observations. Unfortunately it is not possible to systematically compare S7 fluxes to existing data due the difficulty in matching apertures, spatial resolution, spectral resolution, and the all-sky nature of the target set.

The accuracy of the wavelength calibration produced by pyWiFeS is discussed in Childress et al. (2014). The authors show that the dominant uncertainty is the systematic uncertainty due to temperature drift in the instrument between an arc frame being taken and observations of the target. An error of approximately $1-2$ Å resulted from using an arc frame taken in the early afternoon to calibrate an arc frame taken at the end of the following night. The wavelength calibration errors for the S7 data products will be significantly smaller than $1-2$ Å because arc frames were taken on 2 or 3 separate occasions during each S7 observing night. We note that if the error is as high as 0.5 Å for any S7 galaxies, the resulting dispersion in recession velocities between the blue and red extremes of the observed spectra would be only $\sim$20 km s^{-1}.

We note that the S7 gas velocity maps in the appendix (Section 3.12) display a symmetry between blueshifted and redshifted emission (relative to systemic velocity). The symmetry occurs because the NED redshifts used in the line fitting are generally well matched to the systemic recession velocities associated with the calibrated S7 wavelengths. The maps required adjustment for only $\sim$18 galaxies, with required offsets ranging from -90 to $+80$ km s^{-1}. The S7 wavelength vectors are reliable and we expect the offsets to generally be attributable to the external redshifts used in line fitting.

3.3.3 Deriving emission-line products

Fitting emission lines and the stellar continuum

Emission lines for both data cubes and nuclear spectra were fit using lzifu[2] ('Lazy-IFU'; Ho et al. 2016). The lzifu code was designed to perform emission-line fitting on IFU data cubes. It first fits the underlying continuum in each spectrum using stellar spectral templates before fitting the emission lines using multiple Gaussians. The lzifu code models the stellar continuum using the penalized pixel-fitting routine (ppxf; Cappellari & Emsellem 2004), and was configured to use the theoretical single stellar population (SSP) spectra from González Delgado et al. (2005) based on the Padova isochrones. A 5th degree additive Legendre polynomial is fitted simultaneously to the stellar spectral templates.

[2] https://github.com/hoiting/LZIFU

After the continuum is subtracted from a spectrum, LZIFU fits the emission lines using the Levenberg-Marquardt least-squares algorithm as implemented in MPFIT (Markwardt 2009). Emission lines are fitted three times, with each of one, two and three Gaussian components. For a given component (1, 2 or 3), the velocity and velocity dispersion of all emission lines are constrained to be the same. In the output the components are ordered by velocity dispersion, with component 1 being the narrowest. The LZIFU code accounts for instrumental dispersion when measuring the velocity dispersion.

We expect spatial variation in the fitting results to be generally smooth. To encourage the code to produce spatially smooth output, we used the ability of LZIFU to iteratively spatially smooth the fitting results and refit the data. The output fit parameters were smoothed using a kernel of width 5 spaxels and each spaxel was then refit using the 'smoothed' parameter values as initial parameter guesses. Two iterations of this smoothen-refit procedure were performed.

The LZIFU output contains errors on the emission-line fluxes, velocities and velocity dispersions derived from the fitting errors outputted by MPFIT. The MPFIT fitting errors in turn depend on the data cube variances. The covariances reported by MPFIT are propagated into the LZIFU flux errors. The LZIFU errors do not account for uncertainty in the subtracted stellar continuum, and as a consequence the errors in the Balmer line fluxes are generally underestimated when the underlying stellar absorption is strong compared to the line emission. The errors produced by LZIFU are compared to Monte Carlo simulations and discussed in detail in Ho et al. (2016).

The LZIFU output is provided to the community and is described in detail in Section 3.4.2.

Selecting the number of kinematic components in emission lines

The optimal number of Gaussians needed to describe the emission line features across a galaxy differs from spaxel to spaxel. Each galaxy is fit with 1, 2 and 3 Gaussian components using LZIFU. The optimal number of Gaussian components (i.e. 1, 2 or 3) is determined for each spaxel separately using an Artificial Neural Network (ANN) trained by astronomers. The selection of the number of components must be automated because manual classification is impractical for the $\sim 10^4 - 10^5$ spaxels requiring consideration in the S7.

The ANN, LZComp[3] ('Lazy-Components'), is described in detail in Hampton et al. (2017). LZComp is a supervised machine learning algorithm that has been trained using manual classifications produced by three astronomers from the S7 team. The training and testing, described in Hampton et al. (2017), determined LZComp to be equivalent to using an astronomer to make the decisions on the numbers of Gaussian components required for the emission line features in the S7 survey.

An extension in the FITS file output of LZComp indicates the number of components selected in each spaxel. The product FITS files are described in Section 3.4.2.

3.3.4 Emission-line fitting of Seyfert 1 galaxies

Galaxies with nuclei showing very broad components in Balmer lines required special treatment when performing emission-line fitting. Fitting using LZIFU often fails on Balmer lines with extremely broad components, especially when the profiles are asymmetrical. In the most extreme objects, broad H α wings extend past the [SII] doublet; these nuclei cannot be fit using the same method as Sy 2s. Both the Balmer line widths and the relative flux in the broad components vary continuously over the S7 sample, so there is no clear delineation between the Seyfert 1 nuclei and other nuclei.

We identified spaxels with problematically broad Balmer components by checking for a broad H α wing redward of the [NII]-H α complex in each spaxel of each galaxy. The method essentially consisted of the following considerations. The difference between the median of the spectrum in the region $10 - 40$ Å redward of [NII] λ6583 and the continuum background was calculated. Where this flux difference was more than 1.8 times the interquartile range in the continuum (a measure of the noise), the spaxel was flagged as having a broad component. As a S/N cut, spaxels were not considered if the height of the peak of the [NII]-H α complex above the continuum was less than 7 times the continuum interquartile range. Appropriate values for the tolerances were found by experimentation.

There were 14 galaxies in the S7 sample that were identified using this method as having very broad and prominent Balmer line components in nuclear spaxels, which were ESO 323-G77, ESO 362-G18, ESO 383-G35, Fairall 49, Fairall 51, IC 4329A, Mark 1239, NGC 1365, NGC 2617, NGC 3783, NGC 4593, NGC 6860, NGC 7213 and

[3] https://github.com/EliseHampton/LZComp

NGC 7469. For these galaxies, the broad lines were sufficiently broad and/or dominant over the narrow components that it was necessary to subtract out the broad components before fitting the data cubes and nuclear spectra. A total of 316 spaxels over the 14 galaxies had broad-line subtraction. Another six galaxies identified by the method described above had a broad component that was judged to be too narrow or weak to merit special subtraction.

Subtracting out broad H α and Hβ lines from the nuclear spaxels was accomplished by approximately following the method outlined in Greene & Ho (2005). Firstly, 1- and 2-component LZIFU fits were made to the [SII] $\lambda\lambda$ 6716, 6731 lines to constrain the velocity and velocity dispersion of the narrow components. This important step was used to reduce the number of free parameters when fitting the [NII]-H α complex. The [NII]-H α complex was fit using both narrow Gaussians (kinematics set by the [SII] fits) and broad Gaussians (minimum $\sigma_v = 1000\,\mathrm{km\,s^{-1}}$). Fits were performed with up to 4 or 5 broad components for H α and up to 3 or 4 narrow components for H α and both [NII] lines. Corresponding narrow components all had the same velocity and velocity dispersion and the [NII]λ 6583/[NII]λ 6548 flux ratio was fixed to 3. For some galaxies an additional broad Lorentzian H α component was used. The fit with the lowest reduced-χ^2 was used for each spaxel.

When fitting [OIII]-Hβ, some differences in the approach were necessary compared to the method used when fitting the [NII]-H α complex. Again multiple broad Gaussians were used to build up the profile of the broad Balmer line, however often it was necessary to use only one narrow component for Hβ while using 3, 4 or 5 narrow components for [OIII] $\lambda\lambda$4959, 5007. Additionally only the first (narrowest) component of two-component [SII] fits were used to constrain an [OIII]-Hβ narrow component, unlike for [NII]-H α in which both [SII] fit components were used. We note that any FeII emission in this region was not considered. Hence some FeII flux may have been subtracted in the Hβ broad component (contributing to the red wing) and may have contaminated the red wing of [OIII] λ5007.

Data cubes were produced with the fitted H α and Hβ broad lines subtracted, and LZIFU was then used to fit the narrow lines that remained in the data. The narrow-line parameters resulting from the simultaneous fits to the broad lines were not used.

The decompositions into broad- and narrow-spectra are presented in Figures 3.4 to 3.6 in the appendix (Section 3.11) and are discussed in Section 3.5.3.

Although the method used to find the spectrum of the broad components was generally successful and resulted in satisfactory measured narrow-line fluxes in most cases, there are systematic issues with the approach described above. Firstly, an obvious limitation is that there is no physical reason why the narrow- and broad-line regions need to be entirely distinct as opposed to continuously varying, and hence dividing the emission-line flux into 'broad' and 'narrow' parts may in some cases be arbitrary. The line profiles sometimes contained little information that enabled splitting into 'broad' and 'narrow' parts, a problem that was most severe where the narrow components were particularly broad and in the innermost nuclear spaxels when the broad components were very dominant. Often manual tweaks to the number of components and fitting constraints were necessary to ensure that the broad-narrow division 'looked' appropriate, even if the tweaking produced a fit that was statistically slightly worse.

A second issue is that the modeled and measured line profiles were sometimes consistently mismatched in a particular part of the spectrum. This issue was associated with the combination of model line profiles and the fitting strategy. A relatively frequent problem was caused by the broad line fit slightly overestimating the flux around the red wing of [N II]λ6583, (e.g. NGC 2617 in Figure 3.4; where the narrow-line spectrum show a 'dip' from the over-subtraction of the broad component). Another occasional issue was the broad component fit overestimating the flux in the 'flux dip' between H α and [N II]λ6583.

Despite these systematic issues, fitting narrow lines to the broad component-subtracted cubes produced reasonable results, as seen, for example, in the maps for NGC 4593 (Figure 3.13) and IC 4329A and (Figure 3.14) in the appendix (Section 3.12). The maps show fitted emission-line velocities that are spatially consistent with nearby spaxels that did not have broad-component subtraction (spaxels outside the green outline).

As a result of the systematic errors described above, users of the data should carefully consider the appropriate number of narrow-line components that are required in the nuclear spaxels of Seyfert 1 galaxies. Users may decide to consider the narrow-line fluxes measured in broad-component-subtracted spaxels to be approximate lower bounds, and/or only use the narrowest component in multiple-component fits. These caveats are also discussed in Section 3.4.2.

3.3.5 Extraction and analysis of nuclear spectra

The circum-nuclear spectra presented in this work were extracted from the data cubes using an aperture chosen to approximate the circular, 3 arcsec-diameter aperture of an SDSS fibre. A slightly larger diameter of $\sim$4 arcsec was chosen because the S7 targets are very nearby compared to the SDSS sample. There were 13 whole spaxels and zero fractional spaxels in the bin region, which was centered on the 'nuclear' spaxel of each galaxy. The bin region was the union of the following three shapes: a 3×3 square centered on the nuclear spaxel, a column of 5 spaxels symmetrical about the nuclear spaxel, extending 2 spaxels above and 2 below, and a row of 5 spaxels symmetrical about the nuclear spaxel, extending 2 to the left and 2 to the right. Masks showing the aperture shape and location are included in the relevant FITS files (Section 3.4.3). The spectral variances were summed over the same aperture.

Emission-line fluxes for the nuclear spectra given in this work and in Paper II were measured using LZIFU as described above. Spatial smoothing and refitting to obtain spatially smooth results was not applicable for the single nuclear spectra. One-component fits were used for all galaxies except NGC 7469, for which the narrowest component of a two-component fit was used. The LZIFU fitting of the stellar continuum failed in one or both of the red and blue for 9 galaxies, and manually-provided linear continua were used instead. This is indicated in the 'Linear_continuum?' field in the relevant tables in the data release. Both the LZIFU fluxes and flux errors are provided as part of the data release.

Nuclear fluxes for each galaxy were corrected for reddening following Vogt et al. (2013), but only for initial Balmer decrements of $F_{\mathrm{H}\alpha}/F_{\mathrm{H}\beta} > 3.1$. Where it was applied, the reddening correction was set to produce a target Balmer decrement of $F_{\mathrm{H}\alpha}/F_{\mathrm{H}\beta} = 3.1$. For the Seyfert 1 nuclei with broad-component subtraction, the narrow component fluxes were used. Errors in the Hα and Hβ fluxes were propagated through the reddening correction into the de-reddened fluxes.

3.4 Data products

The data products are available to download from the All-Sky Virtual Observatory[4] or the S7 website[5], and consist of the following:

1. A catalogue of the full S7 sample, including ancillary data merged from NED and HyperLeda. The catalogue includes the information presented in Table 3.1 for each galaxy.
2. Data cubes for both the red and blue arms of WiFeS, and additional cubes with broad lines subtracted from nuclear spectra for 14 Seyfert 1 galaxies (Section 3.3.4)
3. LZIFU emission-line fitting output for 1-, 2- and 3-component fits (Section 3.3.3)
4. LZIFU emission-line fitting output where the optimal number of components for each spaxel has been selected by the `LZComp` Artificial Neural Network (Section 3.3.3)
5. Nuclear spectra found by summing the data cubes over a 4 arcsec aperture, and additional broad and narrow-line nuclear spectra for the 14 Seyfert galaxies with special treatment
6. A table of extinction-corrected nuclear emission-line fluxes measured using LZIFU fits to the nuclear spectra (an extended version of Table 3.3 in the appendix (Section 3.10)), and a corresponding table of flux errors
7. A table of associated extinctions, physical aperture sizes, and nuclear Hβ and [OIII] fluxes and luminosities (an extended version of Table 3.4 in the appendix (Section 3.10))

The spectra and cubes are provided in the FITS file format (Pence et al. 2010). The products are described in further detail in the following sections. The products related to the nuclear spectra are described in Section 3.5.

3.4.1 Data cubes

The data cubes have a spatial size of 25×38 spatial pixels ('spaxels'), where each spaxel is 1×1 arcsec^2. The red cubes cover 5400 to 7000 Å in the wavelength

[4] `http://datacentral.aao.gov.au/asvo/surveys/s7/`
[5] `https://miocene.anu.edu.au/S7/Data_release_2`

dimension in uniform increments of 0.44 Å. The blue cubes cover 3500 to 5700 Å in the wavelength dimension in uniform increments of 0.77 Å. In the FITS files for each cube, the 0th extension contains the flux cube, and the 1st extension contains the variance cube.

Additionally, data cubes with the broad H α and Hβ components subtracted from the nuclear spaxels are also provided for the 14 Seyfert 1 galaxies that had broad-component subtraction (Section 3.3.4). For NGC 7213 only, the blue cube with broad-component subtraction is the same as the cube without this subtraction, because H α but not Hβ required the broad-component subtraction.

For both the normal and broad-component subtracted data cubes for these 14 galaxies, an additional extension is provided in the FITS files. This extension contains a mask to indicate which nuclear spaxels had broad-component subtraction.

3.4.2 Emission line fits

Four FITS files containing emission-line fit information are provided for each galaxy. Three of the FITS files correspond to each of the 1-, 2- and 3-component Gaussian fits to emission lines produced by LZIFU (Section 3.3.3). A fourth FITS file contains the 'best' number of components, as determined by the neural network LZCOMP (Section 3.3.3).

Each FITS file containing emission line fit data consists of multiple extensions. The extensions available in each LZIFU product FITS file are detailed in Table 3.2. Most of the extensions contain arrays with measured emission-line fluxes or the errors in these fluxes. Some extensions contain additional information such as the emission-line gas velocity relative to the input systemic redshift ('V'; in km s^{-1}), or the corresponding velocity dispersion ('VDISP'; in km s^{-1}).

In all four emission-line fit files for a galaxy, each extension containing emission-line fluxes contains a data cube. Two dimensions of the cube are the spatial dimensions, with slices in the third dimension corresponding to kinematic components. The 0th slice contains the total emission-line flux summed over all the kinematic components, and the 1st, 2nd and 3rd slices contain fluxes for the 1st, 2nd and 3rd kinematic components, where applicable. A cube of fluxes for the n-component fit contains $n + 1$ slices. The components in each spaxel are ordered by velocity dispersion, with the 1st and 3rd components corresponding to the narrowest and broadest Gaussians

Table 3.2 Indicative extension indices and 'EXTNAME' extension header values in LZIFU product FITS files.

Name	Index [a]	Errors name	Errors index
B_CONTINUUM	1	-	-
R_CONTINUUM	2	-	-
B_RESIDFIT	3	-	-
R_RESIDFIT	4	-	-
B_CONT_MASK	5	-	-
R_CONT_MASK	6	-	-
B_LINE	7	-	-
R_LINE	8	-	-
R_LINE_COMP1	9	-	-
R_LINE_COMP2	10	-	-
R_LINE_COMP3	11	-	-
STAR_V	12	-	-
STAR_VDISP	13	-	-
CONT_CHI2	14	-	-
V	15	V_ERR	16
VDISP	17	VDISP_ERR	18
CHI2	19	-	-
DOF	20	-	-
OII3726	21	OII3726_ERR	22
OII3729	23	OII3729_ERR	24
OIII4363	25	OIII4363_ERR	26
HBETA	27	HBETA_ERR	28
OIII4959	29	OIII4959_ERR	30
OIII5007	31	OIII5007_ERR	32
OI6300	33	OI6300_ERR	34
NII6548	35	NII6548_ERR	36
HALPHA	37	HALPHA_ERR	38
NII6583	39	NII6583_ERR	40
SII6716	41	SII6716_ERR	42
SII6731	43	SII6731_ERR	44
COMP_PREDICTIONS	45	-	-

[a] The Header Data Unit (HDU) with index 0 contains header information but no data

respectively. In the 'best' number of components file, the 'COMP_PREDICTIONS' extension is a mask showing whether `LZComp` chose 1, 2, or 3 components as the optimal number in each spaxel.

The provided emission-line fluxes are subject to the following caveats:

- The [O II] $\lambda\lambda 3726, 29$ and [O III] $\lambda\, 4363$ fluxes are provided as a sum of all components only. Due to reddening and lower S/N in the blue compared to the red, the component breakdowns for these lines are not reliable.

- The total Hβ flux is reapportioned between components to be consistent with the flux-ratios between components for Hα, to ensure consistent Balmer decrements.

- The fitting for the 14 Seyfert 1 galaxies that had special treatment was performed on the broad component-subtracted cubes. The fluxes inside the

> ‘broad-component subtraction’ regions of these galaxies are subject to substantial systematic uncertainties and should be considered on a case-by-case basis. In particular, care needs to be taken in choosing the number of kinematic components to use. The data for the ‘best’ number of components is not necessarily the most appropriate. Users of this data should read the caveats in Section 3.3.4 and inspect Figures 3.4 to 3.6 in the appendix (Section 3.11) or the broad component-subtracted cubes to determine how many kinematic components are appropriate to use for the broad component-subtracted narrow lines. Higher-order kinematic components may describe residuals of the subtraction as opposed to narrow-line emission.

The LZIFU output for 3C278 is missing some emission lines, however this galaxy has very little optical line emission.

3.4.3 Binned circum-nuclear spectra

Two FITS files containing nuclear spectra are provided for each galaxy, corresponding to the red and blue arms of WiFeS. The nuclear spectra are binned over an approximately circular, ∼4 arcsec (4-spaxel) diameter aperture around the nucleus (Section 3.3.5). The 0th extension of each FITS file contains the 1D flux array, the 1st extension contains the corresponding variance array, and the 2nd extension contains a mask identifying the spaxels that were binned to produce the nuclear spectrum.

For the 14 Seyfert 1 galaxies with special treatment, an additional nuclear spectrum file is provided (for each of the red and blue), which is the ∼4-arcsec nuclear spectrum binned from the broad component-subtracted cubes.

Figures 3.4 to 3.6 in the appendix (Section 3.11) compare nuclear spectra before and after broad component-subtraction for the relevant galaxies. These figures show nuclear spectra binned only over the spaxels with special treatment (instead of the ∼4-arcsec aperture) and are further described in Section 3.5.3 below.

Emission-line fluxes measured in the nuclear spectra are described in Section 3.5.1 below.

3.5 Nuclear spectra

In this section we present the results of the LZIFU fitting of the nuclear spectra.

3.5.1 Emission-line fluxes

Table 3.3 in the appendix (Section 3.10) presents extinction-corrected nuclear emission-line fluxes. The full table is available as a data product in this data release (Section 3.4), along with a corresponding table of flux errors. The flux table contains measurements of nuclear emission-line fluxes for 39 emission lines for the S7 sample of 131 galaxies. Table 3.3 corresponds to Table 4 in Paper II but Table 3.3 in this work has data for the full sample. The fluxes for the 14 Seyfert 1 galaxies with special treatment should be used with some caution. The H α and Hβ fluxes are narrow-component fluxes, and users of this data should be aware of the systematic effects discussed in Section 3.3.4. Additionally the higher-order Balmer lines did not have broad-component subtraction so these fluxes may be unreliable or contain significant broad-component contamination.

Table 3.4 in the appendix (Section 3.10) presents extinctions, physical aperture sizes, Hβ and [O III] fluxes and corresponding luminosities from the nuclear spectra for the newly observed S7 galaxies. A full table with data for the entire S7 sample is available in this data release (Section 3.4). Table 2 in Paper II presents similar data as Table 3.4 in this work but for the galaxies in the first data release. The data show that the nuclear extinction in the sample is commonly $A_V \sim 1 - 3$ mag, and the [O III] luminosities vary over approximately four orders of magnitude ($L_{[\mathrm{O\,III}]} \sim 10^{38} - 10^{42}$ erg s^{-1}). The caveats associated with fluxes measured in the 14 broad component-subtracted Seyfert 1 spectra also apply to the Hβ and [O III] fluxes and luminosities in Table 3.4.

3.5.2 Nuclear classifications

In this section we present the classifications of the nuclear spectra using the optical diagnostic diagram divisions of Kewley et al. (2006). Our IFU data ensures that analyses of S7 galaxies do not need to be constrained by single nuclear spectra, but the classifications derived from nuclear spectra are nevertheless informative. We note that the physical aperture covered by the 4 arcsec nuclear spectra varies from

$\sim$100 pc to $\sim$1.9 kpc over the S7 sample, and as a result the nuclear spectra probe widely varying fractions of galaxies in the sample.

Optical diagnostic diagrams showing classifications of nuclear spectra for the S7 galaxies are presented in the upper two panels in Figure 3.3. Although many galaxies lie in the 'Seyfert' and 'LINER' regions of the diagnostic diagrams, a substantial fraction of the galaxies lie in the composite region of the [N II]-H α diagram (above the Kauffmann et al. (2003) empirical extreme-starburst line but below the Kewley et al. (2001) theoretical extreme-starburst line). These spectra are contaminated by light from H II regions, either because of significant star formation close to the active nuclei which is unresolved in the S7 cubes, or because of the summing of spaxels in the S7 cubes to produce the nuclear spectra. Several galaxies lie below the empirical starburst line, and are therefore classified as star-forming and not AGN. These galaxies include NGC 4691, which is not an AGN, the misclassified Seyfert 1 galaxy Fairall 51, some galaxies such as ESO350-IG38 that have among the highest redshifts in the sample and are therefore suffering strong aperture effects, and NGC 4472, which is an early-type galaxy with very little line emission.

We note that the nuclear emission-line ratios result in BPT classifications that are broadly consistent with the source catalogue (Véron-Cetty & Véron 2010). In some cases the higher-quality S7 data results in an improvement over an incorrect prior classification, e.g. NGC 4691, which is classified as a Seyfert 1 in the Véron-Cetty & Véron (2010) catalogue.

Figure 3.3 also shows an interesting relationship between the strength of the forbidden high-ionization (coronal) emission line [Fe VII] λ6087 relative to H α and the diagnostic line ratio [O III] λ5007 / Hβ. The coronal line strength shows a clear positive correlation with [O III] / Hβ, with the correlation being visible in both the bottom-left panel and the coloring of the data in the upper panels. We expect the coronal line emission to occur much closer to the central engine of the AGN than the bulk of the [O III] and Hβ emission, so this correlation may be partly or entirely a consequence of orientation effects (c.f. Rose et al. 2015; Glidden et al. 2016). The theoretical grids published by Davies et al. (2016a) show that the objects with highest [Fe VII] are located in the region of highest ionization parameter. In these objects, radiation pressure will be dominant, which may produce observable dynamical effects in the ENLR. Objects with extreme radiation pressures will naturally produce extensive Compton heated zones which favor the production of observable coronal lines.

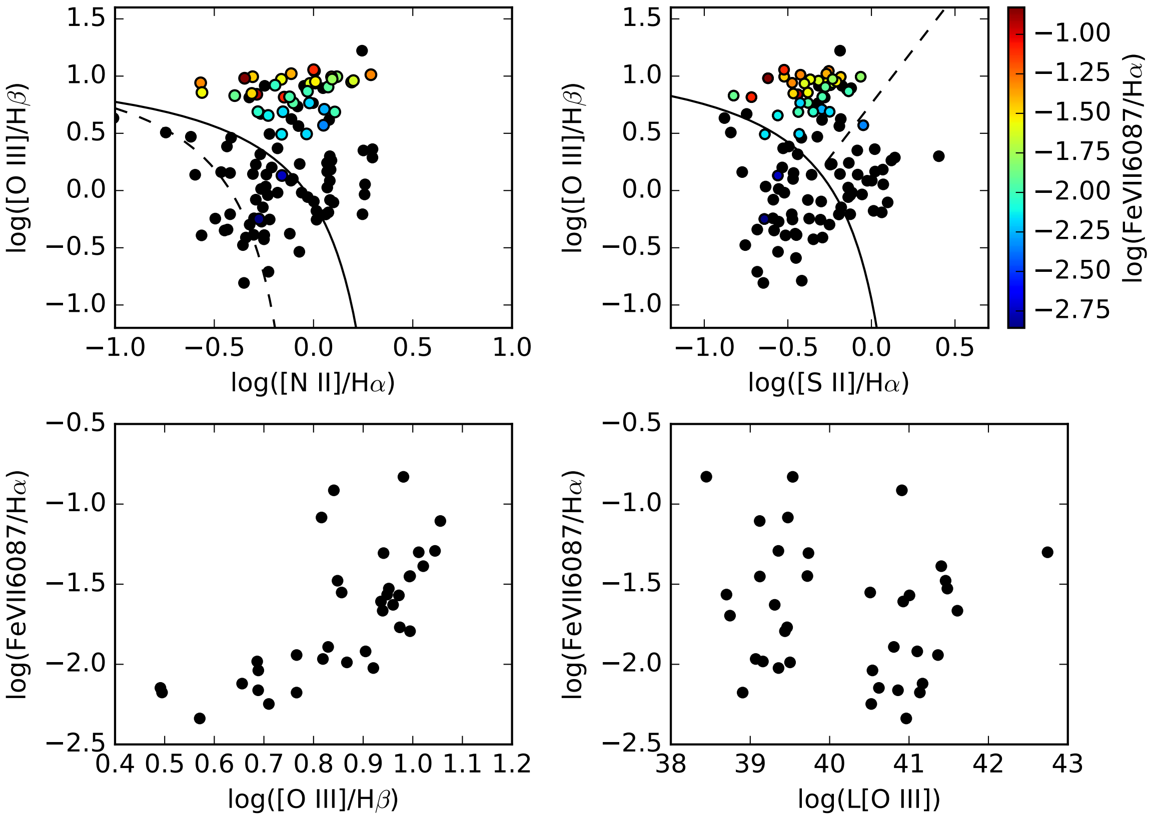

Figure 3.3 Top row: Optical diagnostic diagrams for nuclear spectra for the S7 sample. The solid lines (Kewley et al. 2001) and the dashed line in the top-left panel (Kauffmann et al. 2003) divide H II regions (below) and nebulae with higher ionization states (above). The dashed line in the top-right panel (Kewley et al. 2006) divides LINERs (below) and Seyferts (above). Black data points represent galaxies which have negligible nuclear [FeVII] λ6087 flux. Bottom row: The relative strength of the [FeVII] λ6087 coronal line (for galaxies where it is detected) plotted against the [OIII] λ5007/Hβ diagnostic ratio (left) and plotted against the [OIII] luminosity (right). There is a clear trend of increasing [FeVII] λ6087/H α with increasing [OIII] λ5007/Hβ.

The bottom-right panel of Figure 3.3 shows that the relative coronal line strength is not correlated with the [OIII] luminosity. This non-correlation supports the idea that orientation effects may be important in producing the correlation with [OIII] / Hβ.

3.5.3 Plots of nuclear spectra

Figures 3.4 to 3.6 in the appendix (Section 3.11) show nuclear spectra of the 14 Seyfert galaxies that were identified as having very broad H emission requiring special treatment in emission-line fitting (Section 3.3.4). The figures show spectra summed over the nuclear spaxels identified as having particularly prominent and/or broad emission in Balmer broad-components. For each galaxy the decomposition of the total spectrum into 'narrow' and 'broad' components is shown. The spectra show the diversity of broad-line profiles in the sample and the nature of the residuals remaining after subtraction of the model broad components.

Figure 3.7 in the appendix (Section 3.11) shows nuclear spectra for a selection of galaxies from the new observations. The varying line ratios are evident between the star-forming, LINER and Seyfert galaxies. An artefact of the subtraction of the strong [O I] λ5577 sky line is visible in all but one of the spectra.

3.6 Spatial properties

The spatial properties of the ionized gas in the entire sample of S7 galaxies is illustrated in Figures 3.8 to 3.18 in the appendix (Section 3.12). The galaxies are ordered by RA. For each galaxy the panels show the following (from left to right):

- A $118'' \times 180''$ DSS2 r-band image, with an outline indicating the size, position and orientation of the WiFeS field of view. North is towards the top of each image, and east is to the left.

- A three-color image showing the ionization state of the gas over the WiFeS field of view, with colors chosen to distinguish ENLRs in Seyferts from H II regions. The red channel is H α, the green channel is [N II] λ6584, and the blue channel is [O III] λ5007. In high-metallicity H II regions found in Seyfert nuclei, H α is generally weaker than [N II] λ6584 and [O III] λ5007 is generally weak, so these regions appear red, gold, or yellow. The NLR gas has strong [O III] λ5007 and generally higher [N II]/Hα, so appears blue, turquoise or green. For NGC 5253, the bright lines were saturated so the combination of lines used was Hγ, [N II] λ6584 and [O III] λ4959. A yellow arrow in the top-left indicates the direction of north. This panel is blank for the QSO PKS 0056-572 and the elliptical galaxies with little line emission NGC 4472 and 3C 278.

- A map of the line-of-sight emission-line gas velocity over the WiFeS field of view, from the single-component LZIFU fits (Section 3.3.3). For ∼18 galaxies a constant offset was applied to the data to ensure that the zero of the velocity maps corresponded to the nuclear emission-line velocity. A black circle displayed in the bottom-right shows the size of the seeing FWHM as recorded by the observer. For the 14 Seyfert 1 galaxies with particularly broad and prominent Balmer lines that required special treatment (Section 3.3.4), the green outline delineates the nuclear region where broad components were subtracted before fitting the narrow lines.

- A map of the line-of-sight emission-line gas velocity dispersion over the WiFeS field of view, from the single-component LZIFU fits. The LZIFU fitting corrects the velocity dispersion measurements for the instrumental dispersion in both the red and the blue arms of WiFeS.

The figures demonstrate the wide variety of emission-line gas morphology and kinematics found in the sample, including regular rotation (smooth 'spider diagrams', e.g. NGC 1346), bi-polar ionization cones delineated by enhanced velocity dispersion (e.g. NGC 7582), star-forming rings (e.g. NGC 5728), an apparently counter-rotating core (NGC 1068), and 'ridges' of enhanced velocity dispersion following spiral arms (NGC 6926). Detailed notes are presented on individual objects in Section 3.7.

3.7 Notes on Individual Objects

Section 5 of Paper II presented notes on individual galaxies. In this section we do the same for the galaxies of interest that were not included in the first data release or were otherwise not described in Paper II. The notes are based on inspection of the maps in the appendix (Section 3.12), the S7 spectral cubes (using `QFitsView`) and ancillary data such as HST observations (where stated). Galaxies are listed in order of RA.

MARK938: A well-studied recent merger, with distinct tidal tails. The nature of the excitation has been controversial - Veron-Cetty & Veron (1986) classify it as a Sy 2 but Thean et al. (2000) argue that it should be classified as a starburst rather than a Seyfert. However, our data clearly show it to be a post-starburst galaxy with an A-star dominant continuum spectrum in the blue (very deep Balmer absorption), while the red spectrum is consistent with shock-excited emission. This is visible in all parts of the main galaxy.

ESO 350-IG38: Sy 2 with jet-like ENLR extending ~ 8 arcsec from the nucleus at PA $\sim 210°$. The counter-'jet' is also dimly visible.

IC 1858: This poorly studied highly-inclined galaxy shows a spectrum dominated by old stars. Weak LINER-like emission is visible in the red. The NaI absorption is deep, broad and symmetric, possibly indicating an outflow.

NGC 1194: This galaxy had been classified as a Sy 1, but in our data we see no evidence of broad Balmer lines, and it is now classified as a Sy 2. Schmitt et al. (2003) imaged this galaxy with HST and found the [OIII] emission to be only mildy extended over ~ 2 arcsec. However, we observe an X-shaped ENLR extending over ~ 36 arcsec in [NII]. The opening angle is 30°, and the PA = 170°. The southern lobe is blueshifted, and the northern lobe is redshifted. There is no sign of recent star formation.

NGC 1217: A LINER nucleus with complex dynamics extended within a very smooth elliptical ring of H II regions in fast rotation,

NGC 1266: This galaxy shows an intermediate-age stellar spectrum, suggesting that it is post-starburst. It has a prominent ENLR with a complex, dynamically active, double-lobe morphology extending over ~ 20 arcsec at PA = 0°, roughly orthogonal in PA to the underlying disk. The southern lobe of the ENLR is blueshifted, and both lobes have large velocity broadening. The emission spectrum appears more shock-like close to the nuclear dust lane. The [NI] $\lambda\lambda5158, 5200$ doublet reaches an extraordinary strength here, surpassing Hβ and rivaling [OIII]$\lambda5007$. The [NII] lines are also unusually strong, suggesting an enhancement in the nitrogen abundance, and/or the presence of many low-velocity shocks. This unusual galaxy has a massive AGN-driven molecular outflow and has been shown to have strongly-suppressed star formation (Alatalo et al. 2015). The S7 WiFeS data also reveals a prominent galaxy-wide outflow seen in Na D doublet absorption that will be the subject of a detailed analysis by Rupke et al. (2017, in prep.).

NGC 1320: This high-inclination galaxy has been imaged in [OIII] and [NII] using HST by Ferruit et al. (2000). It has a Sy 2 nucleus, a compact ENLR, and has active star formation largely confined to the narrow inner NW spiral arm. The rotation curve is regular.

NGC 1346: This galaxy appears to be interacting with MCG-01-09-041, located 1.6 arc min. away. A high-excitation nucleus is embedded in a disk of H II regions of high metallicity with an undisturbed rotational signature. It is not clear whether the nucleus is simply a local knot of high star formation activity, rather than being a *bona fide* Seyfert.

NGC 1365: Sy 1 nucleus with strong broad H α and traces of broad Hβ with a number of apparently high-metallicity H II regions in a ring-like structure surrounding it. Some regions of the field have very strong post-starburst A-star signatures but little H II activity. The starburst ring is highly inclined with respect to the outer spiral features (which can be traced leading into the inner ring). A brilliant bubble-like ENLR extends across the WiFeS field orthogonally to the starburst ring at PA $\sim 120°$. The brightest part of this bubble was detected and a dynamical model was presented by Hjelm & Lindblad (1996). The ENLR is also faintly visible on other side of galaxy, and is equally extended (> 15 arcsec).

ESO 420-G13: In [O III] there is a one-side ENLR (PA $\sim 30°$) embedded in a galaxy with a strong post-starburst (A-star) signature. The ENLR can be traced to the edge of the WiFeS field. Close to the nucleus, and on the SW side, there is a bright region of star formation. This probably forms a confining ring to the ENLR. At H α + [N II] the reddened counter-cone of the ENLR is visible. This also extends to the edge of the field.

NGC 1672: A weak LINER nucleus embedded in a star-forming ring of intermediate-metallicity H II regions first imaged by Evans et al. (1996).

NGC 1667: Fairly compact Sy 2 nucleus surrounded by a ring + spiral arms of H II regions. These are fairly metal-rich and share the strong rotational signature of the galaxy.

NGC 1808: An active starburst galaxy with a starburst ring, a warped inner disk, and deep Na D absorption. There is a prominent galaxy-wide outflow that will be the subject of a detailed analysis by Rupke et al. (2017, in prep.). The nucleus has enhanced [N II] but no other sign of being a Sy 2. The H II regions in this galaxy have been catalogued by Tsvetanov & Petrosian (1995).

UGC 3255: A heavily reddened Sy 2 nucleus embedded in an edge-on disk with active star formation. There is evidence of a one-sided ionization cone at PA $\sim 300°$ with large velocity dispersion at [N II].

ESO 362-G08: Obscured Sy 2 nucleus in post-starburst galaxy seen at high inclination. Very deep Na I D-line absorption is seen. An amazing high-excitation "Green Bean" emission region is seen with Sy 2 emission signature on NE side of nucleus; looks to be a lower abundance minor galaxy blueshifted with respect to the main galaxy. The Green Bean displays a separate rotational signature, confirming that it is a dynamically distinct entity. This region had been first described by Fraquelli et al. (2000), but was interpreted in terms of the ejection of an ENLR from the main galaxy.

ESO 362-G18: A somewhat extended velocity-broadened Sy 2 ENLR (imaged with HST by Schmitt et al. (2003)) is seen surrounded by complexes of H II regions and with other H II regions visible across the field. The galaxy has a spiral structure with smooth rotation. In H α the presence of a Sy 1 nucleus is evident.

NGC 2110: This Sy 2 galaxy has a very extended two-sided curved ENLR that extends across the WiFeS field (38 arcsec), emerging from the nuclear region at PA $\sim 0°$. The ENLR displays pronounced bi-polar outflow. The ENLR is much more extended than was revealed by HST [O III] imaging, which shows a narrow, 1-arcsec long jet-like feature at PA = 340°, and a weaker feature at PA = 160° (Mulchaey et al. 1994). There is no evidence of active star formation or H II regions.

NGC 2217: This is a barred spiral (SBa) seen almost face-on. It displays LINER-like emission and very deep and broad Na D line absorption suggestive of an outflow. A bar-like nuclear emission region is surrounded by a Θ-shaped "double-bubble" of LINER emission extending right across the WiFeS field ($\sim$ 38 arcsec). The gas motions suggest a strongly warped disk, with high velocity dispersion seen within the bubble-like cavities. The distribution and kinematics of this ionized gas has been studied by Bettoni et al. (1990).

ESO 565-G19: This poorly studied galaxy contains a LINER nucleus displaying complex knotty dynamics in both H α and [N II]. H II region emission can be detected almost across the full field, and the galaxy displays a smooth rotational signature.

NGC 2945: A LINER nucleus with a strange velocity broadened one-sided LINER jet some 12 arcsec long at PA = 200°. There is also a star-forming ring in rapid rotation with major axis diameter 18 arcsec.

NGC 2974: This E-type galaxy contains a velocity broadened LINER nucleus embedded in a faintly emitting disk with a strong rotational signature. The Na D absorption is deep and wide. The dynamics of this galaxy were studied by Bettoni (1992). In addition there is SAURON data and detailed modeling of both stars and gas by Krajnović et al. (2005), and HST data has been obtained by Emsellem et al. (2003).

NGC 2992: This well-studied interacting edge-on galaxy contains a spectacular double-sided ionization cone with wide opening angle, studied in detail by Allen et al. (1999).

NGC 3100: This S0 galaxy displays deep and broad Na D absorption around the nucleus. A bipolar outflow of gas with a LINER spectrum is seen aligned with the minor axis of the galaxy. In this respect, it is like NGC 1052.

ESO 500-G34: Contains a dynamically active, Sy 2-like ionization cone ENLR extending $\sim$ 22 arcsec E-W along its brightest part. The galaxy itself has a post-starburst spectrum and a number of H II regions are embedded in the plane, which displays a regular rotation curve.

NGC 3281: This Sy 2 galaxy was studied by Storchi-Bergmann et al. (1992), and imaged by HST (Schmitt et al. 2003). Our data show a very extended V-shaped ENLR extending north from the centre with an opening angle of 40°, and a more diffuse bubble-like structure on the other side. The ENLR extent is greater than the 38 arcsec field of WiFeS. The internal dynamics are suggestive of an outflow. No H II regions are visible.

MCG-02-27-009: Displays a faint LINER nucleus embedded in ring of H II regions.

NGC 3312: This galaxy has a LINER nucleus with rotation, with a curved (accretion?) stream. Looks very like NGC 2945. The spectra show deep NaI absorption.

NGC 3393: The HST [OIII] image of this Seyfert 2 galaxy by Schmitt et al. (2003) shows an S-shaped ENLR, extended by 5.3 arcsec (1410 pc) along P.A. = 65 deg and 2.8 arcsec (740 pc) along the perpendicular direction. In our WiFeS [OIII] image, this is simply the inner part of a much more extended X-shaped double-sided ionization cone with enhanced intensity along the major axis. This can be traced across the full 38×25 arcsec WiFeS field. The ENLR is embedded in a faint ring of H II regions with rotation. The H II regions in this galaxy have been catalogued by Tsvetanov & Petrosian (1995). The axis of the ENLR seems to be orthogonal to the rotation.

NGC 3831: This poorly studied galaxy shows a very broad component underlying Hα, so it is probably an obscured Sy 1. There is deep NaI absorption, no signs of recent star formation, and the stellar population is dominated by old stars.

NGC 3858: Although classified as a Sy 2 by Maia et al. (2003), we find a LINER nucleus embedded in a steeply-inclined star-forming ring with a strong rotational signature. There is a second broken ring of H II regions further out.

NGC 4507: This is a bright, Compton-thick (Bianchi et al. 2006) hidden broad-line region (Moran et al. 2000) Sy 2 imaged with HST by Schmitt et al. (2003), who finds an ENLR elongated along PA = $-35°$ in the inner $\sim$2 arcsec. We find a highly dynamically active ENLR with multiple line components close to the nucleus extending both to the SE and NW of the nucleus over a total extent of $\sim$ 20 arcsec. Some faint H II regions are also visible in the field. At larger radii there is a ring of bright H II regions cataloged by Tsvetanov & Petrosian (1995).

NGC 4594: The Sombrero galaxy. It displays LINER emission extended across the WiFeS field along the major axis of the galaxy with ubiquitous deep and broad NaI absorption. There is clear evidence of a broad component underlying H α at the nucleus. This broad component may be time variable since Ho et al. (1997) did not detect it, but a broad component was found in an earlier paper by these authors (Filippenko & Sargent 1985). The extended LINER emission is seen in rotation.

IC 3639: Has a Sy 2 nucleus with an ENLR which can be traced out to a radius of ∼4 arcsec. This is embedded in a rich complex of well-resolved H II regions (catalogued by Tsvetanov & Petrosian (1995)) that extend all over the field. The region surrounding the nucleus shows a post-starburst continuum spectrum dominated by A-type stars.

NGC 4636: A LINER nucleus in an early-type galaxy with a rotating circum-nuclear gas disk.

NGC 4691: This galaxy is dominated by metal rich H II regions with an underlying post-starburst continuum. There is no sign of an AGN.

NGC 4696: A very extensive and dynamically rich fan-shaped LINER. The opening angle is 90°, and the axis is at PA = 180°. Emission can be traced to the edge of the WiFeS field. In some regions the [NII] and H α lines are split into two velocity components, while the outer regions are characterised by narrow FWHM. This object has been previously studied in detail with WiFeS by Farage et al. (2010), which showed that the filaments are shock heated remnants of a minor merger.

ESO 443-G17: A compact H II disk in very rapid and smooth rotation. Kewley et al. (2000) detected a compact radio core in this warm IR galaxy.

NGC 4845: This steeply-inclined Sy 2 galaxy has a magnificent ionization cone with an opening angle of 120° emerging perpendicularly from a circum-nuclear disk of H II regions with its axis at PA = 350°. The counter ionization cone is faintly visible, mainly in [NII] because of the high extinction. Together, both ionization cones fill the WiFeS field of view. The dynamics of the ENLR are dominated by the underlying rotation of the galaxy disk.

NGC 4939: A compact Sy 2 nucleus is seen in [OIII] but it is clearly extended by 16 arcsec along the bar (PA = 5°) in [NII]. However, with HST, a biconical ionization region is seen both in [OIII] and in the UV extended perpendicularly to the disk of the galaxy (Martini et al. 2003; Muñoz Marín et al. 2007). There are a number of faint H II regions in the field. The H II regions in this galaxy have been catalogued by Tsvetanov & Petrosian (1995).

ESO 323-G77: This is a partially obscured Sy 1 with polarised emission close to the nucleus (Schmid et al. 2003). We find a two-sided ionization cone with a remarkably narrow opening angle ($\sim 20°$) extending N-S across the field. The inner region of this galaxy was mapped with HST by Mulchaey et al. (1996). There is evidence of active star formation activity close to the nucleus (strong Hβ emission and deep absorption).
NGC 4968: This Sy 2 galaxy has been imaged in [O III] and [N II] using HST by Ferruit et al. (2000) and in [O III] by Schmitt et al. (2003). With HST there is a fan-shaped ENLR extended towards the SE by ∼1.5 arcsec. This can be traced out to 7 arcsec in our data, and the counter ionization cone is also faintly visible. Previous ground-based data by Pogge (1989) did not detect any extended [O III] emission.
ARK 402: A LINER nucleus embedded in a rotating disk.
NGC 4990: This galaxy has a bright starburst nucleus and is not an AGN.
MCG-03-34-064: Although classified by Aguero et al. (1994) as a Sy 1.8, we find no evidence that the nucleus is anything other than a LINER. The nucleus is surrounded by a rapidly rotating ring of H II regions.
NGC 5128: The Centaurus A galaxy. The highly obscured Sy 2 nucleus and ENLR is seen embedded in a complex of H II regions.
NGC 5135: A Sy 2 with a double-sided ionization cone with opening angle $\sim 40°$. The ENLR can be traced over the WiFeS field (∼ 30 arc sec). H II regions are present and a post-starburst stellar continuum can be traced along the major axis of the bar - c.f. González Delgado et al. (1998, 2001).
ESO 383-G35: This E/S0 galaxy contains a Sy 1 with coronal line emission. It has been imaged in [O III] and [N II] using HST by Ferruit et al. (2000). We find an extensive ENLR that can be traced along the major axis of the galaxy.
NGC 5252: This galaxy displays a spectacular bi-conical ionization structure with arcs, first described by Tadhunter & Tsvetanov (1989). In the bright inner region, strong line splitting is visible. A spectral analysis of this galaxy was performed by Acosta-Pulido et al. (1996); both their data and our data provides evidence for the presence of a broad component to Hα in the nucleus.
IC 4329A: A bright Sy 1 nucleus is surrounded by a compact dynamically active ENLR seen by Colbert et al. (1996). We find a fainter, more dynamically quiescent, X-shaped and limb-brightened ionization cone with an opening angle of 30°, which extends right across the 38 arcsec WiFeS field.
NGC 5427: This galaxy is tidally interacting with NGC 5426. A detailed description of the ENLR in this galaxy and its properties using WiFeS data is given

in Paper I.

NGC 5643: Since this Compton-thick galaxy was known to have a spectacular ENLR (Schmitt et al. 1994), we obtained a 2 field mosaic in order to map it completely. Nonetheless with our greater sensitivity, we find the [O III] emission can be traced right to the edge of the field (over 48 arcsec N-S and 38 arcsec E-W). On the southern side the brightest part of the ENLR is knotty and curved. The H II regions in this galaxy have been catalogued by Tsvetanov & Petrosian (1995).

NGC 5990: A bright post-starbust galaxy with a compact Sy 2 nucleus. There is a bright H II region complex to the NE of the nucleus, apparently of high metallicity.

NGC 6328: This, the closest known GPS galaxy (Tingay et al. 1997), has a bright, spatially extended and velocity broadened LINER nucleus.

IC 4777: A Sy 2 nucleus embedded in an elliptical star-forming ring.

ESO 460-G09: A LINER nucleus is surrounded by a number of H II region complexes.

MCG-02-51-008: This poorly studied galaxy has a bright Sy 2 nucleus with an extensive two-sided ENLR emerging at PA = 110°, but twisting and expanding towards the S on the E side, and towards the N on the W side. This is embedded in a rich star-forming disk with bright H II region complexes.

NGC 6936: A bright, extensive and rotating LINER disk with very prominent and wide Na D-line absorption on the nucleus.

MCG-04-49-001: This galaxy has a very rapidly rotating disk with a pronounced warp. It shows a LINER nucleus surrounded by a ring of bright H II regions.

ESO 287-G42: A LINER nucleus with two spiral arms rich in H II regions. There is a hint of a broad component underlying Hα.

NGC 7172: A two-sided ionization cone with opening angle 120° emerges in the polar direction from a highly dust-obscured nucleus in this highly inclined galaxy, a member of the compact group HCG90. The southern cone is the brighter. A line of H II regions is visible on either side of the central E-W dust lane.

IC 5169: A two-sided ionization cone with opening angle 130° emerges in the polar direction from a bright, rapidly rotating circum-nuclear H II starburst ring. This is surrounded at larger radius by a second ring of fainter H II regions with lower rotational velocities. The intimate connection of the ENLR with the inner starburst ring explains the ambiguities in the earlier classification of the galaxy - see the discussion by Zaw et al. (2009).

IC 1481: This extraordinary galaxy has a post-starburst circum-nuclear continuum spectrum with apparently large reddening at the Sy 2 nucleus itself. The ENLR is very extensive, its brightest portions forming a figure of eight extending $\sim$13 arcsec at PA = 50° either side of the nucleus. Additional knots of emission are visible to the edges of the field.

3.8 Conclusions

We have presented the second and final data release of the *Siding Spring Southern Seyfert Spectroscopic Snapshot Survey* (S7). The S7 uses the WiFeS instrument on the ANU 2.3 m telescope at Siding Spring Observatory to obtain integral field data with a spectral resolution of $R = 3000$ in the blue and $R = 7000$ in the red. The final S7 sample consists of 131 galaxies, including 63 galaxies observed since the first data release. There are approximately 18 Seyfert 1 galaxies, 77 Seyfert 2 galaxies, 27 LINERs, and 11 starbursts. The sample was selected to consist of nearby galaxies ($z \lesssim 0.02$), which are almost all detected in the radio, and are in the southern sky ($\delta < +10°$) at galactic latitudes of $|b| \gtrsim 15°$.

The data products provided with this work include data cubes from both the blue and red arms of WiFeS, emission line fits (with 1, 2 and 3 Gaussian components as well as a 'best' number of components chosen by an artificial neural network), nuclear spectra extracted using a 4 arcsec aperture, and reddening-corrected emission-line fluxes for the nuclear spectra. Maps of gas excitation, gas line-of-sight velocity and gas line-of-sight velocity dispersion were presented for each galaxy. Additionally we have classified the nuclear spectra using optical diagnostic diagrams, demonstrating that the strength of the coronal line [Fe VII] λ6087 is correlated with the diagnostic line ratio [O III]/ Hβ. We have also provided notes on each of the newly observed objects.

The S7 is a basis set for comparison for all future AGN surveys. The large sample size and the wide field of view, high dynamic range and high spectral resolution of the integral field data form a foundation for important insights into the physics of Active Galactic Nuclei.

Acknowledgements

M.D. and L.K. acknowledge support from ARC discovery project #DP160103631. Parts of this research were conducted by the Australian Research Council Centre of Excellence for All-sky Astrophysics (CAASTRO), through project number CE110001020. Prajval Shastri acknowledges the Distinguished Visitor Fellowship at the RSAA, Australian National University where part of this work was undertaken. This research is supported by an Australian Government Research Training Program (RTP) Scholarship. M.N. Sundar acknowledges the Indian Institute of Astrophysics student internship. This research has made extensive use of the National Aeronautics and Space Administration (NASA) Astrophysics Data System Bibliographic Services, the NASA/IPAC Extragalactic Database which is operated by the Jet Propulsion Laboratory, California Institute of Technology, under contract with NASA, and data, software and/or web tools obtained from the NASA High Energy Astrophysics Science Archive Research Center, a service of the Goddard Space Flight Center and the Smithsonian Astrophysical Observatory.

3.9 References

Acosta-Pulido, J. A., Vila-Vilaro, B., Perez-Fournon, I., Wilson, A. S., & Tsvetanov, Z. I. 1996, ApJ, 464, 177
Aguero, E. L., Calderon, J. H., Paolantonio, S., & Suarez Boedo, E. 1994, PASP, 106, 978
Allen, M. G., Dopita, M. A., Tsvetanov, Z. I., & Sutherland, R. S. 1999, ApJ, 511, 686
Allen, J. T., Croom, S. M., Konstantopoulos, I. S., et al. 2015, MNRAS, 446, 1567
Allen, J. T., Schaefer, A. L., Scott, N., et al. 2015, MNRAS, 451, 2780
Alatalo, K., Lacy, M., Lanz, L., et al. 2015, ApJ, 798, 31
Antonucci, R. 1993, ARA&A, 31, 473
Baldwin, J. A., Phillips, M. M., & Terlevich, R. 1981, PASP, 93, 5
Becker, R. H., White, R. L., & Helfand, D. J. 1995, ApJ, 450, 559
Belfiore, F., Maiolino, R., Maraston, C., et al. 2016, MNRAS, 461, 3111
Bettoni, D., Fasano, G., & Galletta, G. 1990, AJ, 99, 1789
Bettoni, D. 1992, A&AS, 96, 333
Bianchi, S., Guainazzi, M., & Chiaberge, M. 2006, A&A, 448, 499
Binette, L., Magris, C. G., Stasińska, G., & Bruzual, A. G. 1994, A&A, 292, 13
Blanc, G. A., Weinzirl, T., Song, M., et al. 2013, AJ, 145, 138
Bryant, J. J., Owers, M. S., Robotham, A. S. G., et al. 2015, MNRAS, 447, 2857
Bundy, K., Bershady, M. A., Law, D. R., et al. 2015, ApJ, 798, 7
Calzetti, D., Armus, L., Bohlin, R. C., et al. 2000, ApJ, 533, 682
Cappellari, M., & Emsellem, E. 2004, PASP, 116, 138
Childress, M. J., Vogt, F. P. A., Nielsen, J., & Sharp, R. G. 2014, Ap&SS, 349, 617
Cluver, M. E., Jarrett, T. H., Hopkins, A. M., et al. 2014, ApJ, 782, 90
Colbert, E. J. M., Baum, S. A., Gallimore, J. F., et al. 1996, ApJS, 105, 75

Condon, J. J., Cotton, W. D., Greisen, E. W., et al. 1998, AJ, 115, 1693
Croom, S. M., Lawrence, J. S., Bland-Hawthorn, J., et al. 2012, MNRAS, 421, 872
Davies, R. L., Dopita, M. A., Kewley, L., et al. 2016, ApJ, 824, 50
Davies, R. L., Groves, B., Kewley, L. J., et al. 2016, MNRAS, 462, 1616
Davies, R. L., Groves, B., Kewley, L. J., et al. 2017, MNRAS, 470, 4974
Diamond-Stanic, A. M., & Rieke, G. H. 2012, ApJ, 746, 168
Dopita, M. A., & Sutherland, R. S. 1995, ApJ, 455, 468
Dopita, M. A., Groves, B. A., Sutherland, R. S., Binette, L., & Cecil, G. 2002, ApJ, 572, 753
Dopita, M., Hart, J., McGregor, P., et al. 2007, Ap&SS, 310, 255
Dopita, M., Rhee, J., Farage, C., et al. 2010, Ap&SS, 327, 245
Dopita, M. A., Scharwächter, J., Shastri, P., et al. 2014, A&A, 566, A41 (Paper I)
Dopita, M. A., Shastri, P., Davies, R., et al. 2015, ApJS, 217, 12 (Paper II)
Dopita, M. A., Ho, I.-T., Dressel, L. L., et al. 2015, ApJ, 801, 42 (Paper III)
Emsellem, E., Goudfrooij, P., & Ferruit, P. 2003, MNRAS, 345, 1297
Elbaz, D., Daddi, E., Le Borgne, D., et al. 2007, A&A, 468, 33
Eracleous, M., & Halpern, J. P. 2001, ApJ, 554, 240
Evans, I. N., Koratkar, A. P., Storchi-Bergmann, T., et al. 1996, ApJS, 105, 93
Farage, C. L., McGregor, P. J., Dopita, M. A., & Bicknell, G. V. 2010, ApJ, 724, 267
Ferrarese, L., & Merritt, D. 2000, ApJL, 539, L9
Ferruit, P., Wilson, A. S., & Mulchaey, J. 2000, ApJS, 128, 139
Filippenko, A. V. 1982, PASP, 94, 715
Filippenko, A. V., & Sargent, W. L. W. 1985, ApJS, 57, 503
Förster Schreiber, N. M., Genzel, R., Bouché, N., et al. 2009, ApJ, 706, 1364
Förster Schreiber, N. M., Genzel, R., Newman, S. F., et al. 2014, ApJ, 787, 38
Fraquelli, H. A., Storchi-Bergmann, T., & Binette, L. 2000, ApJ, 532, 867
García-Benito, R., Zibetti, S., Sánchez, S. F., et al. 2015, A&A, 576, A135
Glidden, A., Rose, M., Elvis, M., & McDowell, J. 2016, ApJ, 824, 34
González Delgado, R. M., Heckman, T., Leitherer, C., et al. 1998, ApJ, 505, 174
González Delgado, R. M., Heckman, T., & Leitherer, C. 2001, ApJ, 546, 845
González Delgado, R. M., Cerviño, M., Martins, L. P., Leitherer, C., & Hauschildt, P. H. 2005, MNRAS, 357, 945
Greene, J. E., & Ho, L. C. 2005, ApJ, 630, 122
Groves, B. A., Dopita, M. A., & Sutherland, R. S. 2004, ApJS, 153, 9
Groves, B. A., Dopita, M. A., & Sutherland, R. S. 2004, ApJS, 153, 75
Hampton, E. J., Medling, A. M., Groves, B., et al. 2017, MNRAS, 470, 3395
Heckman, T. M. 1980, A&A, 87, 152
Heckman, T. M., & Best, P. N. 2014, ARA&A, 52, 589
Helou, G., Khan, I. R., Malek, L., & Boehmer, L. 1988, ApJS, 68, 151
Hjelm, M., & Lindblad, P. O. 1996, A&A, 305, 727
Ho, L. C., Filippenko, A. V., Sargent, W. L. W., & Peng, C. Y. 1997, ApJS, 112, 391
Ho, L. C., Feigelson, E. D., Townsley, L. K., et al. 2001, ApJL, 549, L51
Ho, L. C. 2008, ARA&A, 46, 475
Ho, I.-T., Kewley, L. J., Dopita, M. A., et al. 2014, MNRAS, 444, 3894
Ho, I.-T., Medling, A. M., Bland-Hawthorn, J., et al. 2016, MNRAS, 457, 1257
Ho, I.-T., Medling, A. M., Groves, B., et al. 2016, Ap&SS, 361, 280
Husemann, B., Urrutia, T., Tremblay, G. R., et al. 2016, A&A, 593, L9
Karouzos, M., Woo, J.-H., & Bae, H.-J. 2016, ApJ, 819, 148

Karouzos, M., Woo, J.-H., & Bae, H.-J. 2016, ApJ, 828, 64
Kauffmann, G., Heckman, T. M., Tremonti, C., et al. 2003, MNRAS, 346, 1055
Kehrig, C., Monreal-Ibero, A., Papaderos, P., et al. 2012, A&A, 540, A11
Kennicutt, R. C., Jr. 1998, ARA&A, 36, 189
Kewley, L. J., Heisler, C. A., Dopita, M. A., et al. 2000, ApJ, 530, 704
Kewley, L. J., Dopita, M. A., Sutherland, R. S., Heisler, C. A., & Trevena, J. 2001, ApJ, 556, 121
Kewley, L. J., Groves, B., Kauffmann, G., & Heckman, T. 2006, MNRAS, 372, 961
Krajnović, D., Cappellari, M., Emsellem, E., McDermid, R. M., & de Zeeuw, P. T. 2005, MNRAS, 357, 1113
Kormendy, J., & Ho, L. C. 2013, ARA&A, 51, 511
Leslie, S. K., Kewley, L. J., Sanders, D. B., & Lee, N. 2016, MNRAS, 455, L82
Lípari, S., Mediavilla, E., Garcia-Lorenzo, B., et al. 2004, MNRAS, 355, 641
Magorrian, J., Tremaine, S., Richstone, D., et al. 1998, AJ, 115, 2285
Maia, M. A. G., Machado, R. S., & Willmer, C. N. A. 2003, AJ, 126, 1750
Mancini, C., Förster Schreiber, N. M., Renzini, A., et al. 2011, ApJ, 743, 86
Markwardt, C. B. 2009, Astronomical Data Analysis Software and Systems XVIII, 411, 251
Martini, P., Regan, M. W., Mulchaey, J. S., & Pogge, R. W. 2003, ApJS, 146, 353
McConnell, N. J., & Ma, C.-P. 2013, ApJ, 764, 184
McElroy, R., Croom, S. M., Pracy, M., et al. 2015, MNRAS, 446, 2186
McElroy, R. E., Husemann, B., Croom, S. M., et al. 2016, A&A, 593, L8
Monreal-Ibero, A., Arribas, S., & Colina, L. 2006, ApJ, 637, 138
Moran, E. C., Barth, A. J., Kay, L. E., & Filippenko, A. V. 2000, ApJL, 540, L73
Mulchaey, J. S., Wilson, A. S., Bower, G. A., et al. 1994, ApJ, 433, 625
Mulchaey, J. S., Wilson, A. S., & Tsvetanov, Z. 1996, ApJS, 102, 309
Müller-Sánchez, F., Hicks, E. K. S., Malkan, M., et al. 2018, ApJ, 858, 48
Muñoz Marín, V. M., González Delgado, R. M., Schmitt, H. R., et al. 2007, AJ, 134, 648
Pence, W. D., Chiappetti, L., Page, C. G., Shaw, R. A., & Stobie, E. 2010, A&A, 524, A42
Pogge, R. W. 1989, ApJ, 345, 730
Ricci, T. V., Steiner, J. E., & Menezes, R. B. 2014, MNRAS, 440, 2419
Ricci, T. V., Steiner, J. E., & Menezes, R. B. 2014, MNRAS, 440, 2442
Ricci, T. V., Steiner, J. E., & Menezes, R. B. 2015, MNRAS, 447, 1504
Ricci, T. V., Steiner, J. E., & Menezes, R. B. 2015, MNRAS, 451, 3728
Rich, J. A., Kewley, L. J., & Dopita, M. A. 2011, ApJ, 734, 87
Rich, J. A., Kewley, L. J., & Dopita, M. A. 2014, ApJL, 781, L12
Rich, J. A., Kewley, L. J., & Dopita, M. A. 2015, ApJS, 221, 28
Riffel, R. A., Storchi-Bergmann, T., Winge, C., et al. 2008, MNRAS, 385, 1129
Riffel, R. A., Storchi-Bergmann, T., Dors, O. L., & Winge, C. 2009, MNRAS, 393, 783
Riffel, R. A., & Storchi-Bergmann, T. 2011, MNRAS, 411, 469
Riffel, R. A., & Storchi-Bergmann, T. 2011, MNRAS, 417, 2752
Riffel, R. A., Storchi-Bergmann, T., & Winge, C. 2013, MNRAS, 430, 2249
Rothberg, B., Husemann, B., Busch, G., et al. 2015, IAU General Assembly, 22, 2257803
Rose, M., Elvis, M., & Tadhunter, C. N. 2015, MNRAS, 448, 2900
Sánchez, S. F., Kennicutt, R. C., Gil de Paz, A., et al. 2012, A&A, 538, A8
Sánchez, S. F., García-Benito, R., Zibetti, S., et al. 2016, A&A, 594, A36

Scharwächter, J., Dopita, M. A., Shastri, P., et al. 2016, The Universe of Digital Sky Surveys, 42, 263
Schmitt, H. R., Storchi-Bergmann, T., & Baldwin, J. A. 1994, ApJ, 423, 237
Schmid, H. M., Appenzeller, I., & Burch, U. 2003, A&A, 404, 505
Schmitt, H. R., Donley, J. L., Antonucci, R. R. J., Hutchings, J. B., & Kinney, A. L. 2003, ApJS, 148, 327
Sharp, R., Allen, J. T., Fogarty, L. M. R., et al. 2015, MNRAS, 446, 1551
Singh, R., van de Ven, G., Jahnke, K., et al. 2013, A&A, 558, A43
Storchi-Bergmann, T., Wilson, A. S., & Baldwin, J. A. 1992, ApJ, 396, 45
Storchi-Bergmann, T., Eracleous, M., Teresa Ruiz, M., et al. 1997, ApJ, 489, 87
Storchi-Bergmann, T., McGregor, P. J., Riffel, R. A., et al. 2009, MNRAS, 394, 1148
Storchi-Bergmann, T., Lopes, R. D. S., McGregor, P. J., et al. 2010, MNRAS, 402, 819
Stott, J. P., Swinbank, A. M., Johnson, H. L., et al. 2016, MNRAS, 457, 1888
Tadhunter, C., & Tsvetanov, Z. 1989, Nature, 341, 422
Thean, A., Pedlar, A., Kukula, M. J., Baum, S. A., & O'Dea, C. P. 2000, MNRAS, 314, 573
Thomas, A. D., Groves, B. A., Sutherland, R. S., et al. 2016, ApJ, 833, 266
Thomas, A. D., Dopita, M. A., Shastri, P., et al. 2017, ApJS, 232, 11
Tingay, S. J., Jauncey, D. L., Reynolds, J. E., et al. 1997, AJ, 113, 2025
Tsvetanov, Z. I., & Petrosian, A. R. 1995, ApJS, 101, 287
Ulvestad, J. S., & Ho, L. C. 2001, ApJL, 562, L133
Veron-Cetty, M.-P., & Veron, P. 1986, A&AS, 66, 335
Véron-Cetty, M.-P., & Véron, P. 2006, A&A, 455, 773
Véron-Cetty, M.-P., & Véron, P. 2010, A&A, 518, A10
Veilleux, S., & Osterbrock, D. E. 1987, ApJS, 63, 295
Villar-Martín, M., Arribas, S., Emonts, B., et al. 2016, MNRAS, 460, 130
Vogt, F. P. A., Dopita, M. A., & Kewley, L. J. 2013, ApJ, 768, 151
Wisnioski, E., Förster Schreiber, N. M., Wuyts, S., et al. 2015, ApJ, 799, 209
Zaw, I., Farrar, G. R., & Greene, J. E. 2009, ApJ, 696, 1218

3.10 Appendix: Tables of measured nuclear line fluxes

De-reddened nuclear emission-line fluxes for the newly observed galaxies are listed in Table 3.3. Luminosity distances, extinctions, physical aperture sizes and fluxes and luminosities of the [O III] and Hβ lines are given for the newly observed galaxies in Table 3.4. These tables are discussed in Section 3.5.1. Full versions of both tables are available as part of this data release, with the addition of a table corresponding to Table 3.3 but containing flux errors.

Table 3.3 Measured de-reddened nuclear emission-line fluxes for the newly observed S7 galaxies. Here the second column presents the Hβ flux and the fluxes in the remaining columns are relative to the Hβ flux. For 14 Seyfert 1 galaxies the fluxes were measured after subtraction of broad Hα and Hβ components.

Galaxy	$F_{H\beta}$ (10^{-16} erg cm^{-2} s^{-1})	[FeVII] λ3586	[OII] λ3726	[OII] λ3729	Hη	[NeIII] λ3869	...
ARK402	35	...	1.454	0.695	0.086	...	...
ESO287-G42	29	...	1.535	0.882	...	...	...
ESO323-G77	588	...	0.127	0.243	0.058	0.163	...
ESO350-IG38	6460	...	1.044	1.234	0.062	0.259	...
ESO362-G08	380	...	1.232	0.917	0.049	0.208	...
ESO362-G18	599	0.026	0.443	0.342	0.065	0.687	...
ESO383-G35	850	0.047	0.696	0.893	0.162	0.553	...
ESO420-G13	4169	...	0.422	0.436	0.060	0.142	...
ESO443-G17	2243	...	0.650	0.547	0.022	...	...
ESO460-G09	74	...	2.577	2.246	...	0.232	...
ESO500-G34	3316	...	1.128	1.528	0.079	0.348	...
ESO565-G19	321	...	1.398	0.946	0.021	0.107	...
IC1481	705	...	1.246	2.781	0.151	0.337	...
IC1858	30	...	0.633	...	...	...	...
IC3639	3033	...	0.975	0.271	0.032	0.348	...
IC4329A	1575	...	0.396	0.246	0.058	0.371	...
IC4777	291	...	1.306	1.014	0.026	0.704	...
IC4995	397	0.049	0.734	0.589	0.065	0.817	...
IC5169	951	0.139	0.852	0.769	0.063	0.101	...
MARK938	6812	0.231	6.870	2.277	...	0.766	...
MCG-02-27-009	24	...	1.295	1.197	...	...	...
MCG-02-51-008	98	...	0.807	1.552	0.048	0.445	...
MCG-03-34-064	9067	0.124	0.598	0.857	0.076	1.523	...
MCG-04-49-001	30	...	0.740	1.120	...	...	...
NGC1068	69965	0.072	0.814	0.676	0.002	1.304	...
NGC1194	127	0.229	0.431	1.210	0.119	0.234	...
NGC1217	72	...	0.810	0.591	...	...	...
NGC1266	4667	...	1.995	12.794	...	1.049	...
NGC1320	587	0.065	0.377	0.605	0.064	0.485	...
NGC1346	387	...	0.614	0.570	...	0.058	...
NGC1365	2182	...	0.370	0.507	0.051	0.275	...
NGC1667	515	...	2.899	1.395	...	0.379	...
NGC1672	402	0.016	0.453	0.499	0.072	0.008	...
NGC2110	3848	...	2.315	3.266	0.043	0.830	...
NGC2217	220	...	1.611	0.596	...	...	...
NGC2945	55	...	2.558	0.740	0.043	...	...
NGC2974	145	...	1.733	0.333	...	...	...
NGC3281	550	...	1.252	0.812	0.080	0.684	...
NGC3312	179	...	2.494	1.980	0.025	0.041	...
NGC3390	10	...	1.039	...	...	...	...
NGC3393	1512	0.024	1.120	1.112	0.071	0.825	...
NGC3831	29	...	1.172	1.339	...	...	...
NGC3858	18	...	0.510	0.495	...	...	...
NGC4418	189	...	2.663	2.865	...	0.706	...
NGC4472	235	...	0.253	...	...	...	...
NGC4507	4301	0.072	1.302	0.928	0.075	0.952	...
NGC4593	168	...	0.368	0.289	0.213	0.356	...
NGC4594	469	...	1.031	0.068	...	...	...
NGC4636	119	...	0.552	0.559	0.185	...	...
NGC4691	3424	...	0.825	0.805	0.071	0.017	...
NGC4696	31	...	0.945	0.992	...	...	...
NGC4845	1504	...	0.731	0.868	0.161	0.190	...
NGC4939	649	...	1.261	0.791	0.076	0.852	...
NGC4968	2061	...	0.970	0.678	0.084	1.190	...
NGC4990	1872	...	1.514	1.339	0.067	0.092	...
NGC5128	2255	...	1.384	1.474	...	...	...
NGC5135	2595	...	0.808	0.523	0.055	0.314	...
NGC5252	325	...	1.379	2.329	0.034	0.926	...
NGC5427	124	...	1.375	0.781	0.120	0.792	...
NGC5643	1849	0.047	1.613	1.131	0.084	0.916	...
NGC5990	1996	...	0.566	1.319	...	0.317	...
NGC6328	512	...	0.927	1.557	0.032	0.106	...
NGC6936	56	...	0.948	0.814	...	...	...
NGC7172	143	...	0.545	1.466	...	0.204	...
NGC7682	485	...	1.062	1.789	0.061	0.769	...
PKS1306-241	301	0.462	1.723	1.751	...	0.437	...
PKS1521-300	44	...	0.833	0.638	...	...	...
UGC3255	...	...	...	...	...	...	...

Table 3.4 Derived nuclear extinctions, physical aperture sizes, and Hβ and [OIII] fluxes and luminosities for the newly observed S7 galaxies

Galaxy	Type	$D_{Lum.}$ (Mpc)[a]	A_V (mag.)	Aperture (kpc)[b]	$F_{H\beta}$ ($10^{-16}\times$ erg cm^{-2} s^{-1})	F_{OIII} ($10^{-16}\times$ erg cm^{-2} s^{-1})	log $L_{H\beta}$ (erg s^{-1})	log L_{OIII} (erg s^{-1})
ARK402	SB+Sy 2	76	0	1.48	40	30	39.4	39.3
ESO287-G42	Sy 1	80	0	1.55	30	30	39.3	39.3
ESO323-G77[c]	Sy 1	64	0	1.25	590	1260	40.5	40.8
ESO350-IG38	SB	88	1.33	1.71	6460	22890	41.8	42.3
ESO362-G08	PSB+Sy 2	67	1.72	1.31	380	2850	40.3	41.2
ESO362-G18[c]	Sy 1	53	0.76	1.03	600	5170	40.3	41.2
ESO383-G35[c]	Sy 1	33	1.69	0.64	850	4150	40.0	40.7
ESO420-G13	SB+Sy 2	51	2.19	0.99	4170	6990	41.1	41.3
ESO443-G17	SB+Sy 2	44	2.05	0.85	2240	710	40.7	40.2
ESO460-G09	SB+Sy 2	84	0.88	1.63	70	110	39.8	40.0
ESO500-G34	SB+PSB+Sy 2	52	3.55	1.02	3320	3640	41.0	41.1
ESO565-G19	LINER or Sy 2	70	1.05	1.35	320	740	40.3	40.6
IC1481	SB+Sy 2	87	2.55	1.70	700	1020	40.8	41.0
IC1858	SB	87	0	1.68	30	10	39.4	39.1
IC3639	Sy 2	47	1.95	0.91	3030	17240	40.9	41.7
IC4329A[c]	Sy 1	69	1.65	1.33	1580	9370	41.0	41.7
IC4777	Sy 2	80	1.27	1.55	290	1850	40.3	41.2
IC4995	Sy 2	69	0.74	1.34	400	4710	40.4	41.4
IC5169	SB+Sy 2	44	2.47	0.86	950	1060	40.4	40.4
MARK938	SB+Sy 2	84	4.41	1.63	6810	8260	41.8	41.8
MCG-02-27-009	LINER or Sy 2	65	0.60	1.26	20	70	39.1	39.6
MCG-02-51-008	SB+Sy 2	80	0.95	1.55	100	420	39.9	40.5
MCG-03-34-064	Sy 1	71	1.80	1.37	9070	95060	41.7	42.8
MCG-04-49-001	LINER	86	0	1.67	30	20	39.4	39.3
NGC1068	Sy 2	16	1.76	0.32	69970	768300	41.3	42.4
NGC1194	SB+Sy 2	58	1.27	1.13	130	790	39.7	40.5
NGC1217	LINER	90	0	1.74	70	110	39.8	40.0
NGC1266	LINER	31	5.33	0.60	4670	6730	40.7	40.9
NGC1320	Sy 2	38	1.23	0.74	590	5480	40.0	41.0
NGC1346	SB	58	1.96	1.13	390	170	40.2	39.8
NGC1365[c]	Sy 1	23	1.85	0.45	2180	4850	40.2	40.5
NGC1667	Sy 2	65	2.33	1.26	520	2830	40.4	41.2
NGC1672	SB+Sy 2	19	0	0.37	400	290	39.2	39.1
NGC2110	Sy 2	33	2.39	0.65	3850	16170	40.7	41.3
NGC2217	LINER	23	0.26	0.45	220	360	39.1	39.4
NGC2945	LINER	66	0	1.28	60	40	39.5	39.4
NGC2974	SB+Sy 2	27	0	0.52	140	110	39.1	39.0
NGC3281	Sy 2	46	1.56	0.89	550	4240	40.1	41.0
NGC3312	LINER	41	0.44	0.80	180	330	39.6	39.8
NGC3390	SB	44	0	0.84	10	10	38.3	38.1
NGC3393	Sy 2	54	0.67	1.04	1510	14260	40.7	41.7
NGC3831	LINER	75	0	1.46	30	50	39.3	39.5
NGC3858	SB	82	0	1.59	20	20	39.2	39.3
NGC4418	SB	31	2.88	0.60	190	120	39.3	39.1
NGC4472	SB	14	0	0.27	240	...	38.7	...
NGC4507	Sy 2	51	1.54	0.98	4300	31910	41.1	42.0
NGC4593[c]	Sy 1	39	0	0.75	170	720	39.5	40.1
NGC4594	SB+Sy 2	15	0	0.28	470	310	39.1	38.9
NGC4636	LINER	13	0	0.26	120	50	38.4	38.0
NGC4691	SB	16	1.17	0.31	3420	1490	40.0	39.7
NGC4696	LINER	42	0	0.82	30	20	38.8	38.6
NGC4845	SB+Sy 2	18	3.65	0.34	1500	1700	39.7	39.8
NGC4939	Sy 2	44	0.74	0.86	650	6520	40.2	41.2
NGC4968	Sy 2	42	2.59	0.82	2060	19490	40.6	41.6
NGC4990	SB+Sy 2	45	0.66	0.88	1870	2600	40.7	40.8
NGC5128	Sy 2	8	3.79	0.15	2250	6530	39.2	39.7
NGC5135	PSB+Sy 2	59	1.46	1.14	2600	7350	41.0	41.5
NGC5252	Sy 2	98	0.54	1.91	330	1930	40.6	41.3
NGC5427	Sy 2	37	0.60	0.73	120	990	39.3	40.2
NGC5643	Sy 2	17	1.18	0.33	1850	15910	39.8	40.7
NGC5990	SB+PSB+Sy 2	55	2.70	1.06	2000	4330	40.9	41.2
NGC6328	SB+Sy 2	62	1.05	1.20	510	810	40.4	40.6
NGC6936	SB+Sy 2	84	0	1.62	60	40	39.7	39.5
NGC7172	SB+Sy 2	37	1.62	0.72	140	600	39.4	40.0
NGC7682	Sy 2	73	0.90	1.42	480	4530	40.5	41.5
PKS1306-241	SB+Sy 2	60	2.70	1.16	300	1150	40.1	40.7
PKS1521-300	SB+Sy 2	83	0.48	1.62	40	30	39.6	39.4
UGC3255	LINER	81	...	1.57	...	...	...	...

[a]Using the NED z and the Hubble law, with $H_0 = 70\,km\,s^{-1}\,Mpc^{-1}$.
[b]Diameter of aperture from which the nuclear spectrum was extracted (∼4 arcsec).
[c]Nuclear fluxes for these galaxies were measured after subtraction of H α and Hβ broad components.

3.11 Appendix: Plots of nuclear spectra

3.11.1 Seyfert 1 galaxies

Figures 3.4 to 3.6 show the decomposition of Seyfert 1 nuclear spectra into broad and narrow spectra, and are discussed in Sections 3.3.4 and 3.5.3.

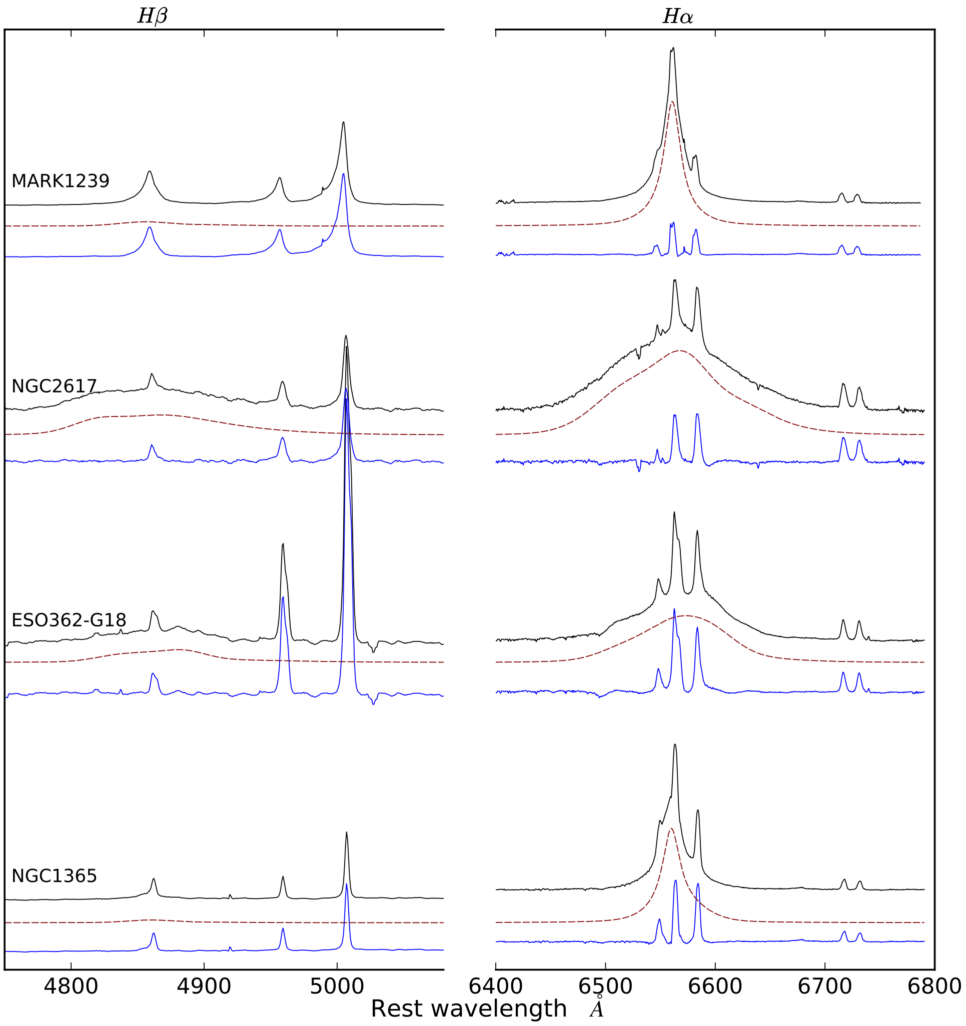

Figure 3.4 Seyfert 1 nuclear spectra showing the decomposition into 'broad' and 'narrow' spectra. Figures 3.4 to 3.6 show the nuclear spectra for the 14 galaxies for which broad-component subtraction was used before fitting the narrow lines (Section 3.3.4). Galaxies are ordered by RA across figures and bottom-to-top in each figure. The decomposition into a 'broad' and 'narrow' spectrum was performed for each relevant spaxel independently; for each galaxy the nuclear spectra shown here were found by summing over the nuclear spaxels that had broad-component subtraction. The left panel shows the Hβ and [OIII] $\lambda\lambda\,4959, 5007$ emission lines, and the right panel shows the H$\,\alpha$ line with the [NII] $\lambda\lambda\,6548, 6583$ lines on either side. The topmost black line shows the total spectrum, the dotted maroon line shows the fitted Balmer line broad spectrum, and the solid blue line shows the narrow-line spectrum remaining after the fitted broad spectrum was subtracted.

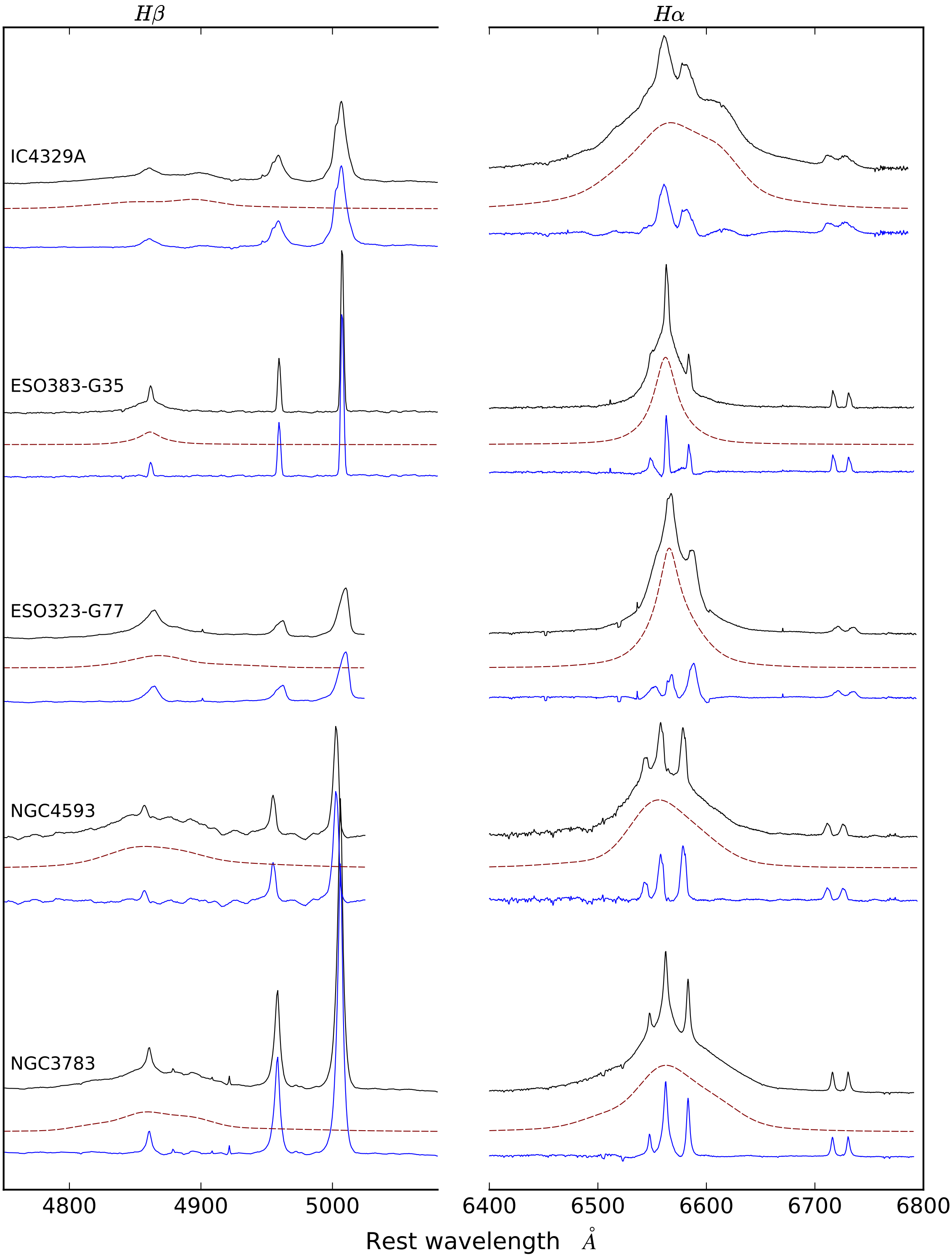

Figure 3.5 As in Figure 3.4

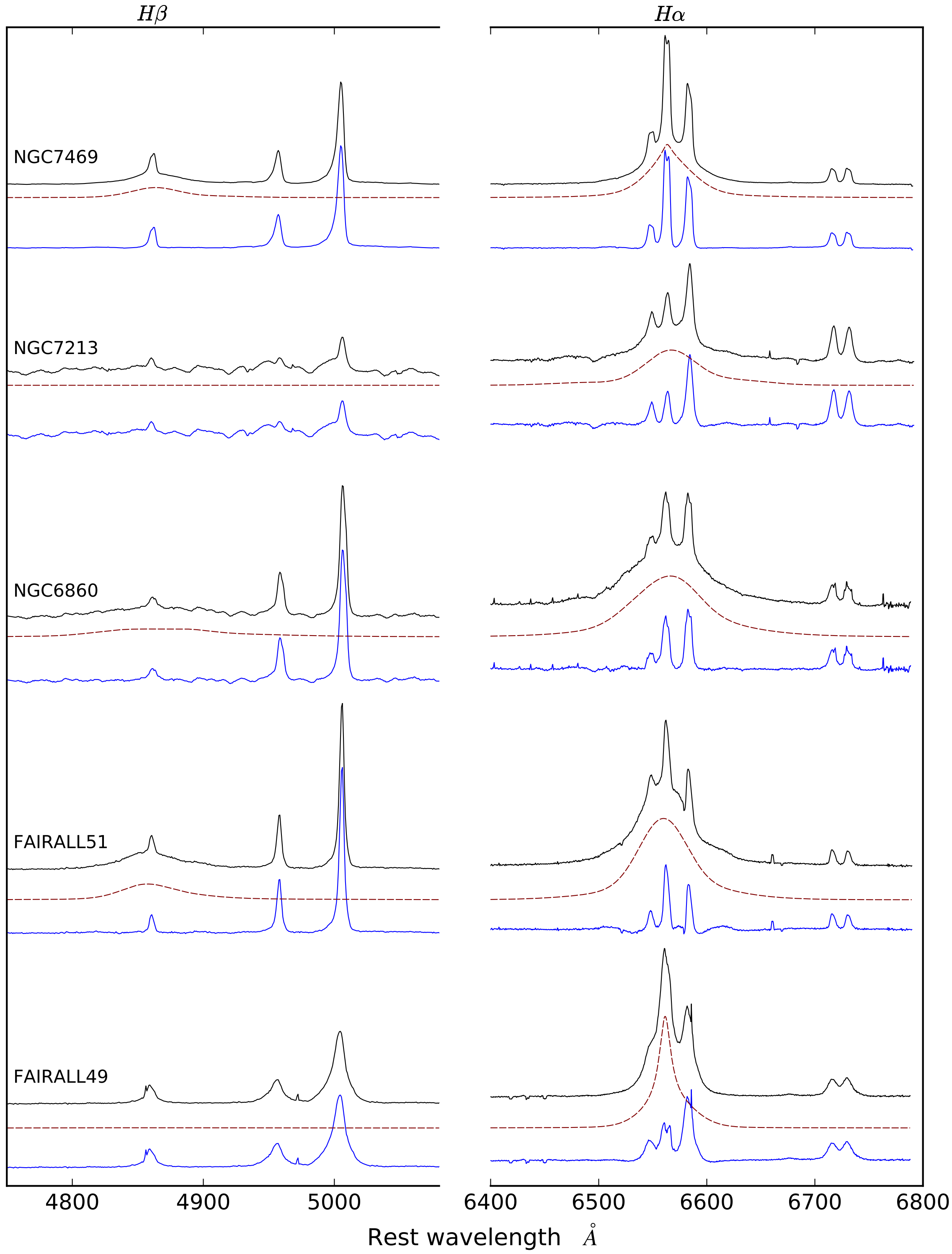

Figure 3.6 As in Figure 3.4

3.11.2 Other galaxies

Figure 3.7 shows nuclear spectra of several galaxies selected from the new observations. The spectra are discussed in Section 3.5.3.

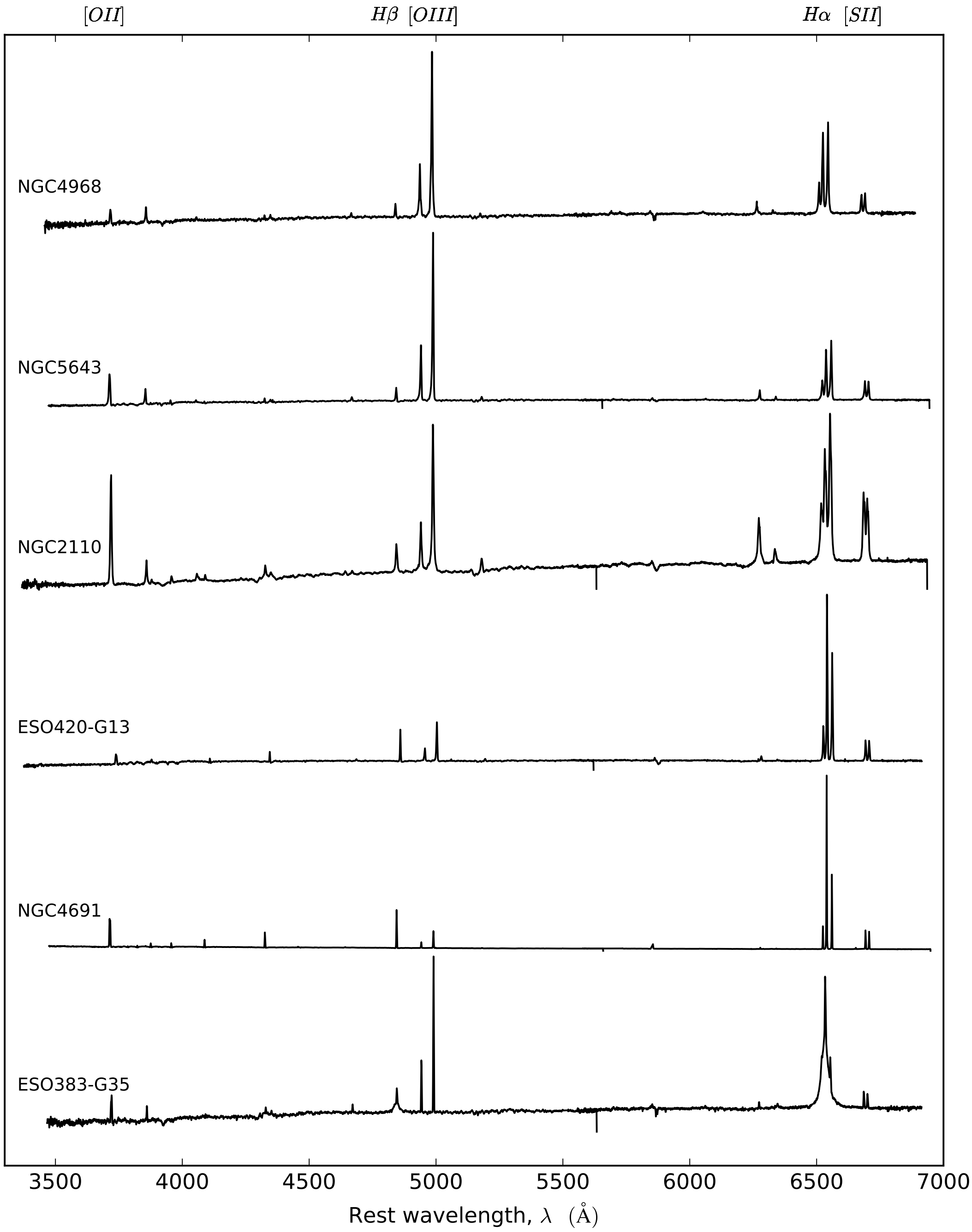

Figure 3.7 Nuclear spectra for a selection of six galaxies from the new S7 observations. From top to bottom: NGC 4968, NGC 5643 and NGC 2110 are Seyfert 2 galaxies, ESO 420-G13 is a 'composite' (AGN/star forming) galaxy, NGC 4691 is star-forming (not an AGN), and ESO 383-G35 is a Seyfert 1 with weak coronal emission.

3.12 Appendix: Maps of gas excitation and kinematics

Images showing gas excitation and kinematics for each galaxy in the S7 sample are presented in the following figures. The figures are discussed in Section 3.6.

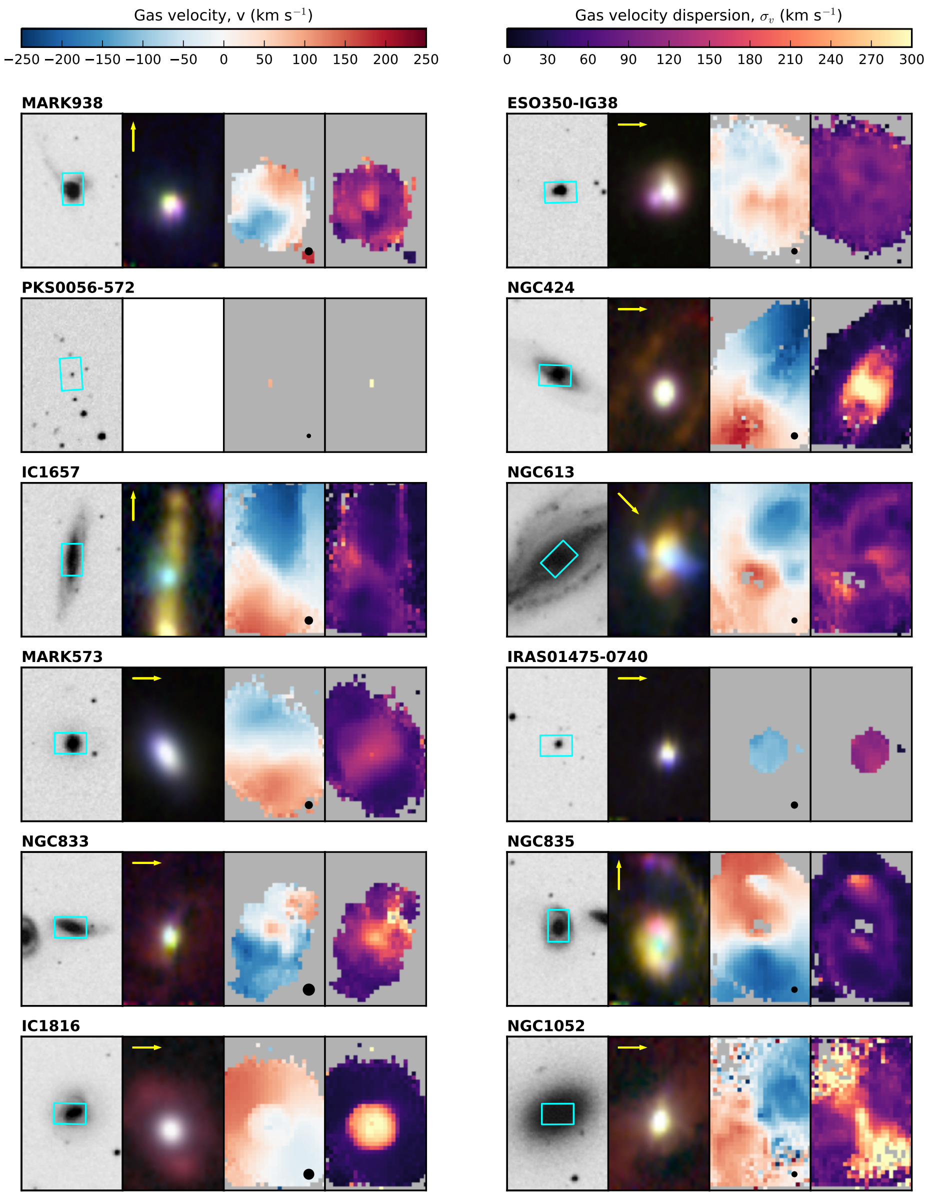

Figure 3.8 Maps for S7 galaxies with RAs between 00^h00^m and 02^h42^m. Galaxies are ordered by RA across rows and then down columns in Figures 3.8 to 3.18. For each galaxy, from left to right: A DSS2 r-band image showing the field of view of the S7 WiFeS observations, a three-color image showing the degree of ionization of the gas, and maps of the emission-line gas velocity and velocity dispersion for the single-component LZIFU fits. Figures 3.8 to 3.18 are further described in Section 3.6.

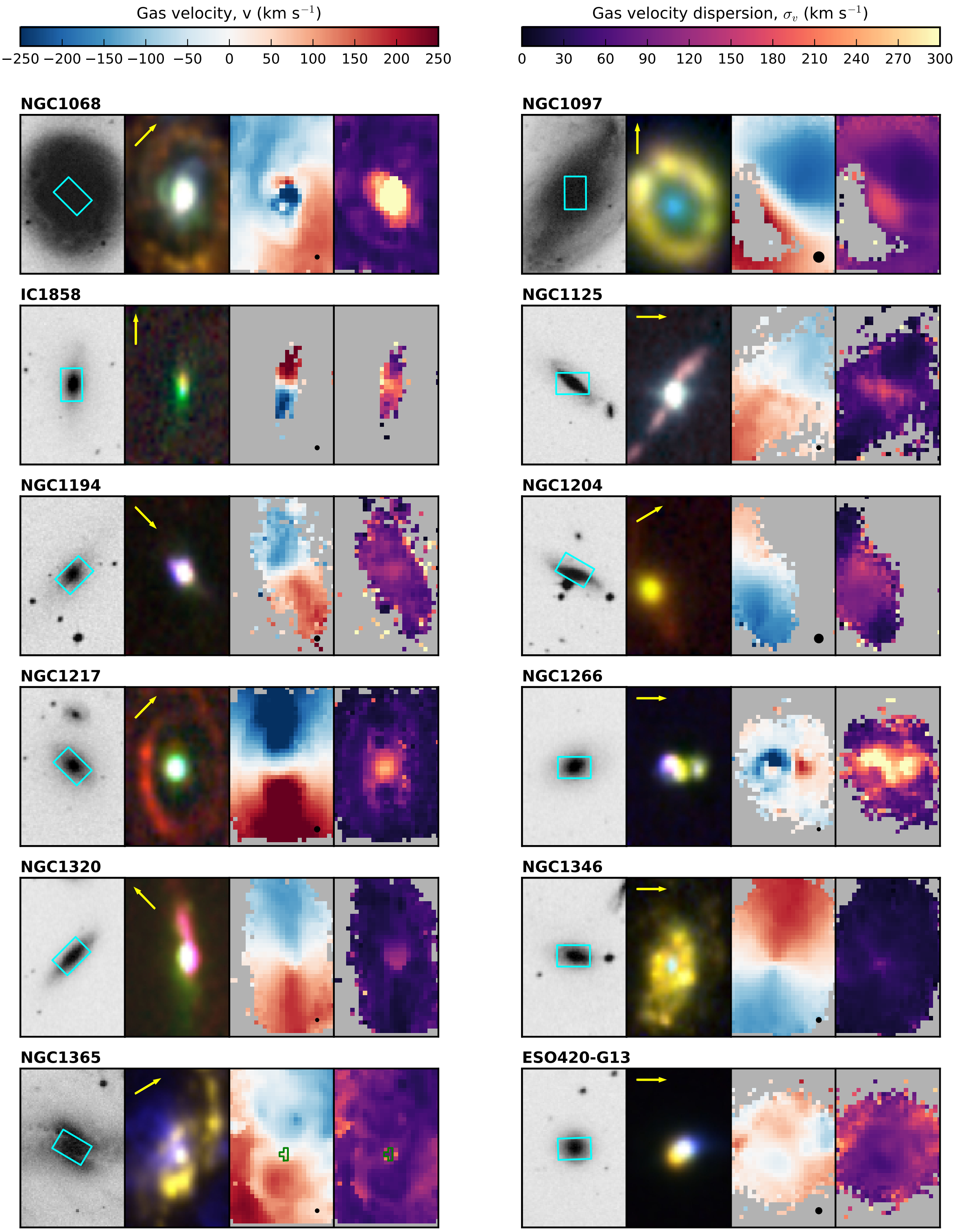

Figure 3.9 As in Figure 3.8, for galaxies with RAs between 02^h42^m and 04^h16^m.

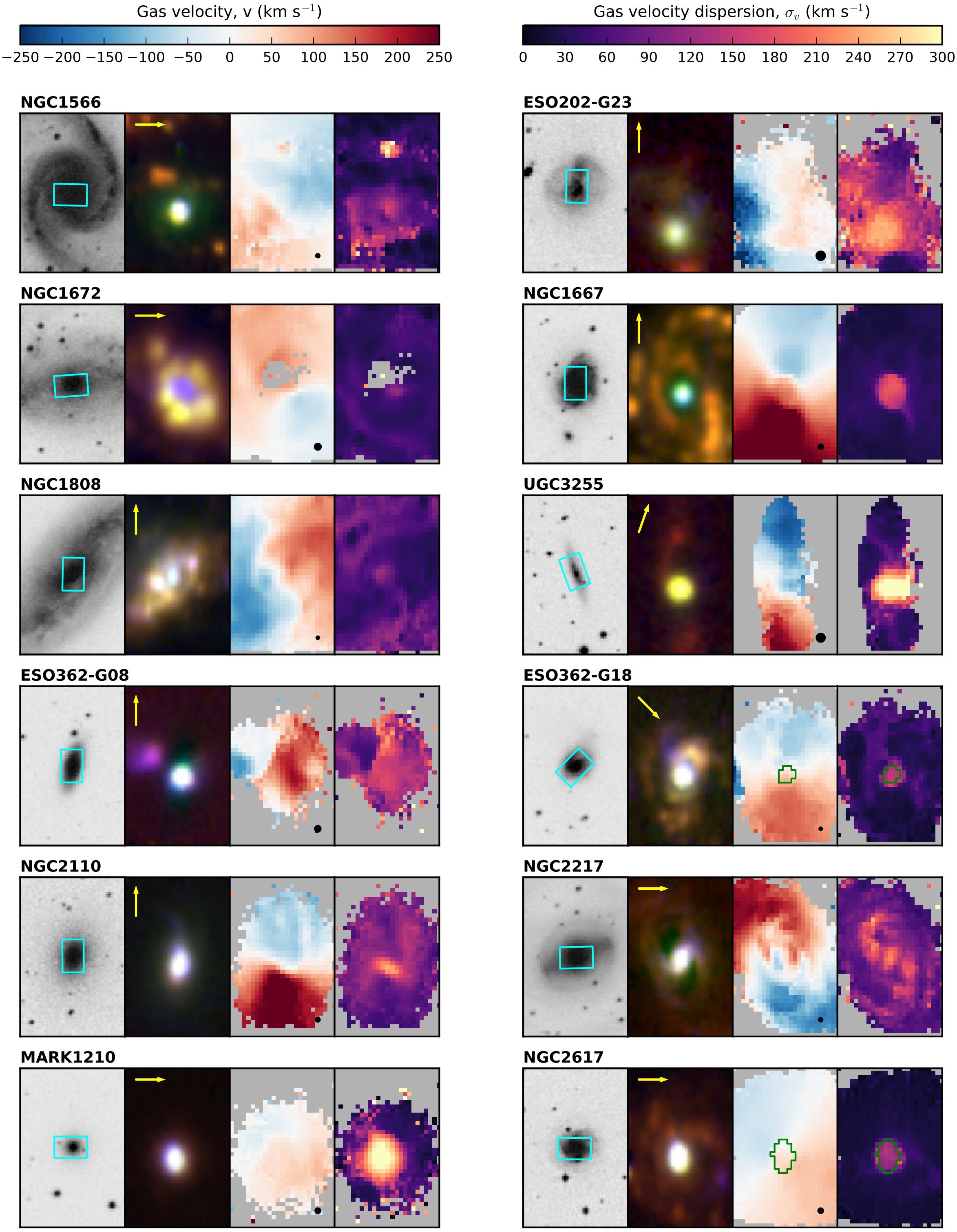

Figure 3.10 As in Figure 3.8, for galaxies with RAs between $04^{h}16^{m}$ and $09^{h}00^{m}$.

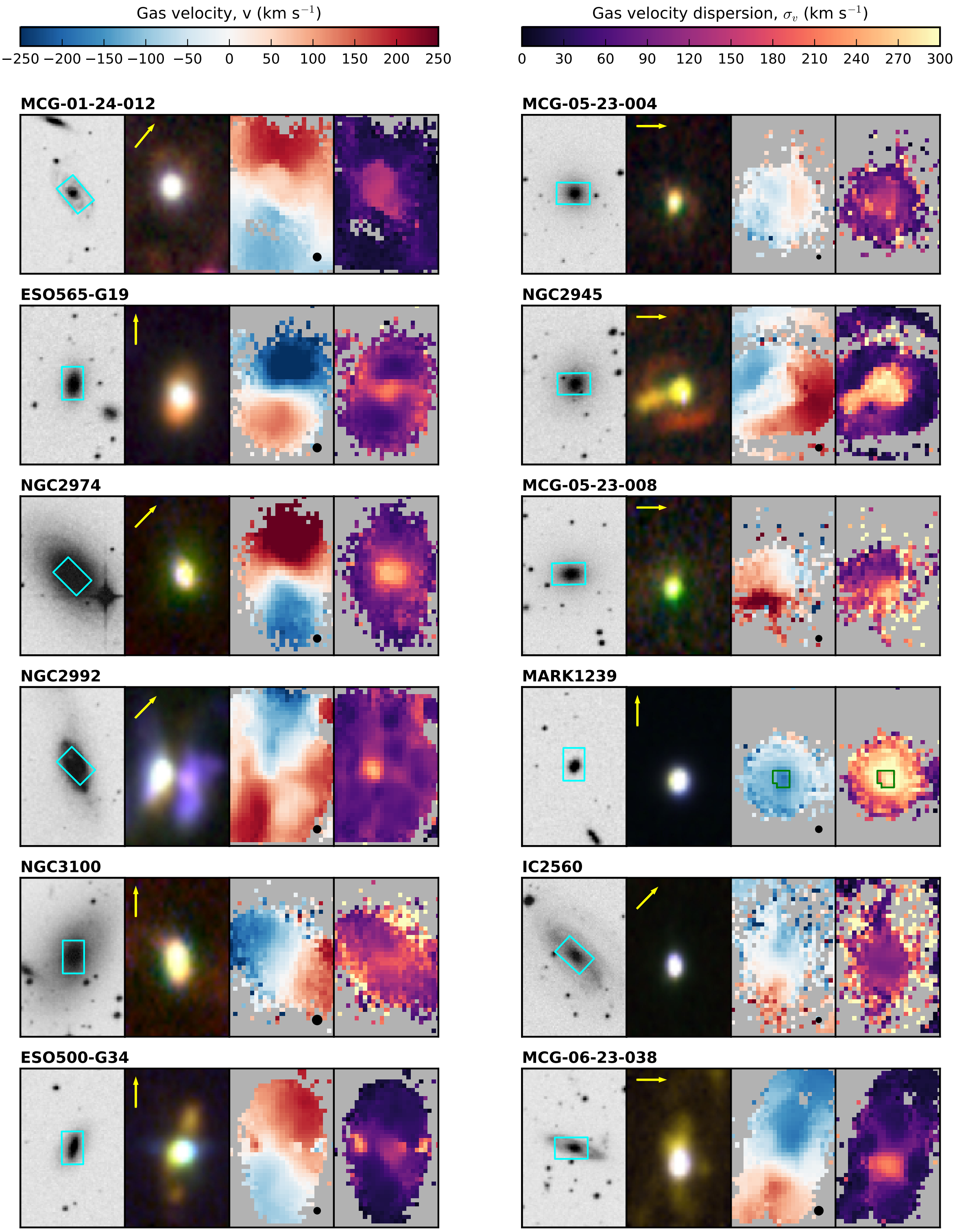

Figure 3.11 As in Figure 3.8, for galaxies with RAs between $09^{h}00^{m}$ and $10^{h}30^{m}$.

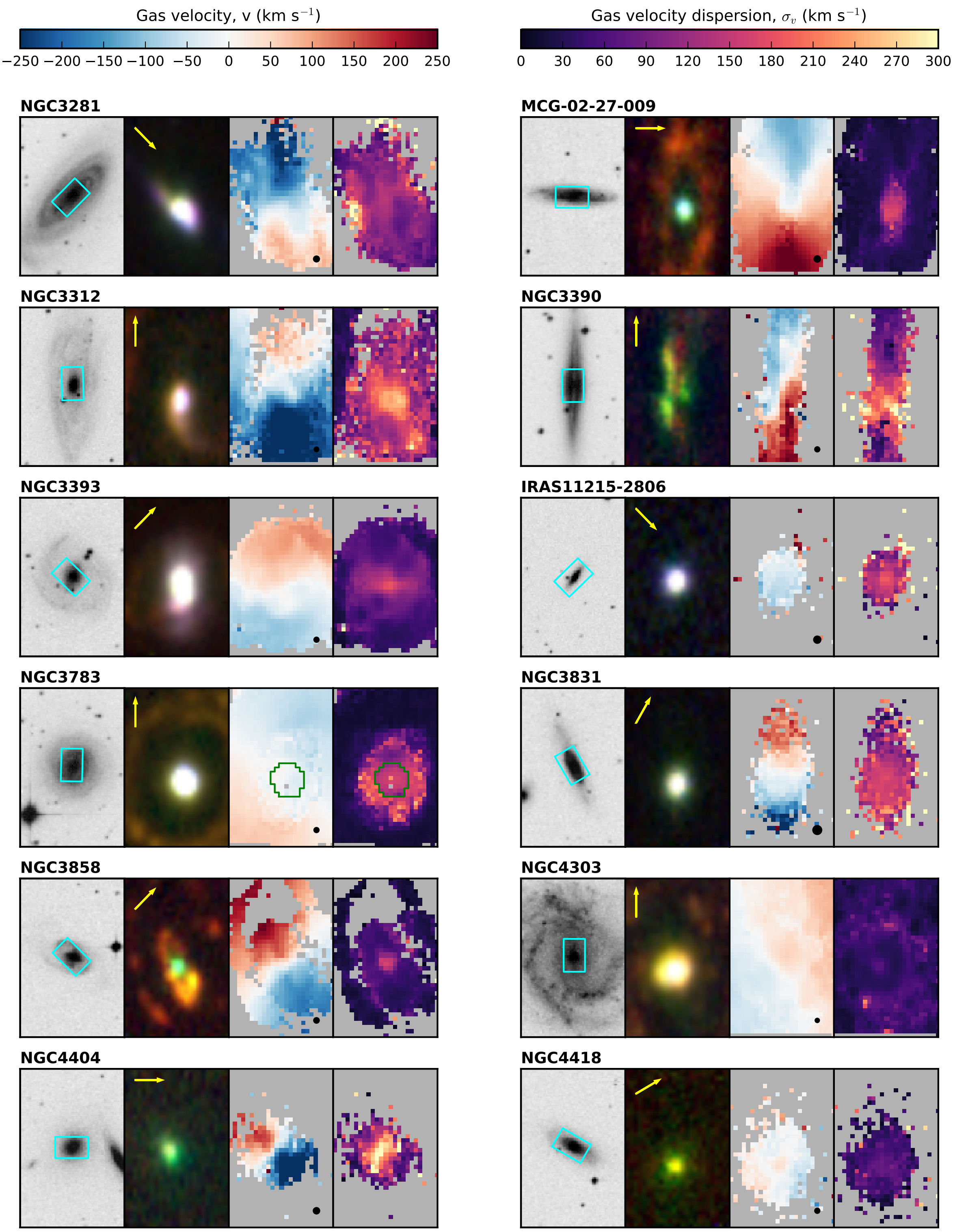

Figure 3.12 As in Figure 3.8, for galaxies with RAs between 10^h30^m and 12^h28^m.

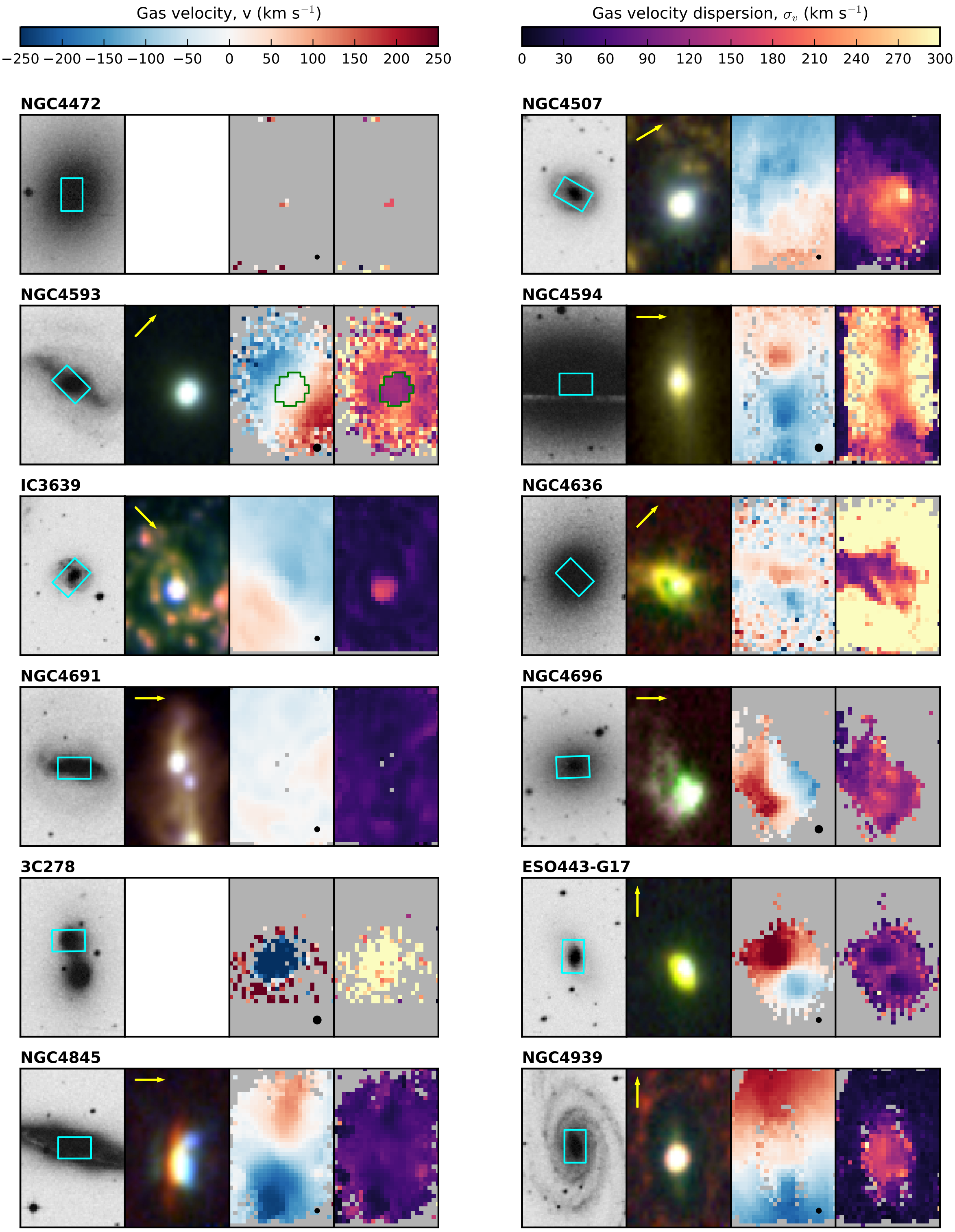

Figure 3.13 As in Figure 3.8, for galaxies with RAs between 12^h28^m and 13^h05^m.

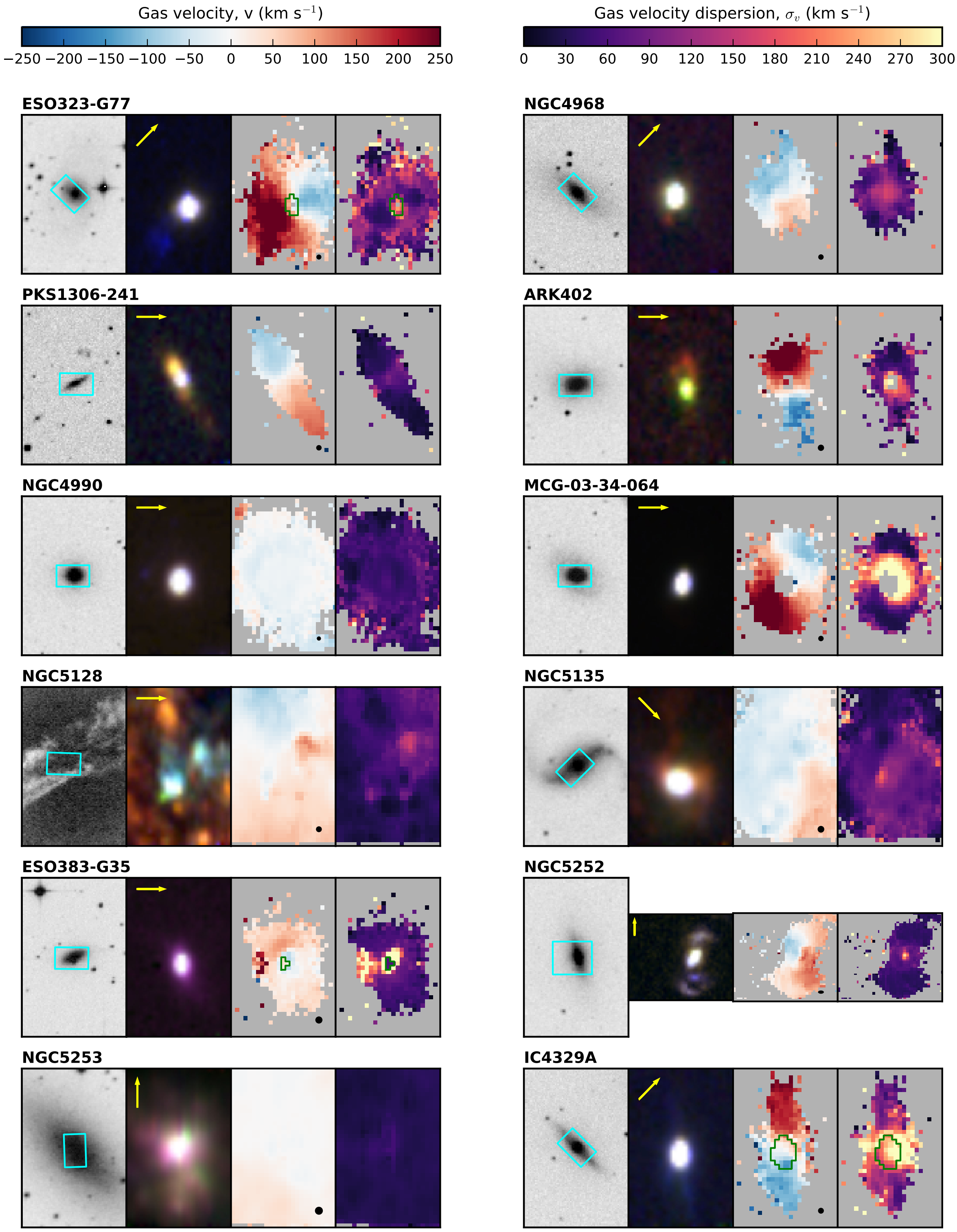

Figure 3.14 As in Figure 3.8, for galaxies with RAs between 13^{h}05^{m} and 14^{h}00^{m}.

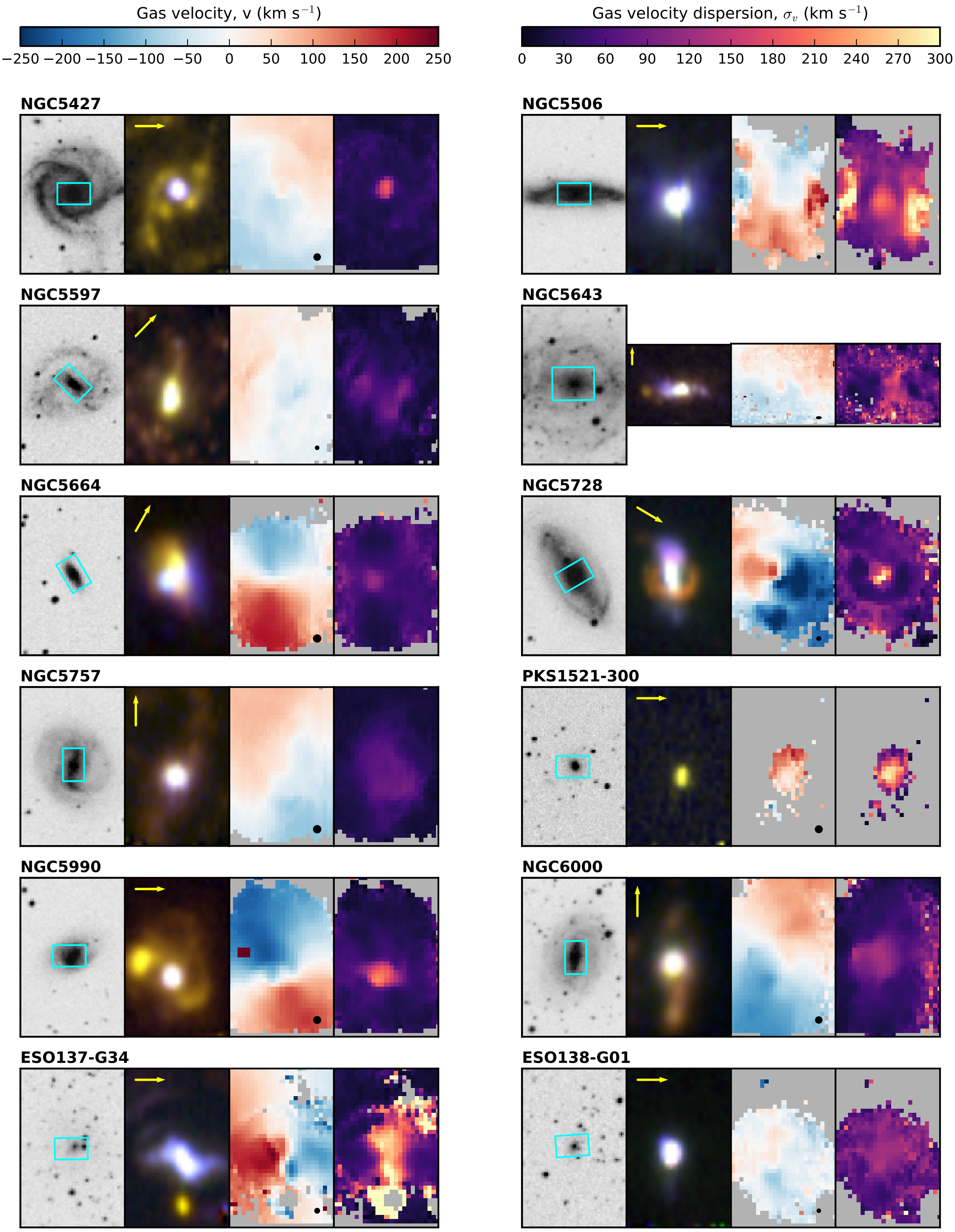

Figure 3.15 As in Figure 3.8, for galaxies with RAs between $14^{h}00^{m}$ and $16^{h}52^{m}$.

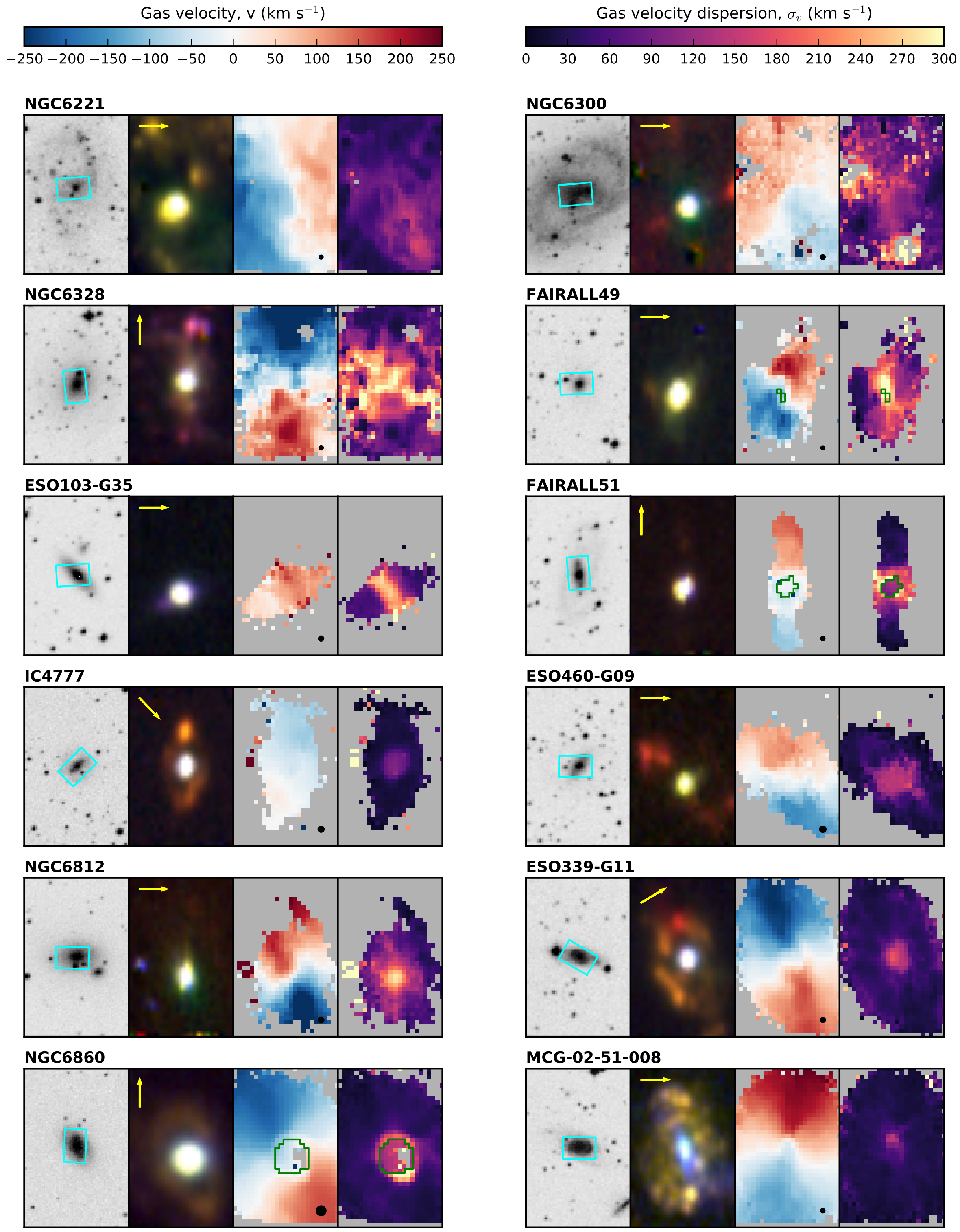

Figure 3.16 As in Figure 3.8, for galaxies with RAs between 16^h52^m and 20^h18^m.

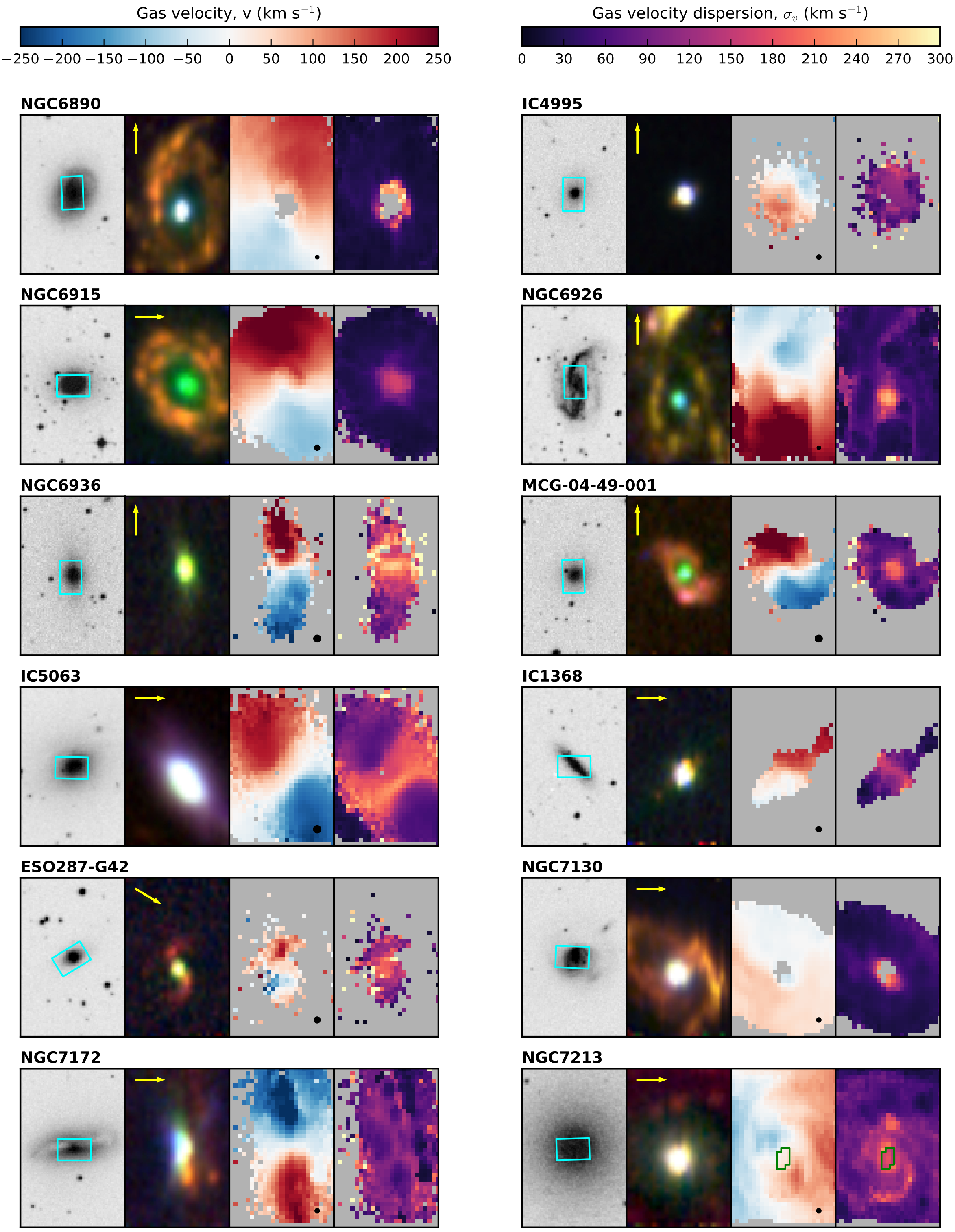

Figure 3.17 As in Figure 3.8, for galaxies with RAs between $20^{h}18^{m}$ and $22^{h}10^{m}$.

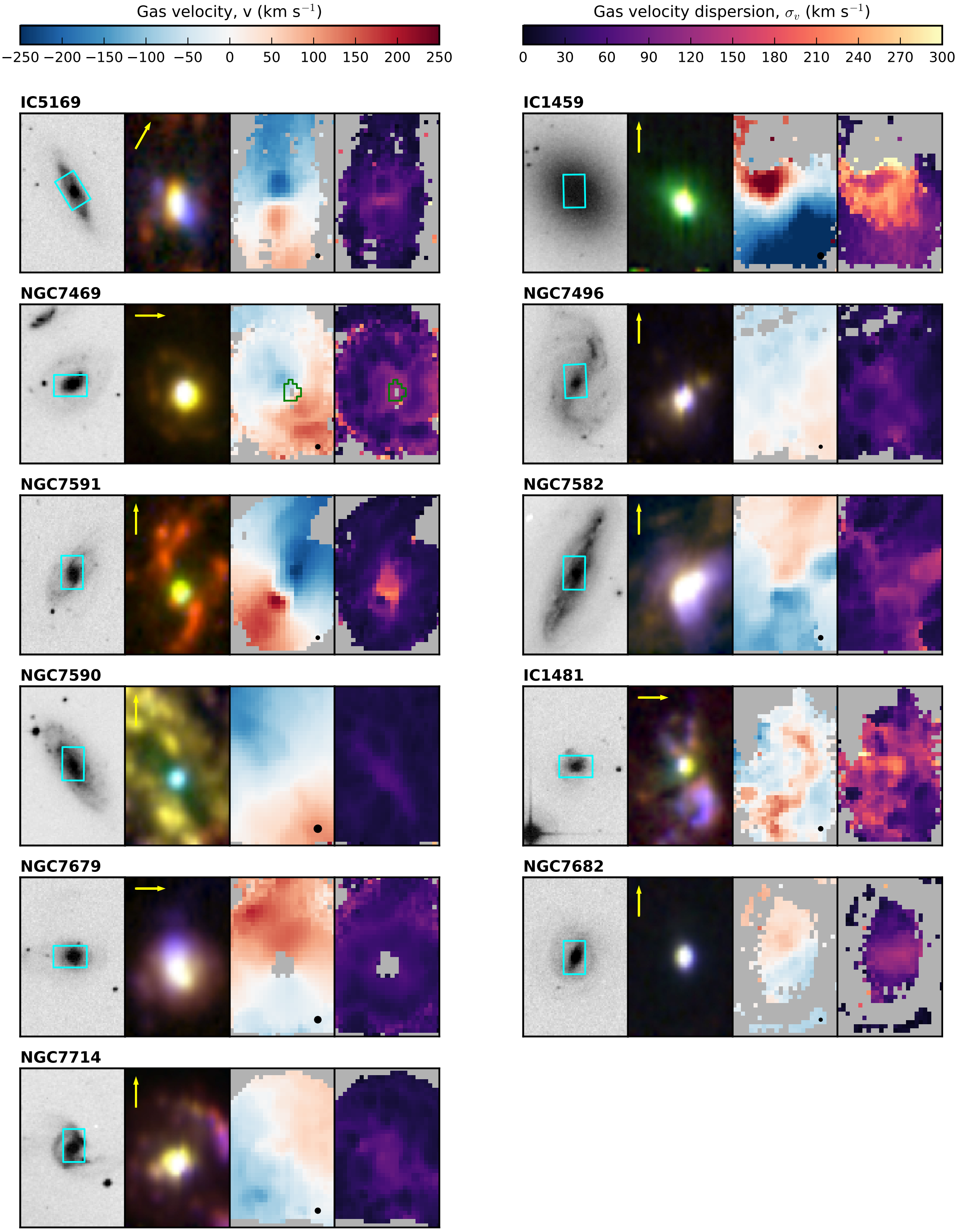

Figure 3.18 As in Figure 3.8, for galaxies with RAs between 22^h10^m and 23^h59^m.

4

A spatially resolved analysis of four Seyfert galaxies

This chapter presents the content of the article *Interrogating Seyferts with NebulaBayes: Spatially probing the narrow-line region radiation fields and chemical abundances* (Thomas et al. 2018). The abstract is as follows:

> NebulaBayes is a new Bayesian code that implements a general method of comparing observed emission-line fluxes to photoionization model grids. The code enables us to extract robust, spatially resolved measurements of abundances in the extended narrow line regions (ENLRs) produced by Active Galactic Nuclei (AGN). We observe near-constant ionization parameters but steeply radially-declining pressures, which together imply that radiation pressure regulates the ENLR density structure on large scales. Our sample includes four 'pure Seyfert' galaxies from the S7 survey that have extensive ENLRs. NGC 2992 shows steep metallicity gradients from the nucleus into the ionization cones. An *inverse* metallicity gradient is observed in ESO 138-G01, which we attribute to a recent gas inflow or minor merger. A uniformly high metallicity and

hard ionizing continuum are inferred across the ENLR of Mrk 573. Our analysis of IC 5063 is likely affected by contamination from shock excitation, which appears to soften the inferred ionizing spectrum. The peak of the ionizing continuum E_{peak} is determined by the nuclear spectrum and the absorbing column between the nucleus and the ionized nebula. We cannot separate variation in this intrinsic E_{peak} from the effects of shock or H II region contamination, but E_{peak} measurements nevertheless give insights into ENLR excitation. We demonstrate the general applicability of NebulaBayes by analyzing a nuclear spectrum from the non-active galaxy NGC 4691 using a H II region grid. The NLR and H II region model grids are provided with NebulaBayes for use by the astronomical community.

Mike Dopita made the excitation maps in the second panel for each galaxy in Figure 4.3. I otherwise authored this chapter and am the sole author of the code NebulaBayes, although its core is heavily based on the approach used by Guillermo Blanc in the code IZI (Blanc et al. 2015).

4.1 Introduction

The impact of active galactic nuclei (AGN) on the evolution of their host galaxies has received considerable attention in the literature over the previous two to three decades (for reviews see e.g. Kormendy & Ho 2013; King & Pounds 2015; Wagner et al. 2016). However, many questions remain regarding the impacts of the 'radiative' (or 'quasar') mode and the 'radio' mode of nuclear activity. Challenges lie firstly in understanding the physical processes by which the radiative and mechanical energy released by accretion couples to the interstellar medium (ISM), and secondly in connecting the resulting outflows, extended narrow line regions (ENLRs), expanding radio lobes, and related phenomena to the concrete mechanisms by which they influence the ISM and hence star formation in the host.

Advancing our understanding of these phenomena requires measuring the physical properties of the ISM. A variety of integral field spectrographs are now routinely used to study active nuclei with high spatial and spectral resolution (e.g. Storchi-Bergmann et al. 2010; Müller-Sánchez et al. 2011; Cresci et al. 2015; Smajić et al. 2015; Dopita et al. 2015), but we currently lack the tools to fully interpret how the

AGN influences the surrounding ISM.

For example, the determination of gas-phase abundances in AGN has received comparably less attention than abundance measurements in H II regions. It is often broad line region (BLR) abundances which are investigated when AGN abundances have been considered (quasar BLR abundances have been studied for decades, e.g. Davidson & Netzer 1979). Work by Dietrich et al. (2003), Nagao et al. (2006a), Juarez et al. (2009) and others on the nebular metallicity of quasar BLRs has shown that there is little evolution of BLR metallicity as a function of redshift, with generally high metallicities observed even for quasars at $z \sim 6$. Nagao et al. (2006a) find that more luminous quasars tend to have a higher metallicity.

Quasar NLR abundances have also been studied. Nagao et al. (2006b) compared NLR quasar rest-frame ultraviolet emission to photoionization models, finding a lack of metallicity evolution and a correlation between luminosity and metallicity, as is the case for BLRs. Dors et al. (2014) present a metallicity indicator for AGN NLRs using UV lines, and apply the diagnostic to high-redshift quasars. Du et al. (2014) studied the relationship between BLR and NLR metallicities, finding that abundances in the different regions are correlated.

The abundances in the Seyfert nuclei of local star-forming galaxies may be estimated using radial abundance gradients. Two Seyfert NLR abundance calibrations were developed by Storchi-Bergmann et al. (1998) by comparing photoionization model predictions to nuclear abundances extrapolated from measured H II region abundances in seven Seyfert galaxies. Likewise, Dopita et al. (2014) used H II region abundances extrapolated to the nucleus to calculate the gas-phase metallicity of the Seyfert nucleus in the galaxy NGC 5427.

An overview of broad emission line, broad absorption line, and narrow absorption line abundance diagnostics for QSOs is provided by Hamann & Ferland (1999). A review of the smaller selection of diagnostics available for NLR abundances is provided by Dors et al. (2015).

Work on measuring NLR abundances is continuing. A new diagnostic based on the N2O2 index was developed by Castro et al. (2017). The authors vary metallicity and ionization parameter in their photoionization model grids, but do not consider variations in the nebular pressure or the ionizing spectrum. Dors et al. (2017) measure N and O abundances in nearby Seyfert NLRs, finding the variation of N/O with O/H to be consistent with H II regions.

Despite the recent progress, measurements of NLR abundances remain less routine than is the case for H II-region measurements. An example of the ongoing challenges in measuring NLR abundances is the recent work of Kawasaki et al. (2017), who investigated using optical diagnostic diagrams to identify low-metallicity AGN, but did not attempt to measure the metallicity of the objects in their sample.

The historical difficulty in reliably and systematically measuring chemical abundances in active galaxies is a major hindrance to understanding how an AGN may influence the distribution of metals in its host. In particular, the chemical abundance set, the spectral shape of the ionizing radiation field, the ionization parameter and the gas pressure all affect the optical narrow-line emission signatures of AGN (e.g. Groves et al. 2004). In this work we present a grid of photoionization models and analysis code that for the first time is able to measure AGN metallicity while taking into account (and simultaneously measuring) the ionization parameter, pressure, and the hardness of the ionizing continuum.

The shape of the ionizing continuum is a very interesting property in its own right, because this most important part of the SED in the extreme ultraviolet (EUV) is impossible to directly observe, and because knowledge of the ionizing spectrum is essential in order to understand the effects of radiative mode AGN on surrounding gas. To date it has not been possible to make robust and systematic measurements of the ionizing radiation field. The radiative hardness may be inferred indirectly using emission-line ratios (e.g. Krolik & Kallman 1988; Dietrich et al. 2005; Kraemer et al. 2008; Dopita et al. 2014), an approach that we take here in our comparison of emission line fluxes to photoionization models.

The ionization parameter is also an interesting quantity in ENLRs, because the spatial distribution of the ionization parameter gives insights into the effects of a radiative mode AGN on the density structure of the ISM. The interplay between radiation pressure and gas pressure regulates the structure of individual NLR clouds (e.g. Dopita et al. 2002) and the NLR on large scales (e.g. Stern et al. 2014). Recently Davies et al. (2016) studied four Seyfert galaxies with integral field spectroscopy and inferred high, spatially-uniform ionization parameters in the nuclear regions of two objects, arguing that in these regions radiation pressure dominates over gas pressure.

We additionally measure the ISM pressure in ENLRs, although our results are the least sensitive to pressure amongst the four parameters we consider. The pressure is nevertheless also vital to understanding AGN feedback – calculations of mass loading and hence energy in outflows are sensitive to the ISM density, which is primarily determined by the pressure (e.g. Müller-Sánchez et al. 2011; Kakkad et al. 2016).

The advances we present here are possible through the use of a Bayesian analysis technique, which allows us to efficiently constrain four parameters simultaneously when comparing observations to a grid of photoionization models. We present a new code, NebulaBayes[1], that is heavily inspired by the code IZI (Blanc et al. 2015) and generalizes its capabilities. The new code is agnostic to the parameters of the input photoionization model grid, and works with an arbitrary number of dimensions – limited only by calculation time and available memory for the interpolated n-dimensional emission-line flux grids. We hope that NebulaBayes will help to solve some of the problems discussed above by providing a general and comprehensive means of comparing emission-line fluxes to theory.

We use NebulaBayes to study IFU data from the *Siding Spring Southern Seyfert Spectroscopic Snapshot Survey* (S7). We analyse a sample of Seyfert galaxies with ENLRs covering a substantial portion of the field of view: ESO 138-G01, IC 5063, Mrk 573, and NGC 2992, as well as a normal star-forming galaxy, NGC 4691.

In the following section (Section 4.2) we present the background and theory behind the NebulaBayes code. In Section 4.3 we describe our NLR and H II region photoionization model grids, and in Section 4.4 we describe the S7 survey, the sample selection and the processing of the observational data. Section 4.5 contains details of how NebulaBayes was applied to the data. The results are presented and discussed in Section 4.6, with some additional discussion in Section 4.7. Our conclusions are listed in Section 4.8.

4.2 Bayesian analysis method

4.2.1 Background

Physical parameters such as metallicity have traditionally been measured from emission line data using specific diagnostics. Example metallicity diagnostics include $R23$ (Pagel et al. 1979; Pilyugin & Thuan 2005), N2O2 (Kewley & Dopita 2002) and N2 (Denicoló et al. 2002; Pettini & Pagel 2004) among many others; a summary of the calibration methods and diagnostics is provided in the introduction of Blanc et al. (2015). The diagnostics are each individually calibrated and use a small number

[1]NebulaBayes is publicly available; see the Appendix for more information

of observed emission line fluxes, so cannot take advantage of additional line fluxes when they are available. The individual diagnostics have historically been heavily favored over techniques that allow for general comparisons between observations and theory.

A means of improving this situation using Bayesian inference was presented by Blanc et al. (2015) with the IDL code IZI. This code simultaneously constrains the ionization parameter and metallicity when provided with any set of observed H II region (or star-forming galaxy) emission-line fluxes and corresponding uncertainties. The calculations in IZI use 2D arrays (with dimensions corresponding to metallicity and ionization parameter) to examine the relative probability of different models over a large parameter space.

The Bayesian inference method compares observations with theory *directly*, so the parameter constraints are conceptually similar to the results of simultaneously calibrating and applying bespoke diagnostics. A set of observed emission line fluxes is compared to a general grid of photoionization models using a technique that is agnostic to the parameters of interest and constrains the parameters in a systematic, general and mathematically clear manner. The maximum possible amount of information may be included – all observed emission line fluxes with their errors and any quantified pre-existing knowledge (i.e. priors) are propagated into the final parameter estimates and uncertainties.

A joint probability density function (PDF) resulting from a Bayesian analysis can be visually and quantitatively interrogated across the parameter space to determine constraints, uncertainties and correlations. Underlying degeneracies and pathological behavior may be revealed by inspecting likelihood PDFs. Priors may then be applied to select and further constrain solutions using knowledge of the physical system.

A Bayesian analysis requires calculating the posterior PDF (described in the following section). Algorithmic sampling methods such as those involving Markov Chain Monte Carlo (MCMC) are commonly used to build up a picture of the posterior PDF using a step-by-step probabilistic exploration of the parameter space. Unfortunately a comparison of emission-line fluxes to predictions using a sampling approach would require running a photoionization model for each visited point in the parameter space. The run-time of a single typical photoionization model (on the order of one to a few minutes) is too long for this approach to be desirable, considering that the data from the model runs could not be reused in general, and that modern instruments may produce many hundreds of spectra in a single observation.

However, IZI uses an approach that is able to compare observed emission-line fluxes to predictions using Bayesian inference without requiring a full run of a sampling algorithm for each spectrum. The method uses a pre-calculated (hence re-usable) grid of photoionization model predictions. The relative probability of a set of parameters describing the observed nebula is directly calculated by comparing the observed fluxes to predicted fluxes found by interpolating between the model grid points. The probability is calculated across the entire parameter space, to produce an n-dimensional joint PDF. This is a 'brute force' approach to Bayesian inference that involves manipulation of arrays representing the entire parameter space, so is only applicable when the parameter space has low dimensionality.

Another recent work applying a similar approach is that of Vale Asari et al. (2016). With their code BOND the authors use three-dimensional grids with parameters for the abundance ratios O/H and N/O, as well as the ionization parameter. A related strategy is used by Pérez-Montero (2014) in the code HII-CHI-MISTRY, which determines parameter values by weighting models in a grid by the reciprocal of the χ^2. Bianco et al. (2016) take a less similar approach in their code PyMCZ, measuring nebular oxygen abundances using specific calibrators and using Monte Carlo sampling to estimate the errors.

Our new code NebulaBayes generalizes the methods used in IZI and BOND, providing parameter estimates and statistical errors from observed line fluxes. A first analysis of ENLR spectra with NebulaBayes was performed by Merluzzi et al. (2018); the inferred parameters were consistent with the results produced by a more detailed analysis with tailored photoionization models. The NebulaBayes software is described in detail in the following section and in the Appendix.

4.2.2 Theory

We use Bayesian parameter estimation to determine the probability of model parameter values given observed data. In this section we follow Section 2 of Blanc et al. (2015).

At the heart of the method is Bayes' theorem, which is readily derived using basic probability theory and reads as follows:

$$p(\boldsymbol{\theta}|D, M') = \frac{p(\boldsymbol{\theta}|M')\, p(D|M', \boldsymbol{\theta})}{p(D|M')}. \tag{4.1}$$

The quantity $p(\boldsymbol{\theta}|D, M')$ is the 'posterior' and is the probability of a particular set of model parameter values $\boldsymbol{\theta}$ being 'true' given the available observed data D and a model M'. We want to evaluate the posterior for many sets of values $\boldsymbol{\theta}$ in order to draw conclusions about the physical system that gave rise to the observed data. The quantity $p(D|M', \boldsymbol{\theta})$ is the hypothetical 'likelihood' of the observed data given the model M' and the values of the parameters $\boldsymbol{\theta}$. The 'prior' $p(\boldsymbol{\theta}|M')$ is assigned carefully by hand and describes the probability of the parameter values considering the model and all previously known information. The normalization $p(D|M')$ is found by normalizing the posterior and is unimportant in parameter estimation problems.

We assume that emission line measurements follow a Gaussian distribution centered at the 'true' value. Let f_i be an emission-line flux measurement (for line i), e_i the associated measurement error, M' a particular model with a set of model parameter values $\boldsymbol{\theta}$, and $f_i'(\boldsymbol{\theta})$ the predicted emission-line flux associated with the values $\boldsymbol{\theta}$. Then the probability of measuring a particular value of f_i given the assumed model M' and $\boldsymbol{\theta}$ is

$$p(f_i|M', \boldsymbol{\theta}) \propto \frac{1}{e_i} \exp\left[-\frac{(f_i - f_i'(\boldsymbol{\theta}))^2}{2e_i^2}\right]. \tag{4.2}$$

Equation 4.2 assumes that $f_i'(\boldsymbol{\theta})$ is a perfect model prediction based on the input parameters. In reality the calculation of predictions from a set of parameters $\boldsymbol{\theta}$ uses physical simulations and hence is associated with inherent uncertainty. Following Blanc et al. (2015), we make an attempt to account for the modelling uncertainty by including systematic errors with the predictions. The measurement errors and systematic model errors are independent, so we simply sum the variances to give a total variance $V_i = e_i^2 + \epsilon^2 f_i'(\boldsymbol{\theta})^2$ where ϵ is the estimated uniform fractional systematic error in the model predictions. This produces an appropriately broader Gaussian distribution:

$$p(f_i|M', \boldsymbol{\theta}) \propto \frac{1}{\sqrt{V_i}} \exp\left[-\frac{(f_i - f_i'(\boldsymbol{\theta}))^2}{2V_i}\right], \tag{4.3}$$

In the case of an upper bound on the observed line flux, we assume that only e_i is supplied, because $f_i < e_i$ and the f_i measurement was discarded. In this case we are interested in the probability of measuring $f_i < e_i$, assuming that $f_i'(\boldsymbol{\theta})$ is the true flux:

$$p(f_i < e_i | M', \boldsymbol{\theta}) = A \frac{1}{\sqrt{V_i}} \int_0^{e_i} \exp\left[-\frac{(f_i - f_i'(\boldsymbol{\theta}))^2}{2V_i} \right] \mathrm{d}f_i \qquad (4.4)$$

for a constant A. Substituting $t = (f_i - f_i'(\boldsymbol{\theta}))/\sqrt{2V_i}$ and using the definition of the error function $\mathrm{erf}(x) = 2\,\pi^{-0.5} \int_0^x e^{-t^2} \mathrm{d}t$, we obtain

$$p(f_i < e_i | M', \boldsymbol{\theta}) = B \left[\mathrm{erf}\left[\frac{f_i'(\boldsymbol{\theta})}{\sqrt{2V_i}} \right] - \mathrm{erf}\left[\frac{f_i'(\boldsymbol{\theta}) - e_i}{\sqrt{2V_i}} \right] \right] \qquad (4.5)$$

for a constant B.

The likelihood, which is the PDF describing the probability of obtaining the emission line measurements given the assumed model and set of parameter values, is

$$p(D | M', \boldsymbol{\theta}) \propto \prod_{i=1}^{m} p_i \qquad (4.6)$$

where there are m measured emission lines, the data D is the full set of measured emission line fluxes and errors $\{f_i, e_i\}$ (with zero or more 'upper bound' measurements for which f_i is excluded), and the contribution of a single line p_i is of the form given in either Equation 4.3 or Equation 4.5.

In Equation 4.6 it is assumed that the p_i contributions are independent. In practice this is not the case, with correlations expected to arise between the p_i because the line fluxes are all normalized to a reference line (Hβ in this work), and because of systematic issues such us uncertainties in reddening corrections.

Much of the constraining power of emission-line observations comes from specific sensitive flux ratios. Hence a treatment in which we compare all possible ratios to predictions might be expected to constrain the parameter space more effectively than using individual line fluxes as the data points. However the expressions above would need to be much more complicated in this case, because the error distributions on the ratios would not in general be close to Gaussian, and the likelihood contributions of the ratios would not be close to independent (each flux would appear in multiple ratios), so Equation 4.6 would need to account for correlations. Nevertheless we are able to take advantage of the constraining power of specific line ratios by using them in priors (described in the Appendix).

The code NebulaBayes calculates the likelihood PDF of Equation 4.6 over the whole parameter space covered by the photoionization models. The likelihood is then multiplied by a prior chosen by the user (also calculated over the entire parameter space), to produce the full n-dimensional joint posterior PDF as per Equation 4.1.

We note that emission lines are weighted equally in Equation 4.6. Given a photoionization model grid, a user of NebulaBayes may make only a small number of choices which are able to modify the results:

1. The choice of the prior
2. The choice of the set of observed emission-lines to use
3. The systematic error on the predicted fluxes, ϵ
4. Choices related to how to deredden the observed data

This small number of options is sufficient to produce significantly differing results – in particular, judicious selection of the prior and of the set of lines to use is essential.

The implementation of NebulaBayes and the straightforward methods of obtaining the code are described in the Appendix.

4.3 Photoionization models

NebulaBayes includes predicted emission-line fluxes over two photoionization model grids, which are also the grids used in this work. The two grids are for H II regions and for NLRs. All models were produced by the MAPPINGS photoionization code, described in Section 4.3.1.

For setting abundances in the models we use the work of Nicholls et al. (2017), which involves a more sophisticated scaling of abundances with metallicity than the uniform scaling that is commonly applied. This scaling accounts for the changing contributions of primary and secondary nitrogen with metallicity and for the changing ratio of α-process elements to iron-peak elements as a function of metallicity.

4.3.1 MAPPINGS

The MAPPINGS photoionization and radiative shock wave modeling code has been developed over three decades. Already in its first iteration (Binette et al. 1985) it was capable of modeling plasmas which are in neither photoionization nor collisional equilibrium (e.g. shocks). The code was subsequently improved with the addition of new physical processes, ions, and atoms (Sutherland & Dopita 1993), dust heating (Dopita & Sutherland 2000), non-equilibrium dust heating and infrared emission (Groves et al. 2004, 2006; Dopita et al. 2005), and treatment of non-equilibrium (κ-distribution) electron energies (Dopita et al. 2013; Nicholls et al. 2012), among many other improvements. The latest version of the code (MAPPINGS V; Sutherland & Dopita 2017) takes advantage of new, highly detailed atomic data, and tracks more than 8×10^4 cooling and recombination emission lines up to densities of order $10^{12}\,\mathrm{cm}^{-3}$. The photoionization model grids described below were computed with MAPPINGS version 5.1.

4.3.2 Narrow line region model grid

The NLR grid uses an OXAF ionizing spectrum (Thomas et al. 2016), which has three parameters: the energy of the peak of the accretion disk emission E_{peak}, the photon index of the inverse Compton scattered power-law tail Γ, and the proportion of the total flux that goes into the non-thermal tail, p_{NT}. The two parameters Γ and p_{NT} are somewhat anti-correlated, because decreasing the hardness of the power-law tail by increasing Γ has a similar effect (at the most relevant EUV energies and at fixed p_{NT}) as scaling up the power-law tail with p_{NT}. The OXAF model does not account for the soft X-ray excess emission; Thomas et al. (2016) showed that including the soft excess does not have a major effect on predictions of the strong optical emission lines. In addition, a soft X-ray excess may arise from the Compton-heated photoionized gas close to the nucleus, rather than being an intrinsic part of the EUV spectrum of the nucleus itself.

For our NLR grid, the only OXAF parameter we vary is E_{peak}, because it is a computational necessity to reduce the number of dimensions. The other parameters are fixed to the fiducial values $\Gamma = 2.0$ and $p_{\mathrm{NT}} = 0.15$. Our final NLR grid has four parameters or dimensions: metallicity, ionization parameter, pressure, and E_{peak}.

The grid was run using the following configuration:

- Oxygen abundances sampling the 12 values $\log\,[\mathrm{O/H}]$ = -1.70, -1.10, -0.70, -0.40, -0.15, 0.00, 0.11, 0.23, 0.32, 0.40, 0.48, and 0.54, using the oxygen-based standard abundance scaling from Nicholls et al. (2017), with the 'local galactic concordance' reference abundance values. In this scale the Solar oxygen abundance is $12+\log\mathrm{O/H} = 8.76$ and our abundances sample 0.02 to 3.5 Solar.

- Ionization parameter at the inner edge of the modeled nebula sampling 11 values in the range $-4.2 \leq \log U \leq -0.2$, uniformly spaced at a logarithmic interval of 0.4 dex

- Initial gas pressures sampling 12 values in the range $4.2 \leq \log P/k$ (cm^{-3} K) ≤ 8.6 uniformly at a logarithmic interval of 0.4 dex. The total pressure is given by the sum of the gas pressure and the radiation pressure, such that the total pressure increases through the model as the radiation is absorbed.

- Values of $E_{\rm peak}$ sampling 6 values in the range $-2.0 \leq \log E_{\rm peak}$ (keV) ≤ -0.75 uniformly at a logarithmic interval of 0.25 dex

- A plane parallel geometry

- A set of depletions onto dust grains based on iron being 97.8% depleted ($\log(\mathrm{Fe}_{\rm free}/\mathrm{Fe}_{\rm total}) = -1.5$; Jenkins (2009, 2014))

- No dust destruction

- An equilibrium, Maxwell-Boltzmann distribution of electron energies ($\kappa = \infty$) (Nicholls et al. 2012)

The total number of gridpoints in the NLR grid is 9504. We note that the predicted intrinsic Balmer decrements ($F_{\rm H\alpha}/F_{\rm H\beta}$) range between 2.79 and 3.54, with a median and 75th percentile of 2.94 and 3.06 respectively. These values compare to the commonly assumed ratio of 2.86 for Case B recombination.

Predicted fluxes for 119 emission lines are included for each point in the grid. The list of lines was selected from a low-abundance H II region, a high-abundance H II region, and a high-excitation NLR MAPPINGS model. The selected lines all have a flux above 1% of Hβ in at least one of the models, have a wavelength between the Lyman limit and 20 μm, and arise from a species with an ionization potential below 100 eV. Lines from iron and magnesium were excluded because we do not allow dust destruction in the MAPPINGS models, so the relevant fluxes are very inaccurate. We also exclude higher-order recombination lines (e.g. H8, Pa7, etc.) that are difficult to predict correctly without a very complete recombination-cascade solution as a function of density. Summed fluxes are included for some commonly considered doublets for convenience. The line list is distributed with NebulaBayes.

4.3.3 HII region model grid

The H ii region grid has three parameters or dimensions: abundance, ionization parameter, and pressure. The grid was run with the same abundances, pressures, depletions and MAPPINGS settings as the NLR grid described above. The ionization parameter was varied over $-4.0 \leq \log U \leq -2.0$ in increments of 0.25 dex. The only other difference was the form of the ionizing spectrum, which varied with metallicity (but not freely with its own parameter). This was to ensure that the stellar and nebular metallicities are approximately matched. Perfect matching of stellar and nebular metallicities is not possible because the stellar atmosphere modelers use older Solar reference abundances, as well as a restricted set of initial abundances.

The ionizing spectra were derived using the slug2 (Krumholz et al. 2015) stellar population synthesis code with the following settings:

- The 'galaxy' (continuous star formation) mode
- A single snapshot of the spectrum after 10^7 years
- A star formation rate of $0.001\, M_\odot\, \mathrm{yr}^{-1}$.
- A Chabrier IMF
- Default Starburst 99 (Leitherer et al. 1999) spectral synthesis mode
- The Padova stellar tracks with thermally pulsing AGB stars
- The five explicitly calculated available metallicities, which were $Z = 0.0004$, 0.004, 0.008, 0.02, 0.05, where $Z = 0.02$ is Solar

The spectra for the five different Z values were interpolated to the 12 oxygen abundances used in the NLR grid. The oxygen abundance-metallicity scaling of Nicholls et al. (2017) was used, and the spectra were linearly interpolated in F_λ space. The exception was that the spectra for 3.0 and $3.5\, Z_\odot$ were the same as for $2.5\, Z_\odot$, to avoid extrapolation. The grid was run with the 12 nebular abundances, with the appropriate spectrum chosen depending on metallicity.

The total number of gridpoints in the H ii region grid is 1296. The list of included emission lines was the same as for the NLR grid except for 26 excluded higher-ionization lines that had no fluxes above 10^{-5} of Hβ. The predicted intrinsic Balmer decrements ($F_{\mathrm{H}\alpha}/F_{\mathrm{H}\beta}$) range between 2.81 and 3.59, with a median and 75th percentile of 2.93 and 3.01 respectively; the distribution is very similar to that for the

NLR grid.

A fully self-consistent modeling of H ii region emission line spectra is a major challenge at present, because the predictions are very sensitive to the assumptions that are used in generating the ionizing spectra. The most important regions of the ionizing spectrum are those defined by the ionization potentials of the key nebular species, and the ionizing flux in these regions varies significantly with the chosen stellar tracks/atmospheres, model assumptions (e.g. stellar rotation, dredge up of helium, mass-loss rates, effects of binarity) and the interpolation schemes used. It is necessary to match the stellar abundances to the nebular abundances for physical consistency, but inconsistent abundances are used between stellar track and atmosphere models. Also, at present the parameter space coverage of stellar evolutionary tracks and model stellar atmospheres is inadequate in both extent and sampling frequency. In this work we make a reasonable attempt to approximately match stellar and nebular abundances; fully self-consistent H ii-region models are currently under development (PI Sutherland).

In a future version of MAPPINGS we intend to incorporate the diffuse super-soft thermal X-ray continuum arising from thermalization of the fast stellar wind through shocks. This may improve the predictions of some lines that arise in the partially-ionized zone.

4.4 Observational data

4.4.1 S7

The *Siding Spring Southern Seyfert Spectroscopic Snapshot Survey* (S7; Dopita et al. 2015) is an optical integral field spectroscopy survey using the Wide Field Spectrograph (WiFeS) mounted on the ANU 2.3 m telescope at Siding Spring Observatory, Australia. The S7 was carried out from 2013 – 2016 and contains a sample of 131 local ($z < 0.02$) galaxies, including approximately 77 Seyfert 2 galaxies, 18 Seyfert 1 galaxies, 27 LINERs, and 11 star-forming-only galaxies. The WiFeS field of view of 38×25 arcsec^2 covers the centre of each galaxy. The resulting data cubes consist of a grid of 1×1 arcsec^2 spatial pixels ('spaxels'), an angular resolution comparable to the median seeing across the survey of 1.5 arcsec. The design and performance of WiFeS are discussed in Dopita et al. (2007) and Dopita et al. (2010).

The spectral resolution of the S7 data is $R = 7000$ in the red (FWHM $\sim 40\,\mathrm{km\,s^{-1}}$ over $540 - 700\,\mathrm{nm}$) and $R = 3000$ in the blue (FWHM $\sim 100\,\mathrm{km\,s^{-1}}$ over $350 - 570\,\mathrm{nm}$), which is higher than comparable surveys and permits analysis of separate velocity components in the emission lines. The data have a high spatial resolution at the very low redshift of the sample, which also allows separation of extended regions ionized by the AGN, star formation, and shocks.

Ongoing analysis of the S7 data motivated the development of the NebulaBayes code. We required a general method to constrain photoionization model parameters not just in H II regions, but also in extended AGN narrow-line regions, in high-ionization nuclear coronal line clouds in AGN, and potentially also in shock-excited regions and LINER nuclei. The approach is required to be computationally efficient when applied to hundreds or thousands of spectra.

4.4.2 Sample selection

The sample selection was driven by our desire to minimize contamination from non-Seyfert excitation and to maximize the area in the S7 field of view which could be analyzed. These objectives ensured that we could usefully compare our data to a NLR model grid and make strong inferences regarding the spatial distributions of physical parameters.

Four Seyfert galaxies were selected from the S7 sample: ESO 138-G01, IC 5063, Mrk 573, and NGC 2992. Images of these objects are shown in Figure 4.1, which illustrates the S7 field of view. These galaxies are the examples that most clearly meet the following criteria:

1. They are Seyfert galaxies with ENLRs extending across the majority of the length and width of the WiFeS field of view
2. In 1-component line fitting to the unbinned data, the excitation across the WiFeS field of view was dominated by emission-line ratios falling in the 'Seyfert' regions of the [N II] and [S II] optical diagnostic diagrams (Figure 4.2), and in particular, there was no significant evidence for excitation by O stars.
3. The signal-to-noise (S/N) was generally sufficient for a high-quality NebulaBayes analysis, i.e. spatially binning to a target S/N of 100 or 150 in H α flux resulted in a satisfactory number of spatial elements being retained

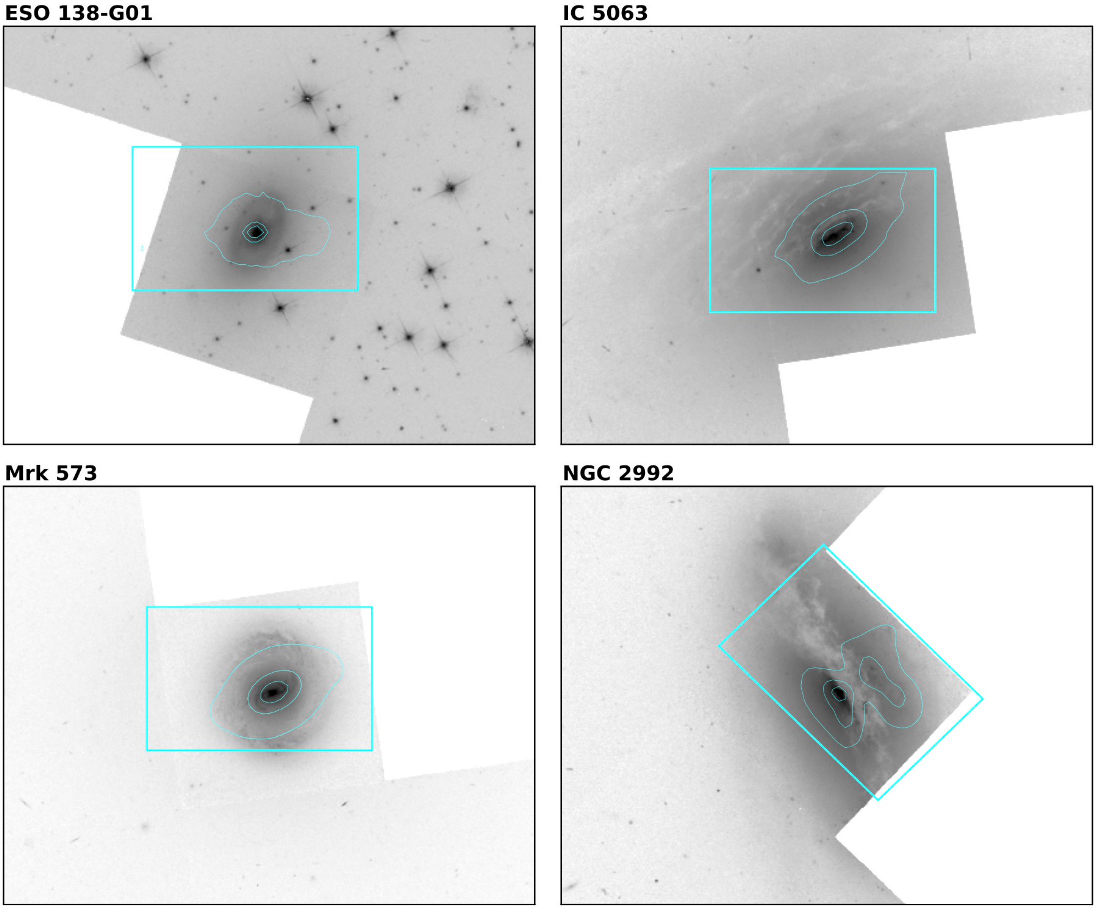

Figure 4.1 Archival HST WFPC2 F606W wide-band optical imaging (Malkan et al. 1998) for the four nearby Seyfert galaxies studied in this work. The cyan rectangles approximately show the 25×38 arcsec^2 field of view of WiFeS. Logarithmically-spaced contours reflect the [OIII] flux map measured from single-component fits to the S7 IFU data. North is toward the top of the page and east is to the left.

A handful of other galaxies in the S7 sample had emission dominated by Seyfert excitation, but over a smaller area of the field of view compared to the selected galaxies (e.g. ESO 103-G35, IRAS 01475-0740). Approximately 30% of the S7 galaxies featured regions of multiple spaxels with Seyfert-dominated emission, but were excluded from our sample because non-Seyfert regions were also present (usually with 'composite' and/or H II-region classifications).

The selection based on BPT/VO diagrams cannot guarantee that the observed emission is only from Seyfert photoionization. There are two key reasons that we expect contamination. Firstly, the classifications of Figure 4.2 are approximate: for example, the LINER-Seyfert distinction is inexact (Kewley et al. 2006) and grids of fast shocks overlap the Seyfert region of the diagnostic diagrams (Allen et al. 2008; Dopita & Sutherland 1996). Secondly, the nature of Seyfert galaxies and the IFU

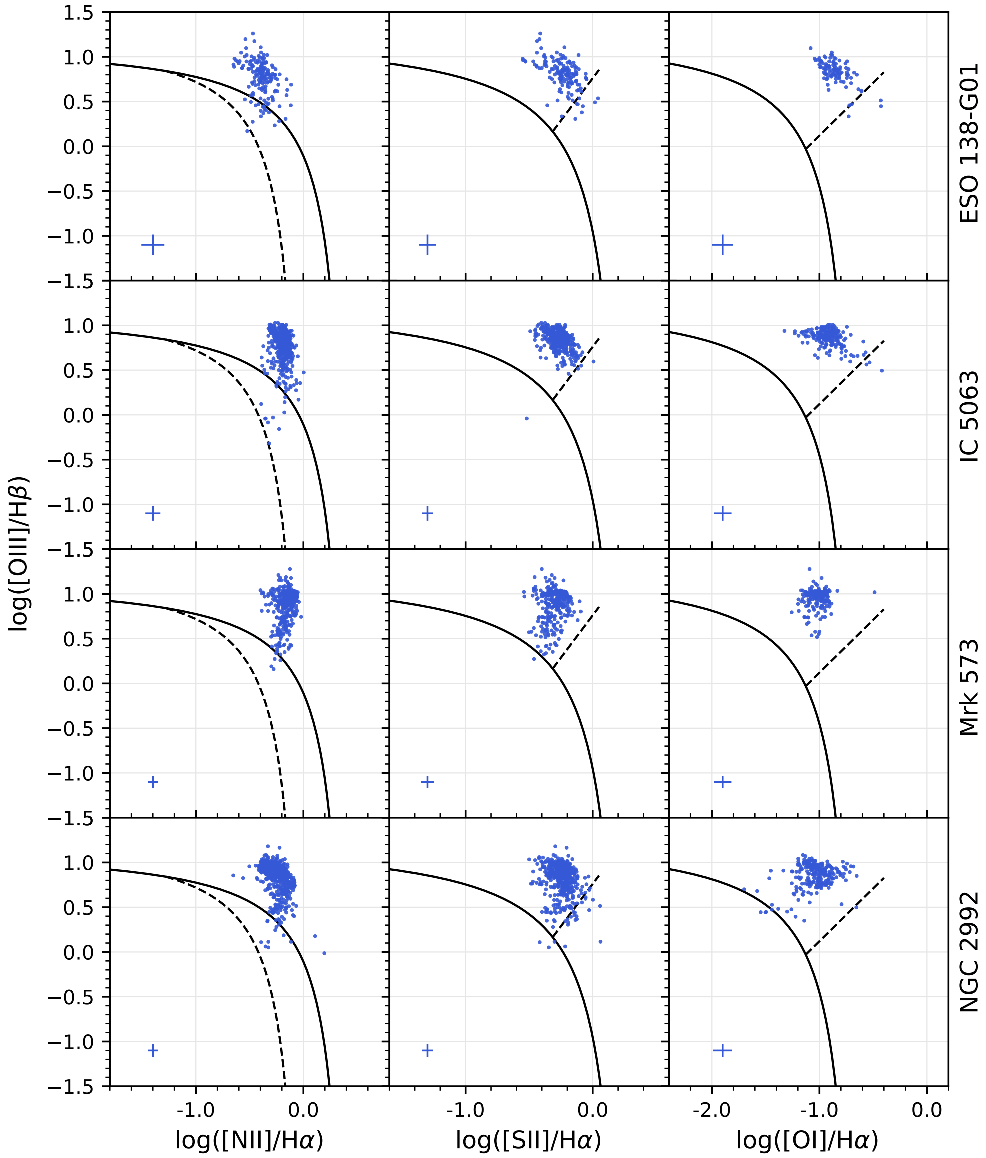

Figure 4.2 Optical diagnostic diagrams (BPT/VO diagrams; Baldwin, Phillips and Terlevich 1981; Veilleux & Osterbrock 1987) showing spatially-resolved emission-line flux ratios for the four selected Seyfert galaxies. The solid line in each panel is a theoretical separation between nebulae associated with star formation (below) and higher-excitation nebulae (above; Kewley et al. 2001). The dotted line in the leftmost panels is an empirical variant of the same division (Kauffmann et al. 2003). The dotted line in each panel of the rightmost two columns separates LINERs (below) and Seyferts (above; Kewley et al. 2006). Each datum is derived from single-component Gaussian line fits for a 1 arcsec square spatial pixel. All line fluxes have S/N > 2, and median error bars are shown in the bottom-left of each panel. Seyfert excitation appears to generally dominate over other sources of excitation in the observed regions of these four galaxies.

data strongly suggests that some contamination will be present. Ubiquitous outflows in Seyfert galaxies are associated with shocks, and the gas that fuels the black hole could equally be forming ionizing young stars. We do not resolve individual nebulae, so our spectra are luminosity-weighted sums of both Seyfert-photoionized and contaminating emission over varying projected areas (spatial scales are shown in Figure 4.3).

There is some evidence of contamination in Figure 4.2. Contaminating spectra will make varying contributions to different line fluxes and will generally skew diagnostic line ratios. Figure 4.2 shows some apparent 'mixing' down into the 'composite' region of the optical diagnostic diagrams for all four galaxies. There are also hints of mixing with 'LINER-like' spectra (due to shocks or photoionization with a low ionization parameter) on the [S II] diagram for all galaxies except Mrk 573. We discuss how spectral contamination may have affected our results in Section 4.6 and Section 4.7.

The sample properties are given in Table 4.1. As well as the four 'pure Seyfert' galaxies, we include the 'pure-H II' galaxy NGC 4691 to demonstrate the application of NebulaBayes to the spectra of star-forming galaxies. This galaxy was only included in the S7 sample because it was misclassified as a Seyfert in the original Véron-Cetty & Véron (2010) catalog.

Table 4.1 The galaxies selected from the S7 sample. The first four are 'pure Seyfert' galaxies that show AGN-dominated optical emission-line excitation across the WiFeS field of view.

Name	RA	Dec.	Redshift z	Morphology [a]	$\log M_*/M_\odot$ [b]	Excitation type [c]
ESO 138-G01	252.83542	-59.2364	0.0091	E-S0	10.8	Seyfert 2
IC 5063	313.00921	-57.0686	0.0113	S0-a	10.6	Seyfert 2
Mrk 573	25.99079	+2.3497	0.0172	S0-a	10.9	Seyfert 2
NGC 2992	146.42500	-14.3264	0.0077	Sa	10.5	Seyfert 2
NGC 4691	192.05421	-3.3331	0.0037	S0-a	9.6	H II

[a] From HyperLeda.
[b] Stellar mass estimated as described in Thomas et al. (2017), except for NGC 4691 for which we used Equation 8 of Taylor et al. (2011) with SDSS g and i magnitudes.
[c] S7 nuclear classification.

The HST imaging in Figure 4.1 shows that the morphologies of the four Seyfert galaxies are much more complicated than the HyperLeda morphological classifications in Table 4.1 suggest. ESO 138-G01 has a stellar ring and Mrk 573 has spiral arms, so these appear to be disky galaxies. IC 5063 and NGC 2992 feature prominent dust lanes.

The Seyfert galaxies have similar stellar masses, typical for the galaxies included in the full S7 sample (the distribution peaks at $\log M_*/M_\odot = 10.7$).

ESO 138-G01, IC 5063 and Mrk 573 were all observed in photometric conditions, but NGC 2992 was observed through some cirrus.

In Figure 4.3 we present maps showing the gas excitation and the kinematics resulting from single-component Gaussian fits to the data. The figure illustrates physical scales on the galaxies and the seeing FWHM for each observation.

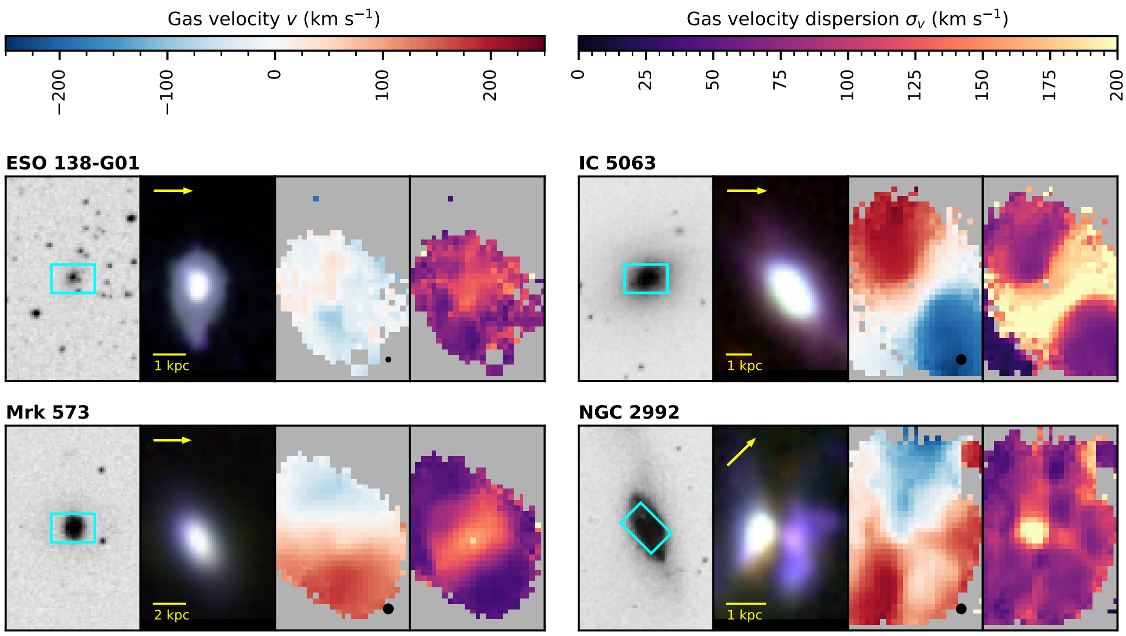

Figure 4.3 Maps for the four selected 'pure Seyfert' S7 galaxies. The panels from left to right: a) A DSS2 r-band image; north is upwards and the cyan rectangle shows the 25×38 arcsec^2 WiFeS field of view. b) A composite image illustrating the ionization state of the gas. The red channel is H α, the green channel is [NII] λ6584, and the blue channel is [OIII] λ5007. ENLRs are generally purple (strong [OIII] λ5007 and generally high [NII]/Hα), whereas H II regions would appear red or gold. The yellow arrow indicates the direction of north in the last three panels. c) The ionized gas line-of-sight velocity from single-component emission-line fits. A black circle in the lower-right shows the seeing FWHM. d) A corresponding map of line-of-sight velocity dispersion. The velocity dispersion maps show evidence of outflows in the ENLRs, especially along the minor axis of IC 5063.

In the following paragraphs we briefly describe the properties of the active galaxies and the features evident in the S7 data.

ESO 138-G01: This galaxy hosts a luminous Seyfert 2 nucleus (Fairall 1988) and has been previously classified as E/S0 but appears more disky than elliptical in Figure 4.1. The large, asymmetric ENLR has a prominent extension to the west, which is also visible in moderate blueshifts in the velocity map in Figure 4.3. An isolated cloud of [O III] emission (too faint to be visible in Figure 4.3) is located $\sim$15″ to the east of the nucleus at the edge of the S7 field of view. The nuclear spectrum boasts a spectacular array of forbidden high-ionization (coronal) emission lines such as [Fe VII] λ6087 and [Fe X] λ6375 (Alloin et al. 1992). Very high ionization lines are also observed in X-ray spectra by De Cicco et al. (2015). We note that De Cicco et al. (2015) measured a soft X-ray photon power law index of $\Gamma = 2.03 \pm 0.14$, an excellent match to the $\Gamma = 2$ we assumed in the photoionization models (Section 4.3.2).

IC 5063: A well-studied galaxy exhibiting both Seyfert 2 excitation and a radio jet that powers a spectacular galactic wind (e.g. Sharp & Bland-Hawthorn 2010; Tadhunter et al. 2014; Morganti et al. 2015; Dasyra et al. 2015). The biconical, outflowing ENLR has a large opening angle of $\sim 90°$ and extends at least $30''$ across the WiFeS field of view. The nuclear line profiles are extremely complex with multiple independent components. There is a hidden broad-line region revealed by spectropolarimetry (Lumsden et al. 2004).

Mrk 573: A Seyfert 2 galaxy that features a black hole accreting near the Eddington limit (Bian & Gu 2007; Kraemer et al. 2009), and an ENLR over 8 kpc in extent that covers most of the WiFeS field of view diagonally from southeast to northwest. The nucleus shows coronal line emission (Dopita et al. 2015). HST photometry and spectroscopy led Fischer et al. (2010) to argue that an inclined ionization cone intersects the inner spiral arms. Rose et al. (2015) estimate the nuclear inclination of Mrk 573 to be 60 ± 5 degrees using WISE infrared colors and arguing that the presence of coronal lines is indicative of an intermediate inclination of the obscuring torus. The excitation of the coronal lines was modeled by Kraemer et al. (2009).

NGC 2992: A disky galaxy interacting with its neighbor NGC 2993 and showing tidal distortions (Toomre & Toomre 1972). Opposing ENLR cones extend with large opening angles either side of the disk, both easily visible due to the high inclination of NGC 2992 (e.g. Allen et al. 1999). The nuclear spectrum is highly variable and has been observed with and without broad Balmer wings at various times over the last four decades (Ward et al. 1980; Allen et al. 1999; Gilli et al. 2000; Lumsden et al. 2004; Trippe et al. 2008). The second panel in Figure 4.3 is brown along the dust lane; the [O III] flux is relatively weak here due to extinction and not because H II regions are dominating the spectrum.

4.4.3 Data processing

We use the reduced data cubes from S7 Data Release 2 (Thomas et al. 2017). The first post-processing step was to perform a subpixel shift of the blue data cube in order to align it with the red cube – the PyWiFeS pipeline (Childress et al. 2014) differential atmospheric refraction (DAR) correction was inadequate and the final analyses were affected unless this correction was made. The sizes of the subpixel shifts were determined by eye and the shifts were performed for ESO 138-G01, IC 5063 and Mrk 573. The corrections were most important for IC 5063 and Mrk 573.

The cubes were spatially binned using a Voronoi tessellation (Cappellari & Copin 2003) based on the S/N of the H α line fluxes in single-component fits to every spaxel. The target S/N was 100 for ESO 138-G01 and 150 for IC 5063, Mrk 573, and NGC 2992. A minimum S/N cutoff was set such that spaxels with a low S/N were not inputted into the binning algorithm; the cutoff was $(\mathrm{S/N})_{\mathrm{min}} = 5$ for ESO 138-G01 and $(\mathrm{S/N})_{\mathrm{min}} = 8$ for the other three galaxies. Minor manual cleanup of the tessellation maps was required, which involved removing isolated spaxels and regularizing bin shapes in low-S/N regions.

The line fitting followed the approach used by Thomas et al. (2017). Gaussian emission-line fitting was performed using LZIFU (Ho et al. 2016) to obtain the measured emission-line fluxes. The LZIFU code wraps PPXF (Cappellari & Emsellem 2004, used to fit the stellar continuum for subtraction) and MPFIT (Markwardt 2009, used to fit Gaussians to the emission lines). The fitting was run with 1-, 2- and 3-component fits for each spatial bin in each galaxy. The velocity and velocity width for each component were fixed by LZIFU for all fitted lines in a spectrum. A small number of fitting failures occurred; at least one from a failure to fit the stellar continuum and other failures presumably due to the complex line profiles in the relevant spectra. The $\sim 2 - 6$ missing bins in each galaxy do not affect our conclusions.

An artificial neural network LZCOMP (Hampton et al. 2017) was used to select the optimal number of kinematic components from 1-, 2- and 3-component fits for each bin. The neural network was trained on the same data as in the S7 Data Release 2 products (Thomas et al. 2017). The training data was produced by multiple astronomers selecting between 1-, 2- or 3- component fits to S7 cubes. The final line fluxes used in the NebulaBayes analysis were the sum of the fluxes in the individual components selected by LZCOMP.

4.5 Application of NebulaBayes

This section describes the approach to constraining the physical parameters of interest in each galaxy, including the choices of emission lines, priors and NebulaBayes settings.

Care is necessary when selecting the emission lines to use in a NebulaBayes analysis. The observed lines do not necessarily all arise in the same gas, and the equal weighting of lines in the analysis may result in a 'dilution' of the constraining power if a significant number of low-information lines are included. The Bayesian method allows the freedom to combine data from all available emission lines in the analysis, but a judicious selection is necessary nevertheless.

For the ENLR analysis we chose to use the 11 emission lines [OII] $\lambda3726 + 29$, [NeIII] $\lambda3869$, HeII $\lambda4686$, Hβ, [OIII] $\lambda5007$, HeI $\lambda5876$, [OI] $\lambda6300$, H α, [NII] $\lambda6583$, [SII] $\lambda6716$, and [SII] $\lambda6731$. This list contains the standard strong optical lines, including all of those used in the optical diagnostic diagrams of Figure 4.2. The species HeII is produced by photons with energies above the ionization potential of 24.6 eV and hence its line fluxes are sensitive to the hardness of the ionizing AGN continuum.

For the H II region analysis we chose [OII] $\lambda\,3726 + 29$, [OIII] $\lambda\,4363$, [OIII] $\lambda\,5007$, HeI $\lambda\,5876$, OI $\lambda\,6300$, [NII] $\lambda\,6583$, and [SII] $\lambda\,6716, 6731$. We also include H α and Hβ which are essential for normalization and reddening-correction.

The equal weighting of emission lines in the NebulaBayes analysis does not take advantage of our prior knowledge of physical parameters revealed by particular diagnostic line ratios. For simplicity we apply only one prior in general, on the flux ratio [SII] $\lambda\,6716$ / [SII] $\lambda\,6731$, which is an electron density diagnostic so constrains the gas pressure. We required an additional contribution to the prior for ESO130-G01, described in Section 4.6.1.

We used traditional BPT/VO classifications to select only 'Seyfert' Voronoi bins for the analysis. The Seyfert classification was required on both the [NII] and [SII] diagrams (Figure 4.2); the [OI] diagram provides little extra classifying power for these data, and was not used. A bin was included in the ENLR analysis if and only if its line flux ratios lie above the Kewley et al. (2001) theoretical extreme-starburst line on the [NII]/Hα diagnostic diagram and above both the Kewley et al. (2001) theoretical extreme-starburst line and the Kewley et al. (2006) empirical

LINER/Seyfert separation line on the [S II]/Hα diagram. We note that shock, H II-region and diffuse ionized gas (DIG) emission may contaminate these spectra despite our cuts; this is further explored in the discussion of the results.

We took advantage of the ability of NebulaBayes to deredden the observed fluxes at every point in the interpolated parameter space. The dereddening is based on matching theoretical Balmer decrements, and this approach allows fair comparisons with regions of the parameter space with predicted Balmer decrements that are higher than usual.

We chose a sampling density of 50 points along each of the four dimensions of the interpolated NLR grids, for a total of 6.25×10^6 points in the predicted flux grid for each emission line. For the 3D H II region grids we chose a sampling density of 200 points along each of the three dimensions, for a total of 8×10^6 gridpoints. The statistical and systematic uncertainties in the results presented here are in general larger than the spacing between the raw (photoionization model) gridpoints, so the exact sampling of the higher-frequency interpolated points is not expected to significantly influence the results.

The default fractional systematic grid uncertainty of $\epsilon = 0.35$ was used. This parameter directly increases the variance V_i in equations 4.3 and 4.5.

4.6 Results

In Section 4.6.1 we present and discuss the results for the galactic nuclei. In Section 4.6.2 we map the spatial distributions of parameter values in the 'pure Seyfert' galaxies, and in Section 4.6.3 we briefly describe the key features of the parameter maps for each galaxy. In Section 4.6.4 we combine interpretations of the various measurements with prior knowledge of the galaxies to glean insights into the properties of each object.

4.6.1 Nuclear spaxels

Below we present and discuss the constraints on the physical parameters obtained from NebulaBayes analyses of the nuclear spectra of each selected S7 galaxy.

Competing solutions for ESO 138-G01

The nuclear region of ESO 138-G01 required special treatment. The likelihood produced by NebulaBayes for a nuclear spaxel is illustrated in Figure 4.4, which shows two degenerate solutions. The figure shows all possible combinations of marginalized 2D joint posterior PDFs, with the PDFs colored black to white through green from low to high probability density. The gray points indicate the locations of the (uninterpolated) model gridpoints. All four 1D marginalized PDFs are illustrated along the diagonal.

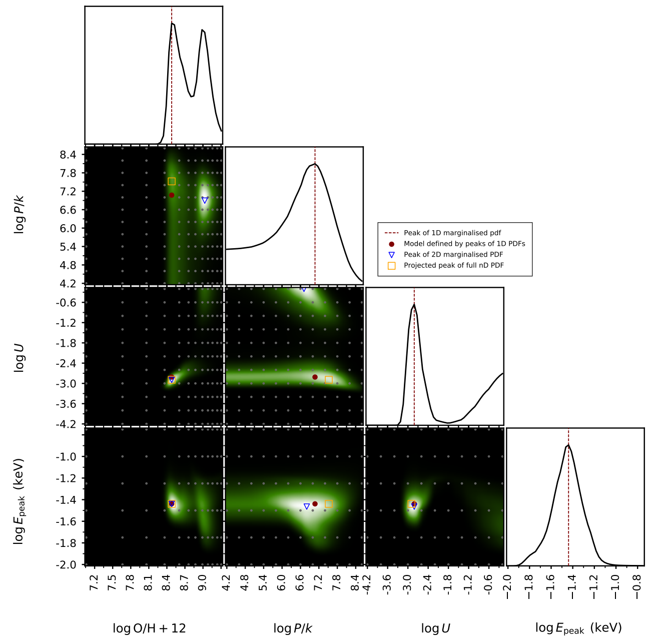

Figure 4.4 Likelihood for a nuclear bin in ESO 138-G01. There is a degenerate solution for $12 + \log \mathrm{O/H}$ and $\log U$, discussed in the text. A prior was applied on the ionization parameter to select the lower-ionization parameter, lower-abundance solution, which is consistent with adjacent bins (Section 4.6.1). Parameter estimates are given in Table 4.2.

The ENLR gas in ESO 138-G01 is stratified, with higher-excitation lines arising in higher-density environments closer to the nucleus (Alloin et al. 1992). The photoionization models do not include dust destruction or cover the extreme regions of parameter space required to properly model the coronal lines, so these lines were not included in the NebulaBayes analysis. Nevertheless, the two competing solutions evident in Figure 4.4 may reflect the different physical regions emitting the high- and low-ionization lines.

One solution, with an ionization parameter of $\log U \sim -3$ and an oxygen abundance of $12 + \log \mathrm{O/H} \sim 8.5$, appears to correspond to the normal NLR gas. The other solution has an ionization parameter pushing the upper limit of the grid and much higher abundances, and may correspond to the coronal-line emitting gas, or alternatively may simply be a false solution. If this high-U solution is in fact caused by contamination of the strong emission lines by the coronal-line gas, the higher inferred abundances would presumably be due to the presence of species liberated from dust, which would provide a greatly enhanced cooling efficiency in the ionized plasma.

We selected the low-U solution because it has reasonable parameter estimates that are consistent with adjacent spatial bins. This solution was chosen by applying an extra prior that was a function of only U. The extra prior was uniform (in logarithmic space) below $\log U = -2.0$, but exponentially decreasing above this value to exclude the high-U, high-metallicity solution. We combined the prior on U with the usual prior on the [SII] ratio in the analysis of all bins in the galaxy, although the U-dependence only affected the results for the nuclear spaxels.

Although the nuclear metallicity measurements may be biased by contamination from the coronal line gas, the consistency between the nuclear results and the metallicity in adjacent, non-contaminated bins (Section 4.6.2) suggests that the metallicity estimates have not been significantly affected. Nevertheless, the upper uncertainties on the oxygen abundance are much larger in the nuclear region of ESO138-G01 than for the other galaxies (Table 4.2).

Results for the Seyfert galaxies

Posteriors for the nuclear bins for the other three selected Seyfert galaxies are shown in Figure 4.5 for IC 5063, Figure 4.6 for Mrk 573, and Figure 4.7 for NGC 2992.

The NebulaBayes parameter estimates for all four galaxies are presented in Table 4.2. The table shows that measured nuclear values of $E_{\rm peak}$ vary from $\log E_{\rm peak}(\rm keV) = -1.77$ ($E_{\rm peak}$= 17 eV) in NGC 2992 to $\log E_{\rm peak}(\rm keV) = -1.41$ ($E_{\rm peak}$= 39 eV) in Mrk 573. The nuclear abundances are half Solar in ESO 138-G01, 1.2 Solar in IC 5063 and approximately twice Solar in Mrk 573 and NGC 2992. This variation in nuclear abundances is surprising, considering the small range in stellar masses, and we discuss the anomalously low values for ESO 138-G01 and IC 5063 in Section 4.6.4.

In Table 4.3 we compare our derived metallicities to the estimates recently reported by Dors et al. (2015, 2017) and Castro et al. (2017). Our inferred metallicities

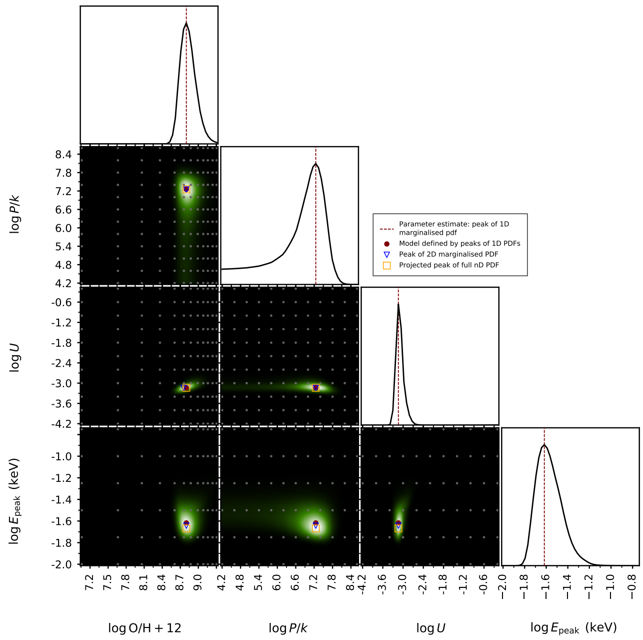

Figure 4.5 NebulaBayes posterior for a nuclear bin in IC 5063. Parameter estimates are given in Table 4.2.

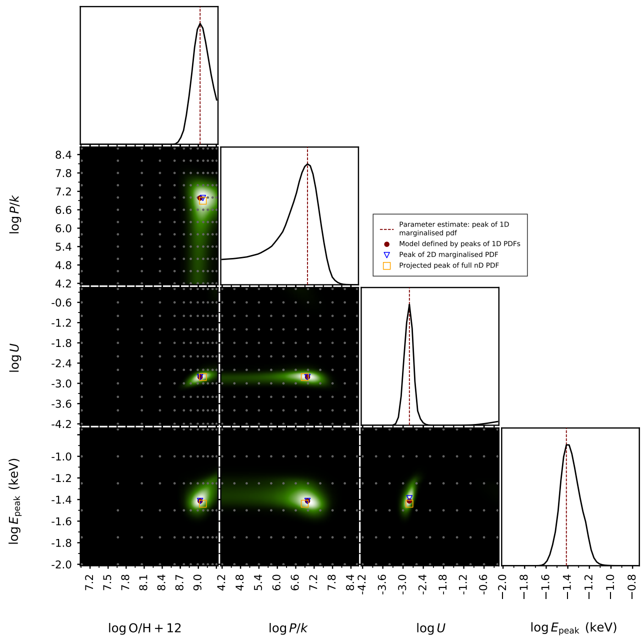

Figure 4.6 NebulaBayes posterior for a nuclear bin in Mrk 573. Parameter estimates are given in Table 4.2.

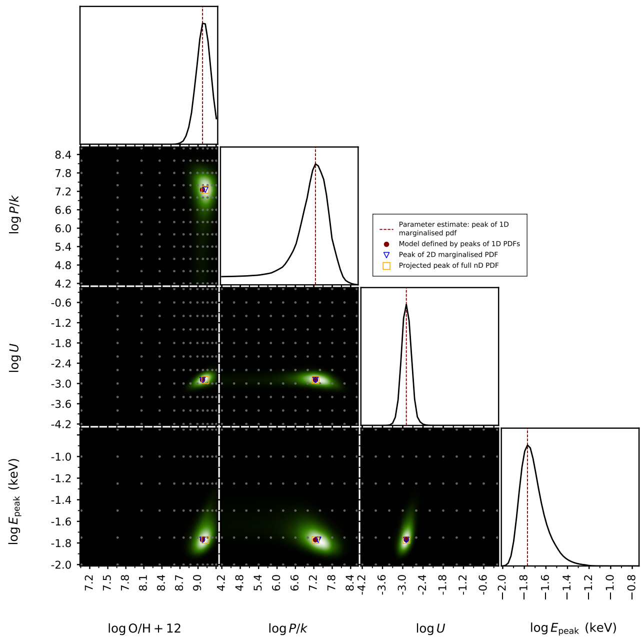

Figure 4.7 NebulaBayes posterior for a nuclear bin in NGC 2992. Parameter estimates are given in Table 4.2.

Table 4.2 NebulaBayes parameter estimates (peak in 1D marginalized posterior PDFs) for a nuclear spaxel in each 'pure Seyfert' galaxy, with bounds of the 68% credible intervals.

Galaxy	$\log\ E_{\rm peak}$ (keV)	$12 + \log$ O/H	$\log\ P/k$ ($\rm cm^{-3}\,K$)	$\log\ U$
ESO138-G01	$-1.44^{+0.18}_{-0.08}$	$8.48^{+0.46}_{-0.05}$	$7.43^{+0.36}_{-2.0}$	$-2.81^{+0.41}_{-0.16}$
IC5063	$-1.64^{+0.18}_{-0.08}$	$8.85^{+0.18}_{-0.14}$	$7.16^{+0.27}_{-1.3}$	$-3.06^{+0.16}_{-0.16}$
MARK573	$-1.41^{+0.15}_{-0.08}$	$9.08^{+0.14}_{-0.18}$	$6.98^{+0.18}_{-1.8}$	$-2.73^{+0.16}_{-0.24}$
NGC2992	$-1.77^{+0.18}_{-0.08}$	$9.08^{+0.14}_{-0.14}$	$7.25^{+0.36}_{-0.99}$	$-2.89^{+0.16}_{-0.16}$

are higher for IC 5063 and Mrk 573 than the comparison values, with the Castro et al. (2017) estimates, Dors et al. (2017) estimates, and all but one of the Dors et al. (2015) estimates lying below our 68% credible intervals. Dors et al. (2017) allowed N/O to vary, which may have introduced systematic effects that contributed to the observed offsets. However, there may be many other reasons for the apparent discrepancies between our measurements and the literature values, including aperture effects, systematic differences due to the use of different sets of emission lines, differences in the shape of the photoionizing spectrum, and systematic differences between models, including the photoionization codes themselves (Castro et al. (2017) and Dors et al. (2017) use CLOUDY). One difference is that we use isobaric (constant gas pressure) models and include pressure as a parameter in our grid, whereas Castro et al. (2017) use a fixed density of $n_e = 500\,\mathrm{cm}^{-3}$.

Table 4.3 Comparison of Seyfert galaxy nuclear metallicity measurements[a] with Dors et al. (2015), Dors et al. (2017) and Castro et al. (2017)

Galaxy	This work	Dors+15[b]	Dors+17	Castro+17
ESO 138-G01	$0.5^{+1.0}_{-0.1}$	0.4, 0.6	0.3	0.6
IC 5063	$1.2^{+0.6}_{-0.3}$	0.6, 0.8	0.6	0.9
Mrk 573	$2.1^{+0.8}_{-0.7}$	0.8, 1.5	1.0	1.2
NGC 2992	$2.1^{+0.8}_{-0.6}$	-	-	-

[a] Metallicities reported as a fraction of Solar, assuming a Solar oxygen abundance of $12 + \log \mathrm{O/H} = 8.76$ where necessary.
[b] Estimates using two different calibrations from Storchi-Bergmann et al. (1998).

A constant density does not allow for the important effects of radiation pressure on the structure of the NLR nebulae (e.g. Dopita et al. 2002; Groves et al. 2004), and we show in recent work that varying the density is necessary to accurately model H II region nebulae (Kewley et al. (2018), submitted). Our measured nuclear pressures of $\log P/k\,(\mathrm{cm}^{-3}\,\mathrm{K}) = 7.0 - 7.4$ correspond to $n_e \sim 500 - 1100\,\mathrm{cm}^{-3}$ for a plasma with a temperature of 10^4 K.

Bennert et al. (2006a) studied a sample of six local Seyfert 2 galaxies with long-slit data, including IC 5063. The nuclear electron density of $n_e \sim 640\,\mathrm{cm}^{-3}$ and temperature of 13900 K measured by the authors (their Table 5 and Figure 6) correspond to a pressure of $\log P/k\,(\mathrm{cm}^{-3}\,\mathrm{K}) = 7.3$ for a fully ionized plasma, which is consistent with our result $\log P/k\,(\mathrm{cm}^{-3}\,\mathrm{K}) = 7.16^{+0.27}_{-1.3}$ (Table 4.2). Bennert et al. (2006a) estimated the nuclear ionization parameter using the [O II]/[O III] ratio; their value of $\log U = -2.7$ compares to our measurement $\log U = -3.06^{+0.16}_{-0.16}$, with the difference presumably due to the significant differences in methodology.

Results for the star-forming galaxy NGC 4691

To demonstrate the capability of NebulaBayes in constraining physical parameters for H II regions, we include an analysis of the nuclear spectrum of the galaxy NGC 4691. This galaxy was included in the S7 sample due to a mis-classification in the source catalogue, and does not show any evidence for optical AGN activity. The results of the analysis are shown in Figure 4.8.

The parameter estimates (with 68% credible bounds) are $12 + \log \mathrm{O/H} = 8.74^{+0.12}_{-0.05}$, $\log P/k\,(\mathrm{cm}^{-3}\,\mathrm{K}) = 6.8^{+0.2}_{-1.8}$ and $\log U = -2.8^{+0.1}_{-0.2}$. The approximately Solar nuclear

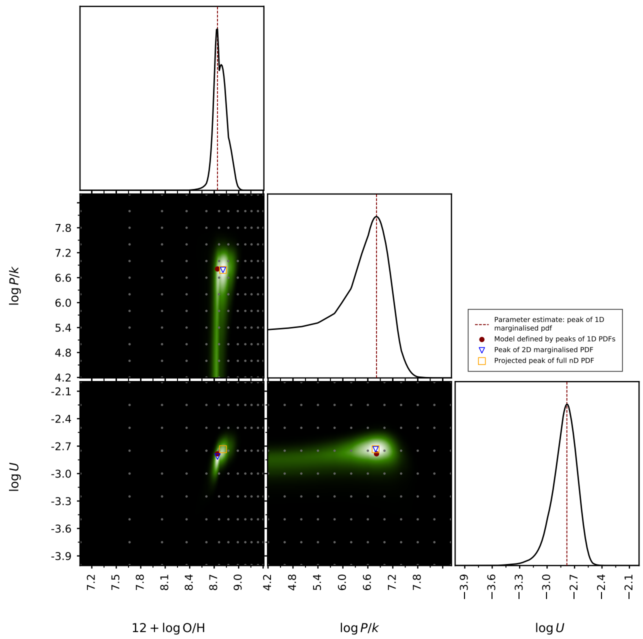

Figure 4.8 NebulaBayes posterior calculated using fluxes from an S7 nuclear spectrum for NGC 4691, using the H II region model grid. The ionization parameter and metallicity are well constrained. The pressure is not well constrained because the [SII] ratio is near the low-density limit.

metallicity is reasonable considering the estimated stellar mass of $10^{9.6}\,M_{\odot}$. For comparison, the diagnostic of Dopita et al. (2016) gives $\log \mathrm{O/H} = 8.94$, which is 0.2 dex higher. The difference may be because the Dopita et al. (2016) diagnostic uses only four of the ten emission lines that we include in the NebulaBayes analysis, or perhaps because the diagnostic was calibrated to photoionization models based on an older version of MAPPINGS to the version used here. Older atomic data was used, and Dopita et al. (2016) used ionizing stellar spectra directly from Starburst99 instead of from SLUG2.

4.6.2 Maps

Maps of parameter estimates for all four parameters across the ENLRs of all four 'pure Seyfert' galaxies are presented in Figure 4.9. Figure 4.10 contains similar maps of the inferred reddening, along with panels comparing E_{peak} to reddening. The black arrows on the maps show the direction of north; east is 90° anticlockwise of north. The physical scales are shown in Figure 4.3; the width of the frames ranges from $\sim$3 to $\sim$7 kpc.

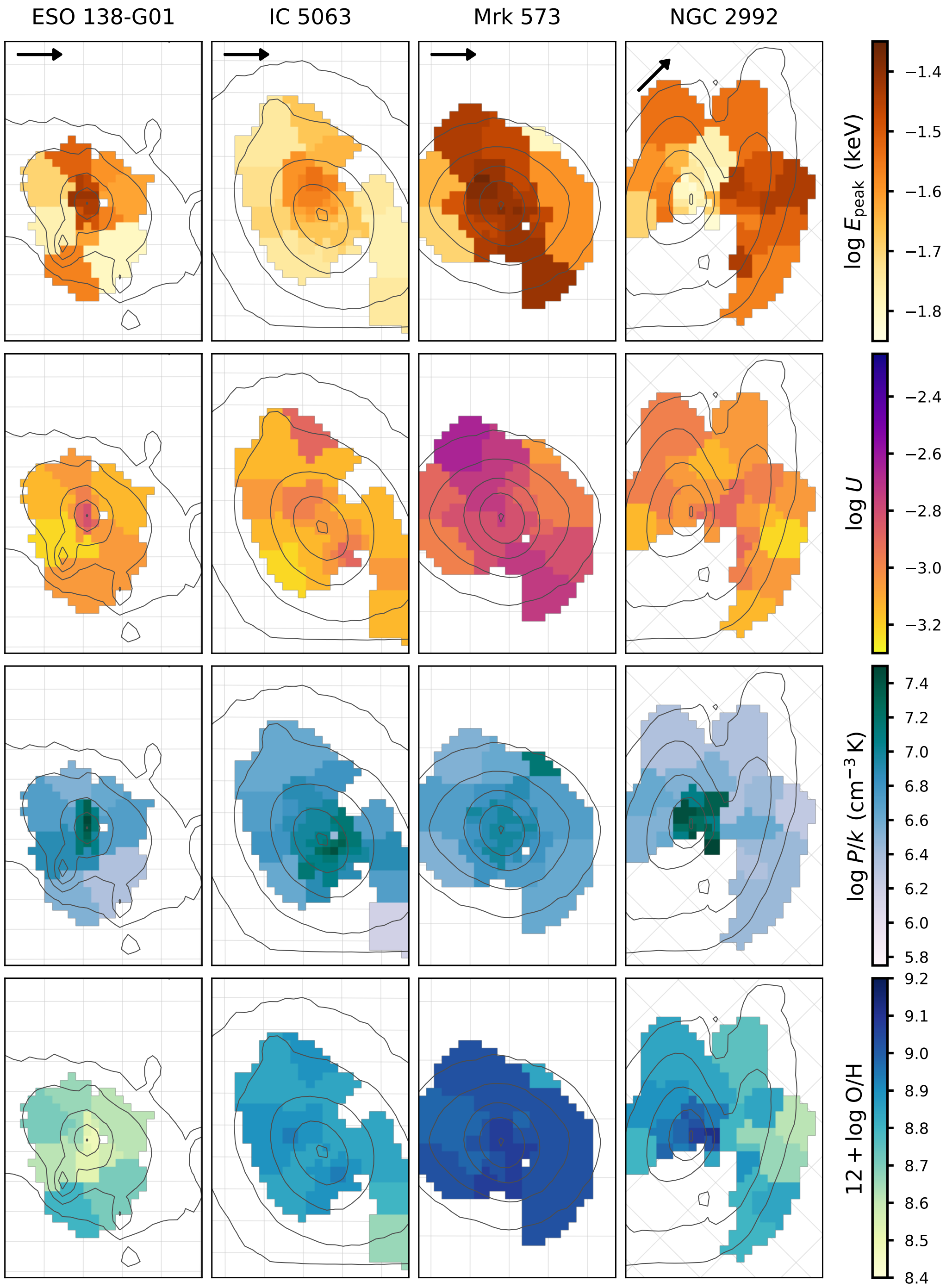

Figure 4.9 Maps of NebulaBayes parameter estimates for the four parameters for each of the four 'pure Seyfert' galaxies. Each measurement corresponds to the peak of the 1D marginalized posterior PDF for the relevant parameter. The black arrows in the topmost panels indicate the direction of north and the logarithmically-spaced contours show the pseudo-continuum derived by summing the red S7 cube in the wavelength direction. The WiFeS field of view is $25'' \times 38''$, made up of $1'' \times 1''$ spatial pixels. Physical scales are shown in Figure 4.3. These results are discussed in Section 4.6.3 and Section 4.6.4.

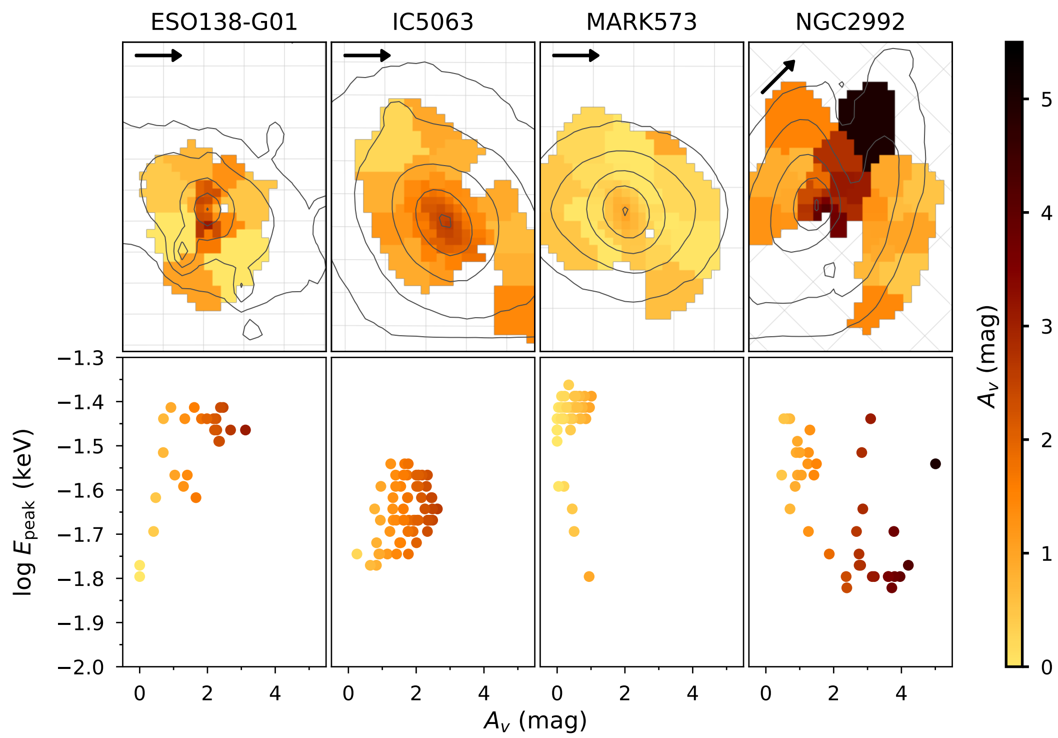

Figure 4.10 The distributions of inferred extinctions for each of the four 'pure Seyfert' galaxies. Top row: Maps of the inferred visual extinction A_V (mag), similar to the maps in Figure 4.9. A dust lane is evident in the upper panel for NGC 2992. The dust lanes are not apparent in the panel for IC 5063, likely because the observed nebular emission lies in the foreground. Bottom row: $E_{\rm peak}$ versus the extinction A_V for the same galaxies, with a point per spatial bin. The 'tails' of lower $E_{\rm peak}$ measurements for ESO 138-G01 and Mrk 573 are presumably due to spectral contamination. There is no clear overall trend of $E_{\rm peak}$ with the degree of reddening, suggesting that local screening of the ionizing radiation by dusty gas is not significantly affecting the $E_{\rm peak}$ values (See Section 4.7 for discussion).

4.6.3 Notes on the parameter maps in Figure 4.9

Hardness of the ionizing continuum

Regions of relatively high inferred radiative hardness generally appear to coincide with the alignment of ionization cones in Figure 4.3. The possible causes of the measured $E_{\rm peak}$ variations are discussed in Section 4.7. Screening of the ionizing radiation is expected to harden the spectrum, so the lower $E_{\rm peak}$ measurements outside the ionization cones are presumably due to spectral contamination rather than intrinsically lower $E_{\rm peak}$ values.

ESO 138-G01: The inferred $E_{\rm peak}$ values are highest in the center, but show a range of values in the larger outer bins. The variation in values is larger than the uncertainties, which are $0.05 - 0.15$ dex below and $0.13 - 0.20$ dex above the estimated values. The ENLR is evidently asymmetric, with harder radiation inferred to the west and east of the nucleus. There is a 'tail' of lower-$E_{\rm peak}$ values in some of the outer bins, which may be due to some combination of contamination from H II regions or DIG and the lower reddening.

IC 5063: $E_{\rm peak}$ values are systematically lower than in the other three 'pure Seyferts'. The smooth apparent decrease in $E_{\rm peak}$ in the central region, from southeast to northwest along the major axis, is comparable in magnitude to the 68% uncertainty ranges of the individual bins ($0.05 - 0.1$ dex below and $0.1 - 0.2$ dex above the estimates). The highest $E_{\rm peak}$ values are offset ∼10 arcsec to the southeast of the nucleus.

Mrk 573: The overall hardest inferred spectrum of the four Seyfert ENLRs studied here, with a large southeast-northwest swathe of the ENLR having $E_{\rm peak} \sim 40$ eV, and uncertainties of only ∼0.1 dex below and ∼0.15 dex above. A small number of bins to the north and south of the nucleus show a softer $E_{\rm peak}$ value. The 'tail' of lower $E_{\rm peak}$ values may be due to star formation contamination, especially considering that the low-$E_{\rm peak}$ regions coincide with the outer ring/spiral features in Figure 4.1.

NGC 2992: $E_{\rm peak}$ is measured to be higher in the ionization cones than in the central north-south dust lane. The $E_{\rm peak}$ range of ∼0.4 dex is larger than the uncertainties in individual bins, which are typically 0.1 dex below and 0.15 dex above. $E_{\rm peak}$ gradients are evident in both the eastern and western ionization cones. Overall the $E_{\rm peak}$ values are higher in the western cone, and the highest $E_{\rm peak}$ values occur over a range of radii in the western cone.

Ionization parameter

The ionization parameter shows remarkably little variation both within or between galaxies, with all measured values falling within $-3.2 \leq \log U \leq -2.6$. The widths of the 68% credible intervals have a median of $\sim 0.3 - 0.4$ dex for all four objects.

ESO 138-G01: The measured U is somewhat higher in the nucleus, but the measurements only vary within 0.2 dex of the median $\log U = -3.1$, with a standard deviation of 0.1 dex.

IC 5063: Again the measured U shows little variation. Two points of interest are local regions of slightly elevated ionization parameter ∼5 arcsec along the major axis either side of the nucleus.

Mrk 573: The highest ionization parameter measured in the four galaxies of $\log U = -2.65$ occurs in the southeastern part of the Mrk 573 ENLR. The distribution is asymmetric and bipolar; slightly higher $\log U$ values are observed along a southeast-northwest axis, with a slight positive radial gradient away from the nucleus in both directions along this axis.

NGC 2992: Both ionization cones and the dust lane show consistently similar U values.

Pressure

All four ENLRs show the highest pressure in the nuclear region, with the pressure in the outer parts approximately a factor of 10 lower than the maximum.

ESO 138-G01: The highest pressures are measured in the narrow east-west nuclear region along the ionization cone axis, where a prior was required to choose the desired solution. In the outer regions the pressures appear higher perpendicular to the cone axis compared to the on-axis pressures.

IC 5063: The highest measured pressure is slightly offset from the nucleus to the northwest.

Mrk 573: The nuclear pressure is lower than in the other galaxies (Table 4.2), and over the observed ENLR the pressures drop only 0.5 dex (the smallest range of the four galaxies). This apparent pressure homogeneity may reflect homogeneity of the entire ENLR (Section 4.6.4).

NGC 2992: There is a remarkable discontinuity between the measured pressure in the dusty nuclear region (where 8 bins have $\log P/k\,(\mathrm{cm}^{-3}\,\mathrm{K}) > 7.3$, with a maximum of 7.5), but lower pressures of $\log P/k\,(\mathrm{cm}^{-3}\,\mathrm{K}) \leq 6.6$ in most of the remainder of the ENLR. The ionization cones are presumably at a lower pressure because they are extraplanar.

Abundances

Two of the four objects show a clear radial gradient in measured abundances. Unfortunately there is no way to disentangle the geometry of the ENLR to measure de-projected gradients.

ESO 138-G01: There is a remarkable *inverse* abundance gradient, with the measured oxygen abundance ranging from approximately $12+\log \mathrm{O/H} = 8.5$ (half-Solar metallicity) in the nucleus up to 8.8 in the outer regions. Overall ESO 138-G01 shows the lowest abundances of the four galaxies studied here.

IC 5063: Apart from an anomalous outer bin, this galaxy shows a tiny range in abundances, with $8.80 \leq 12 + \log \mathrm{O/H} \leq 8.94$. There are two regions of slightly enhanced abundances either side of the nucleus, which have higher values than the nucleus.

Mrk 573: Uniformly high abundances are observed across the ~ 6 kpc of the ENLR, with the highest oxygen abundance of $12 + \log \mathrm{O/H} = 9.1$ ($\sim 3\, Z_{\odot}$) found in the nucleus, and measurements up to only 0.1 dex lower elsewhere in the ENLR (except for another anomalous outer bin).

NGC 2992: A strong abundance gradient is observed in the ENLR gas, and lower abundances are found in the eastern ionization cone compared to the western cone. Measured abundances decrease a massive 0.5 dex between the maximum value measured in the nucleus of $12 + \log \mathrm{O/H} = 9.12$ and the 8.62 measured at the edge of the western ionization cone.

4.6.4 Discussion of results for each galaxy

ESO 138-G01

This is a disky, non-star forming galaxy that features luminous Seyfert 2 AGN activity. The nuclear gas metallicity is slightly sub-Solar, despite the estimated stellar mass of $M_{*} = 10^{10.8}\, M_{\odot}$ (Thomas et al. 2017). In addition we measure an inverse abundance gradient in the ENLR, with abundances reaching up to $\sim$1.1 Solar in outer parts of the ENLR. Alloin et al. (1992) found that this object harbors both an old stellar population and a younger population with an age less than 1 Gyr.

These observations could potentially be explained by a recent minor merger event. In this scenario an infalling smaller galaxy would provide the lower metallicity gas, tidal effects in the merger would funnel the gas to the nucleus, and the relatively unobscured, lower-metallicity Seyfert AGN would result. The radial inflow of accreted gas explains the inverse metallicity gradient, and star formation from the newly accreted gas would explain the younger stellar population. This picture is consistent with the evidence that AGN activity generally lags star formation by a few hundred million years after a gas inflow (e.g. Wild et al. 2010).

Despite the apparent recent arrival of gas into ESO 138-G01, there does not appear to be evidence for current star formation. Goulding et al. (2012) fit a Spitzer-IRS spectrum to determine an AGN to starburst ratio of AGN:SB > 0.9, consistent with our optical emission-line diagnostics in Figure 4.2.

IC 5063

In this galaxy we measure all four parameters to be lower in the nucleus than in adjacent regions. This is likely caused by the large-scale galactic wind, which is evident in the three Gaussian components required to fit the nuclear emission lines (with widths up to $\sigma_v \sim 350\,\mathrm{km\,s^{-1}}$ and offsets between components of over $200\,\mathrm{km\,s^{-1}}$). The observed nuclear ENLR gas appears to be dominated by outflowing foreground material – the sum of the fluxes of the emission line kinematic components is dominated by the broad components in many nuclear bins.

The higher-U, higher-abundance 'knots' either side of the nucleus on the major axis appear to avoid the SW-NE 'stripe' of high velocity dispersion (Figure 4.3). Bennert et al. (2006a) also find that the ionization parameter does not peak in the nucleus, but is highest $5\farcs5$ SE of the nucleus. We speculate that these knots may be associated with lines of sight that avoid the illuminated outflowing extraplanar gas, allowing us to view gas that is more strongly illuminated, higher in abundance, and in fact closer to the nucleus than the gas observed in the nuclear bins. Similarly this geometrical effect may explain the fact that the inferred pressure peaks immediately to the northwest of the nucleus.

The lower values in the nucleus than in adjacent regions are more difficult to explain for E_{peak} than for the other parameters, although the variation is similar in size to the uncertainties. Because screening of the ionizing continuum is expected to increase rather than decrease E_{peak} (as described in Section 4.7), we instead favor shock contamination to explain the lower values. We expect shocks to be associated with the high velocity dispersion in the outflow. It is unclear how shock contamination may have affected the other parameter estimates.

The multi-phase outflow caused by the interaction between the radio jet and ISM in

IC 5063 is well studied (Dasyra et al. 2015; Morganti et al. 2015; Congiu et al. 2017, and references therein). Morganti et al. (2015) consider ALMA data and conclude that the rapidly outflowing $10^7\,M_\odot$ of molecular gas was most likely produced in post-shock cooling. Dasyra et al. (2015) use VLT SINFONI IFU observations to explore the complex 3D outflow structure in the central kiloparsec. High velocity blue-shifted and red-shifted gas was found to be co-located with the north and south radio lobes, which demonstrates that acceleration and scattering of material by the radio jet powers the high velocity nuclear outflows. Congiu et al. (2017) model line fluxes from long slit spectroscopy and argue that there is evidence for shocks significantly contributing to the ionization of high-velocity clouds. The work of Morganti et al. (2015), Dasyra et al. (2015) and Congiu et al. (2017) lends support to our suspicion that shocks are contaminating the summed nuclear line fluxes.

We note that the S7 data for IC 5063 exhibits NaI D-line absorption in neutral outflows backlit by stellar light, which are being explored in detail by Rupke et al. (in preparation).

Mrk 573

In this ENLR we see a double-cone of higher $E_{\rm peak}$ and U values stretching from southeast to northwest across the field of view. The ENLR features low reddening, with a median of $A_V = 0.4$ mag increasing to only ∼1 mag in the nucleus, despite uniformly high measured oxygen abundances of $1.7 - 2.1$ Solar. The presence of coronal lines in the nucleus together with the low reddening and high measured abundances suggest that dust destruction is occurring in this object. Dust destruction must have occurred in the nucleus to produce the coronal lines, but it may also be affecting the ENLR at large. Destroying dust would lower the reddening and would also increase the oxygen abundances inferred from our dusty models. This effect would occur because the dusty models need higher total abundances to achieve the same degree of cooling from free species as lower-depletion nebulae.

The N/O ratio provides further support to a picture in which large-scale dust destruction has occurred. Across all 61 valid ENLR bins shown in Figure 4.9 and Figure 4.10, [OIII] λ5007 is underpredicted in all but two bins, with the median underprediction being 22% of the dereddened observed flux. Conversely [NII] λ6583 is consistently overpredicted, with a median overprediction of 9% and overpredictions ranging up to 47%. The models used a depletion of 8.8% of nitrogen and 22% of oxygen by number onto dust grains. There is more oxygen than nitrogen to be freed by dust destruction, so the underprediction of [O III] λ5007 and overprediction of [N II] λ6583 is consistent with a scenario in which dust destruction has resulted in the N/O ratio being lower in the observed ENLR clouds than in the dusty models.

Confirming a scenario in which dust is destroyed across the ENLR is complicated by our lack of knowledge of the exact depletion of each element and the varying ratio of N to O abundances with metallicity. A more careful analysis would be required to be certain that the N abundance is significantly lower than expected considering the O abundance.

The lack of a significant metallicity gradient over ~ 3 kpc radially in the ENLR and the similar homogeneity of the measured pressures may indicate that radiation pressure-driven winds from the powerful AGN have mixed the ISM outwards. We note that if ubiquitous dust destruction has caused a bad mismatch between physical and modeled depletions and gas-phase abundances, any intrinsic abundance gradient in the ENLR may be masked. Nevertheless, if the AGN is responsible for both the lack of a metallicity gradient and large-scale dust destruction, the AGN may have been in a persistent high state for a considerable period of time. The pervasive AGN influence may be causing an ongoing dearth of star formation through general disruption of the ISM – destruction of dust shielding cool regions of the ISM, heating of the ISM, dissociation of molecular gas, and gas removal.

Fischer et al. (2017) studied gas kinematics in Mrk 573 with the Gemini NIFS IFU and the Dual Imaging Spectrograph at Apache Point Observatory. The authors concluded that outflowing gas currently extends to distances less than 1 kpc, and invoked radiation pressure in the acceleration.

Schlesinger et al. (2009) used HST spectroscopy to study the outflow in Mrk 573. A combination of emission-line diagnostics, thermodynamics (measured pressures and energies) and other data led the authors to conclude that the ENLR nebulae are photoionized and that the AGN outflow is weak and likely thermal. In particular the outflow was found to be unable to strongly shock material in the host galaxy. The low E_{peak} measurements we observe in some outer bins are therefore unlikely to be associated with shock contamination; H II region contamination may instead be the best explanation.

NGC 2992

This galaxy exhibits a variety of different regions in the ENLR. The high-extinction, high-pressure, low-$E_{\rm peak}$ nucleus is almost discontinuous with the eastern and western ionization cones. The nuclear region features a broad Gaussian component in the emission line profiles with a velocity width often exceeding $600\,{\rm km\,s^{-1}}$. The ionization cones show lower abundances, lower pressures, lower velocity dispersions and higher $E_{\rm peak}$ values than the nucleus. The northernmost bin shows 5 mag of extinction, yet the measured parameters conform with the ionization cones rather than the highly-reddened nucleus.

The broad line profiles suggest the lower nuclear $E_{\rm peak}$ values may be attributable to spectral contamination by shocks (related to the AGN or perhaps the interaction with NGC 2993), although H II regions in the galactic disk may also make a contribution. The softer ionizing continuum could also be due to a recent decrease in AGN activity, but the colocation of the broad outflowing lines and galactic disk with the low $E_{\rm peak}$ regions supports shock or H II region contamination as the cause. The varying $E_{\rm peak}$ in the ionization cones does not appear to be associated with variations in local dust obscuration, and may also be associated with shock or H II region contamination.

The ENLR is most remarkable for the strong abundance gradient that is observed. The maximum radial decrease is approximately 0.5 dex in oxygen abundance over approximately 10″ (1.5 projected kpc) in the western ionization cone in Figure 4.9. NGC 2992 has a B-band r_{25} of ∼60″ (de Vaucouleurs et al. 1991), so the magnitude of the ENLR abundance gradient appears to be a large multiple of the typical gradients measured in star-forming disk galaxies, which are in the range -0.4 to -0.2 dex r_{25}^{-1} (Sánchez et al. 2014; Ho et al. 2015). The steep gradient may be due to the ionization cone being out of the plane of the disk, with the z-direction abundance gradient perpendicular to the disk being steeper than the radial gradient.

Unfortunately it is difficult to measure a robust deprojected and normalized gradient. Any attempt at deprojection would need to take into account the unknown morphology of the ENLR and the high inclination of the galaxy ($i \sim 70°$; de Vaucouleurs et al. 1991). Tidal distortions and the high inclination both cause difficulties in accurately measuring r_{25}, so normalization of the gradient may also be challenging. Nevertheless the absolute value of the abundance change is large and the physical gradient is surely relatively steep compared to typical radial gradients in disk galaxies.

Large-scale gas flows in this galaxy may be occurring due to the tidal interaction with its companion and AGN-driven winds; the large abundance gradient may be evidence that AGN outflows have been ineffective at redistributing metals and that tidal forces have so far been ineffective at funneling lower-metallicity material towards the nucleus. Alternatively, tidally-driven low-metallicity gas out of the plane of the galaxy may have been illuminated by the AGN in the ionization cones. A faint 'bridge' of material between NGC 2992 and its companion is visible in DSS images; the extraplanar low-metallicity gas may even originate in the companion galaxy.

Stoklasová et al. (2009) use optical integral field data to study the central region of NGC 2992. A detailed kinematic analysis shows that the emitting species have different line-of-sight velocities, with the [O I] and [S II] line velocities varying most from the other strong lines (our LZIFU fitting did not permit velocity differences between lines). Stellar population modeling by Stoklasová et al. (2009) reveals a population of young stars $\sim 2''$ NW of the nucleus. This result lends some support to the idea of H II region contamination in the nuclear spectra lowering our $E_{\rm peak}$ measurements, but shocks due to the AGN or tidal forces from the ongoing galactic interaction may be more significant contaminants.

High spatial resolution NIR integral field data from SINFONI is studied by Davies et al. (2007), who investigate nuclear star formation in Seyferts. The data does not effectively constrain the star formation rate in the central $3 \times 3''$ of NGC 2992, although the authors find suggestions of recent star formation in the unresolved nucleus.

Davies et al. (2016) have studied NGC 2992 using the same S7 data that we use in this work. The authors visually compared the locus of flux ratios with a photoionization model grid on the BPT/VO diagrams (their Figure 3), inferring a range of ionization parameters of $-3.2 < \log U < 0$. The fitting constraints in this work instead require the ionization parameter to be a relatively constant $\log U \sim -3.0$ and rule out values as high as $\log U \sim 0$ in the nucleus (Figure 4.7; Table 4.2). Our results suggest that the variation in line ratios on the BPT/VO diagrams is due to variations in the metallicity, ionizing continuum, and gas pressure rather than ionization parameter (Figure 4.9), although shock or H II region contamination may also play a role, especially in the nuclear region.

4.7 Further discussion

We have presented the first robust, spatially-resolved measurements of abundances in AGN ENLRs. The four 'pure Seyfert' galaxies show very diverse distributions of metals in the ENLRs. We measure a positive abundance gradient, a strong negative gradient, and nearly uniform high abundances across an ENLR. Our results suggest that Seyfert AGN activity does not always flatten the gas-phase metallicity gradient in host galaxies by driving outflows of metal-rich nuclear material. If this were the case we would not observe the inverse abundance gradient in ESO 138-G01 or the strong positive abundance gradient in NGC 2992. However the large-scale, high-excitation, dust-poor, metal-rich, uniform-abundance ENLR in Mrk 573 suggests that sustained AGN activity has the potential to regulate the ISM on kiloparsec scales.

An important insight is given by the contrast between a) the uniformity of the inferred ionization parameters and b) the ubiquitous radial decline in pressure in the ENLRs. These results strongly imply that radiation pressure determines the density structure of the ISM on kpc scales. The photon number density $n_{\rm ph}$ decreases with the inverse square of the radius; if the ionization parameter $U = n_{\rm ph}/n_{\rm H}$ is nearly constant, then the ISM density (proportional to $n_{\rm H}$) must decline radially at approximately the same rate. This apparent similarity between the radial density distributions of photons and atoms occurs in all four ENLRs and must be caused by a coupling between the radiation field and the material illuminated in the ENLRs. The only feasible coupling mechanism is radiation pressure.

We consider the radiation pressures predicted by the 1D MAPPINGS photoionization models for particular $\log U$ and P values. The $\log U$ measurements correspond to total radiation pressures $P_{\rm rad}/P_{\rm gas} \sim 2-10\%$, where $P_{\rm gas} \equiv P$ is the initial gas pressure. This is a tight but ubiquitous range, which implies that $P_{\rm rad}/P_{\rm gas} \sim 2-10\%$ corresponds to a relatively widespread, long-lived and stable configuration of the ENLRs. It is unclear whether this configuration arises only through $P_{\rm rad}$ influencing the internal structure of individual clouds, or if bulk radiation-pressure driven outflows of the ENLR material are also important. Regardless of the exact effects, we can infer that $P_{\rm rad}$ is an important influence on the ENLR density structure even when $P_{\rm rad}$ is an order of magnitude weaker than $P_{\rm gas}$.

The evidence for an inverse-square density distribution is necessarily indirect. We do not attempt to perform detailed 3D modeling of ENLR geometry or to deproject the observed pressure maps. An inverse-square decrease in ISM density in the ENLRs is rather gradual considering that ENLRs are usually extraplanar. We suggest that this relatively slow radial density decrease is evidence for outflows, including radiation pressure-induced outflows in the ionization cones.

In their long-slit study of six nearby Seyfert 2 galaxies, Bennert et al. (2006a) measured radial profiles in electron density and ionization parameter. Bennert et al. (2006b) used similar methods to study a sample of six nearby Seyfert 1 galaxies. The measured ionization parameters generally decreased with radius but were always within the tight range of $U \sim 1 - 5 \times 10^{-3}$ for the Seyfert 2 galaxies, with the Seyfert 1 galaxies often showing values above and below this range.

Bennert et al. (2006a,b) measured radial electron density gradients using the optical [S II] doublet, finding power-law indices ranging from -1.3 to -0.8 for their Seyfert 2 galaxies and a range of -0.9 to -2.3 for the Seyfert 1 galaxies. In many cases these measurements may be consistent with an inverse-square density distribution; difficulties with the procedure include projection effects, profiles that were generally asymmetric around the nucleus, and unknown temperature gradients causing systematic uncertainties in the density measurements.

Studying the interplay between the ISM density and radiation pressure is complicated by the fact that we observe clouds with a range of physical conditions and galactocentric radii along any given line of sight (e.g. the locally optically emitting cloud (LOC) model of Ferguson et al. 1997). We note that the radiation pressure confinement (RPC) model of Stern et al. (2014) predicts radial profiles of the ionization parameter and density in an ENLR; in the future this or similar models may be compared to the results of NebulaBayes analyses of S7 ENLRs.

We have also presented systematic measurements of the spatial variation in the ionizing AGN continuum across the observed ENLRs. Unfortunately this parameter is almost certainly sensitive to contamination from H II regions, LINER-like emission and the DIG, as well as screening effects due to gas and dust lying between the nucleus and the observed clouds. Contaminating LINER-like emission is expected to be due to shocks, but may also arise from AGN radiation leaking out of the nuclear regions to excite nebulae with a low ionization parameter, and from excitation by post-AGB stars. The likely contamination prevents us from drawing conclusions from the spatial variation in inferred E_{peak} values. Almost all of the observed variation may be due to these confounding effects – indeed our results may be consistent with all luminous Seyferts sharing a similar EUV spectrum with a peak at $\sim$35 $-$ 40 eV. This scenario would be consistent with the speculation by Kraemer et al. (1999) that NLR line ratio variations are affected more by absorbing material internal to NLRs than by intrinsic continuum shape variations. Where variations in the incident continuum are not important, lower $E_{\rm peak}$ values would in fact *diagnose* contamination, which could reasonably be the case in IC 5063 and NGC 2992.

Screening by gas and dust is expected to harden the ionizing continuum, because the opacity of gas is highest at 1 Ryd and decreases towards higher energies, and approximately the same is true for dust grains (e.g. Weingartner & Draine 2001). Figure 4.10 shows that inferred $E_{\rm peak}$ values do not appear to be strongly related to the degree of local dust extinction. Screening associated with the low to moderate extinction may, however, have plausibly made a contribution to the small positive correlations between $E_{\rm peak}$ and A_V for ESO 138-G01 and IC 5063, but contaminating H II regions, DIG or shocks could also play a role. Material that screens the ionizing continuum is not necessarily located in front of or even nearby to the gas excited by the hardened continuum. Hence the absence of strong correlations in Figure 4.10 does not rule out absorption of the ionizing continuum causing the inferred spatial variations in $E_{\rm peak}$.

Contamination by H II regions is in some sense approximately accounted for by our $E_{\rm peak}$ parameter, which can take into account the resulting effective softening of the ionizing continuum (O stars have softer ionizing spectra than Seyfert nuclei). Hence when $E_{\rm peak}$ is lowered by H II region contamination, the metallicity measurement may remain reliable. Evidence in the nuclei of IC 5063 and NGC 2992 suggests that shock contamination is also able to lower the inferred $E_{\rm peak}$ values (Section 4.6.4 and Section 4.6.4), however this effect is not as easily understood. We do not consider the effects of contaminating DIG on the parameter estimates, but we note that DIG is likely to have a low surface brightness relative to NLR clouds, so DIG contamination is the least favored of the possible explanations for the measured $E_{\rm peak}$ variations.

Finally, we briefly consider how our results relate to variations in the available gas in the 'pure Seyfert' galaxies. These galaxies have no significant star formation (no 'pure H II' spectra), despite gas being available to feed the AGN. The environment has likely contributed to fueling the AGN in NGC 2992, which is interacting with a large companion galaxy, and in ESO 138-G01, which has evidence for a recent inflow. The observed large-scale AGN effects may have contributed to the lack of star formation, but conversely the extensive ENLRs may be associated with a lack of gas to hinder the ionizing radiation. These galaxies feature old stellar populations and may have been caught in a short-lived phase when 'quenching' is ongoing or recently completed (e.g. Leslie et al. 2016).

4.8 Conclusions

We have presented the new code NebulaBayes, which implements a general method of comparing observed emission-line fluxes to photoionization model grids. We use NebulaBayes with two grids – a 4D NLR grid over metallicity, ionization parameter U, pressure P and the hardness of the ionizing continuum $E_{\rm peak}$, and also a 3D H II region grid over metallicity, U and P. These grids are included with the code.

NebulaBayes was applied to four 'pure Seyfert' galaxies from the S7 survey - ESO 138-G01, IC 5063, Mrk 573 and NGC 2992, as well as the nucleus of the star-forming galaxy NGC 4691.

Our major conclusions are as follows:

1. We selected four Seyfert galaxies from the S7 survey with line emission dominated by ENLRs over kiloparsec scales. These objects did not exhibit any H II region-like spectra on optical diagnostic diagrams.
2. We present robust, spatially resolved measurements of abundances in AGN extended narrow-line regions (ENLRs)
3. We observe near-constant ionization parameters but steeply radially-decreasing pressures in all four ENLRs, implying that radiation pressure from the AGN has regulated the density structure of the ISM on kiloparsec scales
4. We observe an *inverse* abundance gradient in the ENLR of the E-S0 galaxy ESO 138-G01, and conclude that this galaxy experienced a recent inflow of relatively low-metallicity gas, possibly during a minor merger
5. Our analysis of IC 5063 is likely affected by contamination from shock excitation, and we find that the shock contamination seems to lower the inferred $E_{\rm peak}$
6. The ENLR of Mrk 573 shows high values of $E_{\rm peak}$ and uniformly high metallicity. There are indications that dust is substantially destroyed over kpc scales.

7. NGC 2992 shows steep metallicity gradients from the nucleus into the ionization cones, with the metallicity decreasing by up to half a dex. This demonstrates that tidal forces from the companion galaxy and AGN outflows have not flattened intrinsic metallicity gradients. Our analysis of the nucleus is likely contaminated by shock and possibly H II region emission.

8. We have presented systematic, spatially-resolved measurements of the hardness of the ionizing AGN continuum. Contamination from shock excitation and possibly H II regions has likely lowered the inferred E_{peak} values, so E_{peak} could potentially be used to diagnose contamination of NLR spectra

9. We do not find convincing evidence that screening of the intrinsic ionizing continuum by gas and dust has resulted in harder measured values of E_{peak}.

We anticipate that NebulaBayes will permit a greater understanding of how radiative AGN directly affect the ISM and hence star formation in galaxies. In the future we may 'mix' grids of NLR and H II-region photoionization models to extend the work presented here to Seyferts in the most common type of hosts, star-forming late-type galaxies. This would enable a systematic analysis of the Seyfert galaxies in the S7 sample. The effects of AGN on radial abundance gradients will likely be both more important and more difficult to measure in the Seyfert-hosting late-type galaxies.

Our H II region grid over the three parameters of metallicity, ionization parameter and pressure will enable more robust measurements of H II region abundances in the future.

The NebulaBayes code is very general and could also be applied to other emission-line regions for which physical models are available, for example planetary nebulae. In the future we may also use calculated grids of shock models with NebulaBayes to measure shock parameters in AGN-driven outflows.

Acknowledgements

We thank the anonymous referee for helpful comments. M.D. and L.K. acknowledge support from ARC discovery project #DP160103631. Parts of this research were conducted by the Australian Research Council Centre of Excellence for All Sky Astrophysics in 3 Dimensions (ASTRO 3D), through project number CE170100013. This research is supported by an Australian Government Research Training Program (RTP) Scholarship. The authors made use of the National Aeronautics and

Space Administration (NASA) Astrophysics Data System Bibliographic Services and the NASA/IPAC Extragalactic Database which is operated by the Jet Propulsion Laboratory, California Institute of Technology, under contract with NASA.

Appendix: Implementation of NebulaBayes

The NebulaBayes package is implemented in Python using the standard numerical library *numpy* (Van Der Walt et al. 2011), and works with both Python 2 and Python 3. The code is available online[2] and the package may be quickly installed from the Python Package Index (PyPI)[3].

The code is distributed with the H II region and NLR grids described in Section 4.3, however users may easily use their own custom grids.

The use of NebulaBayes consists of two steps:

1. Initializing a NebulaBayes 'model'.
2. Applying the initialized NebulaBayes model to observed emission-line data.

The (relatively computationally expensive) interpolation of predicted emission-line fluxes across the grid occurs during the first step. The initialized model may then be applied relatively cheaply to a large number of sets of observed emission lines.

The inputs to the initialization step are the following:

1. The input predicted model grid fluxes, specified in several possible ways, and associated parameter names
2. Lists of emission-line names. The model will only be initialized for these lines; hence the model can only later be applied to a subset of these lines.
3. The number of sampling points along each dimension for interpolation of the emission-line grids
4. The systematic relative error on grid fluxes, as a linear proportion (default is 0.35 or 35%)

[2] `https://github.com/ADThomas-astro/NebulaBayes`
[3] `https://pypi.python.org/pypi/NebulaBayes`
Install by typing: `pip install NebulaBayes`

The emission-line names are arbitrary and may refer to line blends or summed doublets as well as individual lines. A low sampling density of interpolated points may be used during initial working and then a higher density used to obtain final results. We note that the final parameter estimates are determined by the interpolated density – a parameter estimate can effectively only take a value corresponding to one of the parameter values in the interpolated grid.

The key inputs to the model-running step are:

1. The observed emission-line fluxes, errors, and line names. Upper bounds are included by setting the flux to $-\infty$.

2. A flag to indicate if NebulaBayes should perform a reddening correction (default False). The code is able to de-redden the observed fluxes *at every gridpoint of the interpolated model grid* to ensure the best possible comparison between the model and observed fluxes. This level of sophistication is necessary for NLR grids over which the variation of the intrinsic Balmer decrement is non-trivial, and is used for all the analysis in this work. The de-reddening method is described in the appendix of Vogt et al. (2013), and uses a relative extinction curve from Fischera & Dopita (2005). The line wavelengths must be supplied if de-reddening is requested.

3. The prior. There are several options available for customising the prior, and users may specify emission-line ratios to use as priors. The default is a bounded uniform prior.

4. A line to use for normalization. NebulaBayes will normalize observed and model fluxes to the chosen line before making further calculations; Hβ was used in this work.

Users are free to correct observed fluxes for reddening prior to using NebulaBayes. The de-reddening method included in NebulaBayes is valid only over the wavelength range $2480 - 12390$Å.

The optional prior is very flexible. The default bounded uniform prior will be flat in linear or in logarithmic space for each parameter, depending on whether the grid values for the parameter are specified in linear or logarithmic space. A user may supply a list of pairs of emission line names, in which case the NebulaBayes code will calculate a prior over the whole grid based on the ratio of each pair of lines (the density-sensitive optical [SII] doublet, for example), using effectively the same formula as Equation 4.2 (but comparing observed and predicted ratios, instead of single fluxes). If multiple line-ratio priors are specified they will all be multiplied together (weighted equally). This option allows users to treat known diagnostic line ratios as priors. The line ratios are compared directly to the model grid, so these priors are similar to line-ratio diagnostics that are 'calibrated on the fly' for the grid in use. Line ratios are useful priors in NebulaBayes because the code otherwise treats the emission lines independently, whereas a specific line ratio (such as the N2O2 index) is able to provide 'prior knowledge' (e.g. to constrain the metallicity).

When NebulaBayes is run on a set of observed lines, the following outputs are available:

1. 'Corner' diagrams containing a lower-triangular matrix of panels showing all possible joint 2D marginalized PDFs and 1D marginalized PDFs (as in Figures 4.4 to 4.8). One of these figures may be written out for each of the likelihood, prior and posterior, and also for the contribution to the likelihood made by each individual line.

2. A table of parameter estimates, including a row for each parameter and columns for lower and upper bounds on the 68% and 95% credible intervals. Each parameter estimate is defined by the peak of the relevant 1D marginalized posterior PDF, and the bounds are calculated from fixed percentiles of the 1D PDF (e.g. 2.5% and 97.5% for the 95% credible interval).

3. A table comparing observed and (interpolated) modeled fluxes at the point of the parameter best estimates.

4. In python code, NebulaBayes returns an object to allow programmatic manipulation of NebulaBayes data. The object holds references to all of the data that NebulaBayes uses in calculations, including the likelihood, prior and posterior PDFs (as regularly-sampled nD arrays).

NebulaBayes performs several checks to try to identify poorly-behaved/pathological posterior PDFs, the results of which are included in the output parameter estimate table. These checks include testing if a parameter estimate is at the lower or upper limit of its modelled range, if more than 50% of the probability is close to the lower or upper bounds, and if the parameter estimate lies within the credible intervals.

We remark on the following NebulaBayes implementation details:

1. Emission-line fluxes are interpolated using linear interpolation, which is necessary to ensure consistent and reliable interpolation behavior over an arbitrary number of dimensions. This method may lead to issues with interpolation accuracy, however it does guarantee that interpolated fluxes increase or decrease monotonically between raw input gridpoints, which is not the case for many standard interpolation routines. Our results generally have uncertainties larger than the intervals between the model gridpoints (e.g. Figures 4.5 to 4.8), so the quality of the interpolation is not a significant issue in this work.
2. The marginalization of PDFs uses trapezoidal integration, again because it is necessary to support an arbitrary number of dimensions.

Users should consider if the density of gridpoints in a custom input photoionization model grid is sufficient for the desired precision of the NebulaBayes parameter estimates, taking into account the use of linear interpolation and trapezoidal integration.

NebulaBayes comes with a unit/regression test suite. One of the tests uses fluxes from a gridpoint of a dummy model grid as the input observed fluxes, in order to ensure self-consistency of the NebulaBayes analysis – i.e. that the output and input grid parameters match.

Although they use very similar methods, there are some differences between NebulaBayes and IZI that we note here. NebulaBayes is more general than IZI because it is agnostic to the set of parameters and works on more than two dimensions; NebulaBayes is supplied with a 3D H II-region grid and a 4D NLR grid (Section 4.3) as opposed to the 2D H II-region grid supplied with IZI (which does not have pressure as a parameter). IZI uses spline interpolation, whereas NebulaBayes uses linear interpolation to handle an arbitrary number of dimensions. Additionally, the treatment of upper bounds differs slightly between NebulaBayes and IZI, with the $P(f_i < e_i)$ in Equation 4.5 differing from the $P(f_i < 1\sigma)$ approach used in IZI.

4.9 References

Allen, M. G., Groves, B. A., Dopita, M. A., Sutherland, R. S., & Kewley, L. J. 2008, ApJS, 178, 20-55

Allen, M. G., Dopita, M. A., Tsvetanov, Z. I., & Sutherland, R. S. 1999, ApJ, 511, 686

Alloin, D., Bica, E., Bonatto, C., & Prugniel, P. 1992, A&A, 266, 117

Baldwin, J. A., Phillips, M. M., & Terlevich, R. 1981, PASP, 93, 5

Bennert, N., Jungwiert, B., Komossa, S., Haas, M., & Chini, R. 2006, A&A, 456, 953

Bennert, N., Jungwiert, B., Komossa, S., Haas, M., & Chini, R. 2006, A&A, 459, 55
Bian, W., & Gu, Q. 2007, ApJ, 657, 159
Bianco, F. B., Modjaz, M., Oh, S. M., et al. 2016, Astronomy and Computing, 16, 54
Binette, L., Dopita, M. A., & Tuohy, I. R. 1985, ApJ, 297, 476
Blanc, G. A., Kewley, L., Vogt, F. P. A., & Dopita, M. A. 2015, ApJ, 798, 99
Cappellari, M., & Copin, Y. 2003, MNRAS, 342, 345
Cappellari, M., & Emsellem, E. 2004, PASP, 116, 138
Castro, C. S., Dors, O. L., Cardaci, M. V., & Hägele, G. F. 2017, MNRAS, 467, 1507
Childress, M. J., Vogt, F. P. A., Nielsen, J., & Sharp, R. G. 2014, Ap&SS, 349, 617
Congiu, E., Contini, M., Ciroi, S., et al. 2017, MNRAS, 471, 562
Cresci, G., Marconi, A., Zibetti, S., et al. 2015, A&A, 582, A63
Dasyra, K. M., Bostrom, A. C., Combes, F., & Vlahakis, N. 2015, ApJ, 815, 34
Davidson, K., & Netzer, H. 1979, Reviews of Modern Physics, 51, 715
Davies, R. I., Müller Sánchez, F., Genzel, R., et al. 2007, ApJ, 671, 1388
Davies, R. L., Dopita, M. A., Kewley, L., et al. 2016, ApJ, 824, 50
De Cicco, M., Marinucci, A., Bianchi, S., et al. 2015, MNRAS, 453, 2155
Denicoló, G., Terlevich, R., & Terlevich, E. 2002, MNRAS, 330, 69
Dietrich, M., Hamann, F., Shields, J. C., et al. 2003, ApJ, 589, 722
Dietrich, M., Crenshaw, D. M., & Kraemer, S. B. 2005, ApJ, 623, 700
Dopita, M. A., & Sutherland, R. S. 1996, ApJS, 102, 161
Dopita, M. A., Groves, B. A., Sutherland, R. S., Binette, L., & Cecil, G. 2002, ApJ, 572, 753
Dopita, M. A., Groves, B. A., Fischera, J., et al. 2005, ApJ, 619, 755
Dopita, M., Hart, J., McGregor, P., et al. 2007, Ap&SS, 310, 255
Dopita, M. A., & Sutherland, R. S. 2000, ApJ, 539, 742
Dopita, M., Rhee, J., Farage, C., et al. 2010, Ap&SS, 327, 245
Dopita, M. A., Sutherland, R. S., Nicholls, D. C., Kewley, L. J., & Vogt, F. P. A. 2013, ApJS, 208, 10
Dopita, M. A., Scharwächter, J., Shastri, P., et al. 2014, A&A, 566, A41
Dopita, M. A., Shastri, P., Davies, R., et al. 2015, ApJS, 217, 12
Dopita, M. A., Kewley, L. J., Sutherland, R. S., & Nicholls, D. C. 2016, Ap&SS, 361, 61
Dors, O. L., Cardaci, M. V., Hägele, G. F., & Krabbe, Â. C. 2014, MNRAS, 443, 1291
Dors, O. L., Cardaci, M. V., Hägele, G. F., et al. 2015, MNRAS, 453, 4102
Dors, O. L., Jr., Arellano-Córdova, K. Z., Cardaci, M. V., & Hägele, G. F. 2017, MNRAS, 468, L113
Du, P., Wang, J.-M., Hu, C., et al. 2014, MNRAS, 438, 2828
Fairall, A. P. 1988, MNRAS, 230, 69
Ferguson, J. W., Korista, K. T., Baldwin, J. A., & Ferland, G. J. 1997, ApJ, 487, 122
Fischer, T. C., Crenshaw, D. M., Kraemer, S. B., Schmitt, H. R., & Trippe, M. L. 2010, AJ, 140, 577
Fischer, T. C., Machuca, C., Diniz, M. R., et al. 2017, ApJ, 834, 30
Fischera, J., & Dopita, M. 2005, ApJ, 619, 340
Georgy, C., Ekström, S., Eggenberger, P., et al. 2013, A&A, 558, A103
Gilli, R., Maiolino, R., Marconi, A., et al. 2000, A&A, 355, 485
Goulding, A. D., Alexander, D. M., Bauer, F. E., et al. 2012, ApJ, 755, 5
Groves, B. A., Dopita, M. A., & Sutherland, R. S. 2004, ApJS, 153, 9
Groves, B., Dopita, M., & Sutherland, R. 2006, A&A, 458, 405
Hamann, F., & Ferland, G. 1999, ARA&A, 37, 487

Hampton, E. J., Medling, A. M., Groves, B., et al. 2017, MNRAS, 470, 3395
Ho, I.-T., Kudritzki, R.-P., Kewley, L. J., et al. 2015, MNRAS, 448, 2030
Ho, I.-T., Medling, A. M., Groves, B., et al. 2016, Ap&SS, 361, 280
Jenkins, E. B. 2009, ApJ, 700, 1299
Jenkins, E. B. 2014, arXiv:1402.4765
Juarez, Y., Maiolino, R., Mujica, R., et al. 2009, A&A, 494, L25
Kakkad, D., Mainieri, V., Padovani, P., et al. 2016, A&A, 592, A148
Kauffmann, G., Heckman, T. M., Tremonti, C., et al. 2003, MNRAS, 346, 1055
Kawasaki, K., Nagao, T., Toba, Y., Terao, K., & Matsuoka, K. 2017, ApJ, 842, 44
Kewley, L. J., Dopita, M. A., Sutherland, R. S., Heisler, C. A., & Trevena, J. 2001, ApJ, 556, 121
Kewley, L. J., & Dopita, M. A. 2002, ApJS, 142, 35
Kewley, L. J., Groves, B., Kauffmann, G., & Heckman, T. 2006, MNRAS, 372, 961
Kewley, L. J., & Ellison, S. L. 2008, ApJ, 681, 1183-1204
King, A., & Pounds, K. 2015, ARA&A, 53, 115
Kormendy, J., & Ho, L. C. 2013, ARA&A, 51, 511
Kraemer, S. B., Turner, T. J., Crenshaw, D. M., & George, I. M. 1999, ApJ, 519, 69
Kraemer, S. B., Schmitt, H. R., & Crenshaw, D. M. 2008, ApJ, 679, 1128-1143
Kraemer, S. B., Trippe, M. L., Crenshaw, D. M., et al. 2009, ApJ, 698, 106
Krolik, J. H., & Kallman, T. R. 1988, ApJ, 324, 714
Krumholz, M. R., Fumagalli, M., da Silva, R. L., Rendahl, T., & Parra, J. 2015, MNRAS, 452, 1447
Lauberts, A. 1982, Garching: European Southern Observatory (ESO), 1982
Leitherer, C., Schaerer, D., Goldader, J. D., et al. 1999, ApJS, 123, 3
Leslie, S. K., Kewley, L. J., Sanders, D. B., & Lee, N. 2016, MNRAS, 455, L82
Lumsden, S. L., Alexander, D. M., & Hough, J. H. 2004, MNRAS, 348, 1451
Malkan, M. A., Gorjian, V., & Tam, R. 1998, ApJS, 117, 25
Markwardt, C. B. 2009, Astronomical Data Analysis Software and Systems XVIII, 411, 251
Merluzzi, P., Busarello, G., Dopita, M. A., et al. 2018, ApJ, 852, 113
Morganti, R., Oosterloo, T., Oonk, J. B. R., Frieswijk, W., & Tadhunter, C. 2015, A&A, 580, A1
Müller-Sánchez, F., Prieto, M. A., Hicks, E. K. S., et al. 2011, ApJ, 739, 69
Nagao, T., Marconi, A., & Maiolino, R. 2006, A&A, 447, 157
Nagao, T., Maiolino, R., & Marconi, A. 2006, A&A, 447, 863
Nicholls, D. C., Dopita, M. A., & Sutherland, R. S. 2012, ApJ, 752, 148
Nicholls, D. C., Sutherland, R. S., Dopita, M. A., & Kewley, L. J. 2017, MNRAS, 466, 4403
Pagel, B. E. J., Edmunds, M. G., Blackwell, D. E., Chun, M. S., & Smith, G. 1979, MNRAS, 189, 95
Pérez-Montero, E. 2014, MNRAS, 441, 2663
Pettini, M., & Pagel, B. E. J. 2004, MNRAS, 348, L59
Pilyugin, L. S., & Thuan, T. X. 2005, ApJ, 631, 231
Rose, M., Elvis, M., Crenshaw, M., & Glidden, A. 2015, MNRAS, 451, L11
Sánchez, S. F., Kennicutt, R. C., Gil de Paz, A., et al. 2012, A&A, 538, A8
Sánchez, S. F., Rosales-Ortega, F. F., Marino, R. A., et al. 2012, A&A, 546, A2
Sánchez, S. F., Rosales-Ortega, F. F., Iglesias-Páramo, J., et al. 2014, A&A, 563, A49
Sánchez, S. F., García-Benito, R., Zibetti, S., et al. 2016, A&A, 594, A36

Schlesinger, K., Pogge, R. W., Martini, P., Shields, J. C., & Fields, D. 2009, ApJ, 699, 857

Sharp, R. G., & Bland-Hawthorn, J. 2010, ApJ, 711, 818

Smajić, S., Moser, L., Eckart, A., et al. 2015, A&A, 583, A104

Stoklasová, I., Ferruit, P., Emsellem, E., et al. 2009, A&A, 500, 1287

Stern, J., Laor, A., & Baskin, A. 2014, MNRAS, 438, 901

Storchi-Bergmann, T., Schmitt, H. R., Calzetti, D., & Kinney, A. L. 1998, AJ, 115, 909

Storchi-Bergmann, T., Lopes, R. D. S., McGregor, P. J., et al. 2010, MNRAS, 402, 819

Sutherland, R. S., & Dopita, M. A. 2017, ApJS, 229, 34

Tadhunter, C., Morganti, R., Rose, M., Oonk, J. B. R., & Oosterloo, T. 2014, Nature, 511, 440

Taylor, E. N., Hopkins, A. M., Baldry, I. K., et al. 2011, MNRAS, 418, 1587

Thomas, A. D., Groves, B. A., Sutherland, R. S., et al. 2016, ApJ, 833, 266

Thomas, A. D., Dopita, M. A., Shastri, P., et al. 2017, ApJS, 232, 11

Thomas, A. D., Dopita, M. A., Kewley, L. J., et al. 2018, ApJ, 856, 89

Toomre, A., & Toomre, J. 1972, ApJ, 178, 623

Trippe, M. L., Crenshaw, D. M., Deo, R., & Dietrich, M. 2008, AJ, 135, 2048

van Zee, L., Salzer, J. J., Haynes, M. P., O'Donoghue, A. A., & Balonek, T. J. 1998, AJ, 116, 2805

Vogt, F. P. A., Dopita, M. A., & Kewley, L. J. 2013, ApJ, 768, 151

Sutherland, R. S., & Dopita, M. A. 1993, ApJS, 88, 253

Vale Asari, N., Stasińska, G., Morisset, C., & Cid Fernandes, R. 2016, MNRAS, 460, 1739

Van Der Walt, S., Colbert, S. C., & Varoquaux, G. 2011, Computing in Science & Engineering, 13, 22

de Vaucouleurs, G., de Vaucouleurs, A., Corwin, H. G., Jr., et al. 1991, Third Reference Catalogue of Bright Galaxies. Springer, New York, NY (USA), 2091 p.

Veilleux, S., & Osterbrock, D. E. 1987, ApJS, 63, 295

Véron-Cetty, M.-P., & Véron, P. 2010, A&A, 518, A10

Weingartner, J. C., & Draine, B. T. 2001, ApJ, 548, 296

Wagner, A. Y., Bicknell, G. V., Umemura, M., Sutherland, R. S., & Silk, J. 2016, Astronomische Nachrichten, 337, 167

Ward, M., Penston, M. V., Blades, J. C., & Turtle, A. J. 1980, MNRAS, 193, 563

Wild, V., Heckman, T., & Charlot, S. 2010, MNRAS, 405, 933

Zaritsky, D., Kennicutt, R. C., Jr., & Huchra, J. P. 1994, ApJ, 420, 87

5

Mixing between Seyfert and HII-region emission in active galaxies

This chapter presents the content of the article *Mixing between Seyfert and H* II-*region excitation in local active galaxies* (Thomas et al. 2018b). The abstract is as follows:

> We fit theoretical models to the emission-line spectra of 2766 Seyfert galaxies from the Sloan Digital Sky Survey (SDSS). The model line fluxes are derived by 'mixing' photoionization model predictions of active galactic nucleus (AGN) narrow line region (NLR) emission and H II region emission. The observed line fluxes in each spectrum were directly compared to the grid of mixed models using the Bayesian parameter estimation code NebulaBayes, thereby measuring the degree of mixing in each spectrum for the first time. We find that the majority of the Balmer line emission in the majority of Seyfert-classified SDSS spectra arises from contaminating H II regions within the fixed-size aperture. Even for spectra with log [O III]/H$\beta \gtrsim 0.9$, a median of $\sim$30% of the

Balmer flux arises in H II regions. We show that the results are qualitatively insensitive to the assumed Seyfert ionizing continuum, and that ionizing spectra with a peak energy of $E_{\rm peak} \sim 40 - 50$ eV produce the most plausible distributions of mixing fractions. The analysis cleanly quantifies how the starburst – AGN 'mixing fraction' increases on the BPT diagram for SDSS galaxies. Apart from the mixing fraction, the models also vary with the ionization parameter in the NLR, the gas pressure, and the metallicity. Measurements for the metallicity in particular will be presented in a companion paper.

5.1 Introduction

The Sloan Digital Sky Survey (SDSS; York et al. 2000) provides a rich spectroscopic sample of galaxies in the local universe, including tens of thousands of galaxies hosting Active Galactic Nuclei (AGN). The SDSS AGN population has been extensively studied, providing insights into many aspects of the population: the host galaxy properties (e.g. Kauffmann et al. 2003; Kewley et al. 2006; Koss et al. 2011; Reines & Volonteri 2015), nuclear activity as a function of galaxy environment (e.g. Miller et al. 2003; Constantin et al. 2008; von der Linden et al. 2010; Khabiboulline et al. 2014) classification of excitation mechanisms (e.g. Kewley et al. 2006; Shirazi & Brinchmann 2012; Bär et al. 2017), gas kinematics (e.g. Greene & Ho 2005), comparisons to AGN emission at other wavelengths (e.g. Kauffmann et al. 2008; Koss et al. 2011; Mateos et al. 2013; Paliya et al. 2018), relative alignment of the host galaxy and active nucleus (Lagos et al. 2011), and the distribution of black hole masses and Eddington ratios (e.g Greene & Ho 2007; Kauffmann & Heckman 2009; Jones et al. 2016) amongst other topics.

A large proportion of SDSS AGN spectra show clear mixing between H II region emission and AGN NLR emission on optical diagnostic diagrams. This mixing is broadly attributable to the summing of emission in the SDSS fiber aperture, but more subtly is associated with the correlation between star formation rate and population-averaged supermassive black hole accretion rate (e.g. Chen et al. 2013) and with the close timing of starbursts and black hole accretion (e.g. Wild et al. 2010). Although integral field data now allows detailed spatial analysis of the mixing of H II and NLR emission (e.g. Davies et al. 2014a,b; Dopita et al. 2014), the effect of H II region contamination on single-fibre SDSS NLR spectra has not been robustly quantified. The H II – NLR mixing significantly complicates detailed photoionization modelling of the SDSS AGN.

In this Letter we tackle the H II – NLR mixing using theoretical models and a general Bayesian method, determining the proportion of the emission arising from each of the two mechanisms for each SDSS AGN spectrum. We demonstrate that the mixing is an important consideration even for the highest-excitation AGN spectra in the SDSS sample.

5.2 Observational data

Our sample is taken from SDSS DR7 (Abazajian et al. 2009), and we use the emission line fluxes provided by the MPA/JHU catalogue[1] (Tremonti et al. 2004). We selected galaxies with redshifts in the range $0.02 < z < 0.37$, which resulted in the g-band covering fraction (proportion of the galaxy light within the fiber aperture) having a 25th percentile, median, and 75th percentile of 0.15, 0.22 and 0.30, respectively. The lower redshift cut involves a trade-off between sample size and potential systematic aperture effects due to low covering fractions (Kewley et al. 2005), and is also determined by the need for the [O II] doublet to be redshifted into the observed wavelength range.

We applied the following further cuts:

1. All fluxes and errors of relevant emission lines were required to be finite and positive
2. A signal to noise (S/N) cut was applied based on the Hβ flux. We required Hβ S/N > 5 and did not use S/N cuts on other lines to avoid biasing the sample (in particular, biasing the metallicities).
3. We required spectra to have a Balmer decrement Hα / Hβ greater than 2.7, because lower values are unphysical, and we require reliable flux calibration and reddening corrections.

After these cuts there remained 2766 Seyfert-classified objects and 51806 H II-classified objects. The spectra were classified using the [N II] and [S II] optical diagnostic diagrams (Baldwin et al. 1981; Veilleux & Osterbrock 1987), following the method

[1] `www.mpa-garching.mpg.de/SDSS/DR7/`
`http://home.strw.leidenuniv.nl/~jarle/SDSS/`

of Kewley et al. (2006). Only the Seyfert- and 'composite'-classified galaxies were included in the analysis, with LINER, star-forming, and ambiguous galaxies being excluded.

5.3 Method

The primary tool we use in our analysis is NebulaBayes[2], a package that performs Bayesian parameter estimation by comparing observed emission line fluxes and errors with an arbitrary grid of model fluxes. NebulaBayes is described in detail by Thomas et al. (2018a).

The MAPPINGS V (Sutherland & Dopita 2017) photoionization model grids we feed into NebulaBayes are 'mixing' grids, derived by combining H II region and NLR model grids. Both grids have dimensions in the parameters of oxygen abundance $12 + \log \mathrm{O/H}$, ionization parameter at the inner edge of the photoionization model $\log U$, and gas pressure $\log P/k$. In addition, the NLR grid has a fourth parameter E_{peak}, which is the peak (on a log-log plot of energy flux versus energy) of the 'big blue bump' ionizing accretion disk emission in the model of the ionizing spectrum (Thomas et al. 2016). The H II and NLR grids used here are the same as those distributed with the NebulaBayes software (Thomas et al. 2018a), with the exception of four intermediate E_{peak} values that have been added to the NLR grid.

The H II and NLR grids were combined into a 'mixing' grid using the following assumptions:

1. The H II regions and NLR clouds within the same aperture have the same metallicity

2. The H II regions and NLR clouds within the same aperture have the same pressure, $\log P/k$

3. There is little sensitivity to the H II region ionization parameter. This parameter was fixed at $\log U_{\mathrm{HII}} = -3.25$, a representative value for high metallicity galaxies that was found by analysing the SDSS H II spectra using NebulaBayes with the H II region grid alone.

4. E_{peak} can be fixed to a single representative value without biasing the results.

[2] `https://github.com/ADThomas-astro/NebulaBayes`

The number of parameters is limited by computational practicalities and by the number of independent line fluxes in each spectrum. A more complex model is unlikely to be justified by statistically significant improvements to model fits.

The 'mixing' is parametrized by $f_{\rm NLR}$, the proportion of the Hβ flux in a 'mixed' spectrum that arises from NLR as opposed to H II emission ($f_{\rm HII} = 1 - f_{\rm NLR}$). This parametrization, first used by Kewley et al. (2001b), is more sophisticated than approaches that use distances on the optical diagnostic diagrams to parametrize the gas excitation (e.g. Khabiboulline et al. 2014). We sampled $f_{\rm NLR}$ at the six values $f_{\rm NLR} = 0.0$, 0.2, 0.4, 0.6, 0.8 and 1.0. In total, there were four parameters in each mixing grid (with a different grid for each considered $E_{\rm peak}$ value): $12 + \log {\rm O/H}$, $\log P/k$, $\log U_{\rm NLR}$ and $f_{\rm NLR}$.

The following emission lines were used in the analysis: [OII] λ 3726+29, [NeIII] λ 3869, [OIII] λ 4363, [OIII] λ 5007, HeI λ 5876, [OI] λ 6300, [NII] λ 6583, and [SII] λ 6716+31. We also included H α and Hβ, which are essential for both normalization and reddening-correction. We used the built-in ability of NebulaBayes to deredden spectra to match the predicted Balmer decrement at every point in the model grid.

Two priors were combined, with equal weighting. These were a prior on the [SII] doublet flux ratio, to constrain the gas pressure, and a prior on the [NII]/[OII] ratio, to help constrain the metallicity.

5.4 Results

5.4.1 Variation in the mixing fraction

Our results for the parameter $f_{\rm NLR}$ are presented in Figure 5.1 on optical diagnostic diagrams, with the classification lines described by Kewley et al. (2006) shown for reference. The results show that the mixing fraction $f_{\rm NLR}$ behaves intuitively by increasing upwards along the mixing sequence from the star-forming sequence to the Seyfert region.

The red line in the left panel of Figure 5.1 is a 'mixing line', which is chosen to be linear in log-log space and follow the upper locus of the H II-AGN mixing sequence. The line connects the median H II-classified point (at $(x, y) = (-0.466, -0.408)$) and the median Seyfert-classified point with $y > 0.9$ (at $(x, y) = (0.003, 0.979)$), where

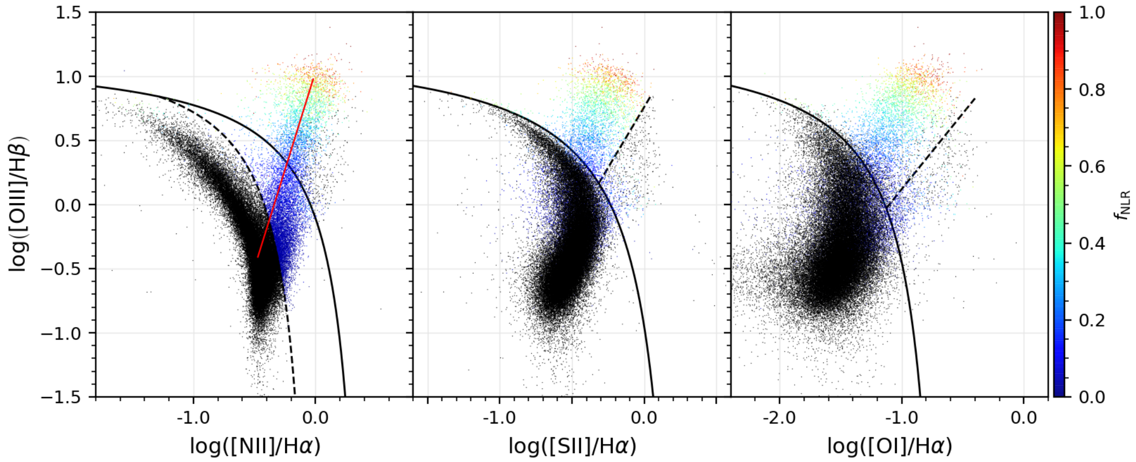

Figure 5.1 Optical diagnostic diagrams showing SDSS data colored by the fitted values of f_{NLR}, the proportion of the Hβ flux that arises in NLR as opposed to H II-region emission. The colored points are classified as 'composite' or Seyfert using the [NII] and [SII] diagrams, with all other classifications shown in black. The dashed line (Kauffmann et al. 2003) in the left-most panel gives an empirical upper-limit on the line ratios of star-forming galaxies, and the solid black lines in all three panels give corresponding theoretical limits (Kewley et al. 2001a). The dashed lines in the rightmost two panels approximately separate Seyferts (above) from LINERs (below; Kewley et al. 2006), and the red line in the leftmost panel is chosen to approximately follow the H II-Seyfert 'mixing sequence'. There is a clear increase in f_{NLR} up the mixing sequence from star-forming galaxies to Seyfert galaxies. This analysis used a Seyfert ionizing spectrum with $E_{\mathrm{peak}} = 45\,\mathrm{eV}$.

$x = \log$ [NII]/Hα and $y = \log$ [OIII]/Hβ. We note that a true 'mixing locus' would be curved in the Figure 5.1 log-log plot.

5.4.2 Effect of the ionizing Seyfert spectrum

The mixing fraction f_{NLR} is degenerate with the parameter corresponding to the hardness of the Seyfert radiation field, E_{peak}. Increasing either quantity has the effect of increasing the effective ionization of a 'mixed' model spectrum. Understanding the effect of E_{peak} allows us to quantify typical f_{NLR} values as a function of the position of SDSS galaxies on the optical diagnostic diagram.

Figure 5.2 shows the inferred mixing fraction f_{NLR} versus projected distance along the mixing line d, for a series of E_{peak} values. The $d = 0$ point was chosen to coincide with the intersection of the red mixing line and the solid black line (extreme starburst line of Kewley et al. 2001a) in Figure 5.1. For $E_{\mathrm{peak}} = 32$ eV the high-f_{NLR} data is clustered at $f_{\mathrm{NLR}} = 1$, presumably because the observed spectra have a higher ionization than the models in the relevant part of the parameter space, resulting in the inferred f_{NLR} being artificially elevated. Conversely, at the other extreme of $E_{\rm peak} = 100$ eV (improbably high considering the ionization potentials of species observed in typical NLRs), all galaxies have a relatively low inferred $f_{\rm NLR}$ value. Results do not change significantly for $E_{\rm peak}$ in the range $E_{\rm peak} \sim 40 - 50$ eV, and we select $E_{\rm peak} = 45\,{\rm eV}$ to use in quantifying typical mixing fractions on the mixing sequence.

The scatter in $f_{\rm NLR}$ may be associated with variations in the three other parameters, which would allow a range of $f_{\rm NLR}$ values to correspond to a single d value. However, a major contribution to the scatter is likely to be variation in the intrinsic $E_{\rm peak}$ values of the AGN population. We expect $E_{\rm peak}$ to increase with the Eddington ratio $\lambda_{\rm Edd}$, and the SDSS Seyfert $\lambda_{\rm Edd}$ distribution is known to have a non-trivial width (e.g. Kewley et al. 2006; Kauffmann & Heckman 2009). Variation in $\lambda_{\rm Edd}$ should cause more scatter at high $f_{\rm NLR}$, and indeed the scatter does noticeably increase with $f_{\rm NLR}$ (and d) in all panels of Figure 5.2.

5.4.3 Measuring typical mixing fractions

We now consider the typical mixing fractions as a function of location on the BPT diagram. Figure 5.3 shows an [N II] optical diagnostic diagram, illustrating the derived lines of 'median mixing fraction'. These green mixing fraction lines correspond to the green vertical lines in the $E_{\rm peak}$= 45 eV panel of Figure 5.2. In Figure 5.3 these lines are drawn perpendicular to the red mixing line, and have a gradient of $m = -0.327$. The intercept b (where $y = mx + b$) for each line is 0.341, 0.676, and 0.893 for $f_{\rm NLR}$= 0.2, 0.4 and 0.6 respectively.

A key result evident in Figures 5.2 and 5.3 is that for the majority of Seyfert-classified SDSS spectra, the majority of the Balmer emission arises in H II regions, and not in the NLRs. Only spectra with log [O III]/H$\beta \gtrsim 0.9$ typically have the majority of the Balmer flux arising in the Seyfert NLRs. These results hold true for all $E_{\rm peak}$ in the range $40 - 50\,{\rm eV}$.

5.5 Discussion

We have clearly demonstrated that modeling of Seyfert emission in the SDSS sample must take H II-region contamination into account. Cuts on BPT classifications may remove AGN spectra with a high degree of H II contamination (e.g. Maragkoudakis

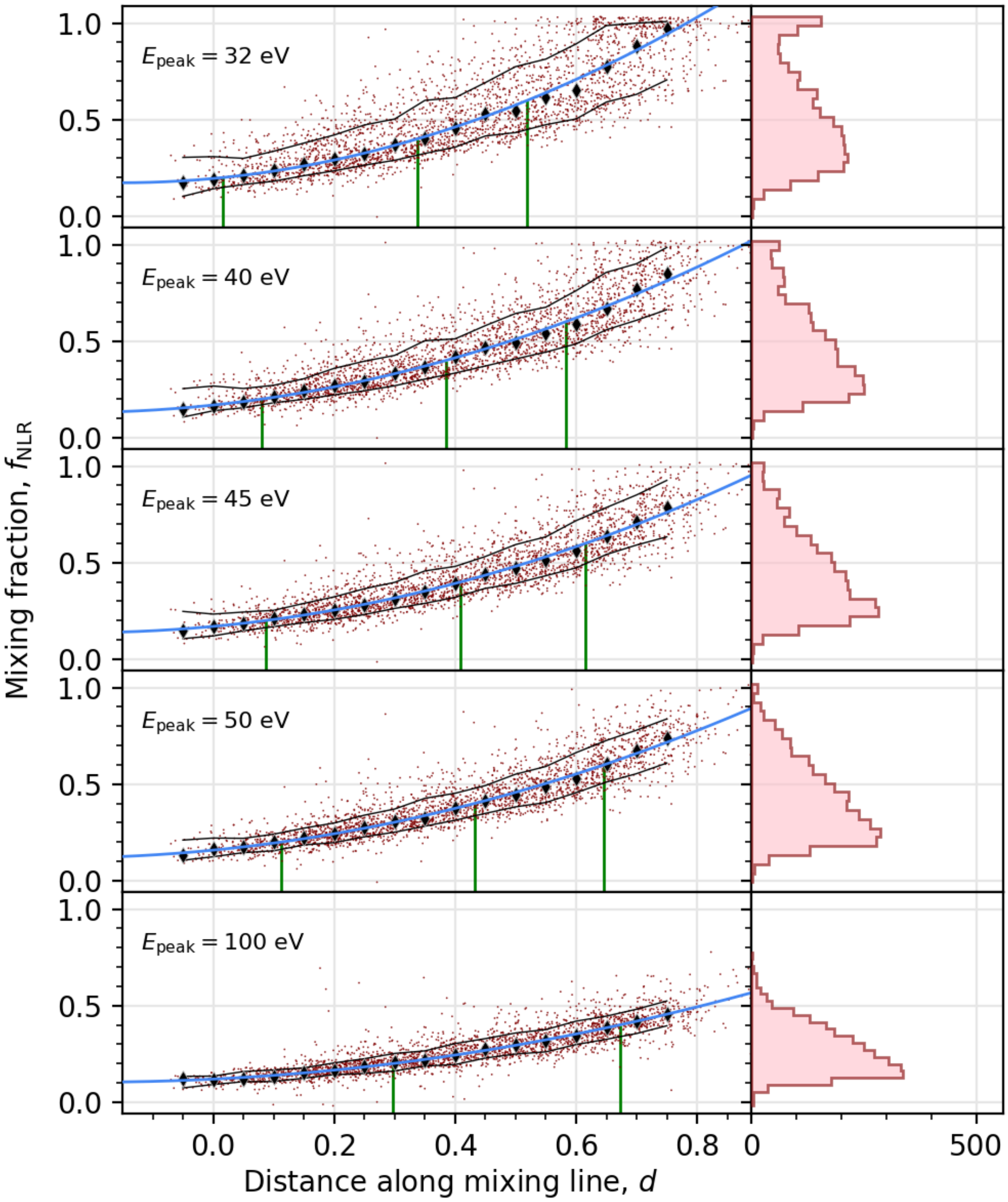

Figure 5.2 The inferred mixing fraction $f_{\rm NLR}$ versus d, the projected distance along the 'mixing line' (the red line in Figure 5.1; the intersection with the Kewley et al. (2001a) line defines $d = 0$). Results are presented for Seyfert-classified galaxies for five values of $E_{\rm peak}$, the peak of the ionizing Seyfert continuum spectrum. Black diamonds show the median in each d-bin, and black lines show the 16th and 84th percentiles. The blue curve is a parabola fitted to the medians and errors. Green vertical lines indicate where 20, 40 and 60% of the Balmer flux arises due to Seyfert photoionization as opposed to H II-region emission, according to the blue fits. For all plausible values of $E_{\rm peak}$, the analysis demonstrates that the majority of the line emission in the majority of Seyfert-classified SDSS galaxies arises in H II regions as opposed to the NLRs. The parameters $E_{\rm peak}$ and $f_{\rm NLR}$ both vary the ionization level of the models and therefore are difficult to disentangle, but the figure shows that the inferred $f_{\rm NLR}$ sequence is qualitatively insensitive to $E_{\rm peak}$, with $E_{\rm peak} \sim 40 - 50\,{\rm eV}$ producing a plausible $f_{\rm NLR}$ distribution.

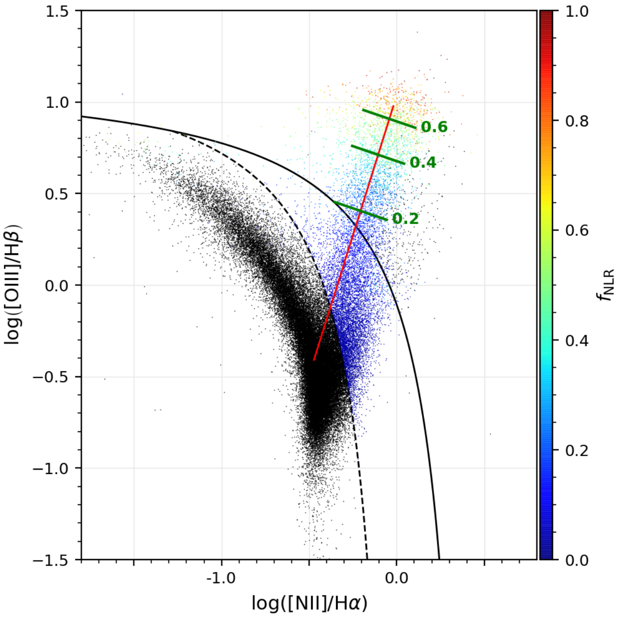

Figure 5.3 Optical diagnostic diagram as in Figure 5.1, but with green lines added to indicate the median mixing fraction $f_{\rm NLR}$ on the H II to AGN mixing sequence. The $f_{\rm NLR}$ estimates were obtained using the 'mixing' model grid with $E_{\rm peak} = 45$ eV.

et al. 2014), but our results show that a large fraction of the remaining spectra are significantly contaminated. A small proportion of LINER galaxies may remain in our Seyfert sample due to the approximate nature of the Seyfert-LINER separation (Kewley et al. 2006). However, these interloping LINERs are unlikely to affect the results (especially considering that ionization parameter varies in our models).

Table 5.1 shows the relative contributions of NLR emission and H II region emission to line fluxes in mixed model spectra. The [O III] emission is dominated by NLR clouds even at low $f_{\rm NLR}$, but the proportional NLR flux contribution is consistently below $f_{\rm NLR}$ for [N II] and [S II]. Evidently [O III] is a highly sensitive tracer of AGN contamination in H II spectra. Conversely, for other lines, the Seyfert-classified spectra may easily suffer significant contamination from H II-region emission. The data in Table 5.1 appears to be consistent with Figure 3 of Kauffmann & Heckman (2009), who also calculate likely H II region contributions to the [O III] flux.

It was necessary when constructing the mixing grid to fix $\log U_{\rm HII}$ (Section 5.3), and we have tested the sensitivity of our results to this assumption by varying the fixed $\log U_{\rm HII}$ value. The analysis presented in Figure 5.2 and Figure 5.3 was performed for the three values $\log U_{\rm HII} = -3.50$, -3.25, and -3.00 with $E_{\rm peak} = 45\,{\rm eV}$. In this experiment the lines of median $f_{\rm NLR}$ values of 0.2, 0.4 and 0.6 all changed by at most 0.07 dex in [O III]/Hβ. Hence, we conclude that our results are insensitive to

Table 5.1 Proportion of the flux in a 'mixed' spectrum that is from AGN NLR models as opposed to H II region models, for each strong optical line. The models have $12 + \log \mathrm{O/H} = 8.990$, $E_{\mathrm{peak}} = 45$ eV, $\log U_{\mathrm{NLR}} = -2.60$, $\log U_{\mathrm{HII}} = -3.25$, and $\log P/k\,(\mathrm{cm}^{-3}\,\mathrm{K}) = 7.40$.

f_{NLR}	Hβ	[OII]$\lambda\lambda3726, 29$	[OIII]5007	[OI]6300	[NII]6583	[SII]$\lambda\lambda6716, 31$
0.0	0.0	0.000	0.000	0.000	0.000	0.000
0.1	0.1	0.213	0.952	0.403	0.092	0.093
0.2	0.2	0.378	0.978	0.603	0.186	0.188
0.4	0.4	0.618	0.992	0.802	0.379	0.381
0.6	0.6	0.785	0.996	0.901	0.579	0.581
0.8	0.8	0.907	0.999	0.960	0.786	0.787
1.0	1.0	1.000	1.000	1.000	1.000	1.000

$\log U_{\mathrm{HII}}$, despite the low f_{NLR} values.

5.6 Conclusions

Mixing between H II region and AGN emission in SDSS galaxies is investigated by explicitly fitting 'mixing' models to the data for the first time. Our conclusions are as follows:

1. We demonstrate that most Seyfert-classified spectra in SDSS have the majority of their Balmer line flux originating in H II regions within the fixed fiber aperture, rather than in the NLR itself

2. We show that our results are insensitive to the hardness of the assumed Seyfert ionizing continuum, and find that ionizing spectra peaking at energies of $E_{\mathrm{peak}} \sim 40 - 50$ eV result in the most plausible distributions of inferred mixing fractions

3. We provide equations of lines that quantify median 'mixing levels' on the [N II] BPT diagram

4. We quantify the contributions to key emission-line fluxes from the model H II and NLR spectra

Acknowledgements

This research was conducted by the Australian Research Council Centre of Excellence for All Sky Astrophysics in 3 Dimensions (ASTRO 3D), through project number CE170100013. B.G. acknowledges the support of the Australian Research Council as the recipient of a Future Fellowship (FT140101202). M.D. and R.S. acknowledge support from ARC discovery project #DP160103631. This research is supported by an Australian Government Research Training Program (RTP) Scholarship.

5.7 References

Abazajian, K. N., et al. 2009, ApJS, 182, 543 (ADS entry)

Baldwin, J. A., Phillips, M. M., & Terlevich, R. 1981, PASP, 93, 5 (ADS entry)

Bär, R. E., Weigel, A. K., Sartori, L. F., Oh, K., Koss, M., & Schawinski, K. 2017, MNRAS, 466, 2879 (ADS entry)

Chen, C.-T. J., et al. 2013, ApJ, 773, 3 (ADS entry)

Constantin, A., Hoyle, F., & Vogeley, M. S. 2008, ApJ, 673, 715 (ADS entry)

Davies, R. L., Kewley, L. J., Ho, I.-T., & Dopita, M. A. 2014a, MNRAS, 444, 3961 (ADS entry)

Davies, R. L., Rich, J. A., Kewley, L. J., & Dopita, M. A. 2014b, MNRAS, 439, 3835 (ADS entry)

Dopita, M. A., et al. 2014, Astronomy & Astrophysics, 566, A41 (Link)

Greene, J. E., & Ho, L. C. 2005, ApJ, 627, 721 (ADS entry)

—. 2007, ApJ, 667, 131 (ADS entry)

Jones, M. L., Hickox, R. C., Black, C. S., Hainline, K. N., DiPompeo, M. A., & Goulding, A. D. 2016, ApJ, 826, 12 (ADS entry)

Kauffmann, G., & Heckman, T. M. 2009, MNRAS, 397, 135 (ADS entry)

Kauffmann, G., Heckman, T. M., & Best, P. N. 2008, MNRAS, 384, 953 (ADS entry)

Kauffmann, G., et al. 2003, MNRAS, 346, 1055 (ADS entry)

Kewley, L. J., Dopita, M. A., Sutherland, R. S., Heisler, C. A., & Trevena, J. 2001a, ApJ, 556, 121 (ADS entry)

Kewley, L. J., Groves, B., Kauffmann, G., & Heckman, T. 2006, MNRAS, 372, 961 (ADS entry)

Kewley, L. J., Heisler, C. A., Dopita, M. A., & Lumsden, S. 2001b, ApJS, 132, 37 (ADS entry)

Kewley, L. J., Jansen, R. A., & Geller, M. J. 2005, PASP, 117, 227 (ADS entry)

Khabiboulline, E. T., Steinhardt, C. L., Silverman, J. D., Ellison, S. L., Mendel, J. T., & Patton, D. R. 2014, ApJ, 795, 62 (ADS entry)

Koss, M., Mushotzky, R., Veilleux, S., Winter, L. M., Baumgartner, W., Tueller, J., Gehrels, N., & Valencic, L. 2011, ApJ, 739, 57 (ADS entry)

Lagos, C. D. P., Padilla, N. D., Strauss, M. A., Cora, S. A., & Hao, L. 2011, MNRAS, 414, 2148 (ADS entry)

Maragkoudakis, A., Zezas, A., Ashby, M. L. N., & Willner, S. P. 2014, MNRAS, 441, 2296 (ADS entry)
Mateos, S., Alonso-Herrero, A., Carrera, F. J., Blain, A., Severgnini, P., Caccianiga, A., & Ruiz, A. 2013, MNRAS, 434, 941 (ADS entry)
Miller, C. J., Nichol, R. C., Gómez, P. L., Hopkins, A. M., & Bernardi, M. 2003, ApJ, 597, 142 (ADS entry)
Paliya, V. S., Ajello, M., Rakshit, S., Mandal, A. K., Stalin, C. S., Kaur, A., & Hartmann, D. 2018, ApJL, 853, L2 (ADS entry)
Reines, A. E., & Volonteri, M. 2015, ApJ, 813, 82 (ADS entry)
Shirazi, M., & Brinchmann, J. 2012, MNRAS, 421, 1043 (ADS entry)
Sutherland, R. S., & Dopita, M. A. 2017, ApJS, 229, 34 (ADS entry)
Thomas, A. D., Dopita, M. A., Kewley, L. J., Groves, B. A., Sutherland, R. S., Hopkins, A. M., & Blanc, G. A. 2018a, ApJ, 856, 89 (ADS entry)
Thomas, A. D., Groves, B. A., Sutherland, R. S., Dopita, M. A., Kewley, L. J., & Jin, C. 2016, ApJ, 833, 266 (ADS entry)
Thomas, A. D., Kewley, L. J., Dopita, M. A., Groves, B. A., Hopkins, A. M., & Sutherland, R. S. 2018b, ApJL, 861, L2 (ADS entry)
Tremonti, C. A., et al. 2004, ApJ, 613, 898 (ADS entry)
Veilleux, S., & Osterbrock, D. E. 1987, ApJS, 63, 295 (ADS entry)
von der Linden, A., Wild, V., Kauffmann, G., White, S. D. M., & Weinmann, S. 2010, MNRAS, 404, 1231 (ADS entry)
Wild, V., Heckman, T., & Charlot, S. 2010, MNRAS, 405, 933 (ADS entry)
York, D. G., et al. 2000, AJ, 120, 1579 (ADS entry)

6

The mass-metallicity relation of local active galaxies

This chapter presents the content of the article *The mass-metallicity relation of local active galaxies* (A. D. Thomas et al., submitted to ApJ).

We systematically measure the gas-phase metallicities and the mass-metallicity relation of a large sample of local active galaxies for the first time. Observed emission-line fluxes from the Sloan Digital Sky Survey (SDSS) are compared to a four-dimensional grid of photoionization models using the Bayesian parameter estimation code NebulaBayes. For the first time we take into account arbitrary mixing between H II region and narrow-line region (NLR) emission, and the models are also varied with metallicity, ionization parameter in the NLR, and the gas pressure. The active galactic nucleus (AGN) oxygen abundance is found to increase by ΔO/H ~ 0.1 dex as a function of host galaxy stellar mass over the range $10.1 < \log M_*/M_\odot < 11.3$. We also measure the metallicity and ionization parameter of 51806 star-forming galaxies for comparison with the sample of 2766 Seyfert 2 galaxies. A systematic offset in oxygen abundance of 0.08 dex is observed between the mass-metallicity relations of the star-forming and active galaxies. We discuss sources of systematic uncertainty that may have contributed to the offset, which include the treatment in the models of diffuse ionized gas (DIG), dust, and the ionizing spectra. Optical diagnostic diagrams are presented with the star-forming and Seyfert data colored by the inferred oxygen abundance and ionization parameter, clearly illustrating the trends in both quantities.

6.1 Introduction

The gas-phase metallicity of a galaxy is the result of enrichment by stellar processes and the exchange of material with its environment (e.g. Lilly et al. 2013). The assembled stellar mass of a galaxy is known to be strongly positively correlated with its metallicity (e.g. Lequeux et al. 1979; Tremonti et al. 2004).

This mass-metallicity relation (or, similarly, the luminosity-metallicity relation; e.g. Zaritsky et al. 1994) has been measured for star-forming galaxies both locally (e.g. Tremonti et al. 2004) and at a range of redshifts (e.g. Zahid et al. 2014; Sanders et al. 2015; Wuyts et al. 2016). However, to date the mass-metallicity relation has not been cleanly measured for galaxies hosting active galactic nuclei (AGN).

Metallicity measurements in AGN have typically focused on the broad-line regions (BLRs) of Seyfert AGN and quasars (Hamann & Ferland 1999), although narrow-line region (NLR) abundances have also received some attention. Emission-line metallicity constraints for NLRs are reviewed by Dors et al. (2015), and include the diagnostics of Storchi-Bergmann et al. (1998) and Castro et al. (2017).

The mixing of H ii region and NLR excitation in Seyfert spectra is a key complication in the use of metallicity diagnostics. The analysis in this study compares observations to 'mixed' models that account for varying contributions from H ii region and NLR emission. Using a statistically powerful sample from the Sloan Digital Sky Survey (SDSS; York et al. 2000) and accounting for H ii-AGN mixing, we are able to investigate the AGN mass-metallicity relation in detail for the first time.

In Paper 1 (Thomas, A. D. et al. 2018, accepted to ApJL; Chapter 5) we studied the degree of mixing between star-forming and Seyfert narrow-line region (NLR) emission in the SDSS Seyfert spectra. In this study we present further results, including the parameter estimates for the metallicity, pressure and ionization parameter. We additionally expand our analysis to the SDSS star-forming galaxies to contextualize the results of the mixing analysis.

6.2 Method

Our approach uses the analysis tool NebulaBayes (Thomas et al. 2018), which performs Bayesian parameter estimation by comparing observed emission-line fluxes and errors with grids of theoretical fluxes.

6.2.1 Observational data

We use the same sample as in Paper 1. The data are taken from SDSS DR7 (Abazajian et al. 2009) and we apply cuts on redshift ($0.02 < z < 0.37$) and standard cuts on optical diagnostic diagrams (Kewley et al. 2006). After additional quality cuts (requiring a signal-to-noise ratio of 5 on the $H\beta$ line only) there remain 51806 spectra classified as star-forming and 2766 spectra classified as Seyfert 2. We consider only these classes in the analyses and deliberately exclude LINER, composite and ambiguous galaxies.

We use the stellar mass estimates of Zahid et al. (2013), which were measured by applying the Le Phare code (Arnouts et al. 1999; Ilbert et al. 2006) to ugriz-band photometry. The analysis used the Bruzual & Charlot (2003) stellar templates with a stellar population age range of $0 - 13$ Gyr, a Chabrier (2003) initial mass function, and a Calzetti et al. (2000) extinction law with a range in color excess of $0 < \mathrm{E(B-V)} < 0.6$.

6.2.2 Model data

For our analysis of the Seyfert galaxies we use a 'mixing' grid that combines MAPPINGS V (Sutherland & Dopita 2017) photoionization models of H II regions and NLRs. The grid has four parameters: oxygen abundance $12 + \log \mathrm{O/H}$, NLR ionization parameter $\log U_{\mathrm{NLR}}$, gas pressure $\log P/k$, and the fraction of the Balmer flux arising in the NLR as opposed to H II regions, f_{NLR}, with the ionizing Seyfert spectrum identical in all models. The H II and Seyfert nebulae are assumed to have the same metallicity and gas pressure. The ionization parameter in the H II-region component is fixed to $\log U_{\rm HII} = -3.25$.

The Seyfert model components use an ionizing spectrum from Thomas et al. (2016) that parameterizes the energy of the ionizing accretion disk emission by its peak energy, $E_{\rm peak}$. In Paper 1 we concluded that values of $E_{\rm peak}$ in the range $40 - 50$ eV result in plausible distributions of $f_{\rm NLR}$ measurements. In the present work we assume $E_{\rm peak} = 45\,{\rm eV}$. The assumptions embodied in the mixing grid are further discussed in Paper 1.

For our analysis of star-forming galaxies, we use a H II-region MAPPINGS grid over the two parameters of oxygen abundance and ionization parameter, with the gas pressure fixed to $\log P/k = 5.4\,{\rm cm}^{-3}\,{\rm K}$. The grid is otherwise identical to that described by Thomas et al. (2018). A diffuse ionized gas (DIG) component is not included in the models.

6.2.3 Application of NebulaBayes

For the mixing analysis we used the emission lines [O II] $\lambda\,3726 + 29$, [Ne III] $\lambda\,3869$, [O III] $\lambda\,4363$, Hβ, [O III] $\lambda\,5007$, He I $\lambda\,5876$, [O I] $\lambda\,6300$, H α, [N II] $\lambda\,6583$, and [S II] $\lambda\,6716+31$. Priors were applied on the [N II]/[O II] (N2O2) ratio (which slightly reduced the scatter in inferred metallicity) and the [S II] λ6731 / [S II] λ6716 line ratio (to constrain the gas pressure).

To fit the star-forming galaxies we applied the NebulaBayes 'line ratio prior' feature (described in the appendix of Thomas et al. 2018), in particular using [N II]/[O II] (N2O2) to constrain O/H and [O III]/[O II] (O3O2) to constrain the ionization parameter, with the N2O2 constraint weighted three times more heavily than the O3O2 constraint. This approach resulted in a smooth metallicity distribution over the entire range in O/H of more than a decade. The Balmer lines H α and Hβ were used for reddening correction and normalization.

We used the ability of NebulaBayes to deredden spectra to match the computed Balmer decrement at every point in the model grid. The dereddening method is described in the appendix of Vogt et al. (2013). For the two-parameter H II region analysis we used cubic interpolation of the model grids.

6.3 Results

6.3.1 Parameter estimates

Figure 6.1 presents optical diagnostic diagrams (Baldwin et al. 1981; Veilleux & Osterbrock 1987) showing the SDSS data colored by the parameter estimates.

There is systematic variation in measurements of the ionization parameter U in both the AGN and star-forming sequences. The gradient for Seyferts is perpendicular to the mixing line, with lower U inferred for data closer to the LINER region (a region associated with low U in the case of photoionized sources, e.g. Binette et al. 1994). The anticorrelation of U with metallicity in star-forming galaxies has been previously noted (e.g. Nagao et al. 2006; Dopita et al. 2006).

Figure 6.2 presents the parameter estimates for the Seyfert spectra as a function of projected distance along the mixing sequence, d. The panel for f_{NLR} is the same as the panel for $E_{\mathrm{peak}} = 45\,\mathrm{eV}$ in Figure 2 of Paper 1.

From Figure 6.2 we note the following:

1. Metallicity: The high $12 + \log \mathrm{O/H}$ measurements (medians of $1.4 - 1.7$ solar) are consistent with the 'mixing' with the high-metallicity end of the H II-region sequence (Figure 6.1). The $\sim$0.1 dex increase in median metallicities with d is likely associated with the $\sim$0.2 dex increase in median stellar mass with d (final panel).

2. Mixing fraction: The f_{NLR} estimates show that the Seyfert-classified SDSS spectra are highly contaminated by H II-region emission, and f_{NLR} increases smoothly along the mixing sequence (the f_{NLR} results are the subject of Paper 1).

3. Ionization parameter: The measured U_{NLR} is typically in the tight range $-3.3 < \log U_{\mathrm{NLR}} < -2.7$, and shows little variation as a function of d. The gradient in $\log U_{\mathrm{NLR}}$ in Figure 6.1 is not evident in Figure 6.2 because the gradient is approximately orthogonal to the mixing line. The lower inferred U at low f_{NLR} (low d) may be due to LINER or DIG contamination.

4. Pressure: The median inferred $\log P/k$ values increase by approximately 1.5 dex along the mixing sequence.

The trend in P/k may arise because NLR pressures are typically higher than the

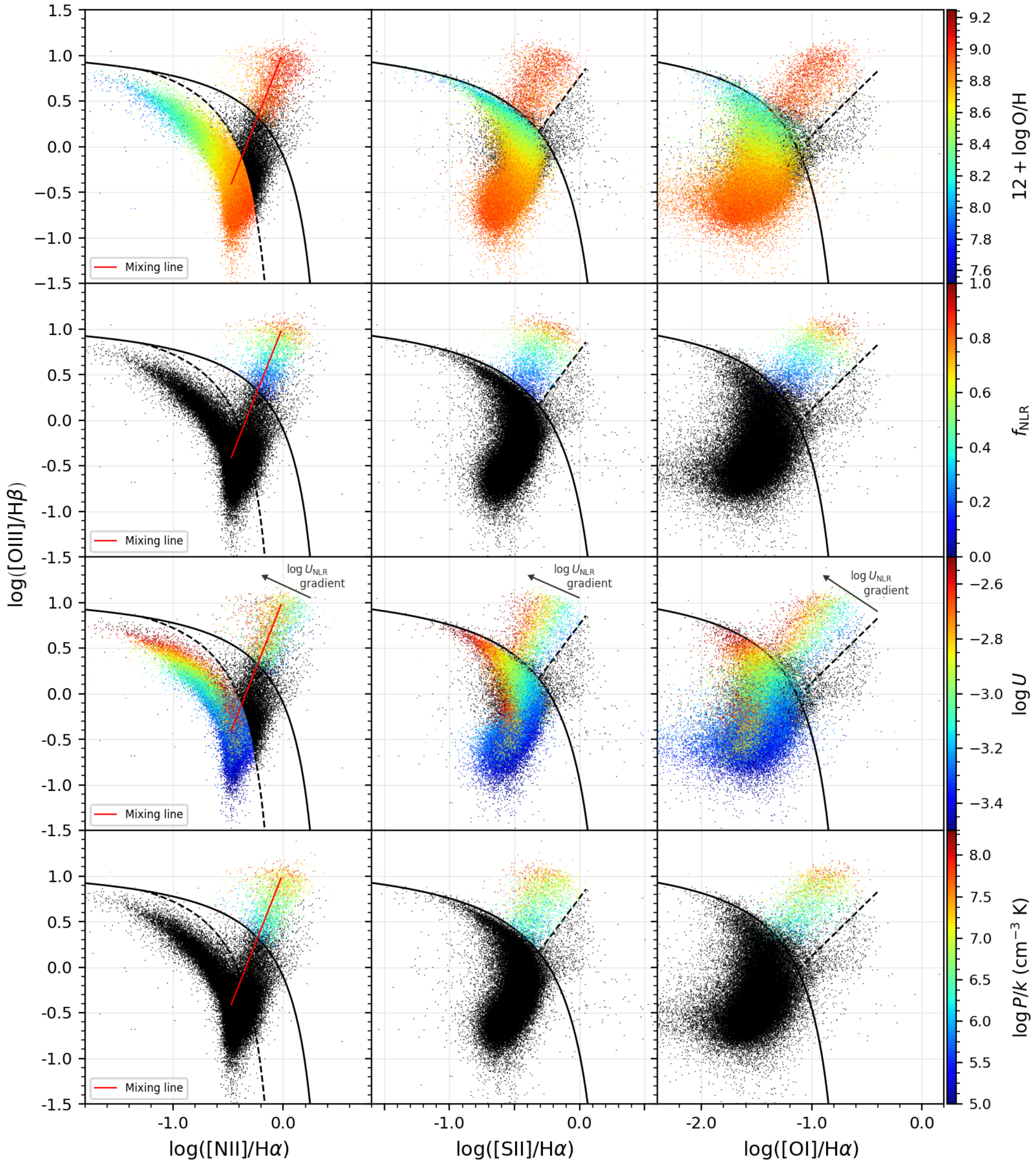

Figure 6.1 Optical diagnostic diagrams for SDSS emission-line galaxies with data colored by the NebulaBayes parameter estimates. Only spectra with 'Seyfert' or 'H II' classifications were analyzed; other data is shown in black below any colored data. The red line in each panel of the leftmost column is an approximate 'mixing line' designed to trace the upper H II-AGN mixing sequence (see Paper 1). The Seyfert ionization parameter estimates are for the NLR component of the mixed models ($\log U_{\rm NLR}$); the H II components had a fixed $\log U_{\rm HII} = -3.25$. From the top row to the bottom, the diagrams show that Seyfert NLRs are generally high-metallicity, highly contaminated by H II emission, systematically varying in $\log U_{\rm NLR}$, and are characterized by a high gas pressure.

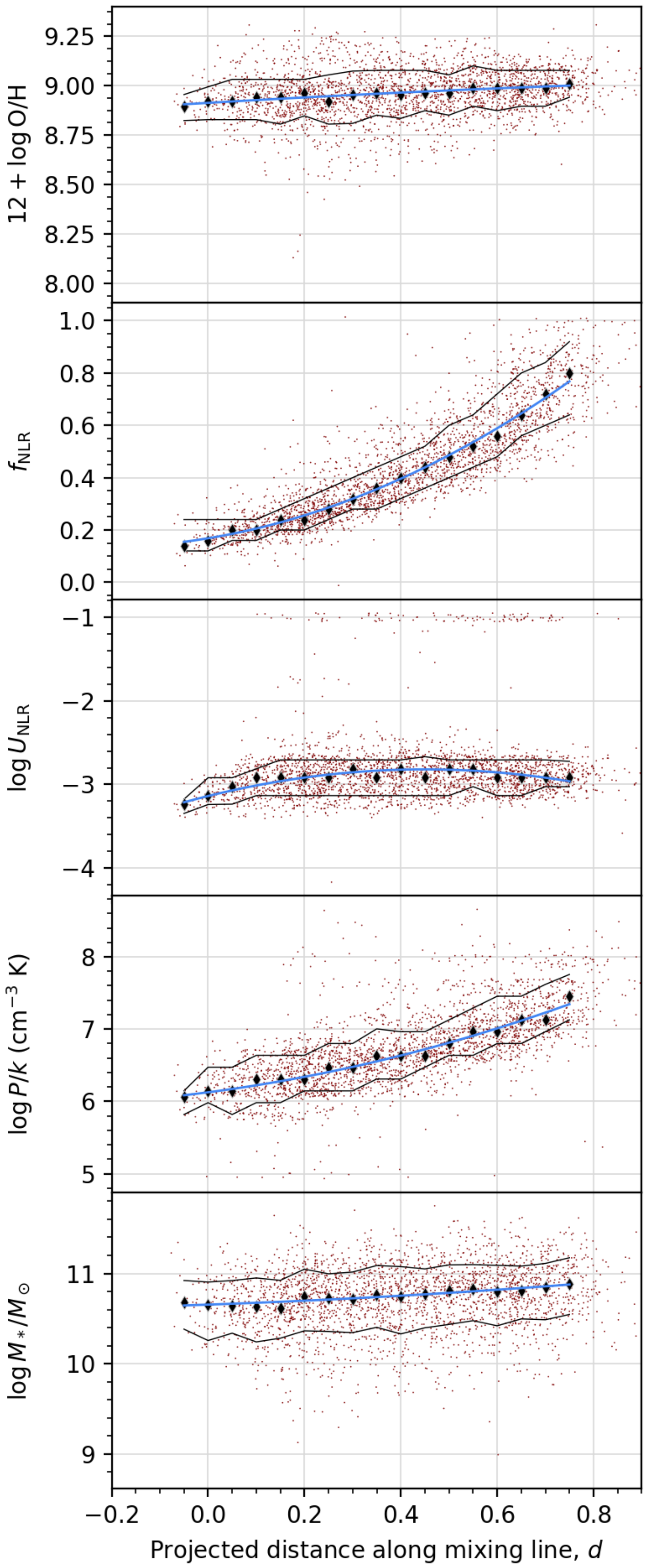

Figure 6.2 Derived values for SDSS Seyfert 2 galaxies plotted against d, the dimensionless projected distance along the mixing line on the log-log BPT diagram (Figure 6.1). The value $d = 0$ corresponds to the intersection of the mixing line and the Kewley et al. (2001) extreme starburst line.

pressures in contaminating star-forming and DIG regions. This explains why the inferred P increases as $f_{\rm NLR}$ increases. However, the models used to derive the parameter estimates assumed that the pressures in the H II and NLR components were equal, and the location and shape of the P/k sequence in Figure 6.2 is likely sensitive to this assumption.

6.3.2 Mass-metallicity relation

Figure 6.3 presents the mass-metallicity relation resulting from our oxygen abundance measurements for both the H II- and Seyfert-classified spectra. We fit a quadratic $a_0 + a_1 x + a_2 x^2$ to the medians and errors in each mass bin, with fitted coefficients of $(a_0, a_1, a_2) = (-0.0647, 1.4426, 0.9510)$ and (-0.1338, 2.9247, -7.0751) for the NLR and H II spectra respectively. The offset between the H II and NLR sequences is discussed in Section 6.4.1.

6.3.3 Comparison to literature

Figure 6.4 shows how our results compare to other mass-metallicity relations in the literature. The well-known systematic offsets between different metallicity calibrations (Kewley & Ellison 2008) are apparent.

6.4 Discussion

Seyfert nuclei are known to generally reside in massive galaxies (e.g. Heckman & Best 2014). Our derived AGN mass-metallicity relation is similar to that of star-forming galaxies, albeit covering only the high-mass end of the relation.

We detect an increase in AGN metallicity with galaxy mass, with the median oxygen abundance increasing by ~0.1 dex over the range $10.1 < \log M_*/M_\odot < 11.3$. This is consistent with the observation of Groves et al. (2006) that [N II] emission generally increases with the stellar mass of SDSS active galaxies, interpreted by the authors as an increase in metallicity with mass.

We confirm the results of Groves et al. (2006) and others that sub-solar AGN are rare in the SDSS sample. Low-metallicity AGN should lie between the 'wings' of the BPT 'butterfly diagram' (e.g. Kawasaki et al. 2017), but in our sample objects

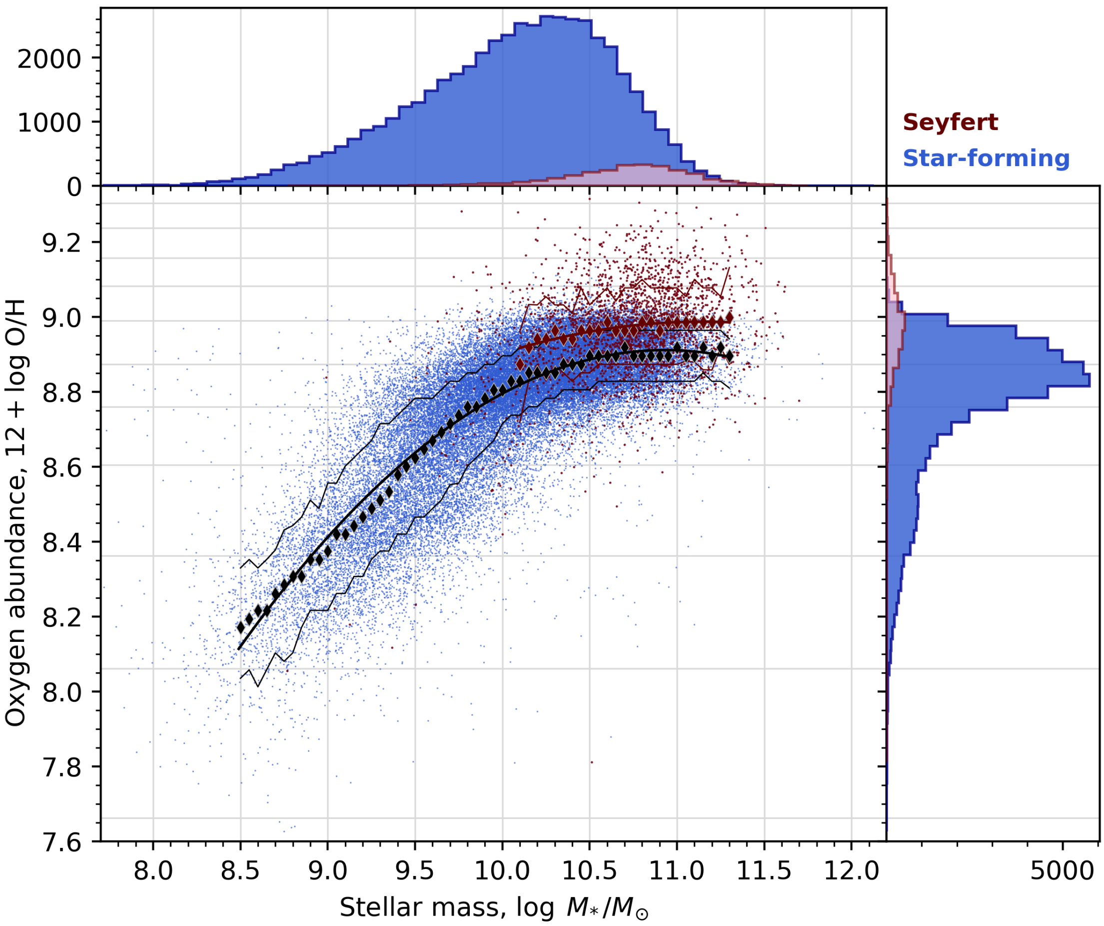

Figure 6.3 The SDSS galaxy mass-metallicity relations resulting from our inferred oxygen abundances. Horizontal gridlines show the photoionization model metallicities used for the H II, NLR and mixed grids. Marginal histograms show the distributions of stellar mass and oxygen abundance for the star-forming galaxies (blue) and the AGN (red). The results reproduce the well-known relationship between galaxy stellar mass and gas-phase oxygen abundance in SDSS star-forming galaxies (e.g. Tremonti et al. 2004). The Seyfert 2 galaxies follow a locus similar to the upper end of the star-forming galaxy sequence.

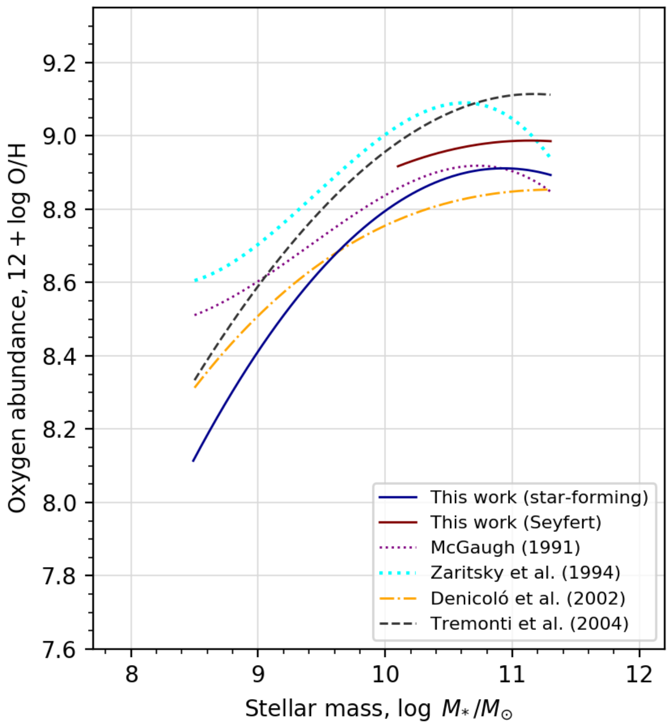

Figure 6.4 Comparison of our inferred mass-metallicity relations with those derived using other metallicity estimates. The equations for the calibrations of McGaugh (1991), Zaritsky et al. (1994), Denicoló et al. (2002), and Tremonti et al. (2004) are as reported in Table 2 of Kewley & Ellison (2008).

in this region are inferred to have unusually high ionization parameter rather than unusually low metallicity (Figure 6.1).

6.4.1 Sources of systematic error

We list the most important causes of systematic uncertainties in our derived metallicities:

1. Omission of DIG in the H II models: DIG contamination is associated with lower pressure, lower ionization parameter, and harder ionising spectra than H II-region emission, and may cause systematic offsets in metallicity measurements (Pilyugin et al. 2018). We expect the mixing analysis to be less sensitive to DIG contamination because NLRs in Seyfert-classified objects are likely far more luminous than DIG, and the NLR models include DIG-like emission from the partially ionized zone.

2. Treatment of dust: Dust destruction is not included in our models but does

occur in AGN NLRs, as evidenced by observations of coronal lines in Seyfert spectra (e.g. Dopita et al. 2015). Dust destruction in NLRs would lead to more free species contributing to line cooling than in models at the same metallicity, resulting in overestimation of metallicities.

3. The ionizing spectra: Ionizing stellar spectra are uncertain (e.g. Morisset et al. 2004) because of model sensitivity to properties such as stellar rotation, helium dredge-up, mass-loss rates, and binarity, and additional issues with stellar track and stellar atmosphere models such as poor parameter-space coverage, interpolation, and inconsistent abundance sets. The ionizing spectra in NLRs are also uncertain, although our $f_{\rm NLR}$ parameter may partially compensate for variations in the ionizing Seyfert spectrum.

4. Treatment of pressure: We fixed the pressure in the H II models and constrained the H II and NLR pressures to be equal in the mixed models. To test sensitivity we experimented with different fixed gas pressures in the star-forming galaxy analysis ($\log P/k\,[\mathrm{cm}^{-3}\,\mathrm{K}] = 4.6$ and 6.2 rather than 5.4 as in Figure 6.3). The different pressures shifted the inferred H II sequence up (for higher P) or down (for lower P) by $\sim$0.05 dex in oxygen abundance.

The systematic offset in oxygen abundance of 0.08 dex between the star-forming and active galaxies in Figure 6.3 is typical of offsets between metallicity calibrations (Kewley & Ellison 2008). We attribute the offset to one or more of the above systematic issues, noting that the H II and NLR models used the same photoionization code (MAPPINGS V) and abundances. The uncertainties in the ionizing spectra and the omission of a DIG contribution in the H II models are favored as important contributors to the offset. Emission from DIG is ubiquitous and contributes $\sim 10 - 70\%$ of the H α luminosity in star-forming galaxies, with later (earlier) types showing contributions at the lower (higher) end of this range (e.g. Lacerda et al. 2018).

6.4.2 Comparison of method with Tremonti et al. (2004)

We observe a greater degree of scatter in Figure 6.3 than was found by Tremonti et al. (2004). This is likely be because those authors used theoretical models by Charlot & Longhetti (2001) that explicitly included contributions from DIG, and that were calibrated using the observed line ratios of nearby galaxies. The differing treatment of DIG may also explain the larger offset between the Tremonti et al.

(2004) and our star-forming galaxy sequence for high-mass galaxies (Lacerda et al. 2018).

Tremonti et al. (2004) did not use priors, but instead used the likelihood to make parameter estimates. Our priors were derived by comparing observed and predicted line ratios, which is conceptually similar to the Tremonti et al. (2004) method.

6.5 Conclusions

We use a Bayesian method to analyze the line emission in SDSS AGN and star-forming galaxies, in particular making systematic measurements of the gas-phase metallicities. The method accounts for mixing between H II-region and NLR emission in AGN for the first time.

We conclude that the inferred AGN metallicities increase with the galaxy stellar mass, as is the case for star-forming galaxies. The SDSS AGN are located in high-metallicity and high-mass galaxies, and are rare or difficult to detect in lower-mass galaxies.

We look forward to applying similar analyses across large samples of AGN with spectroscopic data that is spatially-resolved, beginning with data from the S7 survey (Dopita et al. 2015; Thomas et al. 2017).

Acknowledgements

We thank H. Jabran Zahid for providing the stellar mass estimates used in this work. This research was conducted by the Australian Research Council Centre of Excellence for All Sky Astrophysics in 3 Dimensions (ASTRO 3D), through project number CE170100013. B.G. acknowledges the support of the Australian Research Council as the recipient of a Future Fellowship (FT140101202). M.D. and R.S. acknowledge support from ARC discovery project #DP160103631. This research is supported by an Australian Government Research Training Program (RTP) Scholarship.

6.6 References

Abazajian, K. N., et al. 2009, ApJS, 182, 543 (ADS entry)

Arnouts, S., Cristiani, S., Moscardini, L., Matarrese, S., Lucchin, F., Fontana, A., & Giallongo, E. 1999, MNRAS, 310, 540 (ADS entry)

Baldwin, J. A., Phillips, M. M., & Terlevich, R. 1981, PASP, 93, 5 (ADS entry)

Binette, L., Magris, C. G., Stasińska, G., & Bruzual, A. G. 1994, A&A, 292, 13 (ADS entry)

Bruzual, G., & Charlot, S. 2003, MNRAS, 344, 1000 (ADS entry)

Calzetti, D., Armus, L., Bohlin, R. C., Kinney, A. L., Koornneef, J., & Storchi-Bergmann, T. 2000, ApJ, 533, 682 (ADS entry)

Castro, C. S., Dors, O. L., Cardaci, M. V., & Hägele, G. F. 2017, MNRAS, 467, 1507 (ADS entry)

Chabrier, G. 2003, PASP, 115, 763 (ADS entry)

Charlot, S., & Longhetti, M. 2001, MNRAS, 323, 887 (ADS entry)

Denicoló, G., Terlevich, R., & Terlevich, E. 2002, MNRAS, 330, 69 (ADS entry)

Dopita, M. A., et al. 2006, ApJS, 167, 177 (ADS entry)

Dopita, M. A., et al. 2015, ApJS, 217, 12 (Link)

Dors, O. L., Cardaci, M. V., Hägele, G. F., Rodrigues, I., Grebel, E. K., Pilyugin, L. S., Freitas-Lemes, P., & Krabbe, A. C. 2015, MNRAS, 453, 4102 (ADS entry)

Groves, B. A., Heckman, T. M., & Kauffmann, G. 2006, MNRAS, 371, 1559 (ADS entry)

Hamann, F., & Ferland, G. 1999, ARA&A, 37, 487 (ADS entry)

Heckman, T. M., & Best, P. N. 2014, ARA&A, 52, 589 (Link)

Ilbert, O., et al. 2006, A&A, 457, 841 (ADS entry)

Kawasaki, K., Nagao, T., Toba, Y., Terao, K., & Matsuoka, K. 2017, ApJ, 842, 44 (ADS entry)

Kewley, L. J., Dopita, M. A., Sutherland, R. S., Heisler, C. A., & Trevena, J. 2001, ApJ, 556, 121 (ADS entry)

Kewley, L. J., & Ellison, S. L. 2008, ApJ, 681, 1183 (ADS entry)

Kewley, L. J., Groves, B., Kauffmann, G., & Heckman, T. 2006, MNRAS, 372, 961 (ADS entry)

Lacerda, E. A. D., et al. 2018, MNRAS, 474, 3727 (ADS entry)

Lequeux, J., Peimbert, M., Rayo, J. F., Serrano, A., & Torres-Peimbert, S. 1979, A&A, 80, 155 (ADS entry)

Lilly, S. J., Carollo, C. M., Pipino, A., Renzini, A., & Peng, Y. 2013, ApJ, 772, 119 (ADS entry)

McGaugh, S. S. 1991, ApJ, 380, 140 (ADS entry)

Morisset, C., Schaerer, D., Bouret, J.-C., & Martins, F. 2004, A&A, 415, 577 (ADS entry)

Nagao, T., Maiolino, R., & Marconi, A. 2006, A&A, 459, 85 (ADS entry)

Pilyugin, L. S., Grebel, E. K., Zinchenko, I. A., Nefedyev, Y. A., Shulga, V. M., Wei, H., & Berczik, P. P. 2018, A&A, 613, A1 (ADS entry)

Sanders, R. L., et al. 2015, ApJ, 799, 138 (ADS entry)

Storchi-Bergmann, T., Schmitt, H. R., Calzetti, D., & Kinney, A. L. 1998, AJ, 115, 909 (ADS entry)

Sutherland, R. S., & Dopita, M. A. 2017, ApJS, 229, 34 (ADS entry)

Thomas, A. D., Dopita, M. A., Kewley, L. J., Groves, B. A., Sutherland, R. S., Hopkins, A. M., & Blanc, G. A. 2018, ApJ, 856, 89 (ADS entry)

Thomas, A. D., Groves, B. A., Sutherland, R. S., Dopita, M. A., Kewley, L. J., & Jin, C. 2016, ApJ, 833, 266 (ADS entry)

Thomas, A. D., et al. 2017, ApJS, 232, 11 (ADS entry)

Tremonti, C. A., et al. 2004, ApJ, 613, 898 (ADS entry)

Veilleux, S., & Osterbrock, D. E. 1987, ApJS, 63, 295 (ADS entry)
Vogt, F. P. A., Dopita, M. A., & Kewley, L. J. 2013, ApJ, 768, 151 (ADS entry)
Wuyts, E., et al. 2016, ApJ, 827, 74 (ADS entry)
York, D. G., et al. 2000, AJ, 120, 1579 (ADS entry)
Zahid, H. J., Dima, G. I., Kudritzki, R.-P., Kewley, L. J., Geller, M. J., Hwang, H. S., Silverman, J. D., & Kashino, D. 2014, ApJ, 791, 130 (ADS entry)
Zahid, H. J., Geller, M. J., Kewley, L. J., Hwang, H. S., Fabricant, D. G., & Kurtz, M. J. 2013, ApJL, 771, L19 (ADS entry)
Zaritsky, D., Kennicutt, Jr., R. C., & Huchra, J. P. 1994, ApJ, 420, 87 (ADS entry)

7

Conclusions and summary

In this chapter I summarise the key conclusions of the preceding chapters and expound some potential directions for future work.

7.1 On the ionizing spectra of Seyfert galaxies

In Chapter 2 (published by Thomas et al. 2016), a model of the spectrum of ionizing Seyfert radiation was presented. This new model, OXAF, was based on physical models (Done et al. 2012) that were simplified to remove degeneracies between model inputs and to parametrise the spectrum in terms of only three intuitive parameters. The effects of the SMBH mass and AGN luminosity on the output spectrum are entirely degenerate in the physical model, and these parameters were combined into the parameter E_{peak}, which is the energy of the peak of the accretion disc emission.

The effect of the soft X-ray excess on predictions of the strong optical lines was found to be minor. The soft X-ray excess was therefore excluded from the OXAF model.

The three OXAF parameters are $E_{\rm peak}$, the photon power-law index for the X-ray tail Γ, and the proportion of the total flux that goes to the non-thermal component, $p_{\rm NT}$. All three of these parameters have important impacts on the fluxes of strong optical emission lines predicted by photoionisation modelling.

7.2 The Siding Spring Southern Seyfert Spectroscopic Snapshot Survey

The second and final data release of the *Siding Spring Southern Seyfert Spectroscopic Snapshot Survey* (S7) was presented in Chapter 3 (published by Thomas et al. 2017). This integral field spectroscopy (IFS) survey used the WiFeS instrument on the ANU 2.3 m telescope, configured to take spectra over a $25 \times 38''$ field with $1 \times 1''$ spatial pixels and a spectral resolution of $R = 3000$ in the blue arm and $R = 7000$ in the red arm.

The survey sample was selected to include nearby galaxies ($z \lesssim 0.02$) that are detected in the radio (where data were available), are away form the Galactic plane, and are visible from the southern hemisphere ($\delta < +10°$). In total the sample consists of 131 galaxies, with approximately 18 Seyfert 1 galaxies, 77 Seyfert 2 galaxies, 27 LINERs, and 11 starburst galaxies.

Extensive value-added products are provided with the data release. The data products available for each galaxy include data cubes from the blue and red arms of WiFeS, emission line fitting results (for fits with 1, 2 and 3 Gaussian components as well as a 'best' number of components selected by the artificial neural network LZCOMP; Hampton et al. 2017), nuclear spectra binned in a $4''$ aperture, and nuclear emission-line fluxes that were corrected for interstellar reddening. Figures in Chapter 3 present maps of gas excitation, line-of-sight velocity and velocity dispersion for each galaxy. The nuclear spectra were classified on optical diagnostic diagrams.

7.3 Spatially resolved analysis of Seyfert galaxies

The difficulty in measuring the metallicity of Seyfert-excited nebulae and the lack of integral field spectroscopy of active galaxies have to date prevented measurement of metallicity gradients in Seyfert galaxies. In Chapter 4 (published by Thomas et al. 2018) a new analysis code, NebulaBayes, is presented and used to measure the metallicity of Seyfert extended narrow-line regions (ENLRs) in two dimensions for the first time.

Four galaxies from the S7 survey were selected for being dominated by Seyfert-classified excitation across the WiFeS field of view. These nearby active galaxies are ESO 138-G01, IC 5063, Mrk 573 and NGC 2992, all of which have ENLRs extending over multiple kiloparsecs.

The theoretical data consisted of a MAPPINGS photoionisation model grid over the four dimensions of metallicity, ionization parameter U, pressure P and the hardness of the ionizing continuum E_{peak}. The results simultaneously constrain each of these parameters in every Seyfert-classified spatial bin in all four galaxies.

We observed steep metallicity gradients from the nucleus into the ionisation cones in the edge-on disc galaxy NGC 2992, with the metallicity decreasing by up to half a dex over the observed ENLR extent. In the ENLR of the E-S0 galaxy ESO 138-G01 we measure an *inverse* abundance gradient that we associate with a recent inflow of relatively low-metallicity gas, possibly during a minor merger.

We observe near-constant ionization parameters but steeply radially-decreasing pressures in all four ENLRs, implying that radiation pressure from the AGN has regulated the density structure of the ISM on kiloparsec scales. The systematic measurements of the hardness of the ionizing continuum (parametrised by E_{peak}) show significant spatial variation, with the hardest radiation associated with emission in the 'ionisation cones'. The spatial variation in E_{peak} does not appear to be qualitatively described by either time-varying black hole accretion or by variable filtering of the ionising spectrum by material lying between the nucleus and observed nebulae. Instead we prefer spectral contamination (from shock or HII-region excitation) as an explanation for the E_{peak} variation.

7.4 HII - AGN mixing in Seyfert spectra

The analysis of Seyfert excitation in the Sloan Digital Sky Survey (SDSS) sample has been hindered by the fact that the single nuclear spectrum for each Seyfert galaxy contains emission from nebulae in both H II regions and the AGN NLRs. In Chapter 5 (accepted for publication in Astrophysical Journal Letters) an analysis is presented that solves this problem by fitting models derived by mixing pure AGN and pure H II-region models. The NebulaBayes code is used with a four-dimensional ‘mixing’ grid that has parameters for the metallicity, ionisation parameter in the NLR, gas pressure, and mixing fraction f_{NLR} (proportion of the Balmer flux arising in the NLR component as opposed to the star-forming component).

The results are the first systematic measurement of the H II-region contamination in SDSS Seyfert spectra. We find that the majority of the AGN-classified spectra in SDSS have the majority of their Balmer flux arising in H II regions as opposed to NLR clouds within the fiber aperture. Median ‘mixing levels’ are quantified on the standard BPT optical diagnostic diagram. We also provide a table of contributions to strong optical emission-line fluxes from each of the H II and NLR model components, for the arbitrary mixing of two fiducial H II and NLR models.

The conclusions are not sensitive to the assumed hardness of the ionising continuum. Additionally, we demonstrate that the fixed ionization parameter adopted for the H II regions has only a weak effect on inferred mixing fractions.

7.5 The gas-phase metallicity and mass-metallicity relation of local Seyfert galaxies

Chapter 6 (submitted to Astrophysical Journal Letters) presented a continuation of the work of Chapter 5. The NebulaBayes analysis constrained four parameters, with Chapter 5 presenting the results for only the mixing fraction f_{NLR}. In Chapter 6 the results for the other three parameters were presented, with a focus on the gas-phase metallicity. An analysis of star-forming galaxies was also included to enable comparison with the Seyfert galaxy results.

We presented the first systematically measured mass-metallicity relation for local active galaxies. The AGN are found to lie near the high-mass end of the mass-metallicity relation of star-forming galaxies. We detect a small increase in AGN metallicity over the range of host galaxy stellar masses in the sample. A small offset of 0.08 dex in oxygen abundance is found between the AGN and star-forming galaxy mass-metallicity relations. We discuss some of the systematic issues that may have given rise to this offset.

7.6 Future work

Several avenues for future research are natural continuations of the progress made in this thesis. In particular, the NebulaBayes code is very general and may be applied more widely both to constrain new parameters (e.g. parametrising abundances using both O/H and N/O) and to analyse different types of ionised nebulae (e.g. shock-excited regions and planetary nebulae). These additional analyses will require the computation of new grids of photoionisation (or shock) models. Measuring shock parameters in AGN-driven outflows is one particularly intriguing potential future direction.

Chapter 2 presented the OXAF model of the ionising spectrum of Seyfert galaxies, and the effects of the parameters on predicted emission lines were examined. A logical extension to this work is to constrain the parameters of the OXAF model by comparing observed coronal lines to detailed photoionization modelling. The coronal lines arise in species with high ionisation potentials and therefore effectively probe an otherwise inaccessible region of the SED. Some modelling of coronal lines under various dust destruction scenarios was undertaken during the doctoral candidature, but the research was not sufficiently advanced to include in this thesis.

Many aspects of the data in the S7 survey (Chapter 3) remain to be exploited, including the frequently observed nuclear coronal lines. In particular, the spatial analysis presented in Chapter 4 for four S7 galaxies could be augmented with an analysis using one or more mixed model grids as in Chapter 5 and Chapter 6. Using such an approach it may prove possible to measure the gas-phase metallicity across the field of view of the vast majority of objects in the S7 sample. These techniques hold great promise for ultimately enabling systematic measurements of metallicity regardless of the diagnostic classification of an observed nebula, i.e. regardless of the cause of the ionisation.

The analysis in Chapter 4 included the first example of a gradient in measured metallicities along the vertical (z) direction in a disc galaxy. It may now be possible to constrain the z-metallicity gradients of a sizeable sample of edge-on Seyfert galaxies, using data from integral field surveys such as MaNGA (Bundy et al. 2015) and SAMI (Green et al. 2018), which boast samples of thousands of galaxies.

7.7 References

Bundy, K., et al. 2015, ApJ, 798, 7 (ADS entry)

Done, C., Davis, S. W., Jin, C., Blaes, O., & Ward, M. 2012, MNRAS, 420, 1848 (Link)

Green, A. W., et al. 2018, MNRAS, 475, 716 (ADS entry)

Hampton, E. J., et al. 2017, MNRAS, 470, 3395 (ADS entry)

Thomas, A. D., Dopita, M. A., Kewley, L. J., Groves, B. A., Sutherland, R. S., Hopkins, A. M., & Blanc, G. A. 2018, ApJ, 856, 89 (ADS entry)

Thomas, A. D., Groves, B. A., Sutherland, R. S., Dopita, M. A., Kewley, L. J., & Jin, C. 2016, ApJ, 833, 266 (ADS entry)

Thomas, A. D., et al. 2017, ApJS, 232, 11 (ADS entry)